The Role of ECSIT in Mitochondrial Dysfunction Mediated Cardiomyopathy

Thesis

The Role of ECSIT in Mitochondrial Dysfunction Mediated Cardiomyopathy

Thomas Nicol

Mammalian Genetics Unit, Medical Research Council Harwell Institute, Harwell, UK

The Open University

Discipline: Life and Biomolecular Sciences

A thesis submitted for the degree of Doctor of Philosophy

April 2018

Abstract

The evolutionarily conserved signalling intermediate in the toll pathway (ECSIT) is a 50 kDa protein involved in the function of many pathways and implicated in a variety of phenotypes. It functions as part of the toll pathway by integrating the signal from several toll receptors and facilitating the activation of downstream proteins NFKB, JNK and P38 MAPK. It functions as part of the bone morphogenetic protein pathway through interaction with SMAD4 allowing for normal embryonic development. It also functions as a mitochondrial complex I assembly factor and loss of function leads to a reduction in fully assembled complex I.

As part of a large scale ENU mutagenesis screen, The Harwell Ageing Screen, a novel missense mutation (N209I) was identified in ECSIT which resulted in a hypertrophic cardiomyopathy phenotype in homozygous mutant animals.

Further investigation revealed this phenotype to be a result of a loss of function in ECSIT's role as a complex I assembly factor. Mitochondria from *Ecsit*$^{N209I/N209I}$ hearts showed a reduction in total complex I protein as well as a loss of enzymatic activity and fully assembled complex I. Interestingly, this mitochondrial dysfunction was limited to the heart with other tissues maintaining protein levels and complex I function at or close to wild type levels, suggesting that there may be tissue specific differences in the complex I assembly pathway. Investigation of the assembly pathway using first and second dimensional blue native PAGE suggests that this tissue specific pathway may involve the formation of a previously undescribed fragment of ECSIT that is present in heart tissue but absent from other tissues tested, is associated with fully assembled complex I in wild type mitochondria but absent in *Ecsit*$^{N209I/N209I}$ hearts.

Abbreviations

ADP	Adenosine Diphosphate
ATP	Adenosine Triphosphate
AV	Atrioventricular
BMP	Bone Morphogenetic Protein
BN-PAGE	Blue Native Polyacrylamide Gel Electrophoresis
CFU	Colony Forming Unit
CK	Creatine Kinase
CMR	Cardio Magnetic Resonance Imaging
CPEO (PEO)	Chronic Progressive External Ophthalmoplegia
DCM	Dilated Cardiomyopathy
DMEM	Dulbecco's Modified Eagle's Medium
DNA	Deoxyribonucleic Acid
EDL	Extensor Digitorum Longus
ENU	N-Ethyl-N-Nitrosourea
ETC	Electron Transport Chain
FAD	Flavin Adenine Dinucleotide
FBS	Foetal Bovine Serum
FCCP	Carbonyl Cyanide-4-(Trifluoromethoxy)Phenylhydrazone
FMN	Flavin Mononucleotide
FT-MS	Fourier Transform Mass Spectrometry
GFP	Green Fluorescent Protein

H&E	Haematoxylin and Eosin
HCM	Hypertrophic Cardiomyopathy
HEK293	Human Embryonic Kidney Cells
IMF	Intermyofibrillar
IMM	Inner Mitochondrial Membrane
IMS	Inter Membrane Space
IPGTT	Intraperitoneal Glucose Tolerance Test
LDS	Lithium Dodecyl Sulphate
LPS	Lipopolysaccharide
MEF	Mouse Embryonic Fibroblast
MELAS	Mitochondrial Encephalomyopathy, Lactic Acidosis and Stroke-Like Episodes
MEM	Minimum Essential Medium
MERRF	Myoclonic Epilepsy with Ragged Red Fibres
MHC	Myosin Heavy Chain
MPC	MUTA-PED-C3pde
mRNA	Messenger Ribonucleic Acid
mROS	Mitochondrial Reactive Oxygen Species
mtDNA	Mitochondrial Deoxyribonucleic Acid
MTS	Mitochondrial Targeting Sequence
NADH	Nicotinamide Adenine Dinucleotide
NARP	Neuropathy, Ataxia and Retinitis Pigmentosa
nDNA	Nuclear Deoxyribonucleic Acid

OMM	Outer Mitochondrial Membrane
OXPHOS	Oxidative Phosphorylation
PBS	Phosphate Buffered Saline
PCR	Polymerase Chain Reaction
PCr	Phosphocreatine
PH	Pleckstrin Homology
P_i	Inorganic Phosphate
PN	Perinuclear
PP	Phosphorylation Potential
PPR	Pentatricopeptide Repeat
qPCR	Quantitative Polymerase Chain Reaction
RNA	Ribonucleic Acid
rRNA	Ribosomal Ribonucleic Acid
ROS	Reactive Oxygen Species
SDS-PAGE	Sodium Dodecyl Sulphate Polyacrylamide Gel Electrophoresis
siRNA	Small Interfering Ribonucleic Acid
SNP	Single Nucleotide Polymorphism
SS	Sub-sarcolemmal
TAC	Transverse Aortic Constriction
TAP	Tandem Affinity Purification
TCA	Tri-Carboxylic Acid (Cycle)
TLR	Toll Like Receptor

tRNA	Transfer Ribonucleic Acid
UPR^{er}	Endoplasmic Reticulum Unfolded Protein Response
UPR^{mt}	Mitochondrial Unfolded Protein Response
WPWS	Wolf-Parkinson-White Syndrome

Contents

List of Figures

List of Tables

Chapter 1: Introduction

1.1. Mitochondria

Mitochondria are present in almost all eukaryotic cells where their primary role is the production of ATP (adenosine triphosphate) as an energy source for other cellular processes. Mitochondria themselves are double membrane bound organelles that are believed to have evolved from gram-negative bacteria roughly 2 billion years ago. Through an endosymbiotic relationship with a eukaryotic ancestor, they have gradually lost the majority of their genome and transformed into the organelle that we study today [1].

In the human heart, mitochondria occupy as much as 30% of the myocardial volume [1] and are responsible for producing energy in the form of around 300mg of ATP for every beat [2].

1.1.1. Structure and function

Mitochondria are tubular structures, typically about 0.1-0.5µm across, consisting of an outer and inner membrane each with their own unique properties [3]. The outer membrane is typically smooth in appearance and is permeable to molecules up to approximately 5kDa in size allowing for the natural diffusion of many molecules such as ADP, ATP, ions and small proteins [4]. Whilst the outer membrane is composed mainly of a phospholipid bilayer, the inner membrane has a higher proportion of proteins and in addition to phospholipids contains the mitochondrial specific lipid, cardiolipin [5-7]. It is the specific properties of cardiolipin that allows the inner membrane to fold and form invaginations known as cristae. These are the main sites of the oxidative phosphorylation (OXPHOS) machinery [7, 8].

The arrangement of the two membranes results in the formation of two spaces within the mitochondria. The first, between the two membranes, is the inter membrane space (IMS) and is essential for the mitochondria to perform OXPHOS as it forms a compartment into which protons are pumped, allowing for the establishment of a proton gradient. The other is the space enclosed by the inner membrane, referred to as the mitochondrial matrix which houses the mitochondrial DNA, and is the site of the tricarboxylic acid (TCA) cycle [8].

Despite their similarities in membrane structure, mitochondria are capable of taking on a variety of appearances, from small filamentous or punctate units, to large networks spanning a cell. There are also a variety of mitochondrial subpopulations that may take on different metabolic profiles or roles within a cell. In both skeletal and cardiac muscle these are grouped into subsarcolemmal (SS), intermyofibrillar (IMF) and perinuclear (PN) populations (Figure 1.1) [9-11].

As the name would suggest, perinuclear mitochondria cluster around the nucleus and are thought to be involved in transcription and translation. Intermyofibrillar mitochondria have a small and compact structure and are organised in rows between muscle fibres in order to provide energy to the contractile machinery [12, 13]. Finally, subsarcolemmal mitochondria are slightly larger in appearance and sit immediately adjacent to the sarcolemma. They are slightly larger in size and demonstrate less organisation [9, 13]. There is evidence to suggest that there are considerable differences in SS and IMF mitochondrial metabolism, but that this is dependent on the muscle fibre type and health of the tissue in question [9].

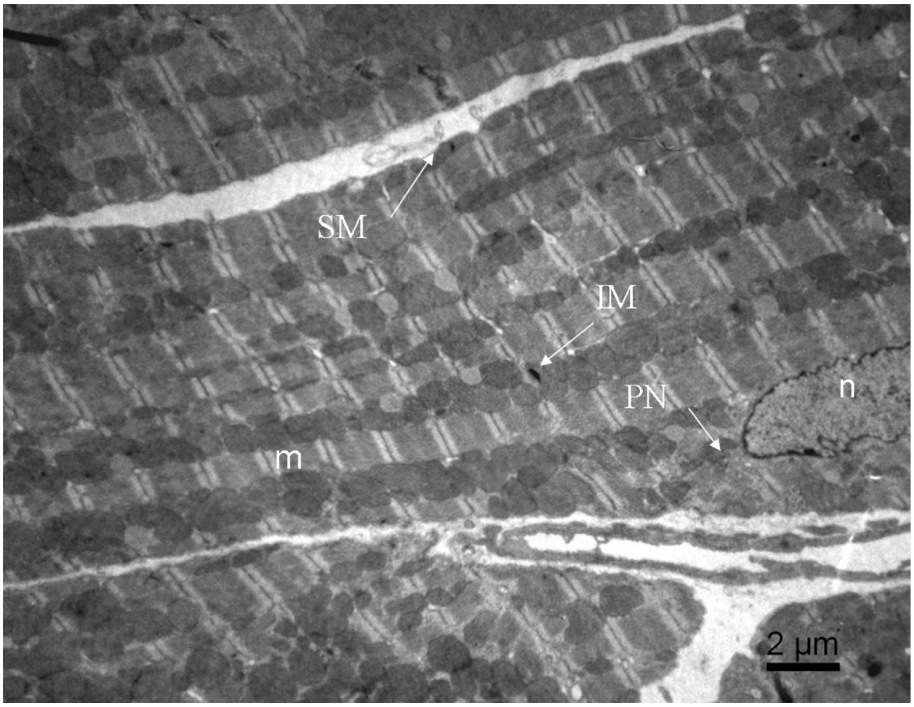

Figure 1.1. A transmission electron micrograph of adult mouse cardiac tissue showing three distinct subpopulations of mitochondria: Subsarcolemmal (SM), intermyofibrillar (IM) and perinuclear (PN) with myofibrils (m) and nucleus (n) for reference points. Adapted from Piquereau et al. (2013) [13].

1.1.2. Biogenesis

The generation of new mitochondria in response to exercise or disease requires a complex system of regulatory control necessitated by the two genome nature of the mitochondria, especially of the complexes that drive oxidative phosphorylation. In total, mitochondrial biogenesis requires the expression and import of over 1000 proteins encoded by nuclear DNA [14]. Biogenesis is triggered by the action of a number of proteins and compounds (Figure 1.2) that sense a variety of situations throughout the cells and tissues of the body. Chief among these is AMPK, which is tasked with monitoring cellular energy levels and responding when the ATP/AMP ratio falls [15]. Some further key pathways involved are the generation of nitric oxide (NO) [16], increased expression of sirtuin 1 (SIRT1) [17], and through the action of TORC (target of rapamycin complex) [18], amongst others.

The expression of the various genes required for mitochondrial biogenesis is under the control of a dedicated set of transcription factors (Figure 1.2). Amongst these are those responsible for direct regulatory control of the OXPHOS chain: nuclear respiratory factors 1 and 2 (NRF1 and NRF2) [19, 20], estrogen related receptor (ERRα) [21], and YY1 [22]. In addition, ERRα and peroxisome proliferator activated receptor α (PPARα) assist in mitochondrial biogenesis through the regulation of the oxidation of fatty acids [23, 24].

In common control over all of these transcription factors is the master regulator of mitochondrial biogenesis, PGC1α (peroxisome proliferator-activated receptor gamma coactivator 1α) (Figure 1.2). PGC1α was first identified as being key to mitochondrial biogenesis in brown adipose tissue where its expression is elevated in response to cold, leading to increased expression of respiratory chain proteins and mitochondrial DNA [25]. It is known to interact with the transcription factors mentioned above, enabling the expression of nuclear genes key for mitochondrial construction. Over expression of PGC1α leads to elevated mitochondrial content in both cultured cells and mouse tissues whilst knockdown animals show a mild OXPHOS defect phenotype under stable conditions but demonstrate severe phenotypes when exposed to challenges such as cold or exercise [26].

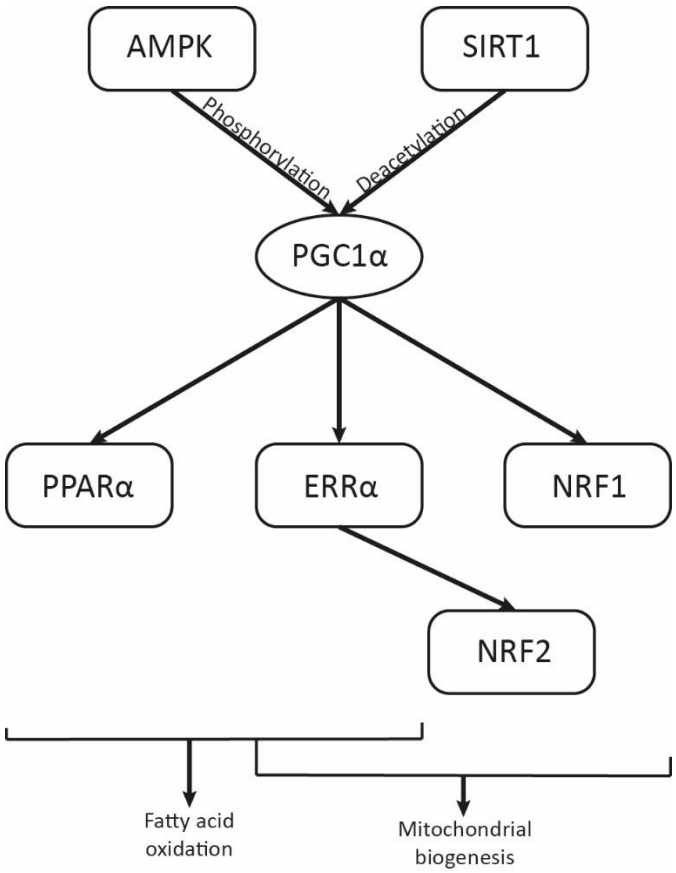

Figure 1.2. Network of key interactions showing how PGC1α acts as a master regulator over mitochondrial biogenesis and how control is maintained over it by proteins such as AMPK and SIRT1.

1.1.3. The Electron Transport Chain

The primary source of ATP production is oxidative phosphorylation (OXPHOS), which takes place on the mitochondrial inner membrane. OXPHOS links oxygen consumption with the transfer of electrons from NADH (Nicotinamide adenine dinucleotide) to O_2 through the mitochondrial electron transport chain (ETC) (Figure 1.3), a set of 5 protein complexes encoded by both nuclear and mitochondrial DNA (mtDNA), that allow for the establishment and utilisation of a H^+ ion gradient across the mitochondrial inner membrane [27].

The degree to which each complex is encoded by mitochondrial or nuclear DNA varies. Complex I (NADH:ubiquinone oxidoreductase) has 44 subunits of which 7 are encoded by mitochondrial DNA (mtDNA)[28]. Complex II (succinate dehydrogenase), III (ubiquinol cytochrome c reductase) and IV (cytochrome c oxidase) are smaller in size and comprise of 5, 11 and 13 subunits each, with only complexes III and IV having mtDNA encoded subunits (1 and 3 respectively) [29]. Complex V (F_1F_0 ATP Synthase) is a complex

molecular motor comprising of 16 subunits of which 2 are mitochondrially encoded [30, 31]. The detail of the origin of each complex and their role in the electron transport chain is explored in more detail below.

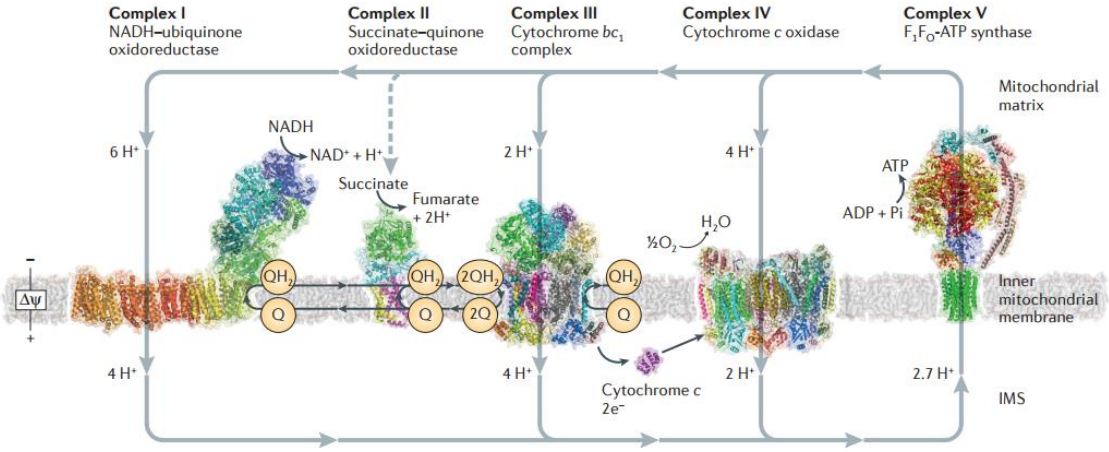

Figure 1.3. A schematic of the mitochondrial electron transport chain demonstrating proton movement and the subunits and structure of the individual transport chain complexes [32].

1.1.3.1. Complex I (NADH:Ubiquinone Oxidoreductase)

Mammalian Complex I utilises a flavin mononucleotide (FMN) and its hydrophobic domain to oxidise NADH (Nicotinamide adenine dinucleotide). NADH in its reduced form is produced by the citric acid cycle and β-oxidation, and its oxidation to NAD^+ allows these other processes to continue to function normally. As a result of the oxidation of NADH, complex I is left with two electrons which it passes through a series of eight iron-sulphur (Fe-S) centres, acting as a series of electron acceptors and donors, ultimately donating the electrons to ubiquinone, reducing it to ubiquinol. The process of oxidising NADH to NAD^+ and reducing ubiquinone is coupled to the translocation of four H^+ ions across the mitochondrial inner membrane, beginning the establishment of a proton gradient [33, 34].

As mentioned earlier complex I is roughly 1mDa in size and consists of 44 proteins. 14 of these proteins are the 'core' subunits and form the overall 'L' shaped structure consisting of two roughly equal in size arms, one extending into the mitochondrial matrix and the other contained within the inner mitochondrial membrane. Of these 14 proteins, 7 (ND1, ND2, ND3, ND4, ND4L, ND5 and ND6) are mitochondrially encoded, and 7 (NDUFV1, NDUFV2, NDUFS1, NDUFS2, NDUFS3, NDUFS7 and NDUFS8) are nuclear encoded [35, 36].

The remaining 30 proteins are known as the accessory subunits and are thought to contribute to the stabilisation and regulation of the complex [37, 38]. It is the matrix arm that contains the 9 co-factors (FMN and 8Fe-S) that are responsible for the electron transport from NADH to ubiquinone. The FMN sits at the tip of the matrix arm whilst the Q domain resides at the apex of the 'L' shape. The 7 subunits of the membrane arm are then responsible for the transport of the 4 protons across the membrane. This is thanks to the formation of four proton transfer routes, one in each of ND2, ND4 and ND5 and a fourth through the interaction of ND1, ND4L and ND6[39].

1.1.3.2. Complex II (Succinate Dehydrogenase)

The oxidation of succinate to fumarate is performed by complex II as part of the citric acid cycle. This reaction occurs on the mitochondrial inner membrane and allows for electrons to be passed to ubiquinone via the flavin-adenine dinucleotide (FAD), three Fe-S centres ([2Fe-2S], [4Fe-4S] and [3Fe-4S]) and heme. However, complex II does not contribute to the establishment of the H^+ ion gradient [40, 41]. Structurally, complex II is homologous to a protein that performs the reverse role in bacteria during anaerobic respiration, fumarate reductase [40] and in fact the two are interchangeable. Complex II contains 4 subunits, 2 of which are hydrophobic and act as membrane anchors, with the remaining 2 being hydrophilic and act as a binding site for the cofactor FAD and the catalytic centre for the reduction of succinate [42, 43].

1.1.3.3. Complex III ($CoQH_2$-Cytochrome C Reductase)

Ubiquinone, having been reduced by complexes I and II to ubiquinol, now undergoes oxidation by complex III in a process known as the 'Q' cycle, which passes the liberated electrons from ubiquinol to cytochrome C [44]. The 'Q' cycle consists of two reactions, the first involves the oxidation of ubiquinol to a semi-quinone, the second oxidises the newly formed semi-quinone to ubiquinone. The 2-step process results in the reduction of cytochrome C and the release of 4 H^+ ions into the inter membrane space, further contributing to the established H^+ ion gradient [45, 46]. Structurally, complex III contains 11 subunits and spans the inner mitochondrial membrane, with the membrane portion consisting of 4 subunits, the transmembrane of 4 and the intermembrane portion of the remaining 3[44].

1.1.3.4. Complex IV (Cytochrome C Oxidase)

The final step in the electron transport chain is the oxidation of cytochrome C and the passing of the electrons to oxygen to allow its reduction to water [47]. The process begins with the acceptance of 2 electrons from cytochrome C and the breaking of the O_2 molecule's bond; this, when coupled with the uptake of 2 H^+ ions from the mitochondrial matrix, forms the first water molecule. The second is formed in a similar fashion, with the process also being linked to the translocation of 4 further H^+ ions across the inner membrane [48]. Structurally, complex IV is a large integral membrane protein consisting of 13 subunits with 2 heme sites and 2 copper sites that are active in the transfer of electrons from cytochrome C to oxygen [49].

1.1.3.5. Complex V (ATP Synthase)

The first 4 complexes of the electron transport chain allow for the establishment of the H^+ ion gradient across the mitochondrial inner membrane. ATP synthase, or complex V, uses this electrochemical gradient to convert ADP into ATP [50, 51]. ATP synthase is comprised of an F_1 and an F_0 subunit. The F_1 subunit is entirely nuclear encoded and comprises of 9 subunits ($\alpha_3\beta_3\gamma\delta\varepsilon$) which sit in the mitochondrial matrix and catalyse the conversion of ADP to ATP via a rotary mechanism powered by the F_0 subunit [52-55]. The F_0 subunit is made up of: a main 'C' ring comprised of 8 identical protein subunits; a peripheral stalk of subunits b, d, F_6 and OSCP; and a number of membrane associated proteins, e, f, g and A6L [53]. It is the main C ring that acts as a rotational motor powering the synthesis of ATP through the F_1 subunit. Protons pass through the C ring at a rate of 8 protons per cycle causing a rotational force to be exerted through the central stalk ($\gamma\delta\varepsilon$) of the F_1 subunit. This rotational motion powers the catalytic activity of the β_3 subunits, producing 3 ATP molecules per cycle, a rate of 2.7 protons per ATP [56].

1.1.3.6. Super-complexes

Relatively small proportions of mitochondrial OXPHOS complexes actually exist as isolated complexes in the inner membrane. Most form large super molecules known as 'super-complexes' or 'respirasomes', binding together with other respiratory complexes to improve efficiency of the OXPHOS machinery and improve complex stability [57]. This improved efficiency is thought to come from the ability of the super-complexes to perform substrate channelling, the passing of a reduced substrate directly from one

catalytic site to the next where it is immediately re-oxidised, thereby removing the delay associated with diffusion of the substrate [58].

In mammalian systems these super-complexes are formed by the interactions between complexes I, III and IV in various stoichiometry. Complex II is rarely seen interacting with the other complexes in this manner whilst complex V is known to form homodimers that may closely interact with other super-complexes without acting as a constitutive component [57].

The most common arrangements found in mammalian systems are; a single complex I associated with a complex III dimer ($I + III_2$), a complex III dimer associated with 1 or 2 complex IV units ($III_2 + IV_{1-2}$), and a single complex I associated with both a complex III dimer and a variable number of complex IV units ($I + III_2 + IV_{1-4}$) [59]. Super-complex formation may also include the integration of accessory subunits such as ubiquinone and cytochrome C, which are essential partners in the substrate channelling process. Evidence suggests that ubiquinone is an essential component of $I + III_2 + IV_{1-4}$, resulting in 2 pools of ubiquinone in the mitochondria; that which is bound in super-complexes and undergoes rapid reduction and oxidation, and that which is free and seemingly plays little role in the OXPHOS process. In contrast, cytochrome C may or may not be incorporated into the super-complex and as a result, fast or slow interactions may occur between complexes III and IV and bound or unbound cytochrome C (Figure 1.4) [60].

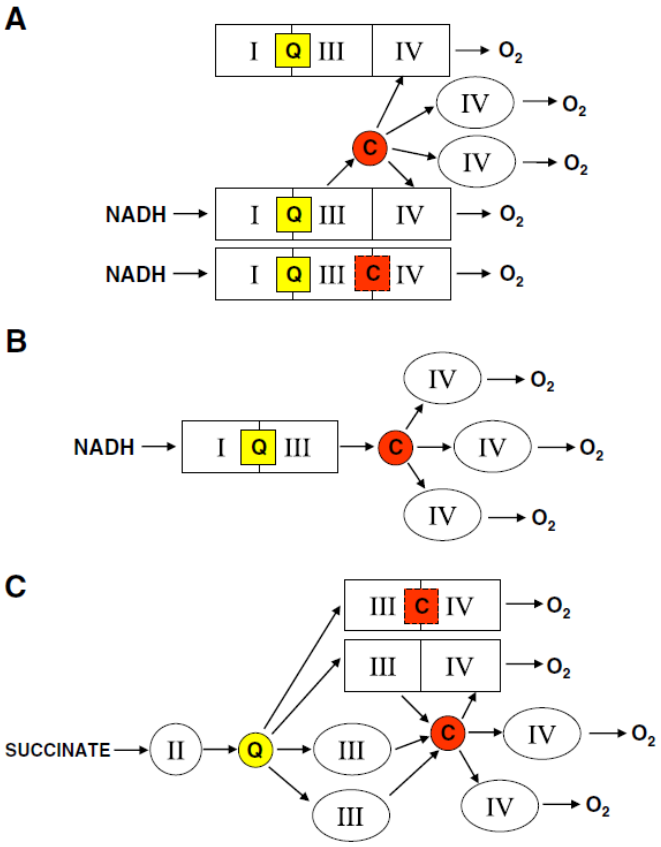

Figure 1.4. The 3 main super-complex formations identified in mammalian mitochondria, demonstrating the primary substrates and the fast and slow interactions with cytochrome C. A – supercomplex of I, III and IV with or without cytochrome C, and electrons being passed between various supercomplex formations. B - supercomplex of I and III, passing electrons to individual complex IV units. C – Electrons entering through complex II passed to various complex III and IV supercomplex arrangements [60].

The formation of the I + III_2 + IV_{1-4} super-complex confers a significant advantage over the free complexes in that it not only allows for substrate channelling but the interaction of the complexes also appears to induce conformational changes that improve the efficiency of the individual complexes. In fact, super-complex formation may be an essential aspect of the OXPHOS machinery, as there is evidence to suggest that it is required for the stabilisation of complex I. Studies have shown that patients with mutations in complex III subunits also exhibit complex I deficiency. These studies demonstrated that in these patients, complex I was formed normally but demonstrated a reduced stability and ultimately a loss of function [61, 62]. It was also demonstrated that whilst complex III was essential for complex I stability, the reverse was not true [61]. Complex IV and cytochrome C were also revealed to be required for complex I stability,

indicating that it is the formation of a complete respirasome that confers complex I stability, and not the interaction with any one other complex [63, 64].

As with the individual complexes, assembly of super-complexes requires the assistance of assembly factors. As the field is fairly nascent, most of what is known comes from work on yeast species, with two assembly factors, RCF1 (respiratory complex factor 1) and RCF2 (respiratory complex factor 2), being identified. A study conducted by Chen et al. (2012) [65], compared the role of RCF1 to its human homologue HIG2A (HIG1 domain family member 2A), by knocking down the latter using siRNA in mammalian cells. This work showed that loss of HIG2A protein resulted in a failure to assemble all super-complexes[65]. Additionally, work by Jian et al. [66] has implicated the mitochondrial scaffold proteins PHB1 and PHB2 as super-complex assembly factors. By knocking down either of these proteins in HeLA cells using siRNA a reduction in super-complex formation was observed, coupled with elevated ROS production [66].

Whist the role of super-complexes is still poorly understood it is becoming clear that their formation is an essential step in the establishment of a functional OXPHOS system and not just a convenient means to improve catalytic efficiencies.

1.1.3.7. Complex I Assembly Factors

As is detailed further in section 1.1.3.8, complex I assembly is an intricate process that requires the assistance of a large number of assembly factors that are not themselves incorporated into the final functional complex. To date at least 13 complex I assembly factors have been identified in mammalian systems. However, the actual function of these assembly factors is still unknown, it is hypothesised that they may act as chaperones, stabilising the intermediate assembly steps to allow the process to continue unhindered [67, 68].

The mitochondrial complex I assembly (MCIA) complex is formed from 5 of these assembly factors and is involved in the early assembly of the P_P-b subcomplex. The 4 core proteins in the MCIA are NDUFAF1 (NADH:ubiquinone oxidoreductase complex assembly factor 1), ECSIT (evolutionarily conserved signalling intermediate in toll pathway), ACAD9 (acyl-coA dehydrogenase family member 9), and TMEM126B (transmembrane protein 126B) with possible involvement from TIMMDC1 (translocase of inner mitochondrial membrane domain containing 1) [69, 70]. This complex

assembles on the inner membrane with TMEM126B acting as the membrane anchor. ECSIT and NDUFAF1 bind to TMEM126B and are joined in turn by a dimer of ACAD9. It is then thought that this 4 protein complex interacts with TIMMDC1 prior to any complex I interaction [68]. The formation of this complex precedes the binding of complex I constituent proteins and appears to be an initiation step for the process of assembling membrane arm of complex I.

Other assembly factors of the membrane arm of complex I include FOXRED1 (FAD dependant oxidoreductase containing 1), TMEM70 (transmembrane protein 70) and ATP5SL (ATP synthase subunit s-like protein) however, the function of these proteins remains poorly understood [71, 72].

Evidence also suggests that the proteins COA1 (cytochrome c oxidase assembly factor 1 homolog) and TMEM186 (transmembrane protein 186) play a role in the assembly of the membrane arm, however this role appears to be more transient than that of the proteins in the MCIA complex. These proteins were identified interacting with sub-assemblies of the proximal portion of the membrane arm (P_P-a) but were not identified in larger subassemblies incorporating both the membrane and matrix arms (Q/P) where members of the MCIA could still be seen [72, 73].

In addition to assembly factors of the membrane arm, there are a number of assembly factors associated with the matrix arm. Amongst these, NDUFAF2 (NADH:ubiquinone oxidoreductase complex assembly factor 2), NDUFAF3 (NADH:ubiquinone oxidoreductase complex assembly factor 3) and NDUFAF4 (NADH:ubiquinone oxidoreductase complex assembly factor 4) have been linked with mutations in patients resulting in deficiencies of complex I levels and activity [74-76]. NDUFAF2 has been shown to interact with the N module of complex I and mutations lead to an accumulation of the matrix arm structural subunits, indicating a role in the late stages of complex I assembly [77, 78]. Evidence suggests that NDUFAF3 is involved earlier in the assembly process as mutations do not lead to obvious accumulations of the matrix arm as was seen with NDUFAF2 [76]. Mutations in NDUFAF4 lead to accumulation of both large and small subassemblies, indicating that it may work in tandem with both NDUFAF2 and NDUFAF3 at both early and late stages of matrix arm formation [75]

Finally, there are assembly factors that appear not to be involved in the assembly of the structural aspect of complex I but with modifications of subunits, or in delivering the Fe-S clusters to the complex. NUBPL is an iron-sulphur protein with an N terminal mitochondrial localisation signal. Through interactions with its CXXC domain, Fe-S clusters may be transported into the mitochondria and delivered to complex I where they are incorporated into key subunits. Knocking down the NUBPL protein in human cells results in the accumulation of matrix arm subassemblies and a reduction in the levels of iron incorporated into complex I [79, 80].

Much is still to be gleaned about the mechanism of complex I assembly factors although there is little doubt that their role is absolutely essential. It is likely that there are more assembly factors yet to be discovered and there remains the possibility that there are tissue specific assembly factors that remain elusive. It is also probable that some redundancy exists in the system, given its essential nature.

1.1.3.8. Complex I Assembly

Given complex I's size, complexity and two genome nature it is unsurprising that its assembly is an intricate process which we are only beginning to come to understand the detail of. As mentioned previously, complex I contains 44 subunits, 7 of which are encoded by the mitochondrial genome and the remaining by the nuclear genome. Involved in its assembly are at least 14 assembly factors which are not thought to comprise part of the final structure but are essential in the intervening steps between isolated proteins and functional complex [71, 72].

The 14 core subunits are considered to be the main driving force behind complex I's function but evidence suggests that many of the remaining 30 accessory subunits are also required for normal function either through stabilisation of the complex structure or through a contribution to the function of one of the modules [35, 81]. As a result, the assembly process has developed to ensure correct integration of both the core subunits as well as the seemingly essential accessory subunits.

The assembly process proceeds in a step wise fashion with individual building blocks or sub-assemblies forming first before joining to form structural or functional portions of the complex and ultimately the complete complex. There are 4 main modules that must be assembled for full function: N, the NADH binding domain; Q, the quinone binding

domain; P_p, and P_D, the proximal and distal portions of the membrane arm involved in proton pumping [82].

Guerrero Castillo et al. (2016) demonstrated that assembly begins within 4 hours of the induction of protein translation with the formation of the mitochondrial complex I assembly (MCIA) complex and its association with constitutive proteins of the P_p-b sub assembly, as can be seen in figure 1.5. Alongside the formation of the P_p-b unit, assembly of the Q/P_p-a unit begins, with the marrying of the fully assembled Q subunit with the adjacent segment of the P_p module. The assembly of the P_D subunits was more difficult to observe and it was published that this module assembles in two sections, P_D-a and P_D-b, which begins around the same time as the P_p-b and Q/P_P-a module formation but doesn't finish until sometime later. Also at this time point, the N subunit has begun to form in two separate building blocks of 71 and 88kDa, these then join over the following 2 hours to form the fully assembled N module.

This 6-hour time point also sees the formation of a large 680kDa complex consisting of the P_p-b and P_D-a modules as well as a 736kDa complex consisting of the P_p-b with the Q/P_p-a module. By 8 hours post translational induction, these two complexes have been replaced by a single large complex consisting of all three of the modules. These data suggest that the binding of P_P-b with either P_D-a or Q/P_P-a is not a highly controlled process and which binding event occurs first is seemingly random. This single large complex (Q/P) now resembles completed complex I with the exception of the missing N module and some accessory subunits as well as the presence of a number of assembly factors. These remaining steps occur with an apparent lack of strict organisation or timing. By 24 hours post translational induction this process results in a significant amount of fully assembled and functional complex I. These fully assembled units are then stabilised by formation of respiratory chain super complexes through interaction with complexes III and IV [72].

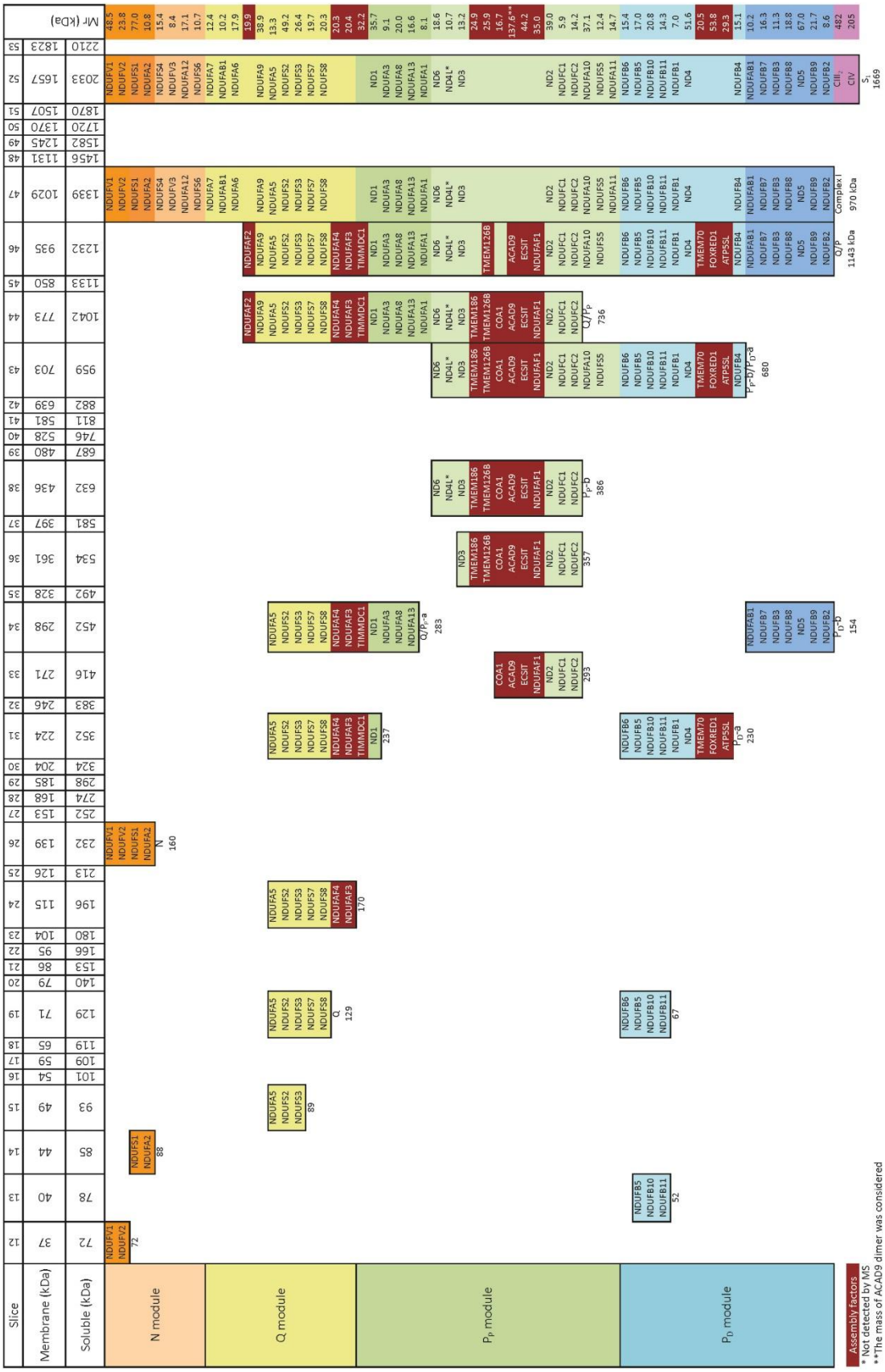

Figure 1.5. Assembly pathway of complex I demonstrating the assembly intermediates created during the course of assembly and the assembly factors associated with each sub-complex. Adapted from Guerrero-Castillo *et al*. (2016) [72].

1.1.4. Mitochondrial Processes

1.1.4.1. Mitochondrial Fusion and Fission

The classical view of the mitochondria as a small, rod shaped organelle isolated from its peers is an outdated one with little to no relevance in modern mitochondrial research. Instead mitochondria are viewed as a dynamic network in constant flux between individual punctate units and large branching networks.

There exist two opposing processes that work in co-operation with mitophagy pathways to maintain functional mitochondria; mitochondrial fusion, and mitochondrial fission. Mitochondrial fusion is the process by which smaller units join to create large networks, allowing for the exchange of respiratory chain components, mitochondrial DNA and maintenance of membrane potential ($\Delta\psi_m$). Mitochondrial fission is the reverse process, whereby networks are divided again allowing for the removal of dysfunctional portions or subunits.

Fusion is governed by 3 GTPases, mitofusins 1 and 2 (MFN1 and MFN2) on the outer membrane and OPA1 on the inner membrane [83, 84]. MFN 1 and 2 form hetero and homodimers between adjacent mitochondrial subunits allowing for the fusion of the outer membrane. OPA1 performs a similar role on the inner mitochondrial membrane although evidence suggests that its expression is not required on both mitochondria for inner membrane fusion to occur [85]. To complicate matters, OPA1 is known to have as many as 8 protein isoforms in humans, with each seemingly playing slightly different roles in mitochondrial dynamics, mtDNA abundance, cristae formation and energetic efficiency. Longer isoforms appear to lend themselves to mitochondrial fusion whilst shorter isoforms focus on cristae structure and OXPHOS efficiency [86]. In mouse this number is reduced, with only 6 isoforms identified [87].

Fission is a more complex process that involves a larger array of proteins. Key amongst these in the mammalian system is dynamin related protein 1 (DRP1). DRP1 is recruited to the outer mitochondrial membrane (OMM) where it oligomerizes and through the action of its GTPase domain contracts around the mitochondrial body, constricting it and creating a ‘pinch point’ [88]. However, as DRP1 lacks a transmembrane domain it is hypothesised that an adaptor protein must be present to recruit DRP1. A number of proteins have been implicated in this role including mitochondrial fission protein 1

(FIS1), mitochondrial fission factor (MFF) and mitochondrial dynamics proteins of 49 and 51 kDa (MID49 and MID51)[83]. Zhang et al. (2016) [89] employed ASTC-a-1 cells exposed to UV light to induce mitochondrial fragmentation in order to dissect the function of a number of these proteins and proposed the following mechanism. The results suggest that DRP1 is dephosphorylated at the inhibitory site of Ser637 and migrates to the OMM where it is recruited by MFF1, which simultaneously stimulates the GTPase activity of DRP1. At the same time, the inhibitory effect of MID51 binding to DRP1 is ablated by the competitive binding of FIS1, thereby liberating DRP1. The model remains incomplete but offers a foundation on which future work can build.

Ultimately the function of mitochondrial dynamics appears to be one of quality control. As mitochondria carry their own genome, without appropriate DNA repair mechanisms and in the presence of high levels of ROS (reactive oxygen species), mtDNA mutations can accumulate over the lifespan of an organism. In addition, mitochondrial OXPHOS units may become defective and membranes can become damaged leading to a loss of membrane potential. All of these issues, if left unchecked could lead to mitochondrially triggered apoptosis. Hence the exchange of mitochondrial components allows for the collection and removal of defective parts by mitophagy and ultimately promotes homeostasis [90].

1.1.4.2. Reactive Oxygen Species Production

Reactive oxygen species (ROS) such as superoxide (O_2^-), hydrogen peroxide (H_2O_2) and hydroxyl (•OH) are primarily produced by complexes I and III as part of normal OXPHOS function. As these compounds can lead to damage of mtDNA and proteins their production is counteracted by antioxidants that mop up ROS and ensure the health of the mitochondria [91, 92].

Under normal conditions the main source of ROS is complex I, which takes electrons from NADH and passes them through the Fe-S centres to ubiquinone; this is assisted by the flavin mononucleotide (FMN) cofactor that initially accepts the electrons from NADH. O_2^- is produced by the reaction of the fully reduced FMN, the level of which is defined by the ratio of NADH to NAD^+, with O_2 [93-95]. This means that deficiencies in the electron transport chain lead to an increased reduction of the mitochondrial NADH/NAD^+ pool, a shift in the amount of fully reduced FMN and an over-production of

ROS. In the case of reverse electron transport, where respiration is driven through complex II substrates, electrons are forced backwards through complex I from ubiquinol, reducing the NADH/NAD^+ pool as well as the FMN, again leading to high ROS production [96, 97].

The link between elevated ROS and cardiomyopathy has been established by a number of studies but the mechanism linking the two remains elusive [98, 99]. Furthermore, the link remains tentative as some animal models of complex I deficiency induced hypertrophic cardiomyopathy (HCM) demonstrate no elevation of ROS or evidence of oxidative stress induced damage [100].

1.1.4.3. Regulation of Energetic Supply and Demand

ATP is required for the normal function of the myocyte during both contraction and relaxation, with levels being maintained at around 10mmol/L by alterations in pathways involving ATP use and synthesis. The primary source of ATP is the mitochondrial electron transport chain and under normal conditions this system is capable of maintaining ATP levels even during periods of increased demand. Typically, reactions that hydrolyse ATP to ADP and P_i are inhibited by the accumulation of the products in a sub cellular compartmental fashion [101]. The oxidation of NADH and $FADH_2$ by the electron transport chain establishes the proton gradient (ΔpH) which is one of the major components (along with membrane potential ($\Delta\Psi_m$)) of the proton motive force ($\Delta\mu_H$) that drives protons through the F_1F_0-ATP synthase, producing ATP. In the healthy heart, NADH and $FADH_2$ are produced primarily by the utilisation of two substrates; glucose, via glycolysis; and fatty acids, via β-oxidation [102]. The utilisation of each substrate is tightly controlled to meet demand and maintain cellular ATP levels. β-oxidation of fatty acids is inhibited by the accumulation of both acetyl-CoA and NADH, whilst glycolysis is inhibited by the accumulation of pyruvate dehydrogenase (PDH). In addition the pathways reciprocally regulate each other through the Randle cycle, with the NADH and acetyl-coA produced by β-oxidation inhibiting glycolysis and the acetyl-coA produced by glycolysis inhibiting β-oxidation [103, 104].

Under normal physiological conditions, β-oxidation accounts for roughly 70% of utilised substrate. During periods of increased demand, the upregulation of substrate utilisation is governed by two main factors, [ADP] and [Ca^{2+}]. Increased ATP usage leads to a drop

in [ATP] and triggers the F_1F_0-ATP synthase to increase the turnover of ADP into ATP. This results in a temporary loss of $\Delta\mu_H$ which acts as a signal drawing more electrons through the ETC. Increased ETC activity elevates the oxidation of NADH and $FADH_2$, and reduces their inhibition of glycolysis and β-oxidation. Increased flow of Ca^{2+} through the cell both from extracellular deposits and the sarcoplasmic reticulum (SR) lead to an increase in [Ca^{2+}] in the mitochondrial matrix. The elevation of [Ca^{2+}] in this fashion stimulates PDH as well as the TCA cycle, elevating the production of NADH and $FADH_2$ [104, 105].

In addition to the electron transport chain, the creatine kinase system plays an important role in buffering ATP levels in order to maintain constant ATP concentrations during fluctuations in supply and demand. Phosphocreatine (PCr) acts by buffering the local [ATP] and providing an energetic reserve during times of high energy demand. Creatine kinase catalyses the reversible phosphorylation of creatine to produce PCr when [ATP] is high, then when [ATP] is low the phosphate group is released back to ADP to restore [ATP]. In addition to its role in buffering and reserve capacity, PCr is more readily diffusible than ATP and is able to act as a shuttle through facilitated diffusion, collecting phosphate from sites of ATP production (mitochondria) and ferrying it to sites of high ATP usage in the muscle fibre [101, 104, 106]. This is possible due to multiple isoforms of creatine kinase in the cell. The mitochondrial isoform (mtCK) which catalyzes the phosphorylation of creatine to phosphocreatine and the cytosolic isoforms (CK-MM, MB and BB) which typically catalyse the reverse reaction, releasing the phosphate group from the creatine to ADP, producing ATP at sites of high demand [107].

The concept of the failing heart having a deficiency of ATP or being ‘energy starved’ has existed for many years and there is a great deal of evidence in support of this concept. The end stage failing heart may have reduced [ATP] in myocardium by as much as 30%, with even greater deficits in phosphocreatine, and the ratio of [PCr]:[ATP] provides a predictive metric for the severity of heart failure [101, 106, 108].

Animals with pressure overload cardiomyopathy, as induced by transverse aortic constriction (TAC), demonstrate a reduced [PCr]:[ATP] very early in the progression of left ventricular hypertrophy, and show an increased relationship between the two as LV remodelling progresses [109]. Furthermore, mice with an inducible deletion of the gene

Slc25a3, resulting in the loss of the mitochondrial phosphate carrier protein (PiC), show a reduction in [ATP] and a severe cardiomyopathy by 10 weeks post deletion [110]. These results support the idea that energy insufficiency plays a key role in the development of cardiac hypertrophy. In contrast to this work, knockout mice lacking functional guanidinoacetate N-methyltransferase (GAMT), unable to produce creatine and maintained on a diet free of it, show no differences in maximal exercise capacity or in the 48 hour survival rate post myocardial infarction [111].

As [ADP] rises, so too does [AMP] as a result of the reaction catalysed by adenylate kinase ($2ADP \leftrightarrow ATP + AMP$). AMP-dependant protein kinase (AMPK) is a molecular sensor of [AMP] and as such can be thought of as a 'fuel gauge' for the mammalian cell. When [AMP] is high, AMPK is activated by the upstream AMPK kinase and begins remodelling cellular processes to improve ATP production. Amongst the pathways AMPK affects are: fatty acid synthesis (reduced), fatty acid oxidation (increased), glucose uptake and metabolism (increased), and mitochondrial biogenesis via PGC1α (increased) [112, 113]. Rats with pressure overload hypertrophy show near normal [ATP] whilst [PCr] is decreased resulting in an elevation of [ADP] and [AMP]. These hypertrophied hearts show activation of AMPK which in turn leads to elevated glucose uptake through GLUT1 and surprisingly a decrease in β-oxidation [114].

1.1.4.4. The Mitochondrial Unfolded Protein Response

The mitochondrial unfolded protein response (UPR^{mt}) is a mechanism for the detection of the accumulation of misfolded proteins within the mitochondria and the upregulation of factors intended to remove and counteract their formation. By necessity it differs from the endoplasmic reticulum unfolded protein response (UPR^{ER}) due to the double membrane structure of the mitochondria [115].

The UPR^{mt} can be activated by any one of a number of mitochondrial stresses including; accumulation of misfolded mitochondrial proteins, mitochondrial ribosome impairment, mitochondrial chaperone or protease inhibition, OXPHOS dysfunction, high glucose metabolism, and high ROS levels [116]. When activated, the UPR^{mt} has three distinct mechanisms of action to counter any non-specific stress, these three prongs are; increased expression of mitochondrial chaperones, inhibition of protein production through translation inhibition and degradation of misfolded proteins by proteases.

The UPR^{mt} can be separated into two distinct sensing mechanisms and their associated responses. The first monitors protein folding in the mitochondrial matrix and is activated by JNK2 (c-JUN N-terminal kinase) and PKR (dsRNA-activated protein kinase), the second monitors the inter membrane space (IMS) and is activated by the phosphorylation of AKT (protein kinase B) [115].

Early work undertaken by Zhao et al. (2002) investigated the UPR^{mt} in a model that introduced a mutant form of the protein ornithine transcarbamylase (OTC) into COS7 cells. It was found that there is a distinct UPR^{mt} that involves the upregulation of the mitochondrial chaperones HSP60 (heat shock 60kDa protein 1 (CPN60)), HSP10 (heat shock 10kDa protein (CPN10)) and MTDNAJ (mitochondrial DNAJ heat shock protein) as well as the protease CLPP (caseinolytic mitochondrial matrix peptidase proteolytic subunit), without any change in expression of factors known to be involved the UPR^{ER}. Central to this pathway are the transcription factors C/EBPβ (CCAAT/enhancer-binding protein) and CHOP (C/EBPβ homology protein). There also seems to be an inferred role for the mitochondrial unfolded protein response elements (*Mure1* and *Mure2*), whose role is yet to be determined, but which have been found in close proximity to CHOP binding sites in many UPR^{mt} genes [117, 118]. Bioinformatics tools have been used to identify the presence of an AP-1 binding site in the promoters of both *Chop* and *Cebpb*

[118]. AP-1 binding sites are the target of C-JUN, a transcription factor which is positively regulated by the NH_2-terminal kinase, JNK2, indicating that this pathway is key for the activation of the matrix portion of the UPR^{mt} (Figure 1.6) [119, 120].

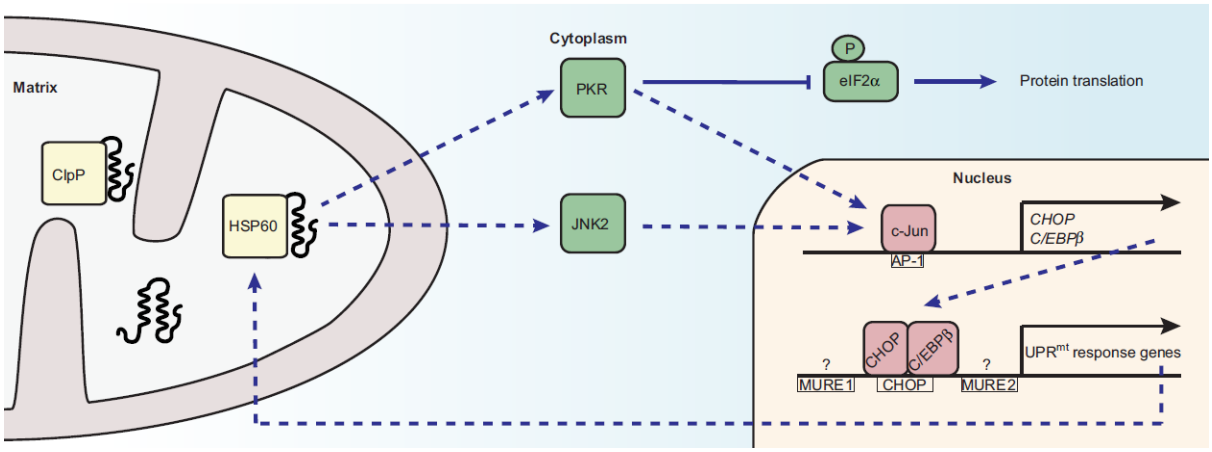

Figure 1.6. Schematic representation of the matrix portion of the UPR^{mt}. Accumulation of misfolded proteins triggers the response via PKR and JNK2 which activate the transcription factor c-Jun, leading to expression of the transcription factors CHOP and C/EBPβ which up regulate the expression of UPR^{mt} genes encoding chaperones such as HSP60 and proteases such as ClpP. [115].

At the same time as there is upregulation of mitochondrial chaperones, there is also a reduction in protein translation in the cytoplasm. This is mediated by the action of dsRNA-activated protein kinase (PKR) which phosphorylates eukaryotic translation initiation factor 2α (EIF2α) and prevents protein translation to reduce the load on the mitochondrial chaperones [121]. It is also worth noting that the action of PKR with the aforementioned protease CLPP also activates the AP-1 binding transcription factor C-JUN [121].

In addition to this core set of proteins identified in the UPR^{mt}, Aldridge et al. (2007) used bioinformatics tools to identify a further six genes under the control of CHOP, that were upregulated during the UPR^{mt} response. In addition to the CHOP site in the promoter region of these genes, the bioinformatics analysis also identified the *Mure1* and *Mure2* regions previously seen in other UPR^{mt} genes. The six genes encode a variety of proteins; from mitochondrial proteases, YME1L and MPPβ; to enzymes, NDUFB2, EndoG and thioredoxin 2; and the import machinery component Tim17a. Whilst the role of these proteins in the UPR^{mt} is not yet fully understood, mutation of the 'Mure' elements

results in a loss of upregulation during UPR^{mt} activation indicating a putative role for these proteins in managing misfolded proteins in the mitochondrial matrix [118].

Fiorese *et al*. (2016) set out to determine if, as in *C.elegans*, there is a key mammalian regulator of the UPR^{mt}. In *C.elegans* this key regulator is ATFS-1, which is normally transported to the mitochondria, but under periods of stress accumulates in the cytosol before entering the nucleus and triggering the UPR^{mt}. Bioinformatics analysis identified 2 proteins with significant homology to ATFS-1, ATF4 (activating transcription factor 4) and ATF5 (activating transcription factor 5). Interestingly, only ATF5 had signs of a mitochondrial localisation signal, and only ATF5 was able to restore the UPR^{mt} in worms lacking the ATFS-1 protein. Further work has confirmed that ATF5 behaves similarly to ATFS-1 in worms, by localising to the mitochondria under normal conditions, but activating the UPR^{mt} under periods of stress. ATF5 primarily promotes the expression of genes with a UPR^{mt}Es promoter, including the chaperones; HSP10, HSP60, MTHSP70 and the mitochondrial protease LONP1 (lon peptidase 1) [122].

More recent work has utilised a mutant form of the protein endonuclease G (ENDOG) (N174A), which accumulates in the IMS and induces mitochondrial stress [123, 124]. The results from this work indicate the existence of a second arm of the UPR^{mt} which is solely concerned with proteins of the IMS (Figure 1.7).

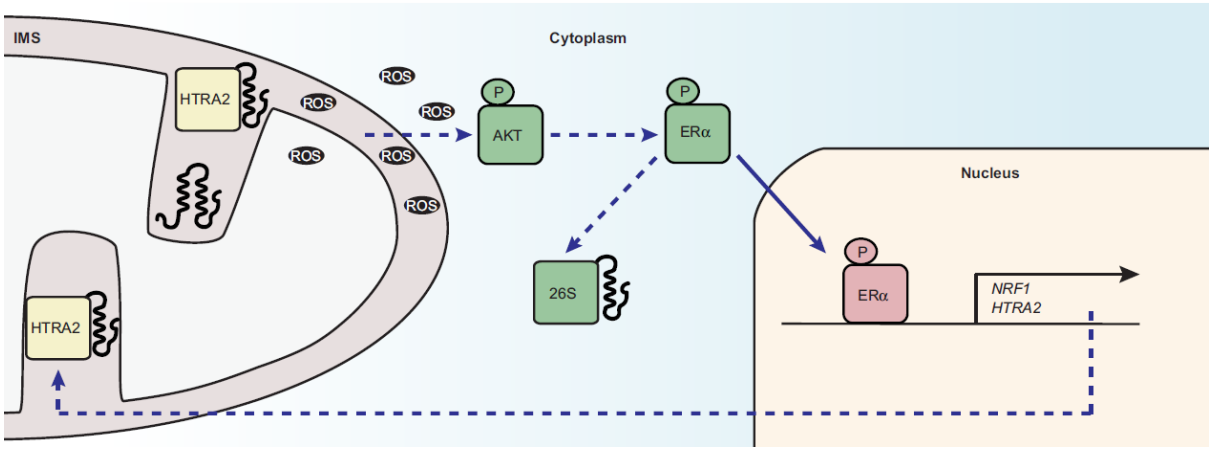

Figure 1.7. Schematic representation of the IMS portion of the UPR^{mt}. In this case accumulation of misfolded proteins results in elevated ROS which activate AKT and lead to activation of the proteasome as well as upregulation of genes such as HTRA2. [115].

Control of the IMS UPR^{mt} is held by protein kinase B (AKT) that becomes phosphorylated due to elevated ROS levels caused by accumulation of misfolded proteins in the IMS.

Phosphorylation of AKT leads to activation and in turn phosphorylation of estrogen receptor α (ERα) at serine 167 [123]. From here the response takes on a 2 step approach, both of which are promoted by ERα activation. The first is the activation of the proteasome to degrade misfolded proteins in the cytosol before they enter the IMS. The second is the increased expression of the protease HTRA2 (high temperature requirement protein A2) which degrades any misfolded proteins that have made it into the IMS [123, 124].

Ultimately, any failure of the UPR^{mt} leads to complete mitochondrial dysfunction without the requirement for loss of mitochondrial membrane potential ($\Delta\psi_m$). This mitochondrial dysfunction can lead to accumulation of PINK1 (PTEN induced putative kinase 1) on the OMM via a currently unknown pathway and the activation of mitophagy [125]. The mechanism of mitophagy is discussed further in section 1.1.4.6.

1.1.4.5. Mitophagy

Mitophagy is the means by which a cell selectively disposes of defective mitochondria through autophagic processes. This typically follows the process of fusion/fission and is a significant portion of the process of mitochondrial quality control. The primary axis for inducing mitophagy involves the proteins PTEN-induced putative kinase 1 (PINK1) and parkin (PARK2) which recognise mitochondria through a drop in membrane potential, $\Delta\psi_m$, and target them for digestion by autophagosomes. As mentioned in the previous section, there is also an unknown mechanism by which PINK1 can accumulate on the OMM without any change in $\Delta\psi_m$, as may be seen during inability of the UPR^{mt} to cope with mitochondrial stress [125].

Under conditions where $\Delta\psi_m$ is high, the serine-threonine kinase PINK1 (63kDa), localises to the outer mitochondrial membrane (OMM) where it is transported to the inner mitochondrial membrane (IMM) by the TOM (translocation of outer mitochondrial membrane) and TIM23 (translocation of inner mitochondrial membrane) complexes. Following insertion into the IMM, PINK1 is cleaved at residue A103 by the presenilin-associated rhomboid-like protein (PARL) to form ΔN-PINK1 (52kDa). This process leads to degradation of PINK1 by the proteasome rendering it inert and allowing for mitochondria with high $\Delta\psi_m$ to be maintained in the cell [126-128]. When $\Delta\psi_m$ is low,

PINK1 remains in the OMM and is unable to be cleaved and targeted for degradation by PARL, leading to its accumulation on defective mitochondria.

When left as a full length protein, PINK1 autophosphorylates at Serine 228 and 402, leading to activation and recruitment of PARK2. Okatsu et al. (2012) demonstrated that pseudo-phosphorylated PINK1 (S228D/S402D) is capable of recruiting PARK2 whilst introducing mutations that inhibit phosphorylation (S228A/S402A) demonstrate the opposite effect [129]. In addition to autophosphorylation, PINK1 is capable of phosphorylating both MFN2, at residues T111 and S442, and ubiquitin, at S65, with both events having independently been shown to be necessary for the translocation of PARK2 to the OMM [130, 131]. As PARK2 is recruited it ubiquitinates proteins such as BNIP3L [132] on the OMM, with the ubiquitination acting as a signal to autophagosomes to degrade the damaged mitochondria [133, 134].

Failure to remove mitochondria by this method leads to accumulation of defective subunits, mtDNA mutations and inefficient OXPHOS and has been associated with elevated levels of systemic inflammation and cardiomyopathy [135, 136]

1.1.5. Genetic Defects of the Mitochondrial Electron Transport Chain

1.1.5.1. Nuclear Encoded Mutations

Of the roughly 1500 proteins in the mitochondrial proteome, only 13 are encoded by the mtDNA, leaving the vast majority to be synthesised in the cytoplasm and transported into the mitochondria [137]. Nuclear genome mutations that lead to mitochondrial defects can be broadly divided into 5 categories according to which genes they effect; nuclear encoded ETC subunits, assembly factors, mtDNA integrity maintenance, mtDNA copy number maintenance and control of mitochondrial gene expression. In the interest of brevity, this section will only focus on those mutations that directly affect the ETC.

Between 1990 and 2014 in the north east of England, 62 individuals were reported with nuclear DNA (nDNA) mutations, corresponding to a prevalence of 2.9 per 100,000 adults (>16 years) [138]. Of these 62, the majority had mutations in the genes SPG7 (spastic paraplegia 7) (17), PEO1 (progressive external ophthalmoplegia) (15), OPA1 (optic atrophy 1) (8), POLG (polymerase gamma) (6) and RRM2B (ribonucleotide reductase M2 B) (5) [138]. None of these proteins are constitutive elements of the electron transport

chain, indicating that even amongst mitochondrial disease, ETC mutations are rare, likely due to the essential nature of many components of the ETC.

As complex I is the largest complex of the electron transport chain it is unsurprising that it is the site of most of the identified nuclear mutations causing ETC deficiency. Of complex I's 37 nuclear encoded proteins, pathogenic mutations have been identified in at least 17, including all seven of the nuclear encoded 'core' subunits and 10 of the remaining subunits [28, 139, 140]. The patients identified so far represent a roughly 60:40 split of those carrying core gene mutations to those with non-core gene mutations [139]. Table 1.1 shows all of the identified mutations in nuclear encoded complex I subunits.

Mutations affecting the core subunit proteins of NDUFV1, NDUFV2, NDUFS1, NDUFS2, NDUFS3 NDUFS7 and NDUFS8, which comprise the main functional portions of the N and Q domains, account for the majority of known mutations [140]. Below I will give a brief overview of mutations identified in these 7 core subunits.

Mutations in *NDUFV1* were first identified in 3 children with symptoms including myoclonic epilepsy, muscular hypotonia and elevated lactate levels. The first 2 patients were found to be compound heterozygotes for 2 mutations (R59X and T423M), with the first mutation leading to a truncated protein, and the second lying in a well conserved region of the protein. The third patient was shown to be homozygous for an A341V mutation, leading to isolated complex I deficiency [141].

An *NDUFV2* mutation was identified in 3 members of a single family whom all suffered from a fatal HCM within the first 12 months of life. The causative mutation was found to be a 4bp deletion in the consensus splice-donor site of intron 2 resulting in the loss of the 66bp exon 2 and a reduction in the amount of NDUFV2 protein produced [142].

3 patients with NDUFS1 mutations were identified through a screening process looking for the disease causing alleles in a group of patients with complex I deficiency. This study identified 3 patients from 3 families, 2 of which had siblings with mitochondrial disease. The first presented with optical atrophy, leukodystrophy and lactic acidosis, with the causative mutation being identified as a deletion resulting in an aspartic acid being substituted for a glycine at residue 252 (D252G). The second patient demonstrated axial

hypotonia, hepatomegaly and hyperlactatemia and carried 2 mutations as a compound heterozygote (R412W and R557X). The final patient had similar symptoms of hyperlactatemia and hypotonia with the addition of microcephalia and pyramidal syndrome. This patient was found to be a heterozygote for a methionine to valine substitution at position 707 (M707V) with the addition of a de novo deletion in the paternal allele [143].

NDUFS2 mutations were identified in members of 3 families with symptoms of complex I deficiency including nystagmus, acidosis, muscle hypotonia, cognitive development and HCM. Further study found 3 mutations within the *NDUFS2* gene, (Arg228Gln, Pro229Gln, and Ser413Pro) all of which resulted in a complex I deficiency as measured by enzymatic assay [144].

A patient with Leigh syndrome was identified with a mutation in *NDUFS3*. Briefly, Leigh syndrome is typically associated with neurological symptoms including epilepsy, nystagmus, ataxia and optic artrophy. A limited number of cases have also been described with cardiac involvement although this is variable [145]. The patient was found to be a compound heterozygote. The first mutation resulted in a well conserved Threonine at position 145 being changed to an Isoleucine (T145I) and the second changed an arginine into a tryptophan at position 199 (R199W). The R199W mutation was found to be paternally inherited and was also found in a healthy brother, with no signs of mitochondrial disease [146].

Patients with mutations in NDUFS7 and NDUFS8 have mostly been identified as sufferers of Leigh syndrome. The first nuclear encoded mutations linked to Leigh syndrome were found in NDUFS8, the first being a proline to leucine change at position 79 (P79L) and the second an arginine to histidine at residue 102 (R102H). NDUFS7 was subsequently also found to be causative of Leigh syndrome with the mutation causing residue 122 to swap from a valine to a methionine (V122M) [147, 148].

Complex II mutations are most commonly found in the gene for the subunit SDHA. An arginine to tryptophan change at reside 554 (R554W) resulted in Leigh syndrome in 2 siblings [149]. Whilst a later study identified a third patient with Leigh syndrome as a result of a paternally inherited W119X mutation and a maternally inherited A83V mutation which resulted in a significant loss of functional complex II [150]. Mutations in

many of the other units of complex II are associated with various cancers. Mutations in SDHB, SDHC and SDHD are associated with paraganglioma and phaeochromocytoma whilst mutations in other TCA cycle enzymes such as fumarate hydratase (FH) can lead to leiomyoma, leiomyosarcoma or renal cell carcinoma. Possibly as a result of blocked metabolism of succinate or fumarate in the mitochondria which then trigger other cellular processes in pre-cancerous cells [151].

Of the 10 nuclear encoded subunits of complex III, only UQCRB, UQCRQ, UQCRC2 and CYC1 have been found to contain mutations resulting in any form of complex III deficiency [152]. The *UQCRB* mutation was discovered in a single patient with a 4bp deletion in exon 4; this resulted in a reduction in complex III levels and symptoms including acute gastroenteritis and lactic acidosis [153].

A change at residue 45 from serine to phenylalanine (S45F) in UQCRQ was identified in 25 members of an Israeli Bedouin family, all of whom developed Leigh syndrome [154]. A mutation in *UQCRC2* was discovered in a family in Mexico, the patients presented with similar symptoms to the *UQCRB* patient mentioned previously. The arginine to tryptophan (R183W) change caused a ~80% reduction in complex III levels and enzymatic activity levels reduced by half [155]. Finally, 2 unrelated mutations have been found in *CYC1* (W96C and L215F). Yeast studies demonstrated an almost total absence of complex III for both mutations. Symptomatically, both patients demonstrated hyper-glycaemia without any developmental delay [156]. The lack of known mutations in complex III probably stems from its essential role in the ETC. Damage to complex III structure or function results in lack of super-complex formation, which is required for complex I stability (see section 1.1.3.6) and it forms the funnel for electrons entering the chain from both complex I and complex II. As a result, mutations in complex III are likely to be too severe to be viable and unlikely to be found in patient populations.

Mutations in complex IV structural subunits are rare, with the majority of complex IV deficiencies being caused by mutations in assembly factors such as SURF1, COX10, COX15, SCO1 and SCO2 [157]. To date, only 3 genes have been found with mutations in complex IV subunits that lead to complex IV deficiency. Of these genes, *COX4I2*, *COX7B* and *COX6B1*, only *COX6B1* has been found to carry a mutation leading to cardiomyopathy. The mutation caused an arginine to cysteine change at position 20

(R20C) of the protein and resulted in an 89% reduction in protein levels and an 83% drop in complex IV enzymatic activity [158].

Disorders of complex V or ATP synthase are also rare, the majority have been traced to mutations in mtDNA, over 30 have been linked to the mtDNA genes *MTATP6* and *MTATP8* [159]. Of those that have been traced to nuclear mutations, most are associated with assembly factors which will be covered in more detail in section '1.1.5.3. Assembly factor mutations', only the genes *ATP5A1* and *ATP5E* have been implicated in human disease with a total of three patients being known. A mutation (R329C) in ATP5A1 of 2 patients led to severe neonatal encephalopathy and was shown to cause an ATP synthase deficiency in both patients [160]. A less severe phenotype was also found in a patient harbouring a homozygous Y12C mutation in ATP5E. This mutation also led to an ATP synthase deficiency as confirmed by a 70% reduction in ATP synthase content when compared to controls [161].

Overall, of the roughly 75 nuclear encoded subunits of the mitochondrial electron transport chain, at least 27 have been implicated in causing conditions associated with mitochondrial deficiency. This is likely an underrepresentation of the real rate of causative mutations in the general population as many mutations are likely to result in phenotypes too severe to be viable. Furthermore, the lack of identified mutations in supernumerary subunits may indicate that these are better tolerated and less likely to be pathogenic.

Subunit	Location	Known Mutations	Clinical Phenotype	Reference
NDUFV1	N	R59X-T423M	Progressive unspecified encephalomyopathy	[141]
		A341V	Leukoencephalopathy with macrocephaly	[143]
		E214K-IVS8+4A>C (Skip exon 8)	Leigh syndrome	[143]
		A432P-c.989-990del (C332X)	Leigh-like syndrome	[145]
		Y204C-C206G	Leigh-like syndrome	[145]
		A4341V	Leukoencephalopathy with macrocephaly	[162]
		R386C	Leukoencephalopathy	[163]
		R257Q-A211V	Leukoencephalopathy	[164]
		E377K	Lethal infantile mitochondrial disease	[74]
NDUFV2	N	IVS2+5_+8delGTAA (Skip exon 2)	Cardiomyopathy and encephalopathy	[142]
		IVS2+5_+8delGTAA (Skip exon 2)	Cardiomyopathy and encephalopathy	[165]
NDUFS1	N	del222leu-D252G	Leukoencephalopathy	[145]
		R421W-R557X	Unspecified Encephalopathy	[145]
		M707V-LS deletion	Leigh-like syndrome	[145]
		Q552K	Leukoencephalopathy	[163]
		L231V	Leigh syndrome	[166]
		D619N-R557X	Leukoencephalopathy	[167]
		R408C	Leukoencephalopathy	[168]
		R408C	Leigh syndrome	[168]
		del211Glu-V228A	Leukoencephalopathy	[169]
		V228A-D252G	Leukoencephalopathy	[169]
		T595A	Progressive cavitating leukoencephalopathy	[170]
NDUFS2	Q	R228Q	Hypertrophic cardiomyopathy/encephalomyopathy	[144]
		P229Q	Hypertrophic cardiomyopathy/encephalomyopathy	[146]
		S413P	Encephalomyopathy	[146]
		M292T-R118Q	Leigh syndrome	[169]
		M292T-M443K	Leigh syndrome	[169]
		M292T-E148K	Leigh syndrome	[169]
		R138Q-R333Q	Leigh-like syndrome	[169]
		M292T-c.866+4A>G ‡	Leigh-like syndrome	[169]
NDUFS3	Q	T145I-R199W	Leigh syndrome	[146]
NDUFS7	Q	V122M	Leigh syndrome	[147]
		R145H	Leigh-like syndrome	[171]
		c.17-1167C>G (Cryptic exon and fs)	Leigh-like syndrome	[172]
NDUFS8	Q	P79L-R102H	Leigh syndrome	[148]
		P85L-R138H	Leigh syndrome	[173]
		P79L	Leigh-like syndrome	[169]
		G154S	Leukoencephalopathy	[74]
NDUFV3	N	None		
NDUFS4	N	K158fs	Unspecificed encephalomyopathy	[174]
		W97X	Leigh-like syndrome	[175]
		R106X	Leigh-like syndrome	[176]
		R106X	Leigh-like syndrome	[176]
		W14X	Leigh-like syndrome	[177]
		IVS1-1G>A	Leigh-like syndrome	[178]
		K154fs	Leigh-like syndrome	[179]

		D119H-K154fs	Leigh-like syndrome	[180]
		c.99-1G>A-K154fs	Leigh syndrome	[74]
		c.99-1G>A-c.351-2A>G	Leigh syndrome	[74]
NDUFS6	N	Exon 3/4 deletion	Lethal infantile mitochondrial disease	[181]
		c.186+2T>A	Lethal infantile mitochondrial disease	[182]
		C115Y	Severe neonatal lactic acidosis	[182]
NDUFA12	N	R60X	Leigh syndrome	[183]
NDUFA13	P_P	R57H	Leigh-like syndrome	[184]
NDUFA11	P_P	IVS1+5G>A ‡	Lethal infantile mitochondrial disease	[185]
		IVS1+5G>A ‡	Encephalocardiomyopathy	[185]
NDUFA7	Q	None		
NDUFA5	Q	None		
NDUFA2	N	IVS2+5G>A	Leigh-like syndrome	[186]
NDUFA10	P_P	c.1A>G-c.425A>G	Leigh syndrome	[187]
NDUFA9	Q	R360C	Myopathy	[188]
		R321P	Leigh-like syndrome	[189]
NDUFS5	P_P	None		
NDUFA1	P_P	G8R	Leigh-like syndrome	[189]
		R37S	Encephalomyopathy	[188]
		G32R	Progressive neurodegeneration	[190]
NDUFA8	P_P	None		
NDUFA6	Q	None		
NDUFA3	P_P	None		
NDUFC1	P_P	None		
NDUFA4	*	C.42+1G>C ‡	Leigh syndrome (COX deficient only)	[191]
NDUFAB1	Q/ P_D	None		
NDUFB4	P_D	None		
NDUFB2	P_D	None		
NDUFB8	P_D	None		
NDUFB11	P_D	R88X	MLS syndrome	[192]
		c.402delG	MLS syndrome	[193]
NDUFB1	P_D	None		
NDUFB10	P_D	E70X-C107S	Lactic acidosis and cardiomyopathy	[193]
NDUFB5	P_D	None		
NDUFB9	P_D	None		
NDUFB7	P_D	None		
NDUFB6	P_D	None		
NDUFC2	P_P	None		
NDUFB3	P_D	None		

Table 1.1. Mutations of nuclear encoded complex I subunits and associated clinical phenotypes. Adapted and updated from Pagniez-Mammeri et al. (2012) [140]. Locations of proteins in modules according to Guerrero-Castillo et al. (2016) [72]. *NDUFA4 does not have a recognized position within complex I. ‡ Mutation results in splicing abnormality.

1.1.5.2. Mitochondrial DNA Mutations

Human mitochondrial DNA is 16.5 kb in length and codes for 37 genes, 22 of which are tRNAs and 2 are rRNAs, the remaining genes are all constituent proteins of the mitochondrial electron transport chain [145]. Due to the large copy number of mitochondrial DNA, mutations may often not lead to symptoms until mutated DNA reaches a threshold level of heteroplasmy in a given tissue, this threshold level may differ from tissue to tissue and can depend on the type of causative mutation [194]. Mitochondrial mutations take on 2 forms, those affecting mitochondrial protein synthesis, and those affecting mitochondrial protein coding genes.

Mutations that affect mitochondrial tRNA, lead to a defect in protein synthesis and an overall reduction in the assembly of mitochondrial proteins, this type accounts for almost 60% of mutations whilst tRNA genes only account for 10% of the mitochondrial genome [194]. Perhaps the most well characterised mitochondrial mutation, an A to G at nucleotide 3423 in $tRNA^{LEU}$, is widely associated with MELAS syndrome. However, evidence has also linked it to a maternally inherited cardiomyopathy without any other signs or symptoms of MELAS [195, 196]. Other tRNAs have also been implicated in mitochondrial disorders, with mutations in the genes *MTTL1* ($tRNALeu^{(UUR)}$), *MMTI* (tRNAIle), *MTTK* (tRNALys), *MTTL2* ($tRNALeu^{(CUN)}$) and *MTTT* (tRNAThr) all being linked to conditions involving cardiomyopathy [145]. Large scale deletions can also lead to the loss of tRNA genes, these mutations are suspected to occur in the germ line rather than be maternally inherited as it is uncommon to find parents or siblings sharing mutations. These mutations can occur anywhere in the mitochondrial genome and typically result in one of three syndromes; Kearns-Sayre, progressive external ophthalmoplegia (PEO), or Pearson's. The threshold level for deletion mutations tends to be lower than that for point mutations with a requirement for roughly 80% of damaged DNA before symptoms become apparent [194].

Mutations in mitochondrial protein coding genes are less common than those in tRNA, accounting for roughly 40% of mutations in the 13 protein coding genes that account for 70% of the genome [194]. Complexes I, III, and IV as well as ATP synthase may be affected by mutations in any of their mitochondria encoded subunits, but complex II is unaffected as it is entirely nuclear encoded [197]. Symptoms are typically noticed in

infants and vary from cardiomyopathy to myopathy, deafness, mental retardation, cataracts, retinitis pigmentosa, epilepsy, encephalopathy and neuropathy. Govindaraj et al. (2013) identified 28 novel mutations in mtDNA from 114 HCM patients. Of these, 10 were non-synonymous and lay in genes encoding electron transport chain proteins including *MTND1*, *MTCOI*, *MTATPase8* and *MTATPase6* [198].

Finally, rRNA mutations are comparatively rare, accounting for about 2% of mutations, and may occur in either the 12 or 16kDa ribosomal subunits. These conditions may be mild, resulting in hearing loss, or more severe, resembling MELAS [197].

1.1.5.3. Assembly Factor Mutations

The complexity and two genome nature of most of the mitochondrial electron transport chain complexes necessitates the involvement of a variety of chaperone and assembly factor proteins which allow for the correct and efficient assembly of the complexes within the mitochondria. Mutations in these assembly factors account for the majority of mitochondrial deficiencies and the resultant diseases [29].

All five of the mitochondrial electron transport chain complexes have a unique set of assembly factors that are required for functional assembly. Despite the identification of many of these assembly factors there is still an incomplete picture and more work is required. This section will primarily focus on complex I assembly factors, although the remaining complexes will be summarised.

In mammals complex I is known to have at least 13 assembly factors involved directly with structural assembly (NDUFAF1, NDUFAF2, NDUFAF3, NDUFAF4, ACAD9, ECSIT, TIMMDC1, TMEM186, TMEM126B, COA1, TMEM70, FOXRED1 and ATP5SL) as well as a number of other chaperones or assembly factors involved in other aspects of forming functional complex I or whose role is not yet fully understood (NDUFAF5, NDUFAF6, NDUFAF7, IND1, DNAJC11, and AIF). Of these 19 proteins, at least 11 (Table 1.2) have been identified in human patients with mitochondrial disease and it is noteworthy that roughly 40% of all patients suffering from mitochondrial disease have no mutations in structural genes [74, 199-202]. Mutations in complex I assembly factors lead to a loss of fully assembled complex I, an accumulation of complex I assembly intermediates and a reduction in enzymatic activity [29, 75, 203].

Subunit	Known Mutations	Clinical Phenotype	Reference
NDUFAF1 (CIA30)	T207P-K253R	Cardioencephalopmyopathy	[204]
	R211C-G245R	Fatal infantile hypertrophic cardiomyopathy	[205]
NDUFAF2 (NDUFA12L/B17.2L)	R45X-LS deletion	Progressive encephalopathy	[78]
	M1L	Progressive encephalopathy	[206]
	Y38X	Leigh syndrome	[77]
	LS deletion	Encephalomyopathy	[207]
	W3X	Leigh syndrome	[208]
	W74X	Leigh syndrome	[74]
	I35SfsX17	Leigh syndrome	[74]
	A73GfsX5	Leigh syndrome	[74]
NDUFAF3 (C3ORF60)	G77R	Lactic acidosis	[76]
	R122P	Encephalomyopathy with macrocephaly	[76]
	M1T-R122P	leukoencephalopathy	[76]
NDUFAF4 (C6ORF66)	L65P	Encephalomyopathy	[75]
	L65P	Encephalomyopathy and Cardiomyopathy	[75]
NDUFAF5 (C20ORF7)	L229P	Dysmorphism and lactic acidosis	[209, 210]
	L159F	Leigh-like syndrome	[211]
	G250V	Leigh syndrome	[212]
NDUFAF6 (C8ORF38)	Q99R	Leigh-like syndrome	[213]
NDUFAF7 (MIDA)	None		
ACAD9	R518H	Exercise intolerance, hypertrophic cardiomyopathy	[214]
	E63X-E413K	Encephalopathy, hypertrophic cardiomyopathy	[216]
	V546L	Hypertrophic cardiomyopathy	[215]
	A170V-H563D	Hypertrophic cardiomyopathy	[217]
	R414S-c.1650_1672dup	Fatal infantile hypertrophic cardiomyopathy	[217]
ECSIT	None		
TMEM186	None		
TMEM126B	G212V	Exercise intolerance	[201]
	c.401delA-G212V	Exercise intolerance	[203]
TMEM70 *	c.317-2A>G	Hypotonia, lactic acidosis, hypertrophic cardiomyopathy	[202]
	c.317-2A>G;c.A628C	Hypotonia, lactic acidosis, hypertrophic cardiomyopathy	[204]
	c.701A>C	Leukoencephalopathy, hypertrophic cardiomyopathy	[204]
COA1	None		
TIMMDC1 (C3ORF1)	None		
FOXRED1	Q232X-N430S	Leigh syndrome	[74]
IND1 (NUBPL)	G56R-D273QfsX31 - del. Dup.	Encephalomyopathy	[74]
ATP5SL	None		
DNAJC11	None		
AIF	None		

Table 1.2. Mutations of complex I assembly factors and associated clinical phenotypes. Adapted and updated from Pagniez-Mammeri et al. (2012) [200]. *Mutations result in complex V deficiency, not complex I.

In the interests of brevity, this report will focus only on those assembly factors identified as part of complex I assembly by Guerrero-Castillo et al. (2016) [72].

Of the 5 assembly factors that form the MCIA complex [69, 70] 3 have been identified with pathogenic mutations, NDUFAF1, ACAD9 and TMEM126B (Table 1.2). In addition to the 2 unrelated patients identified by Nouws *et al.* (2010), Dewulf *et al.* (2016) identified a further 9 patients from 3 families who all suffered from hypertrophic cardiomyopathy and due to mutations in ACAD9. Loss of full ACAD9 function led to decreased levels of the associated proteins NDUFAF1 and ECSIT as well as a reduction in the levels of complex I [214, 215]. The two patients identified with NDUFAF1 mutations also demonstrate a loss of complex I, 30%[204] and ~40%[205] of healthy controls, however, ACAD9 levels were not measured to confirm the reciprocal relationship. In contrast to the other patients with MCIA complex protein mutations, TMEM126B patients display a milder phenotype with a later onset. Most of these patients were identified over the age of 8 years with an exercise intolerance phenotype due to reduced complex I protein levels (10-48% of healthy control) and elevated complex II, III, IV and V levels, possibly as a compensatory mechanism. Of most interest is that these patients all show decreased levels of all of the other MCIA components, raising the question of why these patients display a comparatively mild phenotype [201]. Furthermore, in 2 of these patients it was seen that both ECSIT and ACAD9 were present in super-complexes containing complexes I, III and IV.

Of the remaining characterised membrane arm assembly factors only 2, TMEM70 and FOXRED1, contain known pathogenic mutations. TMEM70 mutations result in a severe phenotype including hypertrophic cardiomyopathy, however these mutations all result in complex V deficiency with no reports of effects on complex I [202]. Only a single patient with Leigh syndrome has been identified with a FOXRED1 mutation [74].

The three known matrix arm assembly factors all have greater numbers of known patients with pathogenic mutations. The NDUFAF2 mutations described in table 1.2 all result in a truncation or complete loss of the protein leading to a significant loss of complex I protein in all cases. The NDUFAF3 mutations were found in 5 patients from 3 families all of whom died before 6 months of age. In contrast to the NDUFAF2 patients, these mutations did allow for the formation of NDUFAF3 protein, although the levels of

complex I in those tested was severely reduced [76]. Finally, NDUFAF4 is the only remaining assembly factor from this list whose place in the assembly pathway was characterised by Guerrero-Castillo et al. (2016) [72]. Six patients from 2 families were identified carrying the same leucine to proline change (Table 1.2), which resulted in a loss of complex I activity which caused encephalopathy in all of the patients and hypertrophic cardiomyopathy in one [75].

It is interesting to note that certain phenotypes appear to be common to different arms of complex I and the associated assembly factors. Assembly factors of the matrix arm appear to have an anecdotal link with Leigh syndrome and encephalopathy whilst those of the membrane arm are more often than not found with a cardiomyopathy in addition to other phenotypes.

In humans, complex II has only two known assembly factors, SDHAF1 (succinate dehydrogenase assembly factor 1) and SDHAF2 (succinate dehydrogenase assembly factor 2), though there are expected to be further undiscovered proteins with an important role as there are at least four assembly factors in yeast [29]. SDHAF1 was the first to be implicated in disease with a study finding 2 families with children exhibiting leukoencephalopathy caused by loss of complex II activity [216]. SDHAF2 mutations have been identified in families with history of certain types of cancer (paraganglioma and phaeochromocytoma), but there remains to be a case of SDHAF2 mutation linked to any classical mitochondrial disease [217].

Complex III again only has two known assembly factors, BCS1L and TTC19, but with complex III deficiencies being rare, possibly due to the catastrophic effect of reduced complex III on super-complex formation, little is known about the involvement of any other assembly factors [29]. A large number of patients with mutations throughout the *BCS1L* gene have been identified with a variety of phenotypes [29]. The BCS1L protein is known to contain 4 domains; a transmembrane domain (TMD), a mitochondrial targeting sequence (MTS), an import auxiliary sequence (IAS) and an ATPase domain [218]; with mutations identified in at least 3, although there appears to be no correlation between the disease caused and the domain affected. The mildest form of disease is Björnstad syndrome which results in sensorineural hearing loss and twisted brittle hair cells (pili torti), mutations that lead to this condition have been identified throughout

the *BCS1L* gene [219]. At the other end of the scale is GRACILE (growth retardation, aminoaciduria, cholestasis, iron overload, lactacidosis, and early death) syndrome, which results in neonatal lethality and may again be caused by mutations anywhere in the *BCS1L* gene [219, 220]. In between these two extremes a number of patients have been identified with phenotypes ranging from encephalomyopathy, lactic acidosis, liver failure and muscle weakness [218, 221-223]. Mutations in the other known assembly factor, TTC19, typically result in neurological impairment although the age of onset is highly variable. The first patients identified with neurological conditions varied in onset from late infancy to 42 years of age [224]. A later study identified another patient with a TTC19 mutation that resulted in Leigh syndrome with early onset at about 13 months of age [225].

Studies in yeast have shown that Complex IV assembly is highly regulated and may involve as many as 40 assembly factors though only a fraction have been identified as causative of human disease [226], however, these will not be covered in detail in this section. The mutations identified in complex IV assembly factors are associated with a wide range of clinical phenotypes ranging from Leigh syndrome and leukodystrophy, to myopathy, cardiomyopathy and lactic acidosis as well as others.

Finally, ATP synthase has a similar situation to that of complex III. Several factors required for assembly have been identified in yeast but of these only two have been found in humans (ATP12 and ATP11), both of which prevent the formation of aggregates of the incomplete F_1 portion of the complex by binding the α and β subunits respectively[227]. A single patient with a tryptophan to arginine mutation (W94R) was described as having a condition resembling COFS (cerebro-oculofacioskeletal) syndrome [228].

It can be seen as a common feature that the majority of assembly factor mutations result in multi-system disorders that invariably prove fatal. Only those mutations affecting the membrane arm of complex I appear to cause milder or mono-systemic disorders. This may be due to a greater degree of toleration for these mutations in the complex I assembly process, it may be due to complex I's earlier point in the ETC meaning a loss of function is less devastating to the overall function of the chain, or it may reflect some

degree of redundancy either across tissue types (different assembly factors in different tissues) or within tissues (other assembly factors can take up the slack).

1.2. ECSIT

In humans, evolutionarily conserved signalling intermediate in toll pathway (ECSIT) is a 431 amino acid adapter protein with 2 identifiable isoforms (50/33kDa) and a third potential isoform based on splice prediction (24kDa) [229, 230]. In the mouse ECSIT contains 435 amino acids and maintains almost 75% sequence homology with the human protein (Figure 1.8), however there is only experimental evidence of a single protein isoform existing in mouse tissues (50kDa).

ECSIT was first identified from a yeast 2 hybrid screen as a signalling intermediate in the toll/IL-1 pathway, where it was shown to regulate MAP3K1 (MEKK-1) [229]. Later work in a mouse knock-out line implicated ECSIT in the bone morphogenetic protein (BMP) pathway. As part of this pathway, ECSIT interacts with SMAD1 and SMAD4 and is involved in mesoderm formation of the early embryo [230]. More recently, ECSIT has been shown to localise to mitochondria where it binds and stabilises the complex I assembly factor NDUFAF1, allowing for the efficient assembly of complex I [231].

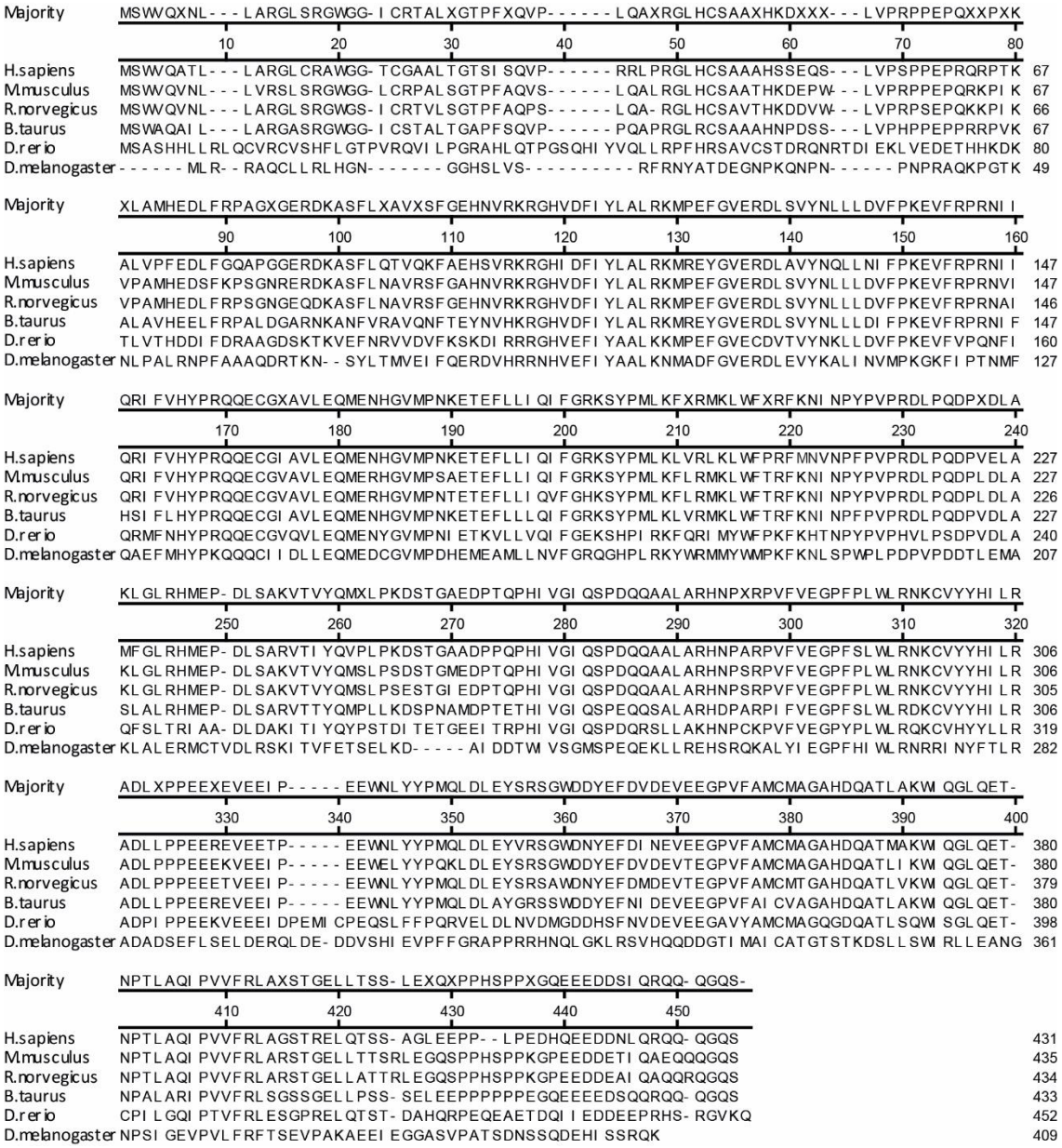

Figure 1.8. Protein sequence alignment of ECSIT protein in *Homo sapiens, Mus musculus, Rattus norvegicus, Bos taurus, Danio rerio* and *Drosophila melanogaster*. Source: ncbi.nlm.nih.gov/homologene.

1.2.1. Protein Structure and Homology

Human ECSIT protein has 3 recognisable domains in the full length protein, an N-terminal mitochondrial targeting sequence (amino acids 1-48), a highly ordered (Figure 1.9) pentatricopeptide repeat region (PPR) (amino acids 90-266) and a less ordered C terminal domain that shows some 3D resemblance to pleckstrin homology domains (amino acids 275-380) [68]. Mouse ECSIT protein maintains roughly 73% sequence homology to the human protein (Figure 1.9) and shows the presence of the same mitochondrial targeting sequence seen in the human protein (amino acids 1-48) (results according to Phyre2 web server) [232]. The PPR motif in mouse is reduced in size from the human protein prediction, 176 vs 129 amino acids. However, the pleckstrin homology domain appears to occupy roughly the same section of the protein from 278 to 379 amino acids, only being 4 amino acids shorter in the mouse.

The N terminal mitochondrial targeting (MTS) sequence is required for the localisation of the protein to the mitochondria where the MTS is cleaved, this results in 2 protein products from the single long ECSIT isoform, a ~50kDa cytosolic form, and a ~45kDa mitochondrial form [231]. Of the remaining two potential domains in the ECSIT protein, only the PPR domain has been shown to have any potential link to mitochondrial processes. These domains are thought to bind RNA in a sequence specific manner, although this has not been demonstrated for ECSIT, and play a role in maturing and stabilising RNA molecules [233]. There is some evidence to suggest that at least one mammalian protein containing at PPR domain, PTCD2, is involved in mitochondrial electron transport chain assembly, and interfering with the PPR domain results in defects of complex I and complex III assembly in a variety of tissues [234, 235].

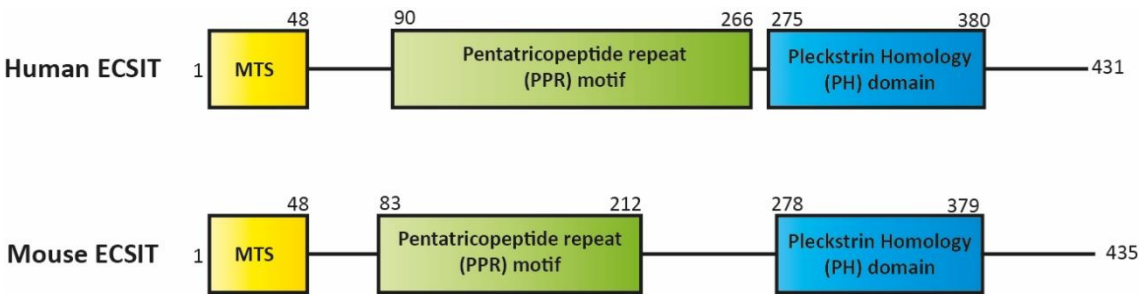

Figure 1.9. Protein domains of human [68] and mouse ECSIT as predicted by Phyre2 webserver [232]. Mitochondrial targeting sequence (MTS) shows no variation between the two models whilst the PPR domain is shorter in the mouse model and the PH domain differs in length by 4 amino acids.

1.2.2. Toll Like Response

As mentioned above, ECSIT was first identified as interacting with the proteins TRAF6 (tumour necrosis factor (TNF) receptor associated factor 6) and MEKK-1/MAP3K1 (ERK kinase kinase-1/Mitogen–activated protein kinase) in the Toll/IL-1 pathway. It was shown that ECSIT binds to the multi-adapter protein TRAF6 and allows for the phosphorylation of MEKK1 (MAP3K1) into an active state. This phosphorylation event leads to activation of NF-κB and promotion of the innate immune response [229]. The work by Kopp et al. (1999) also suggested that the ECSIT-TRAF6 complex leads to activation of the TAK1 protein, allowing it to interact with and phosphorylate TAB1 and 2, offering another pathway by which ECSIT can participate in the toll pathway [229].

Studies around the same time showed that TRAF6, and by association ECSIT, is involved in not only the activation of NF-κB but also in the activation of other aspects of the MAP3K1 signalling cascade, resulting in phosphorylation of JNK, IKK and NF-κB [236]. It was later revealed that the nature of the interaction between TRAF6 and ECSIT is not simply binding but poly-ubiquitination of ECSIT, leading to localisation to the OMM (outer mitochondrial membrane) and degradation [237]. Macrophages deficient in either TRAF6 or ECSIT exhibit reduced mitochondrial ROS and had an increased susceptibility to intracellular bacteria, as was demonstrated by infecting the cells with a strain of salmonella expressing GFP (green fluorescent protein). These infected macrophages showed increased levels of bacterial CFU (colony forming units) at all of the time points tested, indicating that ECSIT may link mROS production with the innate immune system [237].

In the first of two papers, Wi *et al.* (2014) demonstrated that the interaction between TRAF6 and ECSIT occurs between residues 200 and 257 of the human ECSIT protein and in a second paper showed that the poly-ubiquitination of ECSIT by TRAF6 occurs at residue K372 of the human protein, leading to ECSIT interacting directly with the p65/P50 NF-κB proteins, activating them and facilitating their translocation to the nucleus [238]. In addition, this group confirmed the suspicions of Kopp *et al*. (1999) by demonstrating that ECSIT interacts with TAK1 in the region of residues 257-431 of the human protein, resulting in the formation of a TAK1-ECSIT-TRAF6 complex that is activated by TLR4. The formation of this complex activates TAK1, in turn activating IKK

complexes. IKK complexes are then activated to phosphorylate and polyubiquitinate IκB-α which is degraded, liberating p65/P50 NF-κB [239].

In addition to investigating ECSIT's part in the BMP pathway, Xiao *et al*. (2003) knocked down ECSIT in the macrophage cell line Raw 264.1 using shRNA, showing that loss of ECSIT protein leads to loss of NF-κB activation through the toll pathway, but not through the TNFα pathway, indicating that ECSIT works exclusively as an intermediary of the TLR pathway [230].

The role of ECSIT in the innate immune system and in particular the Toll like receptor pathway is demonstrated in figure 1.10, this shows that the result of ECSIT interaction with TRAF6 is the activation of MEKK-1 (MAP3K1) ultimately leading to the activation of NF-κB, JNK and p38 MAPK resulting in stimulation of the innate immune response.

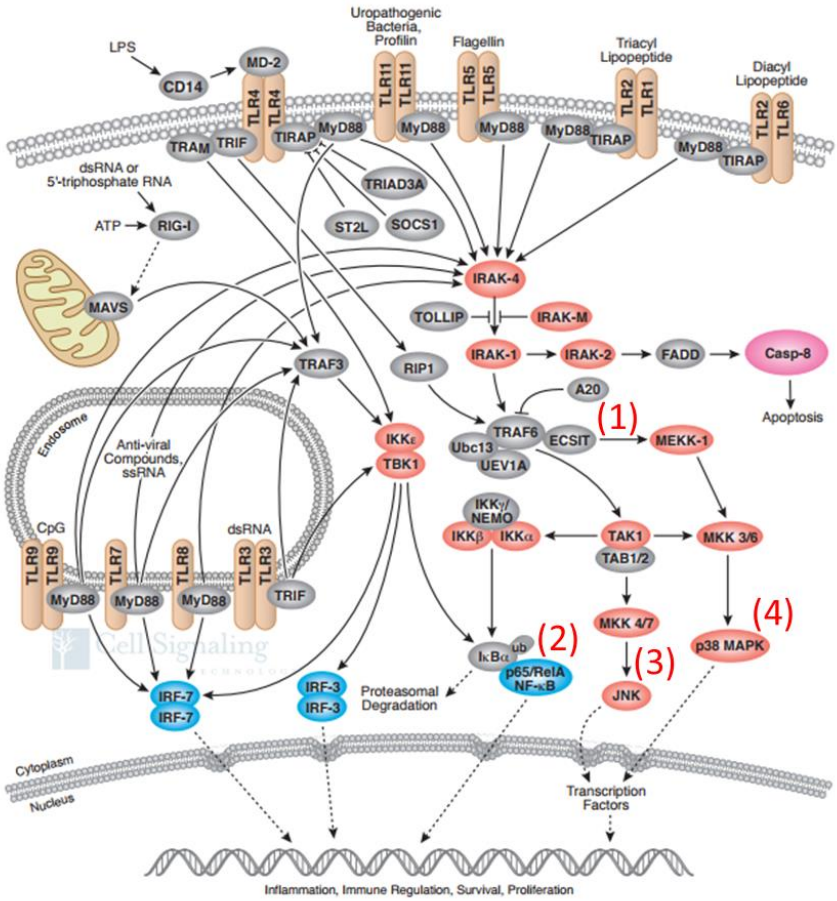

Figure 1.10. Diagram of the Toll-like response and the position of ECSIT (1) in the pathway. Interaction of ECSIT with TRAF6 and MEKK-1 results in the activation of NF-κB (2) through the degradation of IκB-α, and phosphorylation of JNK (3) and p38 MAPK (4) through the activation of MEKK-1 (MAP3K1). Image courtesy of Cell Signaling Technology® (www.cellsignal.com).

1.2.3. Bone Morphogenetic Protein Pathway

In addition to its role in toll-like receptor (TLR) signalling and complex I assembly, ECSIT also has an identified role in the bone morphogenetic protein (BMP) pathway and mouse knockouts show embryonic lethality around the point of gastrulation (E7.5). Mutant embryos demonstrated abnormal development with the loss of mesoderm development and a thickening of the epiblast as well as a loss of downstream expression of the BMP pathway gene, *Tlx2* (T-Cell leukaemia homeobox 2). Ultimately the role of ECSIT in the BMP pathway was found to be as an essential co-factor of SMAD4. Following BMP expression, the ECSIT-SMAD4 complex interacts with SMAD1 and allows the complex to bind the BMP response element of the *Tlx2* promoter, enabling transcription [230].

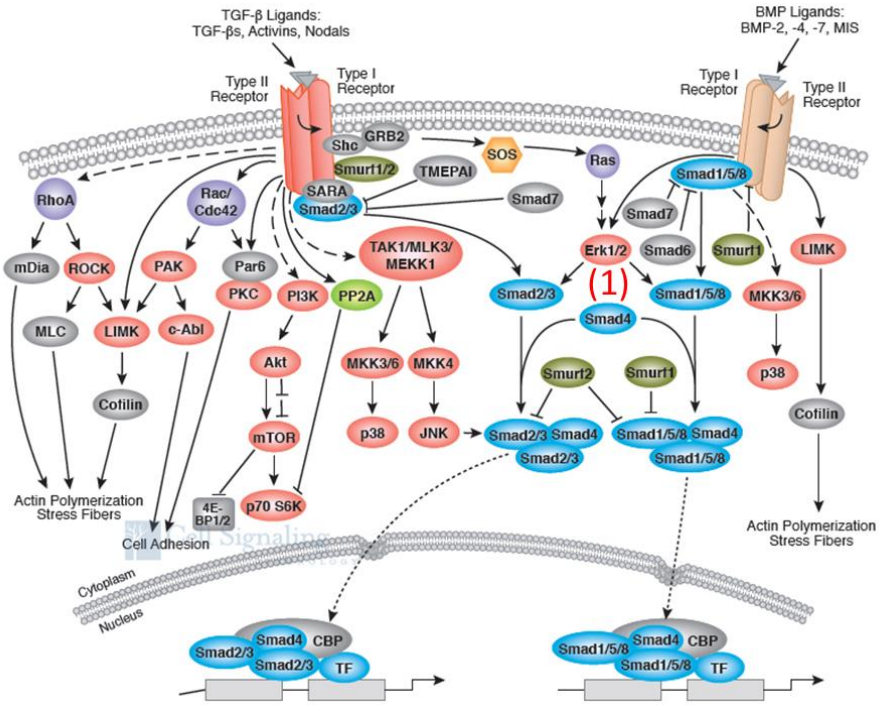

Figure 1.11. Schematic of the BMP and TGF-β pathways. ECSIT interacts with SMAD4 (1) as an essential co-factor leading to *Tlx2* expression. Image courtesy of Cell Signaling Technology® (www.cellsignal.com).

Interestingly, ECSITs interaction with SMAD4 implicates it in the TGF-β pathway (Figure 1.11) as SMAD4 acts as the common cofactor of all TGF-β activated SMAD complexes in the nucleus, possibly through its unique SAD (SMAD-activation domain) [240].

The link between the BMP and TGF-β pathways and innate immunity is well established and ECSIT may function as part of the mechanism linking these essential pathways [241].

1.2.4. Complex I Assembly

The role of ECSIT in the assembly of complex I was first noted by Vogel *et al.* (2007), this work used tandem affinity purification (TAP) of mitochondrial lysates from human embryonic kidney (Hek293) cells containing a tagged form of the known complex I assembly factor NDUFAF1. Amongst the proteins identified by FT-MS (Fourier transform mass spectrometry) were a number of peptides specifically related to ECSIT. Prediction software also identified a cleavable mitochondrial targeting sequence corresponding to the 49 N-terminal amino acids, the presence of which was confirmed by the persistence of a ~45-kDa isoform upon treatment with trypsin and the loss of the non-mitochondrial ~50-kDa isoform under the same conditions. Further work, using a GFP tagged form of ECSIT with and without its N-terminal targeting sequence, confirmed that the 5-kDa fragment is necessary for mitochondrial localisation [231].

The interaction of ECSIT with NDUFAF1 and complex I was confirmed using two-dimensional blue native PAGE analysis of mitochondrial lysates. ECSIT was found in large complexes of ~500, 600 and 850kDa, the same as that of NDUFAF1 in the cell type of interest. siRNA knock-down of ECSIT then showed a severe reduction in complex I levels and a loss of 50% of complex I enzymatic activity [231].

In support of the work completed on the ECSIT-NDUFAF1 interaction, Nouws *et al*. (2010) demonstrated that ACAD9 is also a complex I assembly factor that interacts with both ECSIT and NDUFAF1 and knock down of ACAD9 leads to a decrease in NDUFAF1 and ECSIT protein levels and a reduction in functional complex I levels [214].

Since the initial discovery of ECSIT's interaction with NDUFAF1 and ACAD9, work by Heide *et al*. (2012) has shown that ECSIT forms part of the MCIA complex (Figure 1.12) along with NDUFAF1, ACAD9, TMEM126B and TIMMDC1 [68, 69]. ACAD9 forms a homodimer which acts as the scaffold for the interaction of ECSIT and NDUFAF1, bringing the 3 proteins together. This trimer then interacts with the membrane bound proteins TMEM126B and TIMMDC1 before acting as part of the complex I assembly process [68].

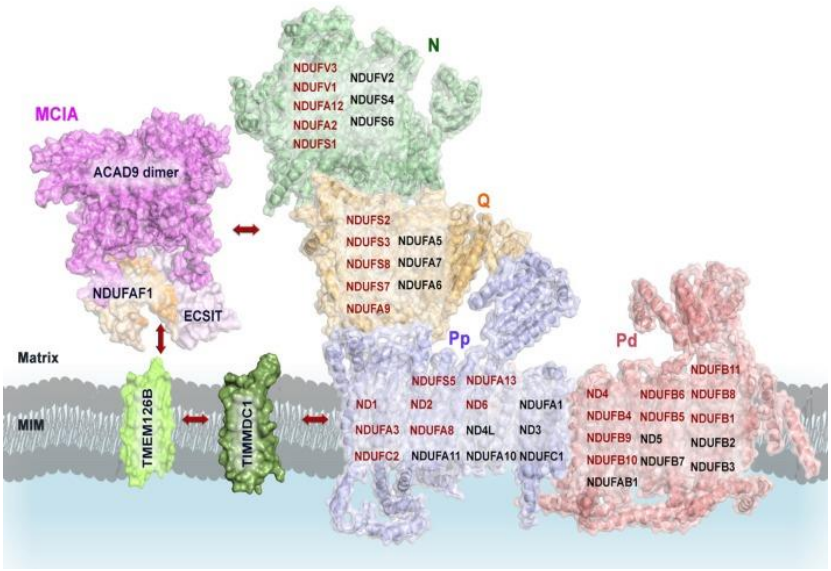

Figure 1.12. Structure and subunits of complex I alongside the proposed formation of the MCIA complex containing ACAD9, NDUFAF1 and ECSIT which go on to interact with TMEM126B and TIMMDC1. [68]

ECSIT protein contains an RNA binding domain in the form of a PPR domain. The same is true for NDUFAF1 which contains an RRM (RNA recognition motif) (Figure 1.13) and whilst no evidence yet exists, this may implicate the MCIA complex in the processing of RNA for complex I proteins [68].

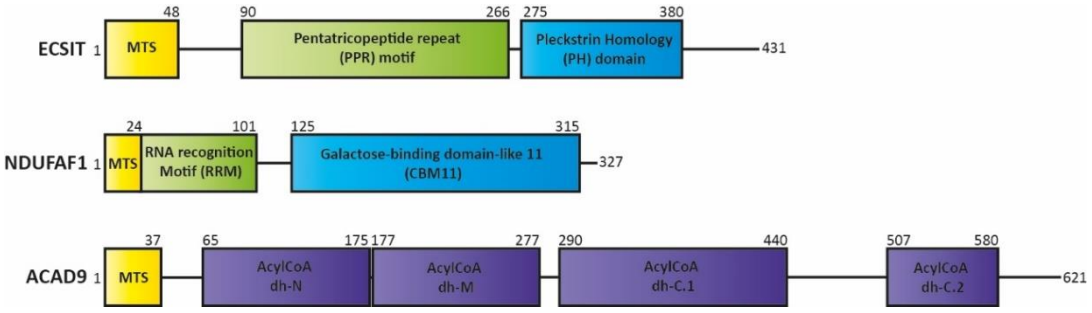

Figure 1.13. Protein domains of human ECSIT, NDUFAF1 and ACAD9 proteins showing RNA recognition motifs within ECSIT and NDUFAF1. ACAD9 has 3 AcylCoA domains denoted as the N, M and C domains with the C domain being split into the C-1 and C-2. Adapted from Giachin *et al*. (2016) [68].

Finally, the role of ECSIT in complex I assembly was confirmed by Guerrero-Castillo *et al*. (2017) in work that dissected the full complex I assembly process and was detailed earlier in section '1.1.3.8. – Complex I Assembly'. By synchronising the complex I assembly process this work demonstrated that the MCIA is involved in the formation of the P_P-b module of the membrane arm of complex I as one of the initial steps of complex I assembly [72].

1.3. Cardiomyopathy

1.3.1. Definition, classification and identification

Cardiomyopathy by its broadest definition is any disease of the heart muscle, of which there are many types with a wide range of genetic and environmental causes (Table 1.3), however this report will focus on the two main kinds of hypertrophic and dilated cardiomyopathy (Figure 1.14).

Disease	Mutated gene	Pathology
Hypertrophic cardiomyopathy	Myosin binding protein C	Increased heart mass
	β-Myosin heavy chain	Left ventricular wall thickening
	α-Myosin heavy chain	Increased cardiomyocyte size
	α-tropomyosin	Myofibrillar disarray
	Troponin T	Decreased volume of left ventricular chamber
	α-Cardiac actin	Interstitial fibrosis
	Troponin I	Enlarged nuclei
	Titin	Ventricular wall stiffness
	Myosin light chains	Inflammation
	Troponin C	
	Vinculin	
	Muscle LIM protein	
	Telothonin	
Dilated Cardiomyopathy	**β-Myosin heavy chain**	Ventricular wall thinning
	Desmin	Ventricular chamber enlargement
	N-cadherin	Cardiomyocyte apoptosis
	α-Cardiac actin	Interstitial fibrosis
	Skeletal muscle myopathies	Enlarged nuclei
	α-Tropomyosin 1	Ventricular wall stiffness
	Muscle LIM protein δ-sarcoglycan	Inflammation
	Lamin A/C	
	TAZ (G4.5)	
	Titin	
	Phospholamban	
	Vinculin	
	Troponin I	
	Troponin T2	
	SCN5A	
	Presenilin 1 & 2	
	Troponin C	
	α-Cardiac actinin	
	Plakoglobin	
Restrictive cardiomyopathy	**Troponin I**	Ventricular wall stiffness
	Desmin	Apoptosis
	α-Cardiac actin	Fibrosis
	Skeletal muscle myopathies	Myofibrillar disarray

	Troponin T	
	β-Myosin heavy chain	
Left ventricular non-compaction	**TAZ (G4.5)**	Trabeculated ventricular walls
	α-Dystrobrevin	Noncompaction of ventricular andocardium
	FKBP12	Necrotic myocytes
	β-Myosin heavy chain	Fibrosis
	α-Cardiac actin	Myofibrillar disarray
	Cardiac troponin	
Arrhythmogenic right ventricular cardiomyopathy	Plakophilin-2	Right ventricular dilation
	Junctional plakoglobin	Right ventricular fibrosis
	Desmocollin-2	Fibrofatty infiltration
	Desmoglein-2	Apoptosis
	Desmoplakin	
Muscular dystrophy-associated cardiomyopathy	Dystrophin	Left ventricular hypertrophy or dilation
	Sarcoglycan	Fibrosis
	Dystroglycan	Apoptosis
	Dystrobrevin	

Table 1.3. Different classifications of cardiomyopathy with associated genetic causes and typical pathological features. Adapted from Harvey and Leinwand (2011) [242]. **Bold** – genetic causes common to more than one classification of cardiomyopathy.

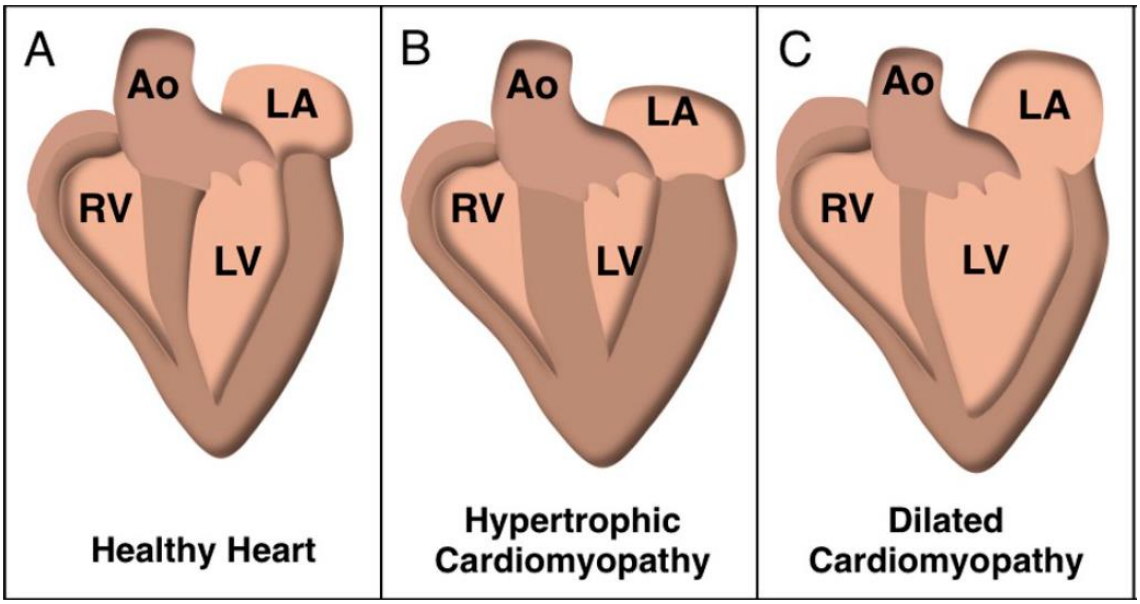

Figure 1.14. Diagrammatic representation of healthy heart (A) vs hypertrophic (B) and dilated (C) cardiomyopathy. Ao – Aorta, RV – right ventricle, LV – left ventricle, LA – left atrium. Hypertrophic cardiomyopathy shows characteristic thickening of the left ventricular (LV) free wall and intraventricular septum (IVS) resulting in decreased LV volume. Dilated cardiomyopathy shows an increase in LV volume and a thinning of the LV free wall and IVS. Taken from Harvey and Leinwand (2011) [242].

Hypertrophic cardiomyopathy (HCM) was first described by Donald Teare in 1957 where he described 8 patients between the ages of 14 and 44 all of whom died of a poorly understood cardiac condition which he then characterised as HCM [243]. Today HCM

affects approximately 1 in 500 people with annual mortality rates around 6 per 10,000 affected individuals [244]. Classical diagnosis of HCM is performed by echocardiography to look for thickening of the left ventricular (LV) free wall, in humans this diagnosis is typically greater than 15mm, without an increase in LV chamber volume. More recently the use of cardiac magnetic resonance imaging (CMR) has improved understanding of the disease and refined risk assessment by providing more detail of the state of not only the LV wall, but also of the mitral valves, papillary muscles and any potential scarring that may have taken place [245]. The genetic causes of HCM are quite well understood with 60% of cases having an identified genetic cause in one of 11 genes encoding proteins of the sarcomere, typically with an autosomal dominant inheritance pattern [245, 246]. Of these 11 sarcomeric genes, 8 are considered to be the core sarcomeric proteins leading to inherited HCM (MYH7, MYBCP3, TNNT2, TPM1, MYL2, MYL3, TNNI3 and ACTC1) [247]. The most common mutations are in beta-myosin heavy chain (*MYH7*) and myosin-binding protein c (*MYBPC3*) which account for between 60% and 70% of cases with an identified genetic variant [245, 247].

Despite the predominance of sarcomeric protein mutations as the cause of HCM, there is also evidence linking ATP regulation to the development of HCM in some patients. Specifically, mutations in the γ_2 subunit protein PRKAG2, have been identified in two families containing a total of 8 affected individuals. The two mutations ('Exon 5:ins Leu' and H142R) lead to HCM, ECG traces with pre-excitation, symptomatic wolf-parkinson-white syndrome (WPWS) as well as a high incidence of sudden death [248].

In addition to these common mutations there is also significant involvement from mitochondrial OXPHOS deficiencies with cardiomyopathy along with encephalopathy being among the most common manifestations of a variety of mitochondrial disorders (See section 1.3.2.) [27].

Whereas HCM is characterised by an increased thickness of the LV wall without an increase of the LV volume, dilated cardiomyopathy (DCM) is characterised by an increase in LV volume and systolic dysfunction, typically without thickening of the LV wall [249]. Whilst the incidence rate for DCM is not as well understood as HCM, conservative estimates put it in the region of 1 in 250 people, though mortality rates are unknown. As with HCM, most DCM is inherited in an autosomal dominant pattern with

a variable, age-dependant variance. However, unlike HCM, DCM has been linked to more than 40 genes including many which are also implicated in HCM. Pathogenic mutations in these 40 genes only account for roughly 30% of known cases of DCM, with the most common being truncation mutants of the protein TITIN. These truncation mutants are found in about 25% of familial cases and 18% of sporadic cases [250].

1.3.2. Mitochondrial Conditions with Cardiac Involvement

Given the essential nature of mitochondria it is unsurprising that defects in mitochondrial OXPHOS function cause a wide variety of diseases with a diverse set of symptoms. Tissues with increased energy demands, such as liver, kidney, brain and heart, are often worst affected [158], but which tissues are affected and which symptoms are present is often unpredictable.

Common amongst the most well characterised mitochondrial syndromes are symptoms resulting from cardiac abnormalities, these can include both myocardial changes and cardiac conduction abnormalities which may include long QT syndromes, increased PR interval, atrioventricular (AV) block and cardiomyopathy (hypertrophic and dilated) amongst others [145]. This section details some of the conditions known to include cardiac abnormalities but is not meant to be exhaustive.

Kearns-Sayre syndrome is a mitochondrial syndrome characterised by pigmentary retinopathy and ophthalmoparesis that affects individuals within the first 2 decades of life. Also present are cardiac conduction abnormalities, hearing loss, cerebellar ataxia, dementia [251] and the condition can ultimately lead to sudden cardiac death [252]. Kearns-Sayre syndrome is a result of large scale deletions of mtDNA which may affect multiple genes involved in the OXPHOS complexes and their assembly.

Myopathy, encephalopathy, lactic acidosis and stroke-like episodes (MELAS) was first described in 1984 where it was described as being clinically separate from both Kearns-Sayre syndrome and myoclonus epilepsy and ragged red fibres (MERRF) [253]. The clinical diagnosis was later defined as requiring 3 key features; stroke before 40 years of age, encephalopathy, and either lactic acidosis or ragged red fibres [254]. The condition may also lead to a variety of other phenotypes including diabetes mellitus, small stature, deafness, cataracts and cardiomyopathy (38% of patients) [145]. The mitochondrial DNA mutation m.3243A>G in the mitochondrial encoded tRNA leucine 1 (MT-TL1) accounts

for roughly 80% of all known MELAS cases [255]. However, the condition has also been associated with as many as 30 other mtDNA mutations [255] including in the complex I subunits MT-ND1[256], MT-ND5[257] and MT-ND6[258].

Leigh syndrome was first described in 1951 by Denis Leigh and is characterised by lesions in the brainstem, thalamus, cerebellum, spinal cord and optic nerves [259]. Clinical symptoms may include respiratory abnormalities, epilepsy, nystagmus, ataxia, optic atrophy, elevated lactate levels and some cases have presented with dilated or hypertrophic cardiomyopathy, although cardiac involvement appears to be dependent on the nature of the mutation [145]. Leigh syndrome can be caused by mutations in either nuclear or mitochondrial DNA and may affect any of the electron transport chain complexes with over 75 individual genes being linked to the condition (Table 1.4) [260]. However the most common are mutations affecting complex I (34%) [261], with the most common individual mutation being m.9176T>G in the gene MT-ATP6 [145, 262].

Biochemical Deficiency	Genes
Pyruvate dehydrogenase	*PDHA1*[a], *PDHB, PDHX, DLAT, DLD, LIPT1, TPK1, SLC19A3, SLC25A19*
Complex I	*MTND1*[b], *MTND2*[b], *MTND3*[b], *MTND4*[b], *MTND5*[b], *MTND6*[b], *NDUFV1, NDUFV2, NDUFS1, NDUFS3, NDUFS4, NDUFS7, NDUFS8, NDUFA1*[a], *NDUFA2, NDUFA9, NDUFA10, NDUFA12, NDUFAF2, NDUFAF5, NDUFAF6, FOXRED1*
Complex II	*SDHA, SDHAF1*
Coenzyme Q10	*PDSS2*
Complex III	*UQCRQ, BCS1L, TTC19*
Complex IV	*MTCO3*[b], *NDUFA4, SURF1, COX10, COX15, SCO2, PET100, LRPPRC, TACO1, ETHE1*
Complex V	*MTATP6*[b]
Combined OXPHOS defects - Pathway affected	
Mitochondrial DNA maintenance	*FBXL4, POLG, SUCLA2, SUCLG1*
Mitochondrial translation	*ΔmtDNA*[c], *MTTI*[b], *MTTK*[b], *MTTL1*[b], *MTTV*[b], *MTTW*[b], *MTFMT, GTPBP3, TRMU, EARS2, FARS2, IARS2, NARS2, GFM1, GFM2, TSFM, C12orf65, PNPT1*
Disease genes that cause secondary impairment of mitochondrial energy generation	
OXPHOS ± PDHc	*HIBCH, ECHS1, SERAC1, AIFM1*[a]
Biotinidase	*BTD*

Table 1.4. Table of human genes containing mutations known to cause Leigh syndrome. Adapted from Lake *et al.* (2016) [260]. Except where denoted, all genes show autosomal recessive inheritance pattern. [a]X-linked inheritance, [b]maternal inheritance, [c]sporadic inheritance.

Other conditions such as Pearson syndrome, myoclonus epilepsy and ragged red fibres (MERRF) and neuropathy, ataxia and pigmentary retinopathy (NARP) have also been linked with cardiomyopathy, but this link is less robust and the number of affected patients is much lower, hence it has not been covered in detail here [145].

1.3.3. Mouse models of Complex I Dysfunction Related Cardiomyopathy

A number of techniques are available for the study of mitochondrial diseases in animal models; these include the production of point mutations, knockout animals, knockdown using siRNA and chemical inhibition amongst others. Here I will focus on the few knockout animal models of complex I deficiency in existence.

At present no technology exists to produce reliable mutations in mitochondrially encoded electron transport chain proteins and no mouse lineages exist with stable mitochondrial mutations, hence all murine models are a result of nuclear encoded mutations [263].

NDUFS4 was the first protein to be globally knocked out in mice that produced a complex I deficiency in mice. However these animals presented with primarily neurological defects and died at 7 weeks of age due to encephalomyopathy and symptoms resembling Leigh syndrome, no cardiological manifestations were observed [264]. Later work involving a tissue specific knockout in cardiac tissue resulted in a ~50% loss of complex I activity and a profound cardiomyopathy as shown by MRI imaging. By assaying mitochondrial hydrogen peroxide production and investigating caspase 3 cleavage this work demonstrated that the cardiomyopathy was not the result of oxidative damage or elevated apoptosis and occurs solely because of complex I deficiency [100].

Another protein, NDUFS6, has also been globally knocked down in a mouse model resulting in a severe cardiomyopathy. Animals demonstrated a 3.2 fold increase in heart weight when compared with wild type mice and a ~90% reduction in complex I activity. This research did not investigate whether there was a relationship with ROS production or increased apoptosis that may ultimately be causative of the cardiomyopathy [265]. Interestingly, this model differs from known human mutations in its presentation, with humans having a system wide disease and early death, although cardiac involvement was not investigated and hence cannot be ruled out.

1.4. ENU Mutagenesis

The discovery that N-Ethyl-N-Nitrosourea (ENU) functioned as a powerful chemical mutagen was first described in 1979 [266] and has since become a valuable tool for the identification of novel genes and pathways associated with mammalian disease. ENU is an alkylating agent which functions by transferring an ethyl or methyl group to the oxygen or nitrogen of nucleotide bases resulting in a DNA adduct that if not corrected leads to a point mutation or small deletion in the genome. ENU typically modifies A/T base pairs either by transversion to T/A (44%) or transition to G/C (38%). G/C to A/T transitions (8%), G/C to C/G transversions (3%), A/T to C/G transitions (5%), and G/C to T/A transitions (2%) are less common [267]. ENU mutagenesis is typically administered

as a series of injections into a male mouse where sperm are mutagenised, allowing for the phenotyping and genetic characterisation of his offspring. Typical dosage leads to a mutation load in the region of one mutation for every 1-1.5Mb [268].

Two of the key advantages of ENU mutagenesis over other systems for genetic modification is the ability to produce a wide range of alleles (hypo, hyper, neo, null, anti) and breeding schemes can be employed to screen for a variety of different mutation types. Single generation breeding can allow for the investigation of dominant or X-linked dominant traits, whilst multi generation schemes can allow for recessive screens. In addition, ENU mutagenesis can be employed in so called 'sensitized strains' which carry a pre-existing mutation or heritable trait to look for modifier genes or regions of the genome associated with a particular trait [269]. A limitation of ENU mutagenesis is the preference for A/T modifications, resulting in the favouring of certain areas of the genome or amino acid changes [268].

1.4.1. The Harwell Ageing Screen

The Harwell ageing screen was a large scale recessive ENU mutagenesis screen using a phenotype driven approach to discover new models of diseases associated with ageing. C57BL/6J male mice were mutagenised with an initial ENU dose of 120mgkg^{-1} followed by two further doses of 100mgkg^{-1} with a week between each dose. Mutagenised mice were then bred with C3H.Pde6b+ females to produce a G_1 cohort. G_1 males were again crossed to C3H.Pde6b+ females to produce a G_2 cohort. G_2 females were genotyped for the presence of the hypomorphic *Cdh23* allele *ahl1* (Inherited from the C57BL/6J parent), this allele is associated with hearing loss and would confound the phenotyping tests planned as part of the screening process. Wild-type animals crossed back to their G_1 fathers to produce an experimental G_3 cohort of roughly 100 male and female carrying a wide variety of genetic modifications. Screening was primarily undertaken on female mice due to issues with singly housing males following long term procedures, but males were screened at a later time point where phenotypes were identified in females from any given pedigree.

Phenotyping tests were carried out longitudinally, typically at an early (3-6 months), intermediate (~12 months) and late (15-18 months) time point with final terminal

procedures undertaken at 18 months of age (Table 1.5) and included a wide variety of systems [270].

Test	Phenotypic Area	Group	Age (weeks)
ECG	Cardiac	All	12
SHIRPA	Neurological	Females (males)	13, 66
Grip strength	Musculoskeletal/neurological	All	13, 66
Slit lamp/ophthalmoscope	Vision	All	15, 49, 65, (73)
Optokinetic drum	Vision/neurological	All	15, 49, 65, (73)
Click box	Hearing	Non *ahl*	14, 26, 39, 50
Auditory brainstem response+click stimulus	Hearing	Non *ahl*	14, 39
Echo-MRI	Growth/body composition	Males (females)	16, 27, 51, 71
DEXA	Musculoskeletal/body composition	Females (males)	16, 51,
X-ray	Musculoskeletal	Females (males)	16, 51, 74
Pupillometry	Vision/neurobehaviour	All	18, 68
Sleep tracking	Neurobehaviour	Females (males)	18, 68
Clinical chemistry	Pathology	Females (males)	28, 53, 80
Fasted bleed	Diabetes/metabolism	Males (females)	17, 28, 52, 80
Fasted insulin	Diabetes/metabolism	Males (females)	33, 57, 72
IPGTT	Diabetes/metabolism	Males (females)	33, 57, 72

Table 1.5. Summary and timetable of phenotyping tests performed during the Harwell Ageing Screen showing tests used, time points performed and sex of animals used. In addition, all animals were weighed every 3 months up until 12 months of age and then monthly. Where a single sex is indicated the other sex was tested where outliers were identified. ECG – electrocardiograph, SHIRPA – Smithkline Beecham, Harwell, Imperial College and Royal London Hospital phenotyping assessment, DEXA – dual energy x-ray absorptiometry, MRI – magnetic resonance imaging, IPGTT – intraperitoneal glucose tolerance test. Adapted from Potter et al. (2016) [270].

1.4.2. ENU Screens for Models of Cardiac Disease

ENU screens have previously been used to investigate novel mutations leading to cardiovascular defects in mice. These screens have focused screening both on adult mice [271] and on identifying defects in the embryonic mouse by using non-invasive *in utero* Doppler echocardiography [272]. Use of colour Doppler to identify defects in mouse embryos was successful in identifying 425 out of 10,091 screened foetuses with cardiac abnormalities, however only small portion of these were mapped and causative genes were not described [273]. It is important to note that limitations with the screening method result in conditions such as hypertrophic cardiomyopathy being under reported in the screen [272].

1.5. Thesis Aims and Objectives

The aim of this project is to characterise a novel model of cardiomyopathy resulting from an ENU induced point mutation in the gene *Ecsit* and identified as part of the Harwell ageing screen. *Ecsit*, the evolutionarily conserved signalling intermediate in the toll pathway, encodes a 50kDa protein known to be involved in innate immunity through the toll pathway, embryogenesis via the bone morphogenetic pathway and in mitochondrial complex I assembly as a key assembly factor with a currently unknown mechanism.

The study will involve the following:

- Phenotyping analysis
    - Characterisation of the cardiomyopathy and longitudinal study to determine disease progression.
    - Characterisation of other body systems, liver, renal, neurological, bone, to determine if there are secondary effects of the mutation which are less prominent than the observed cardiomyopathy.
- Gene identification
    - SNP mapping to identify region of genome carrying mutation.
    - Whole genome sequencing to identify candidate mutations.
    - Sanger sequencing and pyrosequencing, to confirm candidate mutations and isolate causative mutation.
- Functional characterisation of the pathways affected
    - Ex vivo investigation of the BMP pathway.
    - In vitro investigation of the TLR pathway using bone marrow derived macrophages.
    - Protein expression, complex analysis, mitochondrial function analysis, and downstream effects of mitochondrial dysfunction to investigate the mechanism of ECSITs involvement in complex I assembly.

Chapter 2: Materials and Methods

2.1. Materials List

Consumable	Supplier	Product code
2,3-Butanedione monoxime	Sigma-Aldrich	B0753-100G
20% SDS Solution	National Diagnostics	EC-874
2-Mercaptoethanol	Gibco	21985-023
2-Mercaptoethanol (50mM)	Gibco	31350-010
2x Taqman Fast Universal PCR Mastermix	Applied Bioystems	4352042
3,3'-Diaminobenzidine tetrahydrochloride hydrate	Sigma-Aldrich	D5637-1G
70µm cell strainer	Greiner bio-one	542070
96F Without lid Microwell plate	Thermo Scientific	269620
96-Well PCR Plate Non-Skirted	4titude	4ti-0750-25
Accelerator TAAB Embedding Resin Premix	TAAB	T037
Acetonitrile, anhydrous 99.8%	Sigma-Aldrich	271004-1L
Adhesive Film Covers	Abgene	AB-0558
Adhesive Sealing Sheets	Thermo Scientific	AB-0558
Alkaline Phosphatase	New England Biolabs	M0290S
Amersham hyperfilm ECL	GE Life Sciences	28906839
Amersham™ Hybond™ P 0.45 PVDF	GE Healthcare	10600023
Ampicillin Sodium	FORMEDIUM	AMP25
Antimycin A	Sigma-Aldrich	A8764
Bovine Serum Albumin	Sigma-Aldrich	A7906-100G
Bovine Serum Albumin, fatty acid free	Sigma-Aldrich	A8806-5G
Carbonyl cyanide 4-(trifluoromethoxy)phenylhydrazone	Sigma-Aldrich	C2920-10MG
CELLSTAR 10cm Cell Culture Dishes	Greiner bio-one	664-160
CELLSTAR 6 Well Cell Culture Plate, Sterile, With Lid	Greiner bio-one	657-160
CELLSTAR Cell Culture Flasks 25cm2, 50ml, Red filter	Greiner bio-one	690-175

CELLSTAR Cell Culture Flasks 75cm2, 250ml, Red filter	Greiner bio-one	658-175
Collagen from calf skin	Sigma-Aldrich	C9791-100MG
Collagen from calf skin	Sigma-Aldrich	C8919-20ML
Collagenase/Dispase	Roche	10 269 638 001
cOmplete Tablets EDTA-free, EASYpack	Roche	04 693 132 001
Cytochrome C from bovine heart	Sigma-Aldrich	C2037
Cytosine β-D-arabinofuranoside	Sigma-Aldrich	C1768-100MG
D-Mannitol	Sigma-Aldrich	M9546-250G
DMEM (1x) + GlutaMAX™-1 +4.5g/L D-Glucose, -Pyruvate	Gibco	61965-026
DMEM (1x) +4.5g/L D-Glucose, +L-Glutamine, +Pyruvate	Gibco	41966-029
DPBS (1x) -CaCl2, -MgCl2	Gibco	14190-094
Dried Skimmed Milk	Marvel	
EDTA	Thermo Scientific	17892
EGTA	Sigma-Aldrich	E4378-25G
Ethanol, absolute	Fisher Scientific	E/0650DF/17
Foetal Bovine Serum	Gibco	10500064
Glycerol	VWR	444482V
Hardener Component TAAB Embeddding Resin Premix	TAAB	T035
HBSS -Calcium Chloride, -Magesium Chloride, -Magnesium Sulfate	Gibco	14175-095
HEPES Buffer Solution (1M)	Gibco	15630-056
High Capacity cDNA Reverse Transcription Kit	Applied Bioystems	4368814
Horse Serum	Gibco	16050-122

HotShot Mastermix		HS002
Illustra™ DNA Esxtraction Kit BACC2	GE Healthcare	RPN-8502
Isoproterenol hydrochloride	Sigma-Aldrich	I-6501
jetPRIME reagent	Polyplus	114-07
Kanamycin Sulfate from Streptomyces kanamyceticus	Sigma-Aldrich	K4000-1G
L-(-)-Malic acid	Sigma-Aldrich	M6413-25G
LCGreen® Plus+	BioFire	BCHM-ASY-0005
Leibovitz's L-15 Medium (1x) +L-Glutamine +L-Amino Acids	Gibco	11415-049
L-Glutamic acid	Sigma-Aldrich	G8415-100G
L-Glutamine	Sigma-Aldrich	G8540-25G
Lipopolysaccharides from Escherichia coli O55:B5	Sigma-Aldrich	L2880-10MG
Live/Dead Cytoxicity/Viability Kit	Invitrogen	L3224
Medium 199 (1x) +Earle's Salts +L-Glutamine +2.2g/L Sodium Bicarbonate	Gibco	11150-059
MEM Non-Essential Amino Acids Solution (100x)	Gibco	11140-050
Methanol	Fisher Scientific	M/4000/PC17
MicroAmp® Fast Optical 96-Well Reaction Plate w/ Barcode 0.1mL	Applied Bioystems	4346906
MicroAmp™ Optical Adhesive Film	Applied Bioystems	4311971
Mlu1	Promega	R6381
NADH, disodium salt	Roche	10 107 735 001
NativePAGE™ 20x Cathode Buffer Additive	Invitrogen	BN2002
NativePAGE™ 20X Running Buffer	Invitrogen	BN2001

NativePAGE™ 3-12% Bis-Tris Gel 1.0mmx10well	Invitrogen	BN1001BOX
NativePAGE™ 3-12% Bis-Tris Gel 1.0mmx15well	Invitrogen	BN1003BOX
NativePAGE™ Sample Prep Kit	Invitrogen	BN2008
Nitro Blue Tetrazolium	Sigma-Aldrich	N5514-10TAB
Nonidet® P 40 Substitute	Fluka	74385
NuPAGE™ 4-12% Bis-Tris Gel 1.0mmx10well	Invitrogen	NP0321BOX
NuPAGE™ 4-12% Bis-Tris Gel 1.0mmx12well	Invitrogen	NP0322BOX
NuPAGE™ 4-12% Bis-Tris Gel 1.0mmx15well	Invitrogen	NP0323BOX
NuPAGE™ 4-12% Bis-Tris Gel 1.0mmx2Dwell	Invitrogen	NP0326BOX
NuPAGE™ Antioxidant	Invitrogen	NP0005
NuPAGE™ LDS Sample Buffer	Invitrogen	NP0007
NuPAGE™ MOPS SDS Running Buffer (20x)	Invitrogen	NP0001
NuPAGE™ Sample Reducing Agent (10x)	Invitrogen	NP0004
NuPAGE™ Transfer Buffer (20x)	Invitrogen	NP0006
Oligomycin	Sigma-Aldrich	75351
Penicillin-Streptomycin (10,000U/mL)	Gibco	15140-122
Penicillin-Streptomycin (5,000U/mL)	Gibco	15070-063
Phenylephrine	Sigma-Aldrich	P-6126
PhosSTOP EASYpack	Roche	04 906 837 001
Pierce® ECL Western Blotting Substrate	Thermo Scientific	32106
Plasmid Midi Kit (25)	QIAGEN	12143
Potassium hydroxide	Fisher Scientific	P/5640/53
Potassium phosphate monobasic	Sigma-Aldrich	P5655-100G
Precellys Lysing Kit Tissue Grinding CKmix50_7mL	Bertin Technologies	KT03961-1-306.7
Precision Plus Protein™ Dual Color Standard	Bio Rad	1610374
Propan-2-ol	Fisher Scientific	P/7490/21

Protein G Sepharose® Fast Flow	Sigma-Aldrich	P3296-5ML
Proteinase A/G Sepharose®	Abcam	ab193262
Proteinase K Solution	QIAGEN	19133
Pyromark Annealing Buffer	QIAGEN	979009
Pyromark Binding Buffer	QIAGEN	979006
Pyromark Denaturation Solution	QIAGEN	979007
Pyromark Gold Q96	QIAGEN	972807
Pyromark Q96 HS plates	QIAGEN	979001
Pyromark Q96 Vaccuum Prep Troughs	QIAGEN	979011
Pyromark Wash Buffer	QIAGEN	979008
Q5® Site-Directed Mutagenesis Kit	New England Biolabs	E0554S
QIAquick Gel Extraction Kit (50)	QIAGEN	28704
QIAquick PCR Purification Kit (50)	QIAGEN	28104
QIAzol Lysis Reagent	QIAGEN	79306
Quick Start™ Bradford 1x Dye Reagent	Bio Rad	500-0205
Resin Component TAAB Embedding Resin Premix	TAAB	T033
Rneasy® Micro Kit (50)	QIAGEN	74004
RNeasy® Midi Kit (50)	QIAGEN	75144
RNeasy® Plus Mini Kit (50)	QIAGEN	74134
Rotenone	Sigma-Aldrich	R8875-1G
RPMI Medium 1640 (1x) +L-Glutamine	Gibco	21875-034
RT2 SYBR®Green ROX™FAST Mastermix	Qiaqen	7570665
Seahorse XF Assay Medium Modified DMEM (0mM glucose)	Agilent	102365-100
Seahorse XF-24 FluxPak	Agilent	100850-001
Sgf1	Promega	R7103
SOC Outgrowth Medium	New England Biolabs	#B9020S
Sodium acetate	Sigma-Aldrich	S2889-250G
Sodium carbonate decahydrate, 99+%	Acros Organics	213500010
Sodium deoxycholate	Sigma-Aldrich	D6750-100G

Sodium phosphate	Sigma-Aldrich	342483-25G
Streptavidin Sepharose™ High Performance	GE Healthcare	17-5113-01
Sucrose	Fisher Scientific	S/8600/60
Syringe filter 0.2µm	Fisherbrand	09-719c
T4 DNA Ligase	New England Biolabs	M0202S
TBS (10x)	Cell Signaling Technology	12498S
Triton X-100	Sigma-Aldrich	X100-100ML
Trizma® base	Sigma-Aldrich	T6066-500G
Trizma® hydrochloride	Sigma-Aldrich	T5941-500G
Trypsin (0.25%) phenol red	Gibco	25050-014
Trypsin-EDTA (0.05%) phenol red	Gibco	25300-054
Trypsin-EDTA (0.25%) phenol red	Gibco	25200-056
Tween® 20	National Diagnostics	EC-607
Ultrapure Agarose	Invitrogen	16500-500
Western Blotting Filter Paper, 7cmx8.4cmx0.83mm	Thermo Scientific	84783
XL-10 Gold ultracompetent E.coli cells	Agilent	200314

2.2. Primers

2.2.1. Sequencing Primers for Mutation Validation

Primer	Sequence (5' to 3')
Pdgfd Forward	CCTTATTGCTGGTGGCCAGA
Pdgfd Reverse	AAGGCTGGTGCTGTCAAAGT
Trpc6 Forward	ACTATGAAAATTTTCC
Trpc6 Reverse	GCACCTCCGTCACTACCAAT
Ecsit Forward	AAAGGGACGATCACGGTCAC
Ecsit Reverse	TGGATCTGCCCAAAACAGGG

2.2.2. Pyrosequencing Primers

Primer	Sequence (5' to 3')
9-7.16 (*Dync2h1*) Forward	AAAATGCCTTCACAGACAAGT
9-7.16 (*Dync2h1*) Reverse Biotinylated	GAGGTACCAGCATGATTCTCT
9-7.16 (*Dync2h1*) Sequencing Forward	TGAAAACCCACTTCCA
9-14.36 (*Endod1*) Forward	AGGGATCCACAGAGGACA
9-14.36 (*Endod1*) Reverse Biotinylated	CGTGTGGTCAGAACACAAA
9-14.36 (*Endod1*) Sequencing Forward	GAGGACACTGAGCAGG
9-16.63 Forward Biotinylated	AGGCCCCAGAGAGTTTAGAGG
9-16.63 Reverse	CACTCCATATTCCGTTCTCTAGC
9-16.63 Sequencing Reverse	TCCACTCTCCAATTGC
9-20.65 (*Pin1*) Forward	TGGTCGTGCAAACCTGTAATCT
9-20.65 (*Pin1*) Reverse Biotinylated	AATTCAGGCCCTTAAGTTTAGTGG
9-20.65 (*Pin1*) Sequencing Forward	AGTGGGCAAAGGTACT
9-22.07 (*Ecsit*) Forward Biotinylated	CACTGGGTAGGGGTTGAT
9-22.07 (*Ecsit*) Reverse	AAGTTACCCCATGCTCAAG
9-22.07 (*Ecsit*) Sequencing Reverse	TCACCCGATTCAAGA
9-23.24 (*Bmper*) Forward Biotinylated	CTCAGGGTTTTAGAAATGTGG
9-23.24 (*Bmper*) Reverse	CGGCCTGTCTCTAGTCAAA
9-23.24 (*Bmper*) Sequencing Reverse	CAGAAGATGCTGACCTC

9-27.22 Forward Biotinylated	CACTTCCTTCGCTCAGAATGC
9-27.22 Reverse	AGCAAGGACCACACCTTCAACAT
9-27.22 Sequencing Reverse	CTTTGGAAGACATCCC
9-32.13 (*Arhgap32*) Forward Biotinylated	GGGGTGCAGTTTACTTGG
9-32.13 (*Arhgap32*) Reverse	GTGGGAGTCTCCATACCTG
9-32.13 (*Arhgap32*) Sequencing Reverse	ATGCTGGGCAAGTATG
9-44.10 (*Rnf26*) Forward Biotinylated	TTCTGTGGTTGCCTCTTG
9-44.10 (*Rnf26*) Reverse	TTTCCACACGCGTCATAG
9-44.10 (*Rnf26*) Sequencing Reverse	CGTCATAGGCACTTCTG

2.2.3. Lightscanner Primers

Primer	**Sequence (5' to 3')**
Ecsit Forward	TGCTCAAGTTCCTGCGGAT
Ecsit Reverse	CTAGCTTGGCCAGGTCCAAA
Ecsit Lunaprobe	GTTCACCCGATTCAAGATTATCAACCC

2.2.4. Cloning Primers

Primer	**Sequence (5' to 3')**
Ecsit Forward Sgf1	AGGCGATCGCCATGAGCTGGGTGCAGGTCAACTT
Ecsit Reverse Mlu1	GCGACGCGTACTTTGCCCCTGCTGCTGCTCTG
Ndufaf1 Forward Sgf1	GAGGCGATCGCCATGTCTTCCATTCACAAATTACT
Ndufaf1 Reverse Mlu1	GCGACGCGTTCTGAAGAGTCTTGGGTTAAGAA

2.2.5. Site Directed Mutagenesis Primers

Primer	**Sequence (5' to 3')**
Ecsit N209I Forward	CGATTCAAGATTATCAACCCCTAC
Ecsit N209I Reverse	GGTGAACCACAGCTTCATC

2.2.6. Cloning Sequencing Primers

Primer	Sequence (5' to 3')
VP1.5 Forward	GGACTTTCCAAAATGTCG
XL39 Reverse	ATTAGGACAAGGCTGGTGGG

2.3. Vectors and cDNA clones

Vector	Supplier	Code
pCMV6-Entry	Origene	PS100001
pCMV6-AC-His	Origene	PS100002
pCMV6-Entry-ACAD9	Origene	MR209542
pCMV6-Entry-SMAD4	Origene	MR208755
pCMV6-Entry-TRAF6	Origene	MR208489
MGC Mouse *Ecsit* cDNA	Dharmacon	MMM1013-202766953
MGC Mouse *Ndufaf1* cDNA	Dharmacon	MMM1013-202762755

2.4. Primary Antibodies

Antibody (Protein)	Species /clonality	Supplier	Code	Dilution	Size (kDa)
6X His	Rabbit poly	Origene	TA150031	1:1000	N/A
ACAD9	Rabbit poly	Abcam	ab99952	1:500	69
AMPK	Mouse mono	CST	2793	1:1000	62
ATP5A	Mouse mono	Abcam	ab14748	1:1000	53
CD5 – BV421	Rat mono	BD	562739	1:800 (FACS)	N/A
CD11b – PE – CF594	Rat mono	BD	562317	1:200 (FACS)	N/A

CLPP	Rabbit poly	Abcam	ab124822	1:5000	26
COXIV	Mouse mono	Abcam	ab14744	1:1000	17
DRP1	Rabbit mono	Abcam	ab184247	1:1000	82
ECSIT	Rabbit poly	Abcam	ab21288	1:1000	50/45
ECSIT	Rabbit poly	Abcam	ab66380	1:800	50/45
ECSIT	Rabbit poly	Atlas	HPA042979	1:100	50/45
EIF2α	Rabbit mono	CST	5324	1:1000	36
F4/80 - PE	Rat mono	Thermo Fisher	12-4801-80	1:200 (FACS)	N/A
GRP75	Mouse mono	Abcam	ab2799	1:1000	74
HSP60	Rabbit poly	Abcam	ab46798	1:20000	60
JNK	Rabbit poly	CST	9252S	1:1000	54/46
LONP1	Rabbit poly	Abcam	ab103809	1:1000	106
LY6C – FITC	Rat mono	Abcam	ab15686	1:200 (FACS)	N/A
LY6G – BV421	Rat mono	BD	562737	1:200 (FACS)	N/A
MFN2	Mouse mono	Abcam	ab56889	1:1000	86
MHCI	Mouse mono	DSHB	A4.840	1:1 (ICC)	N/A

MHCIIA	Mouse mono	DSHB	A4.74	1:1 (ICC)	N/A
MHCIIB	Mouse mono	DSHB	BF.F3	1:1 (ICC)	N/A
MHCIIX	Mouse mono	DSHB	6H1	1:1 (ICC)	N/A
MTCO1	Mouse mono	Abcam	ab14705	1:2000	40
MT-ND1	Rabbit mono	Abcam	ab181848	1:1000	36
Myc	Mouse mono	Origene	TA150121	1:1000	N/A
NDUFA10	Rabbit poly	Abcam	ab103026	1:500	41
NDUFA3	Mouse mono	Santa Cruz	sc-365351-S	1:1000	9
NDUFA8	Mouse mono	Santa Cruz	sc-398097-S	1:1000	20
NDUFAF1	Rabbit mono	Nijtmans Lab	N/A	1:250	43/38
NDUFB1	Rabbit poly	Abcam	ab201302	1:1000	12
NDUFB11	Rabbit mono	Abcam	ab183716	1:10000	17
NDUFB3	Mouse mono	Santa Cruz	sc-393351-S	1:1000	12
NDUFB8	Mouse mono	Abcam	ab110242	1:2000	22
NDUFC2	Rabbit mono	Abcam	ab192265	1:1000	14
NDUFS2	Rabbit mono	Abcam	ab192022	1:1000	49

NDUFS3	Mouse mono	Santa Cruz	sc-374282-S	1:1000	30
NDUFS8	Mouse mono	Santa Cruz	sc-515527-S	1:1000	23
NDUFV2	Rabbit mono	Abcam	ab183715	1:1000	24
NFκB	Mouse mono	CST	6956T	1:1000	65
OPA1	Rabbit poly	Abcam	ab42364	1:1000	92/86
P38 MAPK	Rabbit poly	CST	9212S	1:1000	43
PARP	Rabbit mono	Abcam	ab32138	1:1000	113
PGC1α	Rabbit poly	Abcam	ab54481	1:1000	105
Phospho AMPK	Rabbit mono	CST	2535	1:1000	62
Phospho DRP1 (Ser616)	Rabbit poly	CST	3455S	1:1000	82
Phospho DRP1 (Ser637)	Rabbit poly	CST	4867S	1:1000	82
Phospho EIF2S1	Rabbit mono	Abcam	ab32157	1:500	36
Phospho JNK (T183/Y185)	Rabbit poly	CST	9251S	1:1000	46/54
Phospho NFκB	Rabbit mono	CST	3033T	1:1000	65
Phospho P38 MAPK (T180/Y182)	Mouse mono	CST	9216S	1:2000	43
PINK1	Rabbit poly	Abcam	ab23707	1:1000	66

SDHA	Mouse mono	Abcam	ab14715	1:10000	70
TOM20	Rabbit poly	Abcam	ab199641	1:1000	16
UQCRC2	Mouse mono	Abcam	ab14745	1:1000	49
VDAC	Rabbit poly	Abcam	ab15895	1:1000	31
α-TUBULIN	Rabbit mono	Abcam	ab176560	1:2000	50

FACS – Fluorescence associated cell sorting, ICC – Immunocytochemistry

2.5. Secondary Antibodies

Antibody	Supplier	Code	Dilution
IRDye® 680LT Goat anti-Mouse IgG (H + L)	Li-Cor	926-68020	1:15000
IRDye® 680LT Goat anti-Rabbit IgG (H + L)	Li-Cor	926-68021	1:15000
IRDye® 800CW Goat anti-Rabbit IgG (H + L	Li-Cor	926-32211	1:15000
IRDye® 800CW Goat anti-Mouse IgG (H + L)	Li-Cor	926-32210	1:15000
Alexa fluor 633 Goat anti-Mouse	Life Technologies	A20146	1:200 (ICC)
Alexa fluor 488 Goat anti-Mouse	Life Technologies	A11029	1:200 (ICC)
Anti Mouse HRP	Promega	W402B	1:1000
Anti Rabbit HRP	Promega	W401B	1:1000

ICC – immunocytochemistry

2.6. Animals

All animals were housed at the Mary Lyon Centre (Harwell, Oxfordshire) according to the Animals (Scientific Procedures) Act 1986 (ASPA) (amended in 2012) and according to MRC guidance issued in 'Responsibility in the Use of Animals in Bioscience Research'. Animals were maintained under the home office project licence 30/3070 (MRC Harwell) – 'New mouse models of human disease' and according to the procedures laid out within. Animal husbandry work was carried out by staff in ward 3 of the Mary Lyon centre.

Animals were caged in individually ventilated cages with no more than 5 animals to a cage, except in cages with nursing mothers. Checks were performed daily and food (RM3 (E) – Dietex - Special Diet Services (irradiated to 3 rads)) and water (Mains water purified by reverse osmosis and chlorinated to 9-13 ppm) supplied *ad libitum*. Standard 12:12 (0700:1900) light dark cycle with 30 minute dawn and dusk periods was maintained throughout. Temperature was maintained between 19 and 22^{o}C with 45-65% humidity. Health screening was performed regularly on sentinel animals to ensure a pathogen free environment.

2.6.1. Original Pedigree

The original muta-ped-c3pde-178 (MPC-178) pedigree from which all further animals were derived was produced from the intercrossing of C57BL/6J mutagenised males to C3H.Pde6b+ females to produce a G_1 cohort (Figure 2.1), heterozygous for any ENU induced mutations. C57BL/6J (G_0) animals were mutagenised using the chemical mutagen N-ethyl-N-nitrosourea (ENU) which induces point mutations throughout the mouse genome. Mice were dosed with 1x120mgkg^{-1} and 2x100mgkg^{-1} with 7 days between each dose. G_1 males were subsequently crossed to C3H.Pde6b+ females to obtain a G_2 cohort. G_2 females were finally crossed to the G_1 male parent to obtain the experimental G_3 cohort carrying both heterozygous and homozygous ENU induced mutations and allowing for screening of dominant and recessive traits [270].

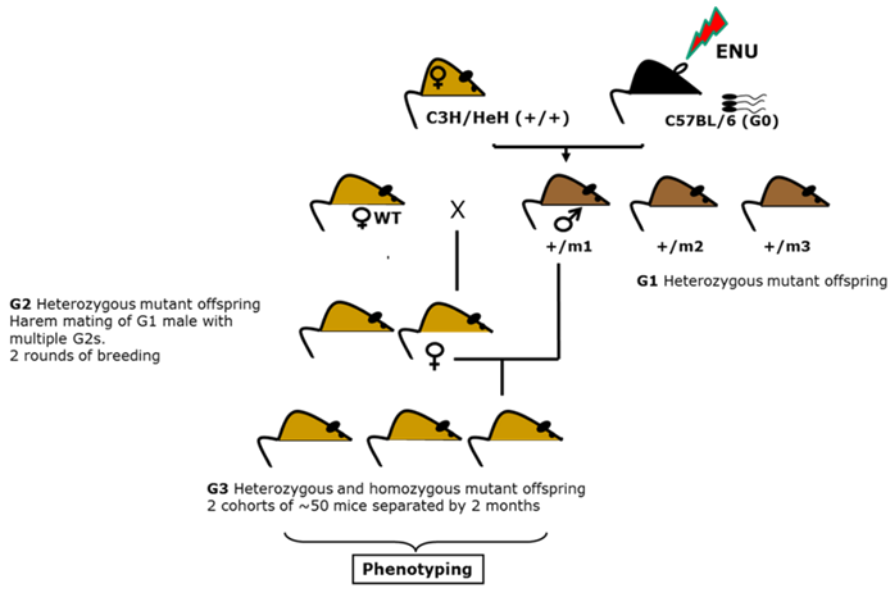

Figure 2.1. ENU mutagenesis and breeding plan for the production of the G_3 experimental cohort. Male C57BL/6J mice are mutagenized and crossed to female C3H.Pde6b+ to produce a G_1 cohort. Through successive rounds of breeding a G_3 experimental cohort is produced that allows for the screening of recessive mutations. Adapted from Goldsworthy and Potter (2014) [274].

The G_3 pedigree was produced as 2 cohorts of approximately 50 animals 3 months apart. With the first (A) cohort undergoing primary screening and the second (B) cohort used to confirm the presence of phenotypes observed in the first.

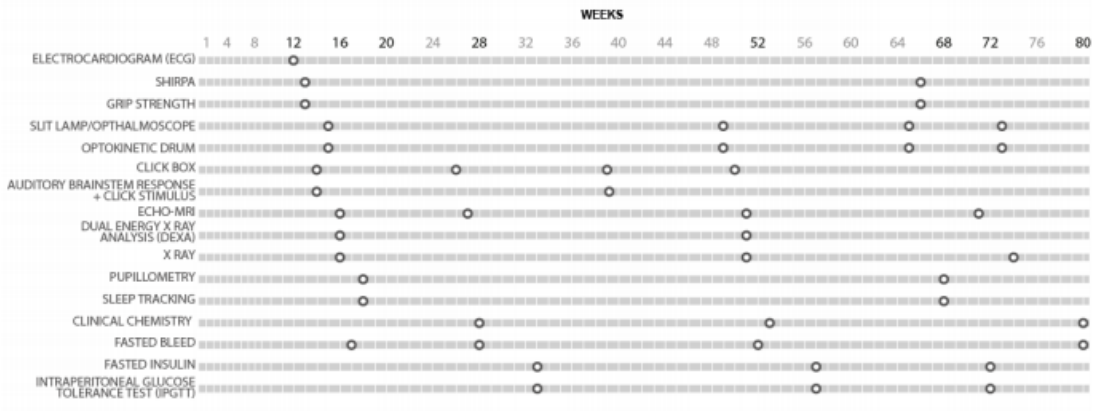

Figure 2.2. Graphical representation of the phenotyping tests undertaken during the Harwell Ageing Screen. Circles represent phenotyping tests carried out at each time point. In addition to these tests mice are weighed every 3 months up until 12 months of age and monthly thereafter. Adapted from Potter *et al.* [270]

Animals were aged for 18 months and screened throughout their lifetimes (Figure 2.2) using a variety of techniques including, clinical chemistry, auditory brain stem response (ABR), optokinetic drum (OKD), ophthalmoscope, X-ray, Dual energy x-ray

absorptiometry (DEXA), grip strength, SHIRPA (Smithkline Beecham, Harwell, Imperial College, Royal London Hospital, phenotype assessment), and Echo-MRI.

The G_3 mating program typically results in one in eight mice from the G_3 cohort which are homozygous for any given ENU induced mutation.

2.6.2. Incipient Congenic Pedigree

Following identification of the cardiac phenotype in the MPC-178 pedigree the line was re-derived from frozen sperm and subsequently backcrossed to C3H.Pde6b+ for 5 generations before intercrossing to obtain the incipient congenic pedigree used for the majority of phenotyping and sample collection. All animals and samples used are from this backcross unless otherwise stated.

2.6.3. Compound Heterozygote

Heterozygous *Ecsit* knockout (*Ecsit*$^{+/-}$) animals on a C57BL/6J background were obtained from the laboratory of Professor Sankar Ghosh at Columbia University (New York, USA) and imported into the Mary Lyon Centre through standardised quarantine procedure. Briefly, sperm is collected from *Ecsit*$^{+/-}$ males and used to fertilise eggs from superovulated donor females. Embryos are imported into the Mary Lyon Centre, implanted into pathogen free female mice and carried to term.

Following import and confirmation of allele transfer, heterozygous *Ecsit* knockout (*Ecsit*$^{+/-}$) males were crossed to incipient congenic heterozygous females (*Ecsit*$^{N209I/+}$) to produce offspring of 4 possible genotypes (*Ecsit*$^{+/+}$, *Ecsit*$^{+/-}$, *Ecsit*$^{N209I/+}$, *Ecsit*$^{N209I/-}$) for further phenotyping and sample collection.

2.7. Phenotyping

2.7.1. Clinical Chemistry

Male and female mice from both backcross one and the incipient congenic pedigree were terminally anaesthetised using Euthatal (pentobarbital) and blood samples collected using a lithium heparin coated capillary tube inserted into the retro-orbital sinus. Blood samples were collected in lithium heparin microvette tubes on ice.

Following collection, plasma is separated by centrifugation at 5000xg at 4^{o}C for 10 minutes and is collected in a separate uncoated micro centrifuge tube. Plasma concentrations of relevant compounds were assessed by the clinical chemistry core at MRC Harwell using an Olympus U400 bio analyser.

2.7.2. Echocardiogram

Echocardiography was performed by the phenotyping core of the Mary Lyon centre at MRC Harwell. Twelve week old male and female mice were anaesthetised with 4% isoflurane (maintained at 1.5%) in oxygen and echo-cardiogram performed using a Vevo 770 high-resolution *in vivo* micro imaging system with a Visualsonics RMV707B Probe (30 MHz). Body temperature was monitored using a rectal thermometer and maintained using a heat lamp at 36-38^{o}C. ECG monitoring was performed using limb electrodes, to which the animals paws were attached using surgical tape and the heart rate maintained at or above 400bpm. Short axis B and M mode images were taken using the papillary muscles as a point of reference for positioning of the probe. Image contrast and gain functions were used for clarity and frame rate of 110Hz used throughout. Measurements were taken from M-mode images using the inbuilt Vevo software.

2.7.3. ECG

ECG was performed on 12 week old male and female animals using an anaesthetised ECG technique. Animals were anaesthetised using 4% isoflurane (maintained at 1.5%) and placed on a corkboard. 25G needles were passed through the skin in both armpits and on either flank into the cork board. ECG cables were attached to the needles and 2 lead ECG readings recorded at 2kHz taken for 90 seconds using a Dual Bio Amp (ML135) (AD Instruments, Oxford, UK) connected to a Powerlab 4/30 (ML866) (AD Instruments, Oxford, UK). A spirometer pod (ML311) (AD Instruments, Oxford, UK) connected to a

spirometry pad placed under the animals chest was used to monitor breathing rate. Anaesthetic regime was monitored in order to maintain steady heart rate (350-450 bpm) and breathing rate (90-120 bpm). Analysis was performed on lead 1 using LabChart pro V.8.1.5 (AD Instruments, Oxford, UK) with ECG analysis plugin with setting for rodent T wave, block averaging, and default detection and analysis parameters. Where software was unable to determine position of ECG parameters these were manually called according to the guidelines set out in Boukens *et al.* (2014) [275].

2.7.4. Intra Peritoneal Glucose Tolerance Test

Intra peritoneal glucose tolerance test (IPGTT) was performed by Mr Laurence Goosey at MRC Harwell. IPGTT was performed on 12 week old male and female wild type and incipient congenic *Ecsit*$^{N209I/N209I}$ animals. Mice were fasted overnight prior to IPGTT assessment. The tail is anaesthetised with EMLA (Lidocaine/Prilocaine) to induce local anaesthesia prior to a 40µL sample of blood being collected in a lithium heparin microvette tube. Plasma is collected from this sample for later analysis. 2g of glucose per kg is then injected by intraperitoneal (IP) injection and animals returned to the home cage. Blood glucose levels are then measured using an Alphatrak (Abbott, UK) at 30, 60 and 120 minutes post glucose injection.

2.7.5. Echo-MRI

Echo-MRI was performed on male and female wild type and incipient congenic homozygous animals (*Ecsit*$^{N209I/N209I}$) at 8, 10, 14 and 18 weeks of age to show the accumulation of fat and lean mass over time. Animals were weighed to determine true body weight before measurements were made on mice using an ECHO MRI-100 (Houston, TX, USA) body composition analyser. Briefly, un-anaesthetised animals were placed into an acrylic tube and restrained using a second acrylic rod. The restrained animal was then placed inside the ECHO MRI-100 and measurements taken using the magnet, taking approximately 60 seconds. Animals were returned to their home cage immediately following measurements. Measurements were also obtained for total water content.

2.7.6. Grip Strength

Grip strength was performed on male and female wild type and incipient congenic homozygous animals (*Ecsit*$^{N209I/N209I}$) at 14 weeks of age. Animal body weights are

collected immediately before hand to provide a crude means of normalisation. Grip strengths are then measured using a grip strength meter with a grid attachment. To obtain a measurement mice are placed on the staging area of the strength meter and gently pulled across the grid by their tail. The machine measure the maximum force before the animal releases from the grid. To measure the strength of the forepaws, the animal's tail is lifted slightly so that the hind limbs are unable to grip the grid. 3 measurements are taken ensuring good contact with the grid and no erroneous readings are taken, the mean of the 3 measurements is taken.

2.8. Mapping and Whole-Genome Sequencing

DNA from affected mice and littermate controls was extracted using Illustra Nucleon BACC2 kit (GE Healthcare) according to manufacturer's protocol and sent to GenProbe Life Sciences Ltd. To be run on the Illumina Golden Gate Mouse MD Linkage Panel, consisting of 1,449 loci and including approximately 4 SNPs (single nucleotide polymorphisms) per 27 Mb interval across the mouse genome (https://products.illumina.com). Because the ENU treatment is carried out on the C57BL/6J father, the region(s) carrying the causative mutation should be either homozygous (recessive line) or heterozygous (dominant lines) for C57BL/6J SNPs in affected individuals, whilst control animals should carry C3H.C3pde SNPs in the same region.

After identifying the candidate region that could contain the causative mutation, the DNA from the G_1 founder of the pedigree was sent for whole genome sequencing (WGS) employing the Illumina HiSeq platform (Oxford Genomics Centre, Wellcome Trust Centre for Human Genetics). The sequence was then analysed by the bioinformatics group based at MRC-Harwell, highlighting the possible coding and non-coding mutations and the confidence in each mutation based on read depth of the WGS.

2.9. Mutation Validation

To confirm the mutations in *Pdgfd*, *Trpc6* and *Ecsit*, DNA was extracted from the tail of an affected G_3 animal and C57BL/6J control animal using the GE Illustra BACC2 kit according to manufacturer's instructions. The relevant locus was then amplified using appropriate primers (section 2.2.1).

Q5 high fidelity DNA polymerase (New England Biolabs) was used as a polymerase. The 50µL reaction contained; 10µL 5X Q5 reaction buffer, 1µL 10mM dNTPs, 2.5µL 10pmol/µL forward primer, 2.5µL 10pmol/µL reverse primer, 5µL 10ng/µL DNA template, 28.5µL ddH_2O, 0.5µL (1 unit) Q5 high-fidelity DNA polymerase. PCR cycling conditions were set with an initial denaturation step of 98°C for 30 seconds followed by 30 cycles of 98°C for 10 seconds, 58°C for 10 seconds and 72°C for 30 seconds. A final elongation step at 72°C for 2 minutes was included before samples were stored at 4°C awaiting PCR purification.

2.9.1. PCR Purification

All samples were purified using a QIAquick PCR purification kit (Qiagen) according to manufacturer's instructions. Briefly, DNA is bound to a silica membrane in a centrifugation column in the presence of a high salt buffer by centrifuging at 17,900xg for 60 seconds. Following binding, buffer is discarded and bound DNA is washed once using the supplied buffer. Finally, DNA is eluted in low salt buffer by centrifuging at 17,900xg for 1 minute.

Following purification samples were sent for Sanger sequencing by Source Bioscience (Oxford) and results analysed using Seqman pro (DNASTAR, USA).

2.9.2. Sanger Sequencing

All sequencing was performed by Source Bioscience (Oxford) (www.sourcebioscience.com). Plasmids (100ng/µl) and PCR products (10ng/µl) from genomic DNA using appropriate sequencing primers supplied (3.2ng/µl) (sections 2.2.1 and 2.2.6).

2.10. Genotyping

Genotyping was performed using one of two methods. Initially animals were genotyped using a panel of SNVs (single nucleotide variants) across the mapped region with pyrosequencing, allowing for both the validation of mutations and the narrowing of the causative region. After genotype to phenotype relationship was more certain, genotyping was performed using a Lightscanner high resolution melting assay.

2.10.1. Pyrosequencing

Initial genotyping was performed on a panel of 9 SNVs across the region of interest identified as part of the next generation sequencing performed on the G_1 animal. DNA was obtained from ear biopsies taken from G_3 animals using KAPA express extract kit (KAPA Biosystems) according to manufacturer's instructions. PCR of the regions of interest was performed using Taq PCR master mix (Qiagen) and the primers listed in section 2.2.2.

Reaction mix is as follows for a 10µL reaction; 5µL Taq PCR master mix, 2.6µL ddH_2O, 0.2µL forward primer (table 5.2.2), 0.2µL reverse primer (table 5.2.2), and 2µL template DNA. PCR cycling conditions are then set with an initial denaturation step of 95^oC for 5 minutes followed by 45 cycles of 95^oC for 15 seconds, 54^oC for 30 seconds and 72^oC for 15 seconds with a final elongation step of 72^oC for 5 minutes.

Following PCR the samples are run on a PSQ HS96A pyro sequencer according to manufacturer's protocol using Pyromark reagents (Qiagen), Streptavidin Sepharose™ high performance beads (GE Healthcare) and the appropriate sequencing primer for each fragment as listed in section 2.2.2.

2.10.2. Lightscanner

Routine genotyping was performed by Lightscanner (Idaho technology, USA) high resolution DNA melting assay using LCGreen and a Lunaprobe developed by the MRC genotyping and mutation detection screens (GEMS) core facility. To distinguish between wild type, homozygous, and heterozygous animals for the single point mutation a 3' blocked oligonucleotide (LunaProbe) is designed that sits directly over the SNP and exhaustive asymmetric PCR is performed. This creates two products, one is the full PCR product between the normal primers (section 2.2.3), whilst the other results from the probe annealing to the complementary strand. PCR products are then gradually heated and the fluorescence of the bound LCGreen dye is measured. The difference in melting temperatures caused by altered affinity of the probe allows for determination of wild type, heterozygous and homozygous samples.

The reaction conditions for a 10µl reaction were 5µl of Hot Shot PCR master mix (Diamond, Clent Life Science, UK), 1µl LCGreen, 0.5µl reverse primer (20ng/µl), 0.1µl forward primer (20ng/µl), 0.5µl probe (20ng/µl), and 0.9µl ddH_2O.

Standard PCR cycling conditions were as follows: starting temperature at 95°C for 2 min, then 55 cycles of 95°C for 30 seconds, 60°C for 30 seconds and 72°C for 30 seconds. The hybridisation step was at 95°C for 30 seconds, 25°C for 30 seconds and 15°C for 30 seconds.

2.11. Histology

Hearts were collected from wild type and *Ecsit*$^{N209I/N209I}$ animals at 0, 1, 2, 4, 6, 8, and 12 weeks of age to investigate the development of the cardiomyopathy phenotype, no preference was made for male or female samples. Animals were culled by cervical dislocation, hearts excised and fixed in 10% neutral buffered formalin. Histology was prepared by the histology core team at MRC Harwell by embedding the fixed hearts in paraffin and sectioning at 4µm using a Finesse ME+ microtome (Thermo Fisher). Transverse sections (T/S) were stained with Haematoxylin and Eosin (H&E).

2.12. Muscle Fibre Typing

Muscle fibre typing was performed by Mr. Saleh Salman Omairi at the University of Reading [276]. Soleus and extensor digitorum longus (EDL) from male wild type and *Ecsit*$^{N209I/N209I}$ animals and frozen over isopropanol on liquid nitrogen. Following freezing, frozen muscle samples were mounted in Tissue Tech freezing medium (Jung) and cooled by dry ice/ethanol. Cryosections taken at 10µM thick were dried for 30 minutes at room temperature before being washed three times in PBS and incubated in permeabilisation buffer solution (4mM HEPES, 3mM $MgCl_2$, 10mM NaCl, 1.5mM Sodium azide, 60mM Sucrose, 0.1% Triton X-100) for 15 minutes. Following permeabilisation, samples were washed in wash buffer (1x PBS with 5% foetal calf serum (v/v) and 0.05% Triton X-100) for 30 minutes at room temperature.

Primary antibodies against MHCI, MHCIIA, MCHIIX and MHCIIB were diluted in wash buffer and incubated overnight at 4°C. The next day samples are incubated in secondary antibody diluted in wash buffer for 1 hour in darkness. Finally, slides were mounted in fluorescent mounting medium and myonuclei visualised with 2.5µg/ml DAPI.

Fluorescence microscopy was performed with Zeiss AxioImegar AI an images captured with Axiocam digital camera. Analysis was performed with Zeiss Axiovision computer software version 4.8.

2.13. Transmission Electron Microscopy

For transmission electron microscopy (TEM), 1mm^3 cubes of left ventricular tissue were fixed in 3% glutaraldehyde and 4% formaldehyde in 0.1 M PIPES and post-fixed with 1% osmium tetroxide in 0.1 PIPES. Samples were taken from the left ventricular free wall of 3 wild-type and 3 Ecsit$^{N209I/N209I}$ males at 16 weeks of age. After serial dehydration in increasing concentration of ethanol, the tissue was embedded in epoxy resin (TAAB) and polymerised overnight at 60˚C. Golden ultrathin sections (70-80 nm) were cut with a diamond knife and collected on copper/palladium grids. To improve contrast, blocks were stained with 2% uranyl acetate and grids were stained with lead citrate.

Images were collected at the Wolfson bioimaging facility at the University of Bristol using a Tecnai 12 Biotwin electron microscope with the assistance of Mrs Judith Mantell. Analysis was performed using FIJI software.

2.14. Mitochondrial DNA quantification

DNA was extracted from left ventricle heart tissue from wild type and *Ecsit$^{N209I/N209I}$* male and female animals (n=3 per group) using Illustra Nucleon BACC2 kit (GE Healthcare) according to manufacturer's protocol and DNA concentrations measured using a Nanodrop 8000 spectrophotometer (Thermo Fisher).

The relative copy numbers of mitochondrial and nuclear DNA were assessed using NovaQUANT™ Mouse Mitochondrial to Nuclear Ratio kit according to manufacturer's instructions. Briefly, purified DNA (1ng/well) is diluted and combined with 2x RT^2 Fast SYBR® Green Mastermix before being aliquoted into the plate of pre-aliquoted primers against 2 mitochondrial (12s, trLEV), and 2 nuclear (BECN1, NEB) genes. The plate is sealed with optically clear lids, briefly centrifuged and copy number assessed using a 7500 Fast real-time PCR system (Applied Biosystems) with a denaturing step at 95^{o}C for 10 minutes followed by 40 cycles of 95^{o}C for 3 seconds and 60^{o}C for 30 seconds.

Analysis was performed using the 'Relative copy number' method outlined in the manufacturers protocol. Ct values of the 2 gene pairs (trLEV/BECN1, 12s/NEB) are compared to obtain the ΔCt value for each pair. The average of the two $2^{\Delta Ct}$ values then gives the average copy umber of mitochondrial DNA per cell.

2.15. Seahorse

All Seahorse analysis was performed using a Seahorse XF24 extracellular flux analyser (Agilent) on cultured cells or isolated mitochondria as described below. In all cases seahorse cartridges were hydrated by loading calibration plate with 1ml of calibrant (Agilent) and incubating overnight at 37^{o}C in a non-CO_2 incubator, any evaporation was replaced the following morning to maintain 1ml of calibrant in all wells. The Seahorse XF24 was also pre-heated to 37^{o}C for at least 8 hours prior to use.

2.15.1. Seahorse on Mouse Embryonic Fibroblasts (MEFs)

MEFs were isolated and cultured as in section 2.24. MEFs were plated on Seahorse XF24 plates at a concentration of 40,000 cells/well in 250µL of MEF culture media and incubated overnight at 37^{o}C, 5% CO_2. The following day MEF culture medium was replaced with CAS medium (Seahorse DMEM, 25mM glucose, 2mM glutamine, 1mM sodium pyruvate, pH 7.2) and incubated at 37^{o}C in a non-CO_2 incubator for 90 minutes.

Seahorse is performed according to protocol laid out in table 2.1 with final concentrations of oligomycin (2.0µM), FCCP (carbonyl cyanide-4-(trifluoromethoxy)phenylhydrazone) (1.0µM), rotenone (2.0 µM) and antimycin A (2.0µM).

Step	Command	Time (Min.)	Compound /Repeats	Step	Command	Time (Min.)	Compound /Repeats
1	Calibrate			**31**	Mix	2	Repeat 3 times
2	Mix	2	Repeat 5 times	**32**	Wait	2	
3	Wait	2		**33**	Measure	4	
4	Measure	4		**40**	Inject		Anti A/Rot
17	Inject		Oligomycin	**41**	Mix	2	Repeat 3 times
18	Mix	2	Repeat 3 times	**42**	Wait	2	
19	Wait	2		**43**	Measure	4	
20	Measure	4		**50**	End		
30	Inject		FCCP				

Table 2.1. Seahorse protocol for measurement of O_2 consumption rate and addition of compounds during MEF assay.

Following Seahorse analysis, the cell plate is retained, washed gently with PBS and total live cell count assessed by live/dead viability/cytotoxicity kit for mammalian cells (Life Technologies). Cells are incubated in 200µl of PBS containing 2µM calcein AM per well. Cells are incubated at room temperature for 30 minutes whilst protecting from light and fluorescence measured (excitation/emission 485/530nm) on a Fluostar OPTIMA plate reader (BMG Labtech, Aylesbury, UK) to determine live cell concentration per well. Seahorse readings are normalised to relative intensity of fluorescent signal rather than true cell count.

2.15.2. Seahorse on Isolated Neonatal Cardiomyocytes

Neonatal mouse cardiomyocytes were isolated and cultured as in section 2.26. Cardiomyocytes were plated into pre-coated seahorse XF24 cell culture plates at a variable cell density (25,000, 50,000, 75,000 or 100,000 cells/well) and seahorse protocol performed according to procedure laid out in table 2.2 with final concentrations of oligomycin (2.0µM), FCCP (1.0µM), rotenone (2.0 µM) and antimycin A (2.0µM).

Step	Command	Time (Min.)	Compound /Repeats	Step	Command	Time (Min.)	Compound /Repeats
1	Calibrate			**31**	Mix	2	Repeat 3 times
2	Mix	2	Repeat 5 times	**32**	Wait	2	
3	Wait	2		**33**	Measure	4	
4	Measure	4		**40**	Inject		Anti A/Rot
17	Inject		Oligomycin	**41**	Mix	2	Repeat 3 times
18	Mix	2	Repeat 3 times	**42**	Wait	2	
19	Wait	2		**43**	Measure	4	
20	Measure	4		**50**	End		
30	Inject		FCCP				

Table 2.2. Seahorse protocol for measurement of O_2 consumption rate and addition of compounds during cardiomyocyte cell density and FCCP concentration titrations.

Following cell density titration the optimal density was selected and FCCP titration was performed by plating freshly isolated cardiomyocytes at this density followed by measurements with variable final FCCP titrations (0, 0.5, 1.0, 2.0, 4.0, and 6.0 µM).

2.15.3. Seahorse on Isolated Mitochondria

Mitochondria for seahorse analysis were isolated from freshly dissected hearts and brains obtained from 15 week old wild type and *Ecsit*$^{N209I/N209I}$ animals culled by cervical dislocation, no preference was made for sex. Samples were kept on ice and homogenised in MSHE+BSA (70mM sucrose, 210mM Mannitol, 5mM HEPES, 1mM EGTA, 0.2% w/v FFA free BSA, 1M KOH) in a Dounce homogeniser using both A and B pestles. Mitochondria are separated from lysate by subsequent centrifugation 800xg for 10 minutes at 4^{o}C twice, discarding the pellet after each step. The supernatant is retained and centrifuged at 8000xg for 10 minutes at 4^{o}C. The remaining mitochondrial pellet is suspended in MSHE+BSA and the concentration measured using a Bradford assay (Bio-rad).

Mitochondria are diluted 1:10 in ice cold mitochondrial assay solution (MAS) (70mM sucrose, 220mM mannitol, 10mM KH_2PO_4, 5mM $MgCl_2$, 2mM HEPES, 1mM EGTA, 0.2% w/v FFA free BSA, 1M KOH) before diluting further in MAS to the desired concentration and loaded onto Seahorse XF24 plates at a concentration of 5µg/well. The plate is centrifuged at 2000xg for 20 minutes at 4^{o}C to ensure mitochondria are adherent.

450µL of MAS containing 10mM pyruvate and 10mM malate is added to the mitochondria in the plate and the plate incubated at 37^{o}C for 10 minutes without CO_2. Measurements are made on the seahorse according to the procedure laid out in table 2.3. ADP, FCCP and Antimycin A are added to give a final concentration of 40µM, whilst oligomycin is added to a final concentration of 20µM.

Step	Command	Time (Min.)	Compound	Step	Command	Time (Min.)	Compound
1	Calibrate			**14**	Mix	1	
2	Mix	1		**15**	Inject		Oligomycin
3	Wait	3		**16**	Mix	0.5	
4	Mix	1		**17**	Measure	3	
5	Wait	3		**18**	Mix	1	
6	Mix	0.5		**19**	Inject		FCCP
7	Measure	3		**20**	Mix	0.5	
8	Mix	1		**21**	Measure	3	
9	Measure	3		**22**	Mix	1	
10	Mix	0.5		**23**	Inject		Antimycin
11	Inject		ADP	**24**	Mix	0.5	
12	Mix	1		**25**	Measure	3	
13	Measure	3		**26**	End		

Table 2.3. Seahorse protocol for measurement of O_2 consumption rate and addition of compounds during isolated mitochondria assay.

2.16. Western Blots

Tissues samples were obtained from terminal wild type and *Ecsit*$^{N209I/N209I}$ male and female animals (n=3 per group) and snap frozen at the time of dissection. Heart, liver, brain, kidney and skeletal muscle taken from the hind limb were stored at -80^{o}C until required. Proteins were extracted from tissue by homogenising in RIPA buffer (150mM NaCl, 1% NP-40, 0.5% DOC, 0.1% SDS, 50mM Tris, pH 7.5) containing phosphatase (Roche) and protease (Roche) inhibitors in precellys CK28 homogenisation tubes.

Proteins were isolated from macrophages by scraping the macrophages from the plate and centrifuging to obtain the cell pellet before lysing in RIPA buffer containing phosphatase and protease inhibitors.

Protein concentration was measured by Bradford assay (Bio-rad) and measured on a µQuant plate reader (Biotek instruments inc., VT, USA). 20µg of total protein was mixed with LDS sample buffer (Invitrogen) and reducing agent (Invitrogen) loaded onto

NuPAGE™ 4-12% Bis-Tris protein gels (Invitrogen). Electrophoresis was performed at 200V for 60 minutes at room temperature in 1x MOPS.

PVDF membrane (GE) is activated in absolute methanol for 1 minute and proteins transferred using X-Cell blot module (Invitrogen) containing 1x transfer buffer (Invitrogen), 20% methanol and 1x anti-oxidant (Invitrogen) according to manufacturer's instructions.

Following transfer, membranes are blocked in either 5% w/v milk powder in phosphate buffered saline (PBS) containing 0.1% tween or 5% BSA (bovine serum albumin) in TBS containing 0.1% tween (for phosphorylated proteins) for 60 minutes with shaking. Primary antibodies (Section 2.4) diluted in 5% milk/PBS-T or 5% BSA/TBS-T are incubated overnight at 4^{o}C before three, 5 minute washes in PBS-T or TBS-T. Secondary antibodies (Section 2.5) are diluted in 5% milk/PBS-T or 5% BSA/TBS-T and incubated for 1 hour. Fluorescent secondary antibodies are protected from light during this and subsequent steps. Membranes are subsequently washed a further 3 times before drying. Blots were scanned using a LI-COR Odyssey Cl-x or SA scanner (LI-COR Biosciences, Cambridge, UK). Image Studio Lite software (LI-COR Biosciences) is used for quantification and analysis (Median, 3 pixel border background).

2.17. Blue Native PAGE

Mitochondria were isolated from frozen heart and brain tissue taken from wild type and *Ecsit*$^{N209I/N209I}$ male and female animals (n=3 per group).

Hearts were lysed in 10mL/g of homogenisation medium A (0.32M sucrose, 1mM EDTA, 10mM tris-HCl, pH7.4, filter sterilised) in an Elvehjem-Potter homogeniser on ice by hand. Homogenate was centrifuged at 1000xg or 5 minutes at 4^{o}C and supernatant retained. Supernatant was centrifuged for 2 minutes at 9000xg at 4^{o}C before removing the supernatant and fluffy coat, leaving behind the mitochondrial pellet. The mitochondrial pellet was subsequently resuspended in 100µL of homogenisation medium A and centrifuged at 9000xg for 10 minutes at 4^{o}C, discarding the supernatant. This wash step is repeated 5 times and the mitochondrial pellet stored at -80^{o}C.

Brains were lysed in 5mL/g of homogenisation medium AT (0.075M sucrose, 0.225M mannitol, 1mM EGTA, 10mM tris-HCl, pH7.4, filter sterilised) in an Elvehjem-Potter

homogeniser on ice by hand. Homogenate was centrifuged at 1000xg for 5 minutes at 4^{o}C and supernatant retained. Supernatant is centrifuged at 12000xg for 10 minutes at 4^{o}C before removing the supernatant and fluffy coat, leaving behind the mitochondrial pellet. The mitochondrial pellet was subsequently resuspended in 100µL of homogenisation medium AT and centrifuged at 12000xg for 10 minutes at 4^{o}C, discarding the supernatant. This wash step was repeated 5 times and the mitochondrial pellet stored at -80^{o}C.

Mitochondria were resuspended in 100uL of appropriate homogenisation medium and the concentration determined by Bradford assay (Bio-rad).

250µg of mitochondria were resuspended in 50µL of native page sample buffer (12.5µL 4x native page sample buffer, 10µL digitonin, 1x protease inhibitors), incubated on ice for 1 hour, and centrifuged at 20000xg for 30 minutes at 4^{o}C. 6.7µL of Native PAGE G-250 sample additive is added before loading 30µg of mitochondria on to NativePAGE™ 3-12% bis-tris gels (Invitrogen). First dimensional electrophoresis was performed with an initial step of 150V for 30 minutes at 4^{o}C, 1x NativePAGE™ running buffer (Invitrogen) was used at the anode, whilst the cathode contained 1x NativePAGE™ running buffer (Invitrogen) with 1x NativePAGE™ cathode buffer additive (Invitrogen). After 30 minutes the cathode buffer was exchanged for 1x NativePAGE™ running buffer with 0.1x NativePAGE™ cathode buffer additive and run for at 250V for a further 90 minutes at 4^{o}C.

First dimensional blots were transferred to PVDF using X-cell blot module containing bicarbonate transfer buffer (1mM $NaHCO_3$, 0.3mM $NaCO_3.10H_2O$) at 60 volts for 1 hour at 4^{o}C. Membranes were blocked in 5% milk in PBS-T (0.1%tween) for 1 hour. Primary antibodies (Section 2.4) were diluted in 5% milk/PBS-T and incubated overnight before three, 5 minute washes in PBS-T. Secondary antibodies (Section 2.5) were diluted in 5% milk/PBS-T and incubated for 1 hour before proteins are visualised using Pierce™ ECL reagent (Thermo scientific) and Amersham hyperfilm ECL (GE Life Sciences) developed using an Mi-5 x-ray film processor (Medical Index, Germany).

For second dimension BN-PAGE, first dimensional gels are cut out and incubated in 1% SDS with 1% beta-mercaptoethanol for 1 hour before loading into a NuPAGE 4-12%

1.0mmx2D well gel. Gels are run at 200V for 50 minutes at room temperature in MOPS. Only male samples were used for second dimensional blots.

Proteins are transferred to PVDF membrane using X-Cell blot module (Invitrogen) containing 1x transfer buffer, 20% methanol and 1x anti-oxidant (Invitrogen) according to manufacturer's instructions. Following transfer, membranes are blocked in either 5% w/v milk powder in PBS containing 0.1% tween for 1 hour. Primary antibodies (Section 2.4) diluted in 5% milk/PBS-T are incubated overnight at 4^{o}C before three, 5 minute washes in PBS-T. Secondary antibodies (Section 2.5) are diluted in 5% milk/PBS-T and incubated for 1 hour, protecting from light. Membranes are subsequently washed a further 3 times before drying. Fluorescent blots are scanned using a LI-COR Odyssey Cl-x or SA scanner (LI-COR Biosciences, Cambridge, UK). Image Studio Lite software (LI-COR Biosciences) is used for analysis.

2.18. In-Gel Activity assay

As described in section 2.16. mitochondria were isolated from wild type and *Ecsit*$^{N209I/N209I}$ male and female hearts and brains and run on first dimensional NativePAGE™ 3-12% Bis-Tris gels. First dimensional electrophoresis was performed with an initial step of 150V for 30 minutes at 4^{o}C, 1x native PAGE running buffer was used at the anode, whilst the cathode contained 1x NativePAGE™ running buffer with 10x NativePAGE™ cathode buffer additive. After 30 minutes the cathode buffer was exchanged for 1x NativePAGE™ running buffer with 1x NativePAGE™ cathode buffer additive and run for at 250V for a further 90 minutes at 4^{o}C.

Following electrophoresis proteins were not transferred to PVDF membrane but the gels removed from the casings and stained as below.

2.18.1. Complex I

For complex I activity gels were stained for 1 hour in 10mls of buffer containing 150µM NADH, 3mM nitro blue tetrazolium and 2mM Tris-HCl (pH 7.4). The oxidation of NADH to NAD^+ results in the reduction of the nitro blue tetrazolium dye and the appearance of a deep blue staining. The depth of stain is proportional to the activity of complex I in the gel. Following 1 hour of incubation, the gels are scanned using a desktop PC scanner

and can be analysed by importing the images into Image Studio (Li-Cor Biosciences, Cambridge, UK).

2.18.2. Complex IV

For complex IV activity gels were stained for 1 hour in buffer containing 2.3mM DAB (3,3'-diaminobenzidine), 1g/l cytochrome C, 2mM sucrose and 50mM sodium phosphate buffer (pH 7.4). In this case, cytochrome C oxidised by complex IV reacts with DAB to give a dark brown stain on the gel corresponding to the activity of complex IV. Following 1 hour of incubation, the gel was scanned using a desktop PC scanner and was analysed by importing the images into Image Studio (Li-Cor Biosciences, Cambridge, UK).

2.19. ROS assay

Reactive oxygen species were measured indirectly by assessing the levels of 4-hydroxynonenal (4-HNE) in wild type and *Ecsit*$^{N209I/N209I}$ heart tissue. 4-HNE is the product of lipid peroxidation by reactive oxygen species and was measured using an HNE adduct competitive ELISA from Cell Biolabs Inc. according to manufacturer's instructions.

Briefly, whole hearts from 3 male and 3 female wild type and *Ecsit*$^{N209I/N209I}$ animals were homogenised in PBS and normalised to a protein concentration of 5mgml^{-1}. An ELISA plate is coated with HNE adduct before incubation with known and unknown samples before addition of anti-HNE polyclonal antibody is added. This is followed by washing and incubation with an HRP-conjugated secondary antibody. The plate is washed again and substrate added and incubated for up to 20 minutes before stop solution is added. Finally, absorbance is measured at 450nm on a Fluostar OPTIMA plate reader (BMG Labtech, Aylesbury, UK) and values of unknown samples are determined by comparison to a standard curve.

2.20. ADP:ATP quantification assay

ADP:ATP ratio was assessed using Enzylight™ ADP/ATP ratio kit (Bioassays systems). For this, 5µl of whole heart lysate from 3 male and 3 female wild type and *Ecsit*$^{N209I/N209I}$ animals was normalised to a concentration of 5mgml^{-1} by Bradford assay. The lysate is treated sequentially with two solutions to measure the concentration of ATP and ADP in the lysate. In the first reaction D-luciferin reacts with ATP in the presence of luciferin

to produce a light signal proportional to the concentration of ATP. In the second reaction, ADP is converted to ATP via an enzymatic reaction, allowing for the ATP concentration to be measured again via the same reaction as the first measurement.

The ADP:ATP ratio (R) is calculated by subtracting the background signal obtained following complete ATP reaction after the first reaction (B) from the ADP reaction signal (C) and divide the result by the signal obtained from the initial ATP reaction (A). $R = \frac{C-B}{A}$

2.21. Cloning and Transfection

Full length *Ecsit* and *Ndufaf1* cDNA clones (Dharmacon) in pCMV-SPORT vector were transformed into 100µl of XL-10 gold E.coli (Agilent) by incubating on ice for 30 minutes with 4µl of 2-mercaptoethanol before heat shocking at 42^{o}C for 30 seconds and returning to ice for a further 2 minutes. Pre-warmed SOC media is added (900µl) is added and bacteria plated on 100µg/mL ampicillin LB-agar plates before colonies were picked and grown overnight at 37^{o}C with shaking in 100µg/mL liquid LB media. DNA was extracted using QIAprep Spin Miniprep Kit (Qiagen) according to manufacturer's protocol. Briefly, bacteria were pelleted and lysed before neutralised lysis buffer is centrifuged to pellet cell membranes and organelles. Supernatant is applied to a supplied spin column and DNA bound by centrifugation. Bound DNA was briefly washed before being eluted in 10mM Tris buffer.

PCR was performed using primers (Section 2.2.4) against the 3' and 5' ends of the respective ORFs that introduce restriction enzyme sites (Sgf1, Mlu1). PCR is performed using a touchdown protocol with an initial denaturation of 95^{o}C for 10 minutes followed by cycles of 95^{o}C for 10 seconds, 62^{o}C (2x), 60^{o}C (2x), 58^{o}C (2x), 56^{o}C (15x) for 20 seconds and 72^{o}C for 4 minutes with a final elongation step of 10 minutes.

PCR amplified ORF was purified using QIAquick PCR purification kit (Qiagen) (Section 2.9.1) according to manufacturer's protocol of binding DNA to a spin column, washing briefly and finally eluting in 10mM tris buffer.

pCMV6-ENTRY and pCMV6-AC-HIS vectors were transformed into XL-10 gold E.coli and DNA extracted as above (pCMV6-ENTRY is grown in 25µg/ml kanamycin, pCMV6-AC-HIS in 100µg/ml ampicillin LB media).

ORF and vector DNA are digested using Sgf1 and Mlu1 restriction enzymes (Promega) in restriction buffer C (Promega) for 3 hours at room temperature. Alkaline phosphatase is added to vector digestions, but not to ORF, for a final 30 minutes.

Following digestion, DNA is again purified using QIAquick PCR purification kit (Section 2.9.1), or QIAquick gel extraction kit (Qiagen) for vector DNA, after being run on a 1.3% agarose gel (tris borate EDTA (TBE) and gel-red) at 200V for 90 minutes to separate the excised fragment. Gel extraction differed from PCR purification in that the excised agarose slice was solubilised at 50^{o}C for 10 minutes in the supplied buffer and isopropanol added to a final concentration of 20%, before the DNA was bound to the supplied column in the same manner.

ECSIT ORF was ligated into pCMV6-AC-HIS vector and NDUFAF1 into pCMV6-ENTRY using T4 DNA ligase (NEB) for 60 minutes at room temperature. Ligated vector and ORF were transformed into XL.10 gold E.coli as before and DNA extracted using a plasmid midi kit (Qiagen) according to manufacturer's protocol (an up-scaled version of the mini-prep). Correct ligation and orientation was confirmed by Sanger sequencing (Section 2.9.2) with supplied VP1.5 and XL39 sequencing primers (Section 2.2.6).

pCMV6-AC-HIS-ECSIT was then used as a template for site directed mutagenesis of the N209I mutation using Q5 site-directed mutagenesis kit (NEB) and primers (table 5.2.5) designed to introduce the point mutation. PCR is performed according to manufacturer's protocol with an initial denaturation of 98^{o}C followed by 25 cycles of 98^{o}C for 10 seconds, 62^{o}C for 30 seconds and 72^{o}C for 2 minutes. KLD reaction was performed according to the kit instructions for 5 minutes at room temperature before mutagenised vector was transformed into 50µL of NEB-5α E.coli by incubating on ice for 30 minutes and heat shocking at 42^{o}C for 30 seconds. 950 µL SOC media is added and plated on 100µg/mL ampicillin LB plates overnight before colonies are picked and grown for a further 24 hours in liquid LB (100 µg/mL ampicillin) at 37^{o}C with shaking overnight. DNA is again extracted using plasmid midi kit (Qiagen).

Vector DNA is transfected into HEK-293T cells grown in a 6 well plate using jetPRIME® reagent (Polyplus) according to manufacturer's protocol. Briefly, 2.5x10^{5} cells/well are pre-plated 24 hours prior to transfection in DMEM (high glucose, glutamax) supplemented with 10% FBS and 100U/ml penicillin-streptomycin (Section 2.23). 2µg of

DNA (1µg of each vector for co-transfection) is diluted in 200µL of jetPRIME® buffer and 4µL of jetPRIME® reagent added. Mixture is incubated at room temperature for 10 minutes following a brief vortex and centrifugation. Finally, mixture is applied drop-wise to media containing cells and incubated at 37°C with 5% CO_2 for 48 hours.

ACAD9, TRAF6 and SMAD4 were purchased pre cloned into the pCMV6-Entry vector and transformed into XL.10 gold *E.coli*, grown and DNA extracted as above.

2.22. Co-Immunoprecipitation

48 hours following transfection, HEK293T cells transfected with relevant vectors to express ECSIT or associated proteins were briefly washed with PBS and lysed in RIPA buffer (150mM NaCl, 1% NP-40, 0.5% DOC, 0.1% SDS, 50mM Tris, pH 7.5) with protease inhibitors (Roche) with manual scraping. Protein concentration was assessed by Bradford assay (Bio-Rad) and protein diluted to 1mg/ml 1ml of protein lysate was pre-cleared with 20µl of protein G sepharose bead slurry (Sigma) for 1 hour to remove native immunoglobulins. Protein G beads were removed by briefly spinning at 1000xg for 1 minute and the supernatant incubated with 4µg of relevant antibody (Section 2.4) over night to bind the protein of interest. Following antibody binding, lysate was incubated with 20µl of protein G sepharose bead slurry for 1 hour to bind antibody and attached protein/s. Beads were again pelleted by centrifugation at 100xg for 1 minute and washed 3 times in RIPA buffer. Beads were left in 30µl of RIPA buffer and 1x LDS sample buffer (Invitrogen) and reducing agent (Invitrogen) added before boiling the sample at 95°C for 10 minutes to dissociate the beads from the bound antibody.

Samples were loaded onto NuPAGE™ 4-12% Bis-Tris protein gels (Invitrogen) and run as with western blots (Section 5.13), before being transferred to PVDF membrane (Section 2.16).

2.23. Growth and maintenance of HEK-293T Cells

HEK-293T cells (ECACC) were maintained in DMEM (high glucose, glutamax) with 10% FBS and 100U/ml penicillin-streptomycin. When required, cells were split 1:20-1:40 by first washing with pre-warmed D-PBS, and detached using 0.05% trypsin. Following detachment of cells, trypsin was deactivated using twice the volume of complete media

and seeded into 20mls total volume of complete DMEM in a T-75 flask or other appropriate cell culture container where required.

2.24. Mouse Embryonic Fibroblast Isolation and Culture

MEFs were harvested from 12.5-14.5dpc (days post coitum) mouse embryos by removing the head, heart and liver and washing gently in ice cold PBS. Harvested embryos were minced in 1.5mLs of 0.25% trypsin and incubated at 37^{o}C for 5 minutes followed by homogenisation using a 21 gauge needle. Trypsin was deactivated using 5mLs of MEF culture media (DMEM (high glucose, pyruvate), 10% FBS, 50µM β-mercaptoethanol, 1x non-essential amino acids, 100U/ml penicillin streptomycin) and incubated overnight at 37^{o}C, 5% CO_2. The following day media was changed for fresh MEF culture media and maintained at 37^{o}C, 5% CO_2. When required, MEFS were split 1:20 after washing with PBS and detaching using 0.25% trypsin.

2.25. Bone Marrow Derived Macrophage Isolation

12 week old Wild type and *Ecsit*$^{N209I/N209I}$ animals were sacrificed by cervical dislocation and femur, tibia and fibula dissected from both hind limbs without damaging the epiphyses of any of the bones. Samples were kept on ice whilst dissection was performed.

In a laminar flow hood, excess muscle was removed by scraping with a scalpel blade and the epiphyses of the femur and tibia removed, exposing the bone marrow. Bone marrow was flushed from the bone cavity with a 25G needle and syringe containing 1-2mls of PBS containing 0.6mM EDTA and flow through collected. Collected cells were pelleted by centrifugation at 400xg for 7 minutes at 4^{o}C. Supernatant was removed and cells resuspended in 5mls of PBS containing 0.6mM EDTA. Cell suspension was filtered through a pre-wetted 70µm cell strainer and the cell strainer washed with 10mls of PBS containing 0.6mM EDTA. Cells were again pelleted at 400xg for 7 minutes (4^{o}C). Red blood cells were removed by resuspending the pellet in 3mls of red blood cell lysis buffer (155mM NH_4Cl, 12mM $NaHCO_3$, 0.1mM EDTA) and incubated for 1 minute before diluting in 10mls of PBS (0.6mM EDTA) and again pelleted at 400xg. Cells were resuspended in PBS (0.6mM EDTA) one last time to measure cell concentration using a sceptre cell counter (Merck Millipore). Cells were pelleted and washed once in DMEM (pyruvate, glutamine) containing 10% FBS, 100U/ml penicillin-streptomycin to remove

EDTA. Finally, cells were plated at a concentration of $2.5x10^6$ cells/mL in DMEM (pyruvate, glutamine) containing 10% FBS, 100U/ml penicillin-streptomycin and 100ng/ml of macrophage colony stimulating factor (MCSF) (Cell Guidance Systems). Cells were maintained at 37°C, 5% CO_2 with media changes on day 3 and 6. On day 7 cells were harvested by manual scraping with PBS (0.6mM EDTA). Cells were counted again and re-plated at a concentration of $6x10^6$ cells/well of a 6 well plate in DMEM (pyruvate, glutamine), 10% FBS, 100U/ml penicillin-streptomycin, 100ng/mL MCSF. Plated cells were activated with 100ng/ml of lipopolysaccharide (LPS) added directly to the media and incubated for 24 hours at 37°C, 5% CO_2.

Activated cells were harvested by manual scraping with PBS (0.6mM EDTA) and cells pelleted before lysis (Section 2.16).

2.26. Cardiomyocyte Isolation

Cardiomyocytes were isolated from wildtype and *Ecsit*$^{N209I/N209I}$ neonatal mice between 1 and 3 days old, no preference for sex was made. Animals were sacrificed by cervical dislocation and skin sterilised with 70% ethanol. Hearts were dissected and gently washed in Ca^{2+}/Mg^{2+} free PBS supplemented with 20mM BDM (2,3-butanedione monoxime) before mincing in 250µL of isolation medium (Ca^{2+}/Mg^{2+} free HBSS supplemented with 20mM BDM and 0.0125% w/v trypsin). Minced hearts from 6-10 animals were incubated overnight in 10mL of isolation medium at 4°C with gentle agitation.

The following day, isolation medium was replaced with 5mLs of digestion medium (L15 medium, 20mM BDM, 1.5mg/mL Roche collagenase/dispase enzyme mix) and 5mLs of L15 medium supplemented with 20mM BDM before oxygenating for 1 minute. The oxygenated sample was then incubated for 30 minutes at 37°C with gentle agitation before digested fragments were triturated 10-20 times with a 10mL stripette. Cell suspension was passed through a pre-wetted 70µM cell strainer and the flow-through collected. Cardiomyocytes were pelleted by centrifuging at 100xg for 5 minutes at room temperature and resuspended in plating medium (65% DMEM high glucose, 19% M-199, 10% horse serum, 5% FCS, 100U/ml penicillin-streptomycin) before being plated on uncoated 10cm tissue culture plates for 3 hours at 37°C, 5% CO_2. Media was washed over the plate after 3 hours, leaving the adherent fibroblasts stuck to the plate, this step

was repeated once more before the cardiomyocyte suspension was plated at $1.5x10^5$ cells/cm^2 on collagen coated tissue culture plates.

24 hours post plating, plating medium was replaced for maintenance medium (78% DMEM high glucose, 17% M-199, 4% horse serum, 100U/ml penicillin-streptomycin, 1µM AraC, 1µM isoproterenol) and cultured at 37°C, 5% CO_2 for up to 5 days [277].

2.27. Immunoprecipitation for Mass-Spec

Immunoprecipitation was performed by one of 3 methods. For methods 1 and 2 proteins were extracted from wild type hearts by homogenisation in precellys tubes in a precellys homogeniser (Bertin instruments) in either RIPA buffer (150mM NaCl, 1%NP-40, 0.5% DOC, 0.1% SDS, 50mM Tris, pH 7.5) or incomplete RIPA buffer (150mM NaCl, 1% NP-40, 0.5% DOC, 50mM Tris, pH 7.5) with the inclusion of 1x protease inhibitor cocktail (Roche) and 1x phosphatase inhibitor (Riche).

Lysates were cleared by centrifuging at 10,000xg for 15 minutes at 4°C before protein concentration was determined by Bradford assay (Bio rad).

5mg of total protein at a concentration of 2mg/mL was pre-cleared by incubating for 1 hour with 30µl of protein G sepharose bead slurry (Sigma) at 4°C for 1 hour with rotation to remove native immunoglobulins. Following pre clearance, samples were centrifuged at 1,000xg for 1 min to remove protein G beads and supernatant incubated overnight with 20µg of antibody.

Following overnight incubation, antibody was bound by incubation with 30µl of protein G sepharose beads for 1 hour at 4°C with rotation. Beads were collected by centrifugation (1,000xg, 1 min) and washed 3 times in 500µL lysis buffer. Antibody and bound protein were recovered by addition of 30µl of lysis buffer containing 1X LDS sample buffer (Invitrogen) and reducing agent (Invitrogen) before samples were run on an SDS-PAGE gel as in section 2.16.

For method 3 proteins were extracted from wild type hearts by homogenisation in precellys tubes in a precellys homogeniser (Bertin instruments) in a mild homogenisation buffer (0.5% Triton X-100, 50mM HEPES, 150mM NaCl, 1mM $MgCl_2$, 1mM EGTA, pH 7.5) containing 1x protease inhibitors (Roche). Following lysis, samples

were cleared by centrifugation at 16,000xg for 20 minutes at 4^{o}C and concentration assessed by Bradford assay (Bio rad).

Preclearing of 1mg total protein (2mg/mL) was performed by incubation with 50µl of Protein A/G sepharose beads for 30 minutes at 4^{o}C with rotation. Beads were removed by centrifugation at 16,000xg for 10minutes at 4^{o}C.

Supernatant was incubated with 1µg of antibody for 1 hour at 4^{o}C with rotation before the addition of 30µl of protein A/G sepharose bead slurry and continued incubation overnight. Beads are collected by centrifugation (16,000xg, 10 mins, 4^{o}C) and washed three times in lysis buffer. Antibody and bound protein were collected by addition of 30µl of lysis buffer containing 1x LDS sample buffer (Invitrogen) and 1x reducing agent (Invitrogen) before western blot was performed.

2.28. Fluorescence Associated Cell Sorting (FACS)

FACS analysis was performed by Dr Pratik Vikhe at MRC Harwell. For analysis blood was collected by terminal retro-orbital sinus bleed following terminal overdose of pentobarbital using lithium heparin capillary tubes and lithium heparin collection tubes. 25µl of whole blood was diluted in 175µl of FACS buffer (5mM EDTA, 0.5% foetal calf serum, PBS) in 96well V bottom plates. Blood was centrifuged at 2000rpm for 2 minutes and the pellet resuspended in red blood cell lysis buffer (155mM NH_4Cl, 12mM $NaHCO_3$, 0.1mM EDTA) and incubated at room temperature for 5 minutes before centrifuging at 2000rpm for 2 minutes. The pellet was resuspended in 200µl of FACS buffer and transferred to 96 well FACS analysis plate, centrifuged as previously and washed once more in FACS buffer. Following washes the pellet was suspended in 200µl of FACS buffer and the Fc receptor blocked by 1µl of CD16/32 antibody followed by incubation at room temperature for 10 minutes. Cells were centrifuged again at 2000rpm for 2 minutes and pellet suspended in 100µl of staining solution (FACS buffer + anti-F4/80 (1:200), anti-CD11b (1:200), anti-Ly6g (1:200), anti-Ly6c (1:200) and anti CD5 (1:800) followed by 20 minutes at room temperature in dark. Cells were washed with FACS buffer and fixed in 100µl of 0.5% PFA for 10 minutes at room temperature in the dark. Finally, cells were washed twice in FACS buffer and resuspended in 210µl of FACS buffer and analysed using BD FACSCanto™ II system. FlowJo software (Tree Star™) was used to analyse the data.

2.29. Quantitaive Real Time PCR

For *Tlx2* expression, E7.5 embryos from wild type x wild type and *Ecsit*$^{N209I/N209I}$ x *Ecsit*$^{N209I/N209I}$ matings were collected, pooled and frozen on dry ice. RNA was extracted from pooled embryos using RNeasy Micro Kit (Qiagen) according to manufacturer's protocol and concentration measured using a Nanodrop 8000 spectrophotometer (Thermo Fisher). Briefly, pooled embryos are lysed in 350µl of RLT buffer before addition of 350µl of 70% ethanol. The RNA is then bound to a supplied spin column by centrifugation for 15 seconds at 8000xg. Flowthrough is discarded and membrane incubated with 70µl of RDD buffer containing DNAse I for 15 minutes at room temperature. Following incubation, the membrane is washed once with RW1 buffer, once with RPE buffer and once with 80% ethanol with each wash followed by centrifugation at 8000xg for 15 seconds. Finally, the RNA is eluted in 14µl of RNAse free water and concentration calculated.

RNA was diluted to a concentration of 100ng/µl and cDNA synthesised using high capacity cNDA reverse transcription kit (Thermo Fisher). Briefly, 10µl of diluted RNA is combined with 2µl of 10x RT buffer, 0.8µl of 25x dNTP mix (100mM), 2µl of 10x RT random primers, 1µl of multiscribe reverse transcriptase and 4.2µl of nuclease free water. The solution is then incubated on a PCR block at 25^{o}C for 10 minutes followed by 37^{o}C for 120 minutes and 85^{o}C for 5 minutes. cDNA is stored at -20^{o}C until qRTPCR is run.

The synthesised cDNA is diluted 1:25 to give a final concentration of 2ng/µl, suitable for taqman assay. Diluted cDNA (5µl) is combined with 10µl of 2X Taqman fast universal PCR master mix (Thermo Fisher), 1µl of relevant Taqman assay and 4µl of nuclease free water. The combined reagents are plated in a MicroAmp Fast Optical 96-wel Reaction plate (Thermo Fisher), the plate sealed with optically clear adhesive film and run on a 7500 fast real-time PCR system (Applied Biosystems). Taqman assays used were specific for the target gene *Tlx2* (Mm00437109_g1) and the endogenous controls *B2m* (Mm00437762_m1), *Gapdh* (Mm99999915_g1), and *Hprt1*(Mm00446968_m1). *Hprt* was selected for comparison as it demonstrated the least variability between samples.

2.30. Statistical Analysis

Statistical analysis was performed using GraphPad Prism 7 (GraphPad software, CA, USA). Data are presented as mean ± SEM unless otherwise stated. Comparisons between 2 groups were performed using unpaired Student's t-test, an F test was performed to determine if there was a significant difference in variance between groups and where appropriate a Welch's correction was included. For more than two groups, one (single variable) or two way (two variables) ANOVA was used with Bonferroni's multiple comparison test for testing between groups. Correlations were assessed by linear regression. Results were considered significant at $p<0.05$. All phenotyping tests were performed blind to genotype of animals and in the case of echocardiograph, analysis was too performed blind. However, downstream molecular biology techniques were performed with prior knowledge of the genotype of samples being handled.

Chapter 3: Phenotypic Characterisation, Genetic Mapping and Confirmation of Mutation

3.1. Introduction

The aim of the Harwell Ageing Screen was to identify new mouse models of diseases associated with ageing by mutagenizing male mice and ageing their G_3 descendants for 18 months. During this time, the mice underwent a range of phenotyping tests across a range of physiological systems. As a result of this rigorous phenotyping regime a number of phenotypes of interest, resulting from ENU-induced mutations, were identified across the physiological systems that were part of the screening program [270].

This chapter will focus on the identification, mapping, sequencing and further phenotyping of a small number of mice from pedigree MPC-178, which all exhibited a hypertrophic cardiomyopathy phenotype before 6 months of age. The pedigree was re-derived from original G_1 founder DNA in order to continue work after the identified affected animals were sacrificed. Whole-genome sequencing identified a candidate gene (*Ecsit*) and further phenotyping and inheritance testing confirmed the recessive nature of the trait. Despite *Ecsit* being thought to be ubiquitously expressed, the phenotype appears to be localised primarily to the heart with only small defects in weight gain and kidney function being observed.

3.2. Mapping

Mice were initially identified as part of the Harwell Ageing Screen when approximately 15 mice from the initial G_3 pedigree (78 mice) showed various signs of ill health (sudden weight loss, hunched appearance, piloerect coat, inactivity) or died suddenly. Four of these mice were collected for systematic necropsy and were noted to have enlarged hearts by visual inspection. Histology from this original pedigree revealed characteristic signs of hypertrophic cardiomyopathy: enlargement and disorganisation of the cardiomyocytes and the presence of vacuolation (Figure 3.1).

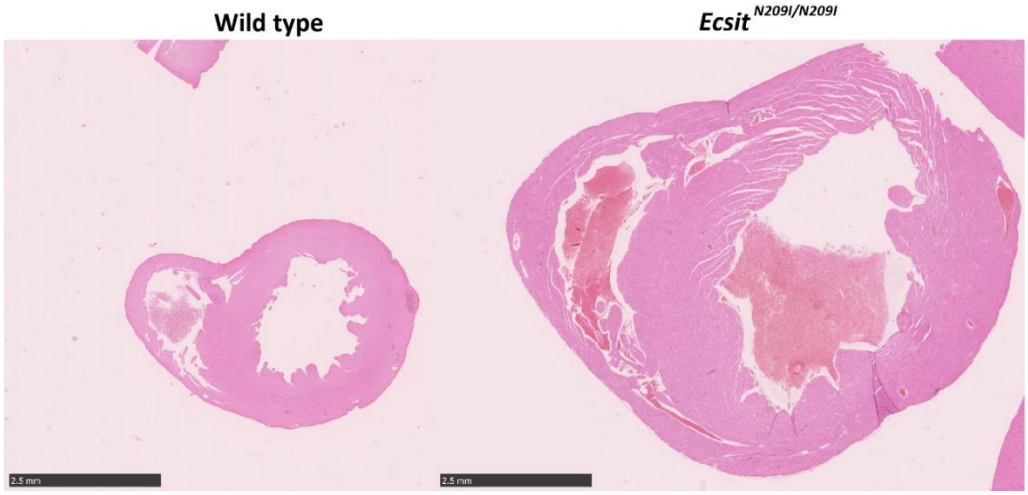

Figure 3.1. Histology of wild type and *Ecsit*$^{N209I/N209I}$ heart from original pedigree showing enlargement of cardiac muscle with presence of disorganisation and vacuolation of cardiomyocytes in *Ecsit*$^{N209I/N209I}$ heart.

The number of affected mice (15/78) suggested that this was a recessive mutation and no founder G_1 or G_2 mice were found to be affected. Using the hypertrophic cardiomyopathy as the affected trait, the causative mutation was mapped to a 46Mb region of C57BL/6J origin at the proximal end of chromosome 9 spanning 8 SNPs of the golden gate panel (1449 SNPs total) (Figure 3.2). Mapping is based on SNP variations between the C57BL/6J and C3H.Pde6b+ founder strains with the knowledge that any ENU induced mutations must lie in a region of the genome inherited from the C57BL/6J ancestor.

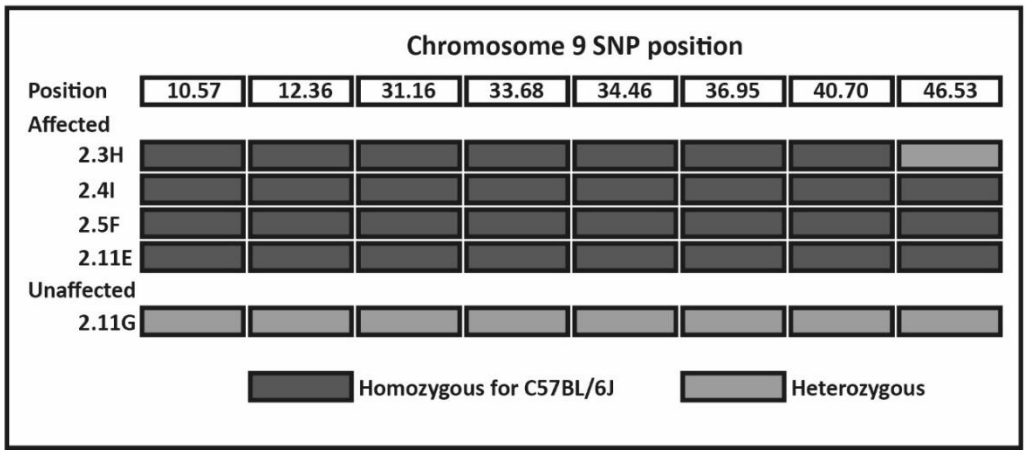

Figure 3.2. SNP mapping panel results showing results for affected and unaffected animals across the region identified. SNP positions demonstrate a region from the proximal end of Chromosome 9 up to 46.53Mbs as homozygous for C57BL/6J (2.3H) that must contain the causative mutation.

3.3. Whole Genome Sequencing

DNA from the G_1 founder male was sent for whole genome sequencing (WGS) to determine the nature of the causative mutation. Whole genome sequencing was utilised instead of exome sequencing to include the possibility of a mutation in a non-coding portion of the DNA being causative of the phenotype. Results were analysed by the MRC Harwell bioinformatics team who aligned the sequences with the C57BL/6J reference sequence (NCBIM38/mm10), determined read depth and annotated the mutations [270]. The results identified 37 high confidence mutations within the mapping region (Table 3.1) however none of these were found to cause coding changes in any protein coding genes. Twenty-five lay in intergenic regions, whilst eleven were identified as intronic variants and 1 was a 3' UTR variant in the gene *Sidt2.* Only one missense variant was identified in the region of interest, a medium confidence A to T change at position 916 in the gene *Ecsit*. The mutation results in an asparagine to isoleucine change at residue 209 in the ECSIT protein (N209I). Whilst it is feasible that non-coding mutations could result in the observed phenotype, I initially concentrated on those mutations that affected protein coding as our experience to date shows that the majority of causative mutations cloned within the Harwell Ageing Screen resulted in a change to protein sequence.

Position	Reference	Alternate	Functional Class	Gene Name
3312365	A	G	Intergenic variant	-
5017927	T	A	Intergenic variant	-
5139754	T	A	Intergenic variant	-
5391313	T	G	Intergenic variant	-
5726491	T	C	Intergenic variant	-
6253838	A	T	Intron variant	*Pdgfd*
7169444	T	C	Intron variant	*Dync2h1*
8532327	G	A	Intergenic variant	-
8560942	T	C	Intron variant	*Trpc6*
8948900	T	C	Intron variant	*Pgr*
9282243	T	A	Intergenic variant	-
12502691	T	A	Intergenic variant	-
14147347	T	C	Intergenic variant	-
14360948	T	C	Intron variant	*Endod1*
14535993	C	G	Intergenic variant	-
16632293	T	A	Intergenic variant	-
17778686	C	A	Intergenic variant	-
18057518	C	A	Intergenic variant	-
20231528	T	C	Intergenic variant	-
20656400	T	C	Intron variant	*Pin1*
22074703	A	T	Missense variant	*Ecsit*
23247306	T	C	Intron variant	*Bmper*
25035963	G	A	Intergenic variant	-
27226439	T	C	Intergenic variant	-
27449832	G	A	Intergenic variant	-
32135464	T	C	Intron variant	*Arhgap32*
35578580	G	A	Intron variant	*Pate2*
35941372	G	A	Intergenic variant	-
35960065	G	A	Intergenic variant	-
36371877	A	T	Intergenic variant	-
37016075	G	T	Intron variant	*Pknox2*
41610811	T	C	Intron variant	.
42189413	A	T	Intergenic variant	-
43404358	A	G	Intergenic variant	-
43593770	A	G	Intergenic variant	-
44105948	A	G	Intron variant	*Rnf26*
45938935	T	A	3’ UTR variant	*Sidt2*
46898334	G	A	Intergenic variant	-

Table 3.1. List of high confidence mutations in the 46Mb region identified from SNP mapping. The *Ecsit* mutation is shown in grey as the only coding mutation (medium confidence) identified in the region.

3.4. Mutation Validation

To confirm the validity of the WGS, three of the mutations were selected for confirmation by Sanger sequencing. The mutations in *Pdgfd* (platelet derived growth factor d), *Trpc6* (transient receptor potential cation channel, subfamily C, member 6) and *Ecsit* (Evolutionarily conserved signalling intermediate in toll pathway) were considered to be the most interesting candidate genes given their potential role in pathways with a link to cardiac function (Table 3.2). Results from Sanger sequencing of a G_3 affected animal (Figure 3.3) confirm the WGS results and demonstrate that all three mutations are present in the G_3 offspring.

Gene	Mutation	Link to cardiac function
Pdgfd	Intron mutation	Recruits macrophages and increases blood pressure when overexpressed [278].
Trpc6	Intron mutation	Forms a calcium permeant cation channel, other calcium channels linked to cardiac conditions [279].
Ecsit	N209I	Linked to mitochondrial function, dysfunction commonly associated with cardiomyopathy [231].

Table 3.2. The three genes containing mutations considered most likely to be causative of the phenotype in affected animals. *Ecsit* was considered to be the best candidate at this point due to direct links with cardiomyopathy whilst the remaining two only showed tentative links via other proteins with loosely similar functions.

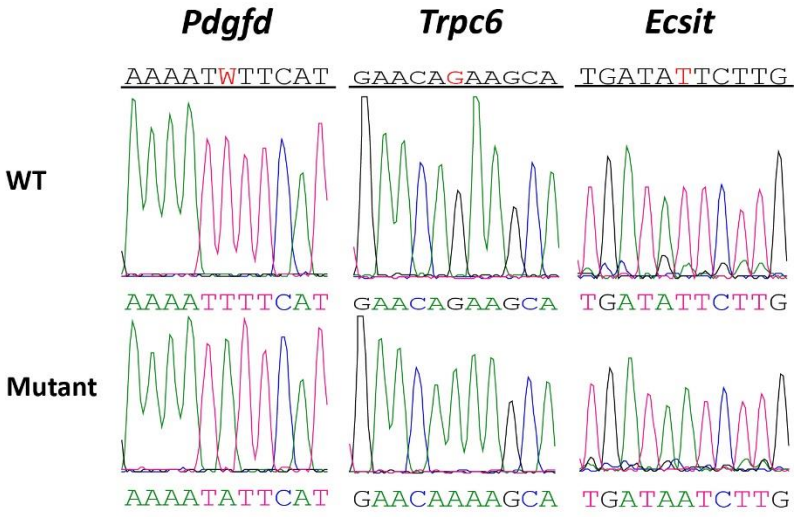

Figure 3.3. Sanger sequencing results from Pdgfd, Trpc6 and Ecsit showing confirmation of mutations from WGS in a G_3 homozygous for the critical interval.

3.5. Narrowing the causative region

In order to begin narrowing the causative region to confirm that *Ecsit* contained the causative mutation the line was rederived from frozen G_1 sperm and heterozygous offspring crossed to C3H.Pde6b+ females in order to obtain a new cohort. Pyrosequencing was performed on ear clips taken from this pedigree, this allowed for both genotyping of animals and for confirmation of a number of the remaining intron variant mutations. A selection of mutations were used as markers, spanning the region to search for recombinants. A number of the single nucleotide variants (SNVs) were unsuitable for use in pyrosequencing due to the inability to design pyrosequencing primers in the region of the mutation (High GC content, repetitive sequence). The validated results shown in figure 3.4 demonstrate the expected pyrosequencing traces from each of the validated SNVs for both WT and mutant.

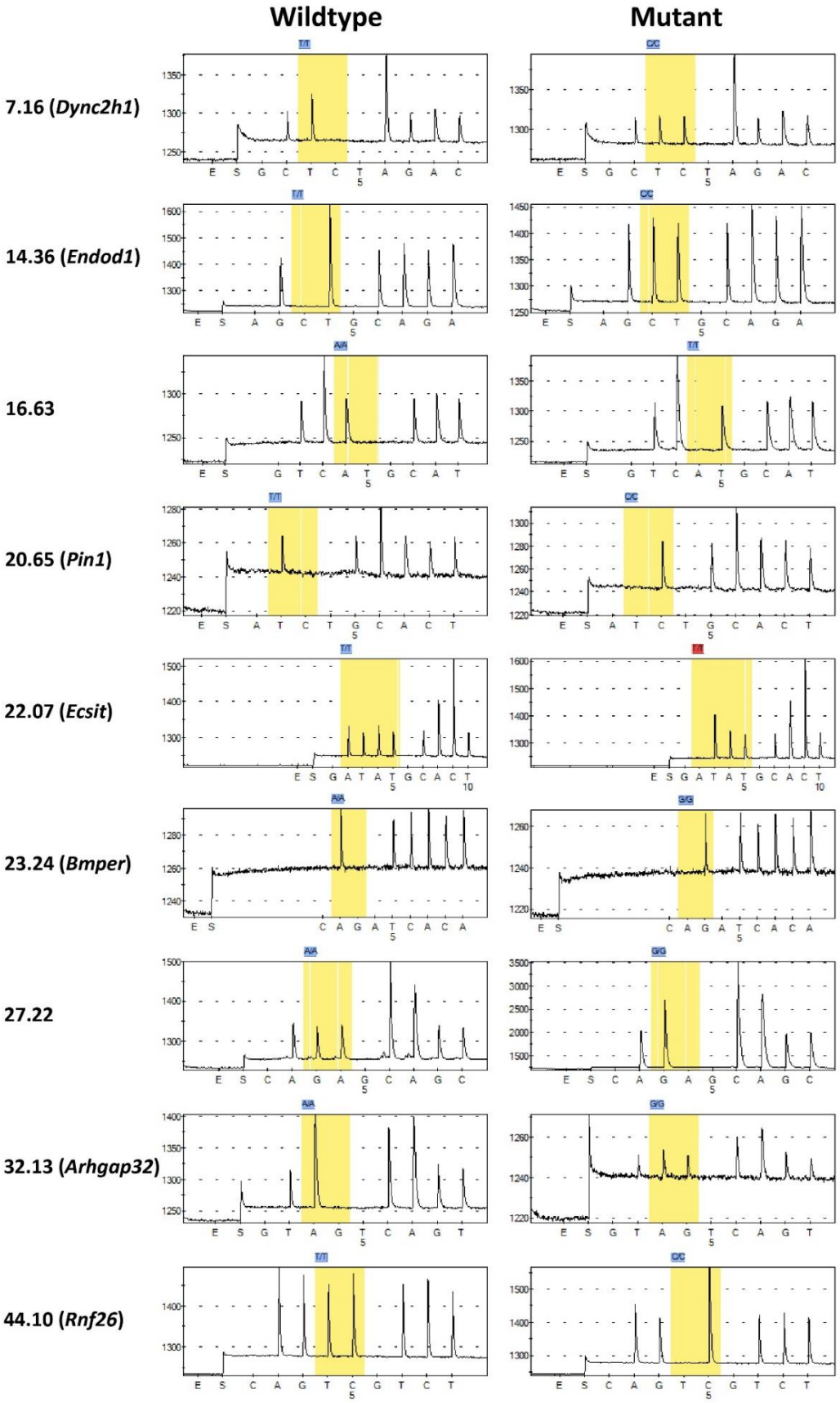

Figure 3.4. Example traces from each of the pyrosequencing primer sets used to genotype the SNVs in affected and control animals. The results confirm the WGS data for the mutations tested.

Pyrosequencing results from the initial cohort of 39 mice showed 7 animals with portions of the region of interest that were homozygous for all or some of the 5 SNVs tested (7.16, 14.36, 22.07, 23.24 and 32.13). Further SNVs were introduced to genotype later pedigrees to further narrow the region where possible. Of the 39 animals, 6 were later shown to be affected by cardiomyopathy by echocardiography, with these 6 all homozygous for the *Ecsit* mutation. The one animal without cardiomyopathy (2.1i) was only homozygous for SNV 7.16, indicating that this animal carries the mutation *Pdgfd* and thus eliminating this mutation from consideration (Table 3.3). A further animal (1.1b) carried a region resulting from a crossover event between SNVs 14.36 and 22.07 and was also shown to be affected by the cardiomyopathy phenotype. This allowed for the subsequent elimination of both the *Pdgfd* and *Trpc6* mutations from consideration as they both lay in this heterozygous region and whilst this animal showed a cardiomyopathy phenotype, other animals with heterozygosity across the region displayed no phenotype (Table 3.3).

These data also confirm that the trait is inherited in a recessive fashion as no heterozygous animals were found to be affected by the cardiomyopathy phenotype.

Animal	Affected?	9_7.16	9_14.36	9_22.07	9_23.24	9_32.13
1.1b	Yes	HET	HET	HOM	HOM	HOM
2.1i	No	HOM	HET	HET	HET	HET
1.1g	No	WT	WT	WT	WT	WT
1.1n	No	HET	HET	HET	HET	HET
1.1i	Yes	HOM	HOM	HOM	HOM	HOM

Table 3.3. Example pyrosequencing results across the region tested for 5 animals of the initial rederived pedigree. Results for animal 1.1b (confirmed affected by echocardiography) eliminate the region up to SNV 14.36 (*Endod1*), thus eliminating *Pdgfd* and *Trpc6* as candidates as they lie upstream of this SNV. 2.1i also demonstrates a homozygous region around 7.16

3.6. Protein structure prediction

To predict the effect that the N209I mutation may have on ECSIT, a selection of protein prediction algorithms were consulted through their online interfaces. Consistent results (Table 3.4) show that the N209I mutation is predicted to cause a deleterious change to protein structure or function and may result in disease. Whilst this is only a prediction it is informative that all software packages used reached the same conclusion and offered a starting point from which to begin work on the ECSIT protein.

Software	**PANTHER**	**PhD-SNP**	**SIFT**	**SNAP**	**Meta-SNP**	**SNAP2**	**Provean**
Score	0.783	0.648	0.000	0.560	0.644	52	-7.252
Outcome	Disease	Disease	Disease	Disease	Disease	Effect	Deleterious

Table 3.4. Protein prediction scores and expected outcome from a variety of SNP prediction softwares. Panther[1] (0-1, >0.5 Disease), PhD-SNP[1] (0-1, >0.5 Disease), SIFT[1] (0-1, <0.5 Disease), SNAP[1] (0-1, >0.5 Disease), Meta-SNP[1] (0-1, >0.5 Disease), SNAP2[2] (-100-100, >50 Effect), Provean[3] (-13-4, <-2.5 Deleterious). [1]http://snps.biofold.org/meta-snp, [2]rostlab.org/services/snap, [3]provean.jcvi.org.

3.7. Production of phenotyping cohorts

Further phenotyping was delayed until an incipient congenic line was obtained to reduce the potential effects of the mixed genetic background and to eliminate mutations outside of the region of interest. To obtain the incipient congenic line *Ecsit*$^{N209I/+}$ males were crossed to C3H.Pde6b+ females for 5 generations. Genotyping was performed by pyrosequencing across the region described above at each generation, selecting animals heterozygous for the mutation in *Ecsit* and where possible eliminating any other sections of the region. The pyrosequencing panel was expanded to assist with this narrowing of the region.

3.7.1. Inheritance

As the global deletion of *Ecsit* in mice is known to be lethal [230], it was important to test for the viability of *Ecsit*$^{N209I/N209I}$ animals. To demonstrate that the Ecsit^{N209I} mutation was not homozygous lethal, the total number of mice for each genotype that were obtained as part of the incipient congenic backcross line were compared to predicted numbers for typical Mendelian inheritance from Het intercross matings (1:2:1). The total number of mice that were genotyped post weaning was 587 throughout the projects lifetime giving a Mendelian ratio of 146.75:293.5:146.75. The actual ratio of mice genotyped was 158:270:159 (Figure 3.5) giving a chi-square value of 0.1521 (two-tailed

Chi square), indicating that the N209I mutation does not result in elevated pre-weaning lethality.

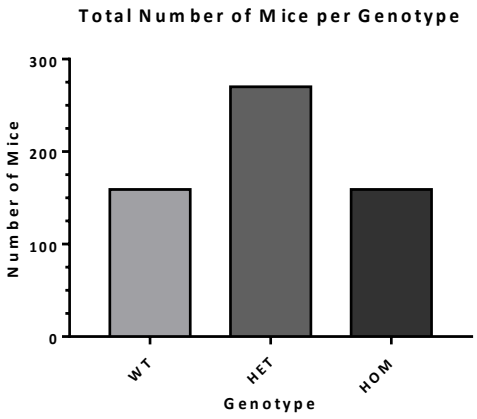

Figure 3.5. Total numbers of mice from each genotype from incipient congenic mice.

3.8. Phenotyping

Phenotyping was undertaken to examine a number of physiological systems to determine if the phenotype observed in the heart was isolated or part of a syndromic condition. Some phenotyping tests were unable to be performed at late time points due to the sensitivity of affected animals to general anaesthesia and as such were omitted. As a result, phenotyping tests shown below focus on metabolism and the function of organs with high energy demand such as the heart, liver, kidneys and skeletal muscle. Except where stated, all following phenotyping was undertaken on animals from the incipient congenic line (Backcross 5 intercross).

3.8.1. Clinical Chemistry

The concentrations of a variety of minerals, metabolites and enzymes can provide clues to the function of various organs and systems within the body and may indicate which organs are most severely affected by the ECSIT N209I mutation. To investigate this, terminal plasma samples were collected from 16 week old animals from both the original re-derived pedigree (back cross 1) (M:F, WT 11:7, HET 15:6, HOM 5:5) and from the incipient congenic backcross animals (back cross 5) (M:F, WT 13:17, HOM 7:14). Samples were taken from wild type, *Ecsit*$^{N209I/+}$, and *Ecsit*$^{N209I/N209I}$ male and female animals, but as no meaningful differences in any tests were seen between wild type and *Ecsit*$^{N209I/+}$ animals, *Ecsit*$^{N209I/+}$ animals were excluded from further analysis. No

significant differences were observed between male and female animals and as a result, values were not separated.

The electrolytes sodium, potassium and chloride are responsible for a variety of roles in the body, including signalling, blood pressure homeostasis, maintaining cellular pressure, propagating action potentials and acid-base homoeostasis amongst others. The levels of the electrolytes sodium and chloride (Figure 3.6) show no significant changes indicating that the N209I mutation in ECSIT is not affecting the maintenance of these ions. However, average potassium concentration in *Ecsit*$^{N209I/N209I}$ animals was significantly elevated over control animals in both backcrosses tested, which may be caused by failure of the kidneys to remove high levels of potassium from the blood.

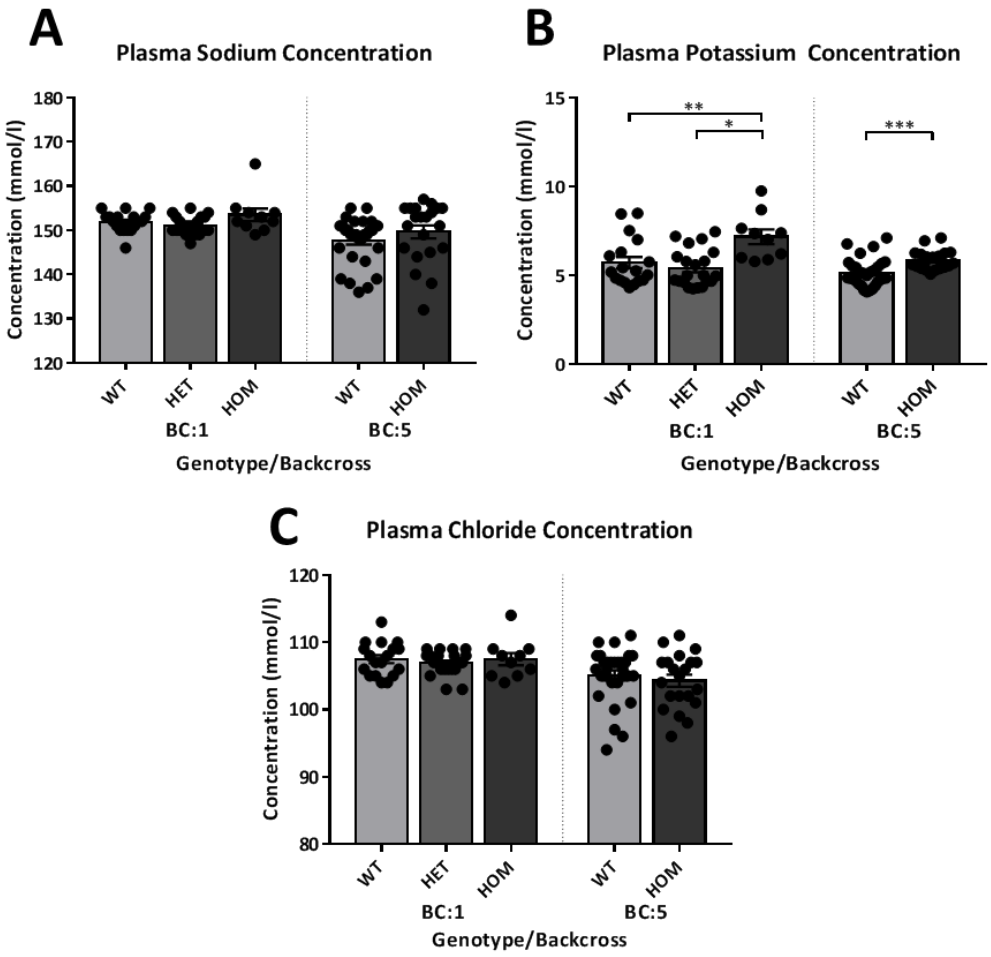

Figure 3.6. Plasma concentrations of the electrolytes, sodium (A), potassium (B) and chloride (C) in backcross 1 and 5 animals. Results show no significant differences in sodium or chloride concentration between any genotypes tested but do demonstrate a significant elevation in potassium levels in *Ecsit*$^{N209I/N209I}$ animals over controls in both backcrosses. Mean ± SEM, *p<0.05, **p<0.01, ***p<0.001.

Kidney function can be assessed by measuring the levels of urea and creatinine in plasma as these two compounds are typically filtered out by the kidneys during normal healthy function. *Ecsit*$^{N209I/N209I}$ animals show a significant elevation of both urea and creatinine in *Ecsit*$^{N209I/N209I}$ animals (Figure 3.7) compared to controls in both the backcross 1 and incipient congenic lines. Taken together with the elevation of potassium (Figure 3.6) these data could indicate a loss of function of the kidney filtration barrier as potentially harmful compounds are not being removed effectively from the blood.

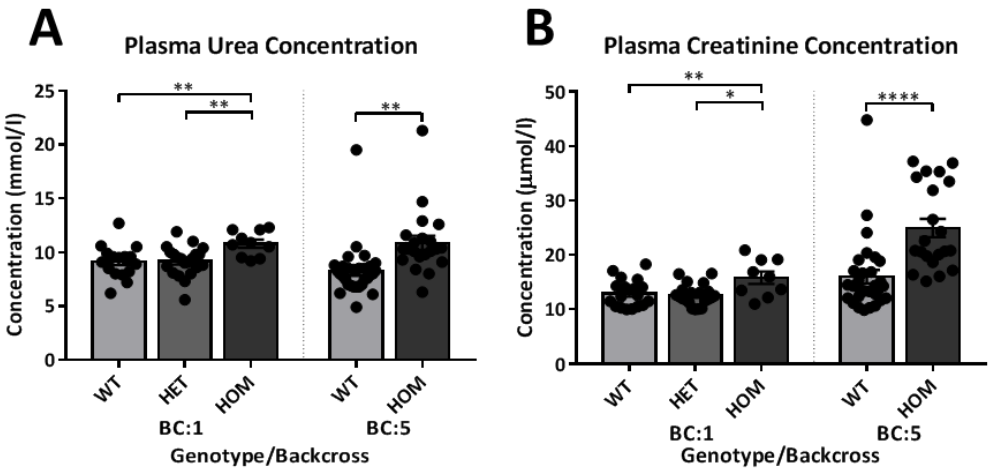

Figure 3.7. Plasma concentrations of the kidney function markers urea (A) and creatinine (B) in backcross 1 and 5 animals. Results demonstrate a significant elevation of both Urea and Creatinine in *Ecsit*$^{N209I/N209I}$ animals over controls in both backcrosses. Mean ± SEM, *p<0.05, **p>0.01, ****p<0.0001.

The liver is essential to normal metabolic function and there are many compounds that can measure different aspects of liver function (Figure 3.8). Proteins such as albumin are produced by the liver to regulate oncotic pressure of the blood and as a carrier for compounds with low solubility in water [280]. Total protein content and albumin concentration of plasma show no significant difference between *Ecsit*$^{N209I/N209I}$ animals and controls in either backcross tested indicating that this function of the liver is unaffected.

Bilirubin concentration shows mild elevation in *Ecsit*$^{N209I/N209I}$ animals compared to controls in both backcrosses. As bilirubin has a potential role as an antioxidant, this may indicate an upregulation due to increased reactive oxygen species either in the liver, the circulation or other tissues [281]. However, the difference between the groups is very small and may not be biologically relevant, despite being statistically significant.

Alkaline Phosphatase (ALP) dephosphorylates compounds throughout the body and elevated levels may be associated with a variety of liver conditions [282]. However, whilst the differences seen between *Ecsit*$^{N209I/N209I}$ and wild type animals here (Figure 3.8) are statistically significant, the levels seen in *Ecsit*$^{N209I/N209I}$ are not outside of the reference ranges established at MRC Harwell for wild type animals (57-136 U/l) indicating that this elevation may not be biologically significant.

Aspartate transaminase (AST) and alanine transaminase (ALT) are enzymes that catalyse the conversion of aspartate and α-ketoglutarate to oxaloacetate and glutamate, and L-alanine and α-ketoglutarate to pyruvate and L-glutamate, respectively. These reactions are reversible and serve to provide the substrates of a variety of metabolic processes. ALT and AST both show no significant differences between genotypes in the backcross 1 animals tested (Figure 3.8). Interestingly, AST does show a slightly elevated average AST level in *Ecsit*$^{N209I/N209I}$ animals from the incipient congenic backcross (Figure 3.8). However, with the exception of a single outlier, these values all lie within the ranges established for wild type mice at MRC Harwell (37-104 U/l) and are unlikely to truly represent a liver phenotype.

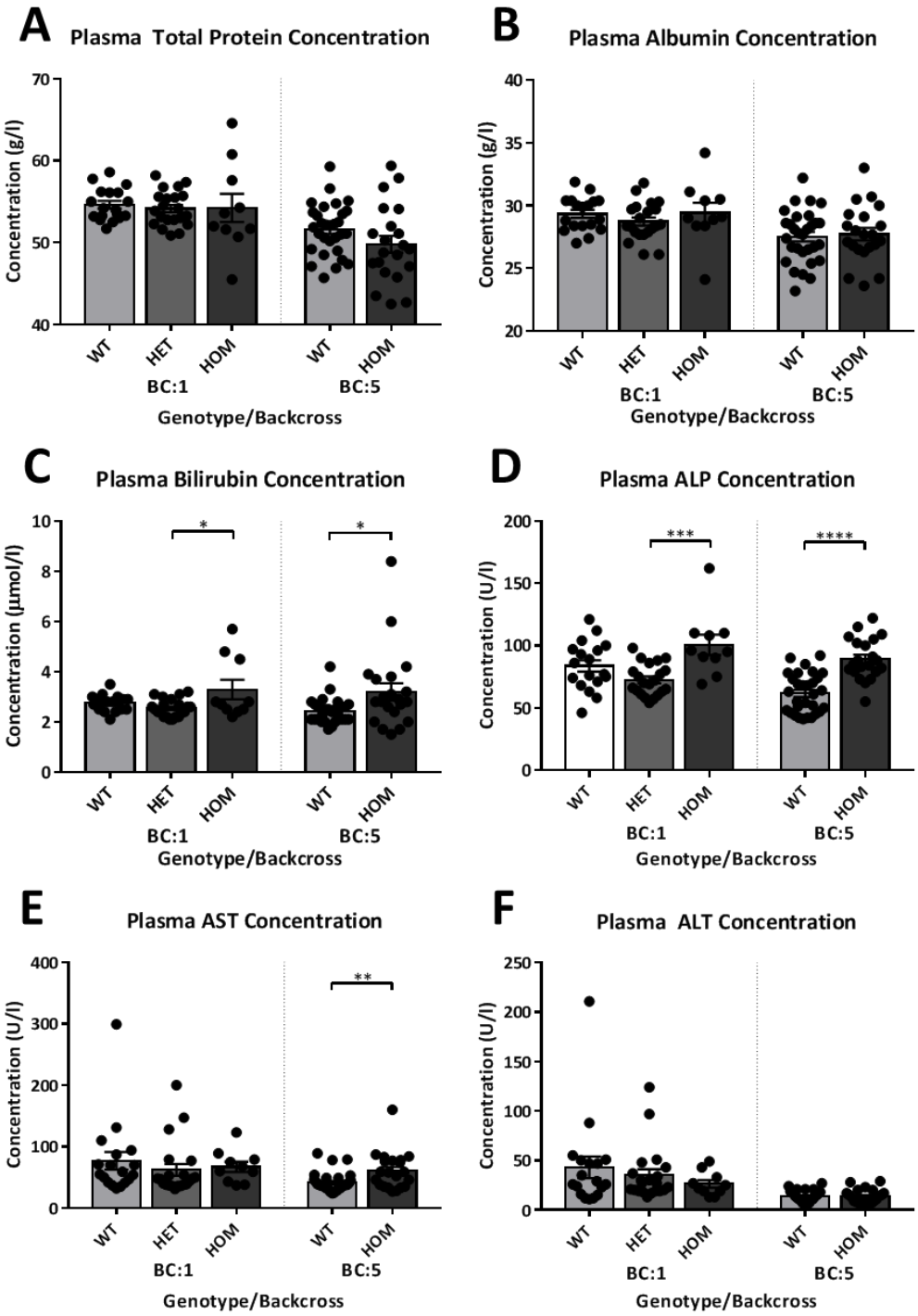

Figure 3.8. Plasma concentrations of the liver function markers total protein (A), albumin (B), bilirubin (C), ALP (D), AST (E) and ALT (F) in backcross 1 and 5 animals. Results show no significant differences in either total protein, or the specific protein, albumin, levels between any genotypes in either backcross. Bilirubin and ALP levels are elevated in *Ecsit*$^{N209I/N209I}$ animals over heterozygotes in the original backcross and over wild types in the incipient congenic line. AST also demonstrates a difference between wild type and *Ecsit*$^{N209I/N209I}$ animals in the incipient congenic line although no differences were apparent in the original backcross line. Finally, ALT shows no significant differences between any groups tested. Mean ± SEM, *p<0.05, **p>0.01, ***0<0.001, ****p<0.0001.

Calcium and inorganic phosphate levels in all groups from both backcross lines show no significant differences between genotypes indicating that there are no changes in the maintenance of these minerals, which are typically associated with bone health (Figure 3.9).

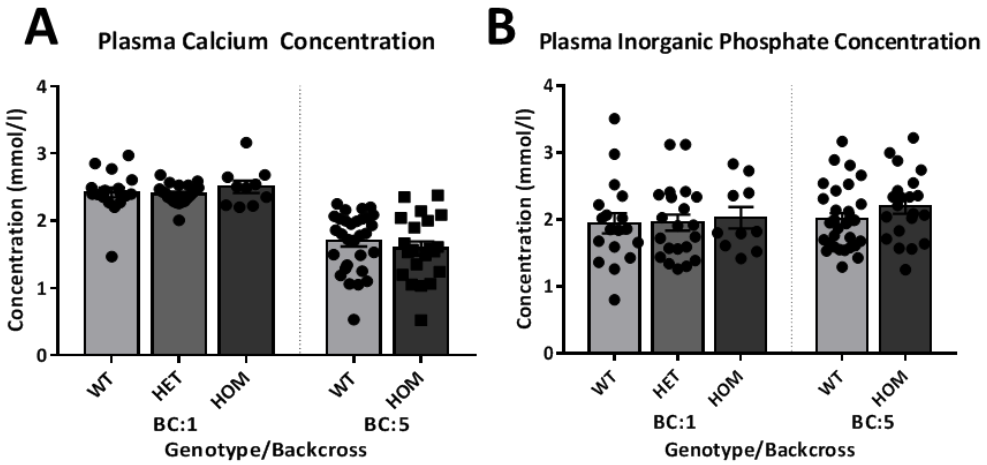

Figure 3.9. Plasma concentrations of the minerals calcium (A) and inorganic phosphate (B) in backcross 1 and 5 animals. Results show no significant differences in either mineral between any of the groups compared. Mean ± SEM.

The lipids, cholesterol, high density lipoprotein (HDL) and low density lipoprotein (LDL) are primarily synthesised as part of cell membranes and for the transport of fat between cells. Elevated levels of cholesterol and LDL are significant risk factors for atherosclerosis whilst HDL is considered protective. Whilst results (Figure 3.10) show no significant differences in total cholesterol levels, HDL levels in *Ecsit*$^{N209I/N209I}$ animals appears significantly decreased when compared to control animals. Crucially, this is coupled with an elevation of LDL in *Ecsit*$^{N209I/N209I}$ animals compared to wild types in the incipient congenic line. However, it is apparent from figure 3.10 that whilst the averages of these compounds differ, there is significant overlap between the ranges seen in wild type and *Ecsit*$^{N209I/N209I}$ animals.

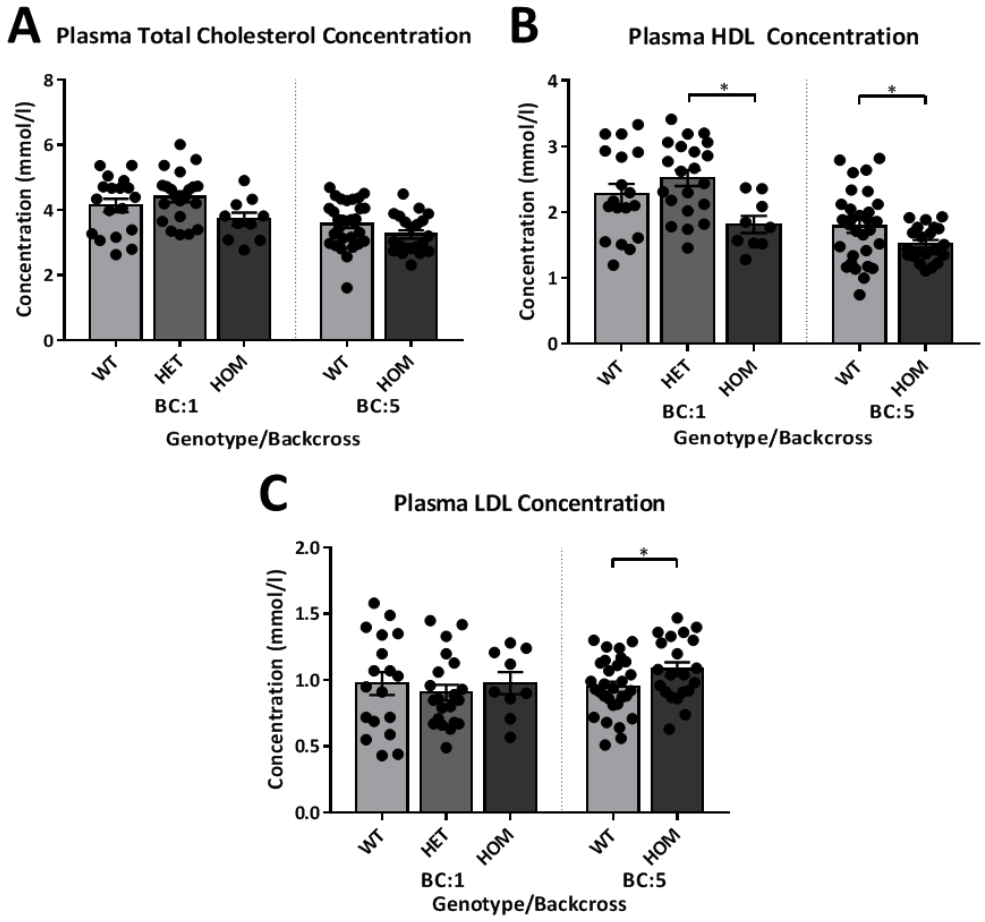

Figure 3.10. Plasma concentrations of the lipids, cholesterol (A) high-density lipoprotein (HDL) (B) and low-density lipoprotein (C) in backcross 1 and 5 animals. Results show no changes in total cholesterol levels in any of the groups compared, however, HDL levels are marginally reduced in *Ecsit*$^{N209I/N209I}$ animals in both backcross when compared to controls. Also of interest is the marginal elevation of LDL in *Ecsit*$^{N209I/N209I}$ in the incipient congenic backcross animals when compared to wild types. Mean ± SEM, *p<0.05.

Circulating triglycerides are a high energy density molecule that is broken down via lipolysis into glycerol and free fatty acids (FFA) which are then metabolised as part of glycolysis, gluconeogenesis or beta-oxidation to provide substrates for the TCA cycle. Ketone bodies are produced by the liver from free fatty acids during periods of fasting to provide the body with a substrate which can be converted into acetyl-CoA and enter the TCA cycle.

There were no significant differences (Figure 3.11) between genotypes in the backcross 1 animals. However, in the incipient congenic line, *Ecsit*$^{N209I/N209I}$ animals show a significant reduction in circulating triglycerides, and an elevation of both glycerol and

ketone bodies when compared to wild type animals. Taken together these data suggest an increase in metabolism of triglycerides in the liver to form substrates for the TCA cycle, similar to what is seen during periods of fasting [283].

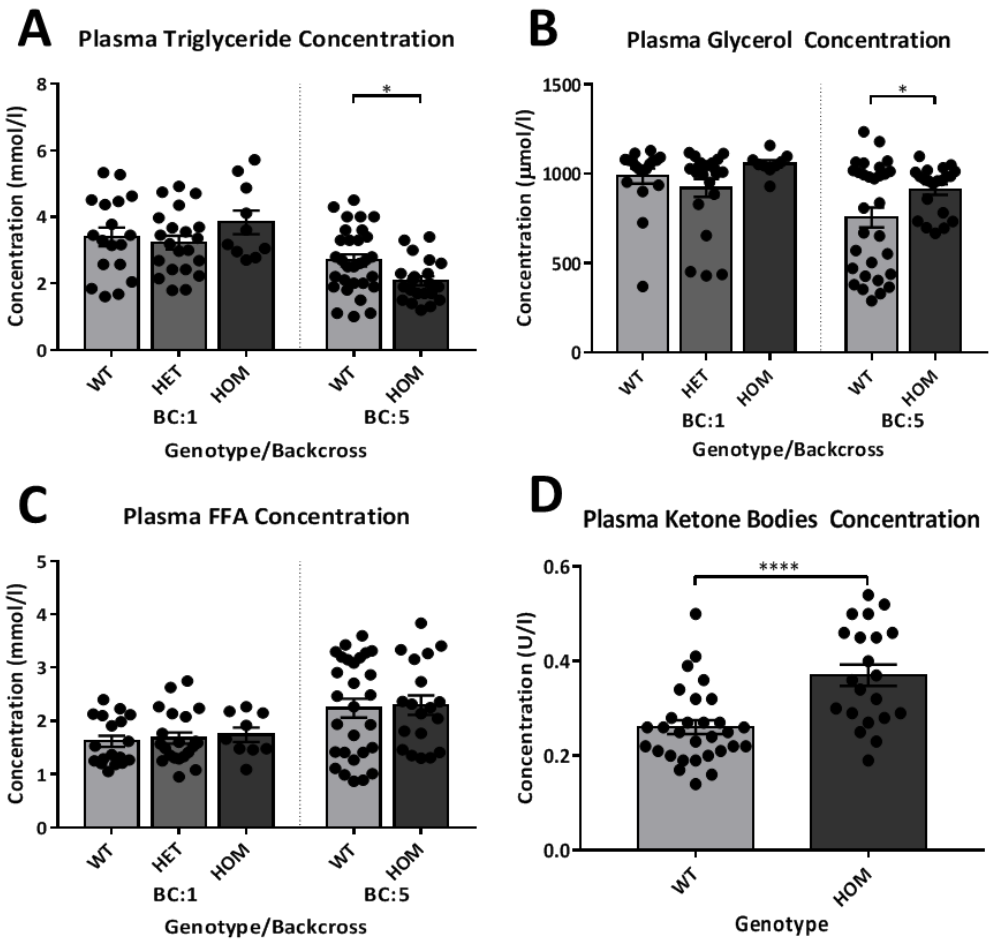

Figure 3.11. Plasma concentrations of the fatty acid metabolism products, triglyceride (A), glycerol (B) and free fatty acids (FFA) (C) in backcross 1 and 5 animals. Ketone bodies (D) were only tested in the incipient congenic backcross and not in the earlier backcross. Results show no differences in any of the metabolites between genotypes in the backcross 1 animals. However, in the incipient congenic animals there is a marginal decrease in total triglyceride levels and a similarly marginal elevation of glycerol in *Ecsit*$^{N209I/N209I}$ animals compared to wild types. Ketone bodies also show a significant elevation in *Ecsit*$^{N209I/N209I}$ animals compared to wild types. Mean ± SEM, *p<0.05.

Glucose and fructosamine are typically elevated in plasma in diabetes mellitus as the glucose is unable to be taken into tissues and subsequently reacts with an amine group to form fructosamine resulting in elevated levels of this compound too. Results here (Figure 3.12) demonstrate a reduction in plasma glucose levels and a corresponding reduction in fructosamine in *Ecsit*$^{N209I/N209I}$ animals in the incipient congenic backcross

animals. This may indicate an increased metabolism of glucose which in turn results in a reduction in fructosamine levels however, these results are taken from non-fasted animals and these results may not be representative of real differences between genotypes.

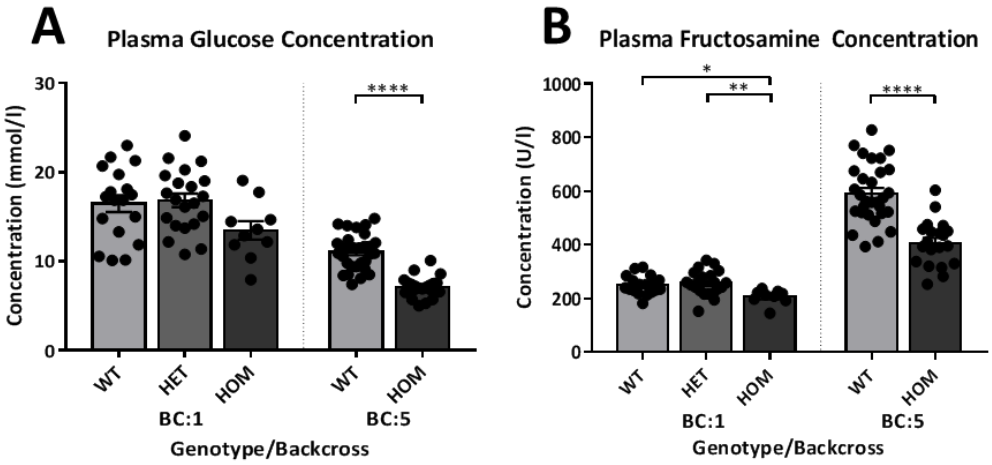

Figure 3.12. Plasma concentrations of the diabetic markers glucose (A) and fructosamine (B) in backcross 1 and 5 animals. Glucose levels show a significant reduction in *Ecsit*$^{N209I/N209I}$ animals compared to wild types in the incipient congenic line, whilst the back-cross 1 animals show a marginal decrease which does not reach a significant level. Meanwhile, fructosamine levels are significantly reduced in *Ecsit*$^{N209I/N209I}$ animals compared to controls in both backcross groups. Mean ± SEM, *p<0.05, **p<0.01, ****p<0.0001.

Lactate dehydrogenase and creatine kinase are enzymes which are typically contained within cells and their presence in plasma can be indicative of tissue damage. Cytosolic creatine kinase is comprised of two different subunits, B – Brain and M – Muscle, and there are 3 possible isoforms as a result, MM, BB and MB, each with varying proportions in different tissues. In humans CK-MM is the majority cytosolic form in skeletal muscle (97%), CK-BB is the predominant form found in brain, colon, stomach and bladder, whilst CK-MB is relatively uncommon in most tissues (2-3% of skeletal muscle) but is found in considerable amounts in heart tissue (15-40%) along with CK-MM. Following cardiac injury, serum levels of total and CK-MB are known to rise peaking roughly 24 hours after injury and returning to baseline after about 72 hours in humans [284]. In contrast, the mouse heart has very low levels of CK-MB and the predominant form is CK-MM, accounting for roughly 90-95% of cytosolic CK activity, with CK-MB only contributing roughly 5% to total cytosolic CK activity [285].

Results illustrated here (Figure 3.13) show no significant changes in CK levels between wild type and *Ecsit*$^{N209I/N209I}$ animals. However, this test does not distinguish between the CK isoenzymes and only measures total CK levels, however, had a difference been apparent, further investigation would have been relatively simple with the use of an ELISA.

Lactate dehydrogenase catalyses the conversion of lactate to pyruvic acid and is a tetramer primarily composed of different subunits LDH-M and LDH-H. Through varying the proportions of the 2 subunits in the tetramer there are 5 main isoenzymes that are present in different tissues (LDH-1 (4H), 2 (3H1M), 3 (2H2M), 4 (1H3M), and 5 (4M)). Under typical conditions LDH-2 is the form found in plasma, however following cardiac damage LDH-1 levels may become elevated in the plasma and result in a shift in the ratio of LDH-1:LDH-2 [286]. From the results illustrated here (Figure 3.13) it is apparent that there are no significant changes in total LDH levels and no further investigation was undertaken.

As neither of these enzymes show elevation at the total enzyme level it was therefore unnecessary to investigate the ratios of the two to determine if there is significant tissue damage. Further investigation could have been undertaken using cardiac troponin levels as a more accurate test of myocardial infarction [287] but given that these samples were taken from animals prior to any signs of ill-health, this is unlikely to be informative.

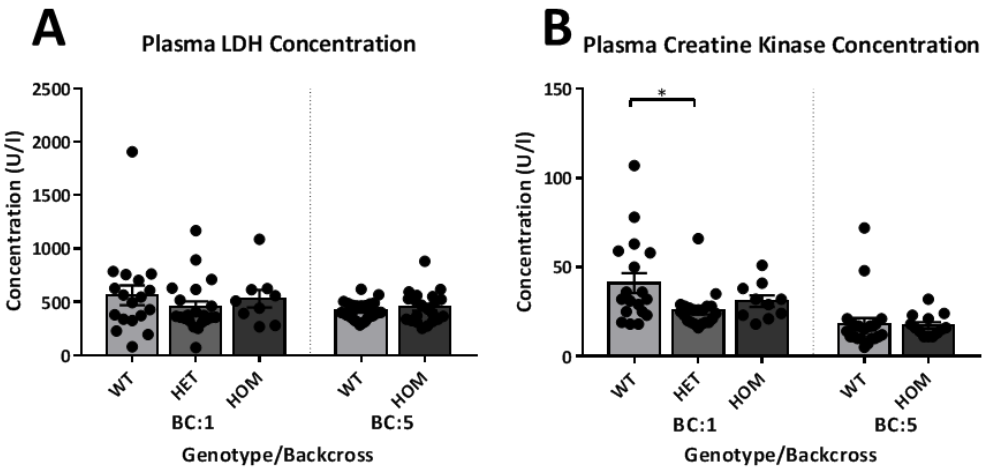

Figure 3.13. Plasma concentrations of the tissue damage markers lactate dehydrogenase (LDH) (A) and creatine kinase (B) in backcross 1 and 5 animals. Neither compound shows a significant difference between wild type and *Ecsit*$^{N209I/N209I}$ animals in either of the backcrosses tested. Mean ± SEM, *p<0.05.

Finally, iron is a major constituent of heme and differences in iron levels may indicate blood disorders or a nutritional deficiency. Results (Figure 3.14) show no differences in iron concentration in the plasma of any animals tested.

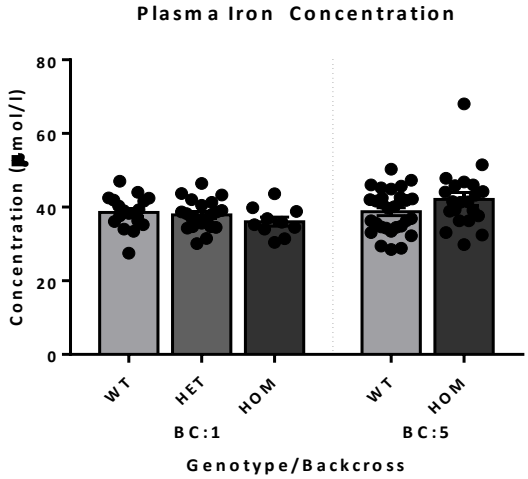

Figure 3.14. Plasma concentrations of iron in backcross 1 and 5 animals showing no difference between any of the genotypes in either backcross tested. Mean ± SEM.

Individually these clinical chemistry results do not appear to reflect any major changes in organ function or general metabolism, with many differences being either small or falling within the expected ranges established for wild type animals. However, when considered together these results demonstrate an impairment of kidney as well as liver, although to lesser extent. In addition results seem to demonstrate an increase in the metabolism of both glucose and triglycerides which may reflect a change in the general metabolic phenotype of *Ecsit*$^{N209I/N209I}$ animals.

3.8.2. Body weight

Body weight was measured every 2 weeks from 6 weeks of age up until 16 weeks of age. Males and females were separated for the purpose of analysis due to sex differences in the wild type controls. From the results it is apparent that *Ecsit*$^{N209I/N209I}$ animals display a reduced body weight from as early as 6 weeks of age, and whilst they do show a small increase in body weight over time, this is mostly accounted for by growth up to the age of 10 weeks which then plateaus (Figure 3.15). The slope of the curve, representing the growth curve from 6 to 16 weeks of age, is significantly different (simple linear regression) between wild type and *Ecsit*$^{N209I/N209I}$ animals in both males ($p=0.0026$) and females ($p=0.04$).

Despite the differences in overall body weight, measurements of the femur (Figure 3.16) show no significant differences between wild types (n=23) and mutants (n=24). This indicates that despite differences in body weight, the growth of the mutant animals is not stunted and is attributable to lean and fat mass accumulation rather than overall reduced body size.

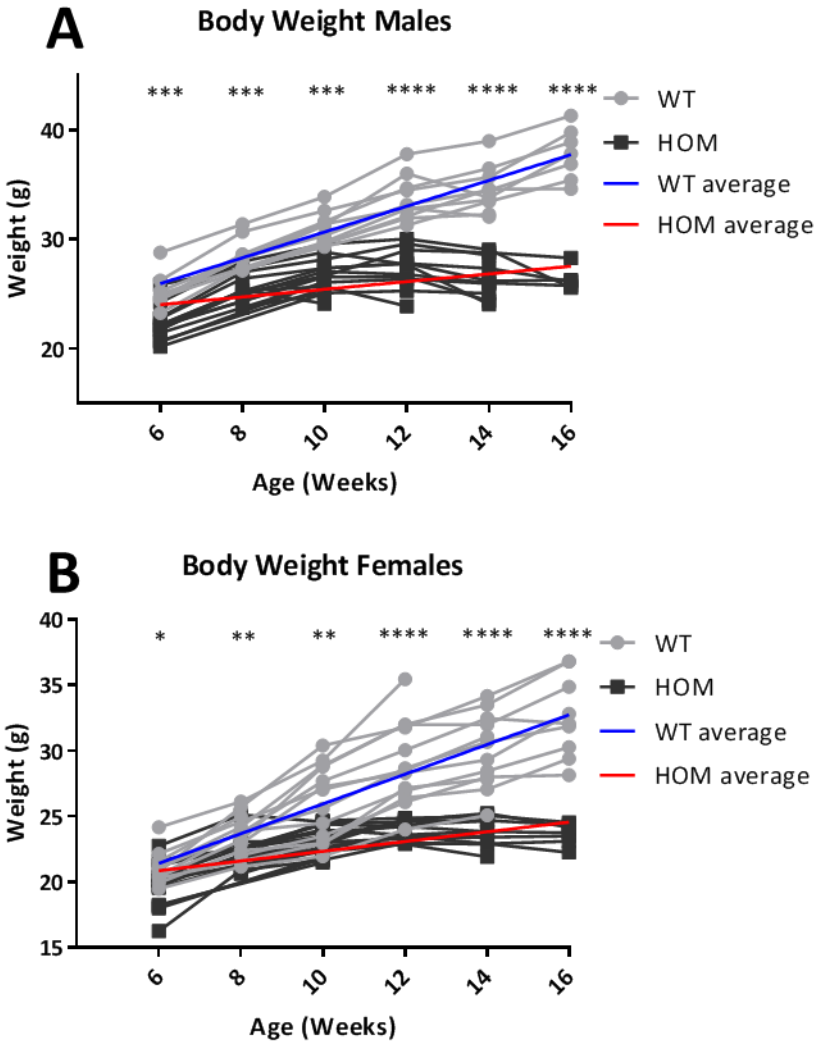

Figure 3.15. Weight against time of male and female wild type and *Ecsit*$^{N209I/N209I}$ animals. Results show a significant difference between genotypes from 6 weeks of age with the rate of growth of mutant animals (simple linear regression) significantly reduced compared to wild types. Each time point was also tested for significance with a standard t-test, demonstrating that differences in weights are apparent from 6 weeks of age. *p<0.05, **p<0.01, ***p<0.001, ****p<0.0001.

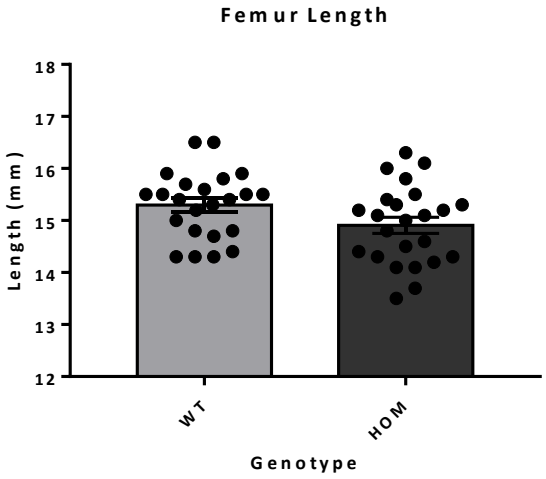

Figure 3.16. Length of femurs (mm) measured from wild type and *Ecsit*$^{N209I/N209I}$ animals. (Mean ± SEM).

3.8.3. Body Composition

To determine the fat and lean mass composition of wild type and *Ecsit*$^{N209I/N209I}$ animals Echo-MRI was performed. Echo-MRI is a simplified form of nuclear magnetic resonance imaging (MRI) that gives only a composition analysis instead of the images typically associated with the technique. Echo-MRI performed on wild type and *Ecsit*$^{N209I/N209I}$ animals demonstrates significant differences in total body weight, lean mass and fat mass (both absolute and expressed as a % of total body weight). *Ecsit*$^{N209I/N209I}$ animals show a reduction in body weight, fat mass and lean mass when compared to sex and age matched wild type animals. Sexes were separated as differences were seen between *wild type* males and females across all time points (graph not shown), n numbers shown in table 3.5. The results show that mutant animals do not increase in overall body mass (Figure 3.17) from 8 weeks of age primarily due to a lack of accumulation of fat mass (Figure 3.18) and lean mass (Figure 3.19) in both sexes.

At 8 weeks of age, wild type and *Ecsit*$^{N209I/N209I}$ animals are statistically indistinguishable from their sex matched counterparts in terms of all 3 parameters measured, indicating normal growth up to this point. However, after 8 weeks of age, differences begin to emerge. By 10 weeks, males have measurably less fat mass than wild type animals (Figure 3.18) and females overall body mass is statistically different from that of wild types (Figure 3.17). At 14 weeks, greater differences are apparent in body weight in both sexes in terms of both body weight (Figure 3.17) fat mass (Figure 3.18). Finally, at 18

weeks differences can be seen in fat, lean and total mass in both sexes when comparing to wild type controls.

Time Point	Male WT	Female WT	Male *Ecsit*$^{N209I/N209I}$	Female *Ecsit*$^{N209I/N209I}$
8 Weeks	9	8	12	12
10 Weeks	6	10	4	7
14 Weeks	6	10	3	5
18 Weeks	7	6	3	6

Table 3.5. n Numbers for each time point and genotype used in Echo-MRI experiment.

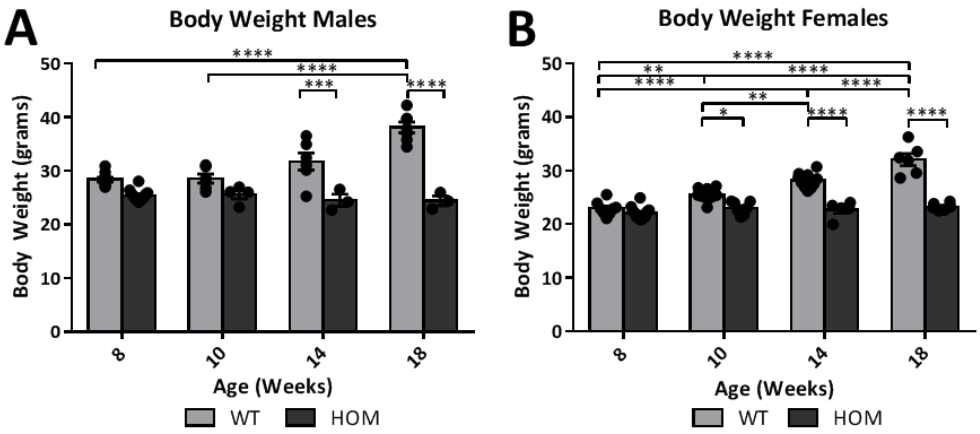

Figure 3.17. Body weight of wild type and *Ecsit*$^{N209I/N209I}$ animals demonstrates that whilst wild types increase in size between 8 and 18 weeks of age, mutant (male or female) animals do not grow in terms of absolute body mass beyond 8 weeks of age when compared to *wild type* controls. Mean ± SEM,*p<0.05, **p<0.01, ***p<0.001, ****p<0.0001. Any comparison not labelled should be considered non-significant (ns).

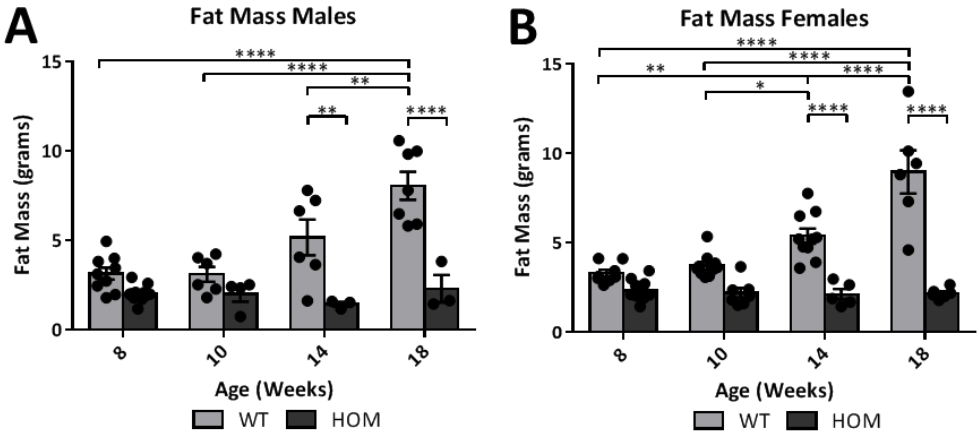

Figure 3.18. Absolute fat mass measurements show that both male (A) and female (B) wild type animals continue to accumulate fat mass beyond 8 weeks of age whilst *Ecsit*$^{N209I/N209I}$ animals do not. This becomes more apparent as the animals age (Mean ± SEM, *p<0.05, **p<0.01, ***p<0.001, ****p<0.0001). Any comparison not labelled should be considered non-significant (ns).

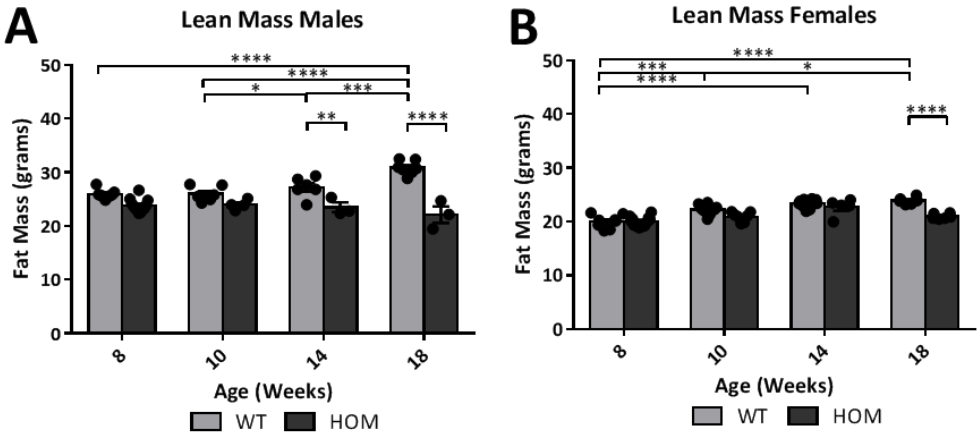

Figure 3.19. Absolute lean mass measurements show that both male (A) and female (B) wild type animals continue to accumulate lean mass beyond 8 weeks of age whilst *Ecsit*$^{N209I/N209I}$ animals do not. By 14 weeks of age this difference is apparent in male animals and at 18 weeks of age both sexes show a significant reduction in lean mass compared to sex matched wild type controls. (Mean ± SEM, *p<0.05, **p<0.01, ***p<0.001, ****p<0.0001). Any comparison not labelled should be considered non-significant (ns).

3.8.4. Grip Strength

Grip strength was assessed in 14 week old male (WT:10, HOM: 8) and female (WT:9, HOM:13) animals to determine if a muscular phenotype was associated with the cardiomyopathy phenotype seen in *Ecsit*$^{N209I/N209I}$ animals. This might be expected with a systemic myopathy as is common with complex I disorders and might be associated with a mutation in an assembly factor such as ECSIT. Male and female results were not separated as no significant differences were present between sexes. Grip strength results can be demonstrated as raw values, or expressed as a value normalised to the animal's body weight. Below (Figure 3.20), the absolute values show no difference in grip strength between wild type (n=19) and *Ecsit*$^{N209I/N209I}$ (n=21) animals either in the fore paws only or in all 4 paws. However, when the data is normalised to body weight (Figure 3.21) the mutant animals demonstrate an increased grip strength of both the fore paws and all 4 paws. This is most likely due to the decreased body weight of the mutant animals as is seen in section '3.8.2 – Body Weight' and '3.8.3 – Body Composition'.

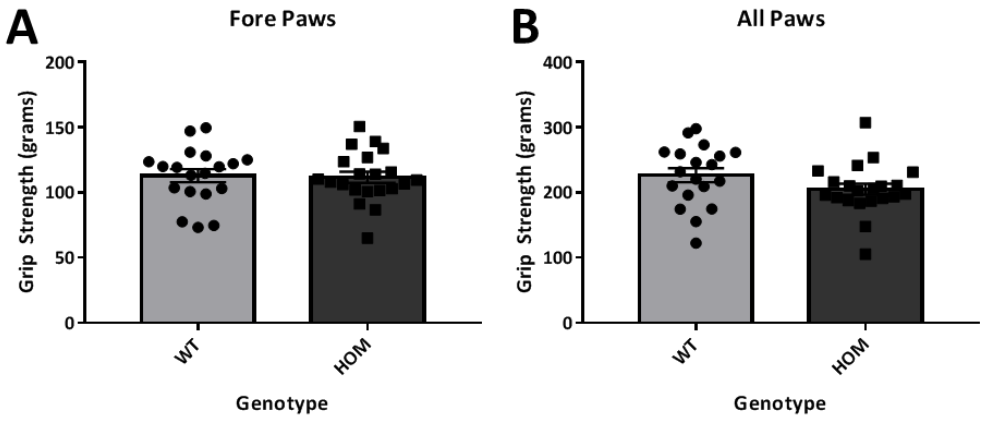

Figure 3.20. Absolute grip strength measurements of fore paws (A) and all paws (B) showing no differences between wild type and *Ecsit*$^{N209I/N209I}$ animals. (Mean ± SEM).

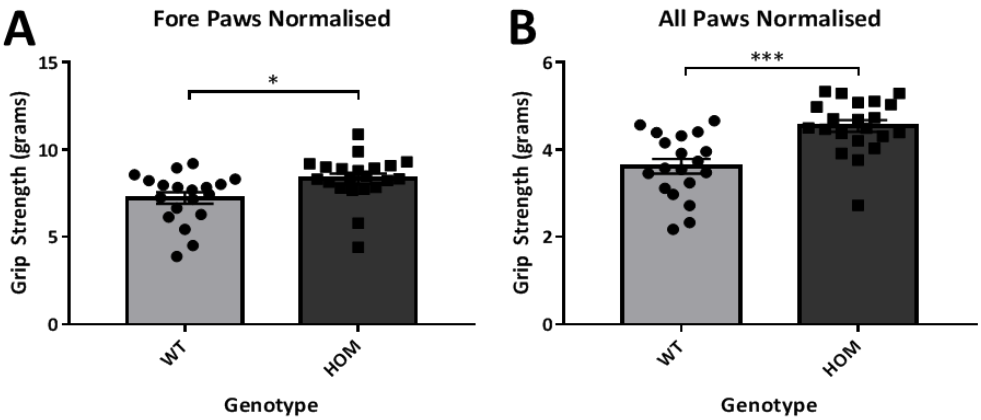

Figure 3.21. When normalised to body weight, grip strength results show a significant increase in both the fore (A) and all paw (B) measurements in *Ecsit*$^{N209I/N209I}$ animals over wild type controls. (Mean ± SEM, *<0.05, ***p<0.001).

3.8.5. IPGTT

An intraperitoneal glucose tolerance test (IPGTT) measures the ability to take up glucose into tissues following a glucose challenge. It reflects the ability to both sense glucose, secrete insulin and to respond to insulin in key insulin sensitive tissues. In type 2 diabetes there will be insulin resistance and defects in insulin secretion. Impaired glucose tolerance typically precedes the development of a diabetic phenotype.

An inability to effectively regulate glucose levels is typically indicative of a diabetic phenotype which may be related to mitochondrial dysfunction in certain tissues (heart, muscle and liver) [288]. Results from wild type and *Ecsit*$^{N209I/N209I}$ male (WT:10, HOM:10) and female (WT:8, HOM:10) animals reveals a small but significant difference in blood glucose levels 60 minutes post injection. This difference takes the form of a decrease in plasma glucose levels rather than the increase that would be expected in a diabetic phenotype. Male and female results were not separated as no significant differences were seen between sexes. This difference does not persist across all time points (Figure 3.22) suggesting that the affected animals demonstrate no long term benefits to glucose metabolism and are unlikely to have a real primary phenotype as a result of the N209I mutation. These data reflect a minor change in the ability to dispose of glucose but are unlikely to significantly affect the maintenance of normal glucose homeostasis.

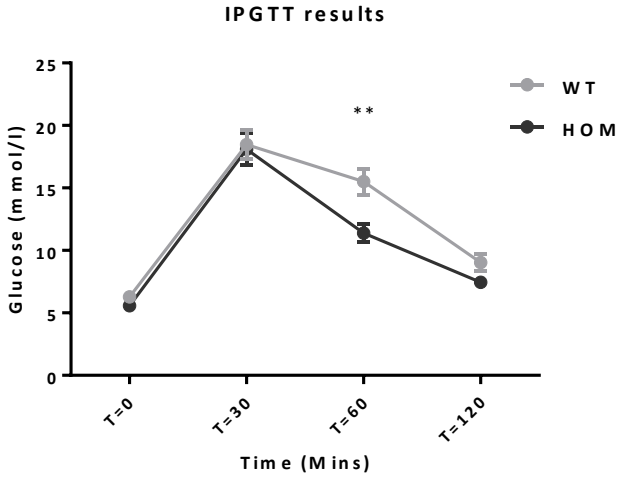

Figure 3.22. IPGTT results from wild type (n=18) and *Ecsit*$^{N209I/N209I}$ (n=18) animals. (Mean ± SEM, **p<0.01).

3.8.6. Tissue Weights

Tissue weights were assessed at the time of death (16 weeks) to assess the cardiomyopathy phenotype and which other tissues may be affected as a result of congestion of the left or right heart. Male (WT:10, HOM:10) and female (WT:12, HOM:14) samples were not separated as no difference in sexes was observed. Heart, lung and liver weights can be analysed as absolute values or normalised to the animal size either as a % of total body weight or by normalising to the length of the long bones, such as the femur. Below the weights of these tissues are expressed in all three ways. These three tissues were selected to assess the hypertrophy of the heart. Left ventricular hypertrophy would lead to increased lung weight due to congestion of the pulmonary circulation. Similarly, an increase in liver size would indicate right ventricular hypertrophy due to congestion of the systemic circulation.

Heart weights show a significant increase in *Ecsit*$^{N209I/N209I}$ (n=24) animals over wild type controls (n=22) in terms of absolute values (Figure 3.23) as well as both types of normalisation used (Figures 3.24 and 3.25), indicating a robust enlargement of the heart muscle that is not affected by animal size or weight. Similarly, lung weights demonstrate the same trend across the board, suggesting that the left ventricle is hypertrophied and causing congestion in the pulmonary circulation. In contrast, liver weights do not show an increase across any of the three categories. Absolute liver weights (Figure 3.23) are decreased in *Ecsit*$^{N209I/N209I}$ animals compared to controls, and the same holds true when normalised to femur length (Figure 3.25). However, when liver weight is normalised according to the animal's overall bodyweight (Figure 3.24) there are no significant differences in tissue weights between the genotypes. In summary these data demonstrate that there is no increase in liver weight and it is possible to speculate that there is little to no hypertrophy of the right ventricle.

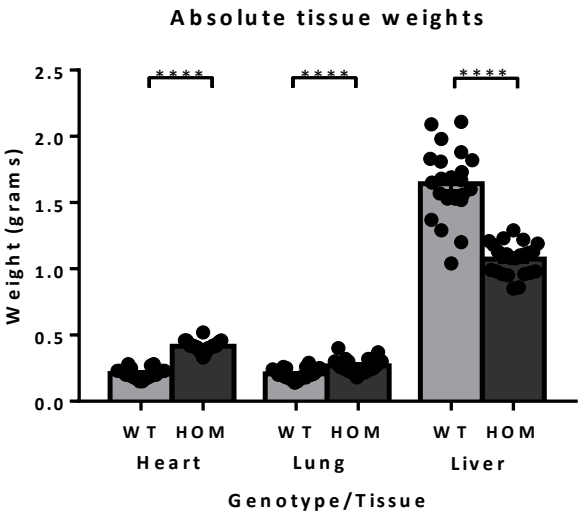

Figure 3.23. Absolute values for all tissue weights, showing an increase in heart weight and lung weight and a decrease in liver weight of *Ecsit*$^{N209I/N209I}$ animals compared to healthy wild type controls. (Mean ± SEM, ***p<0.001, ****p<0.0001)

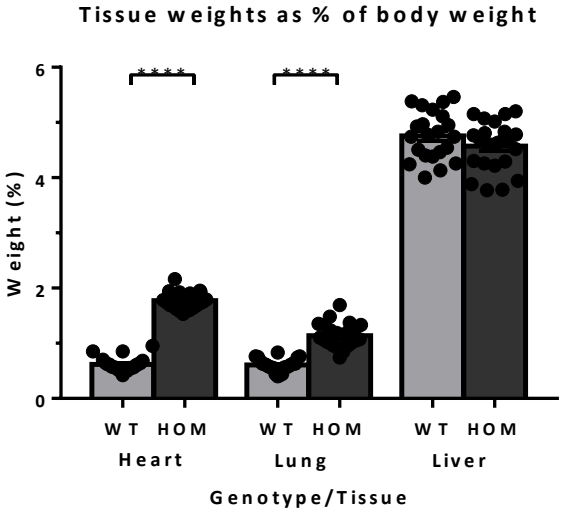

Figure 3.24. Tissue weights normalised to total body weight of the animal. Heart and lung weights still demonstrate a significant elevation in *Ecsit*$^{N209I/N209I}$ animals over wild type. Whilst liver does not show any significant difference. (Mean ± SEM, ****p<0.0001)

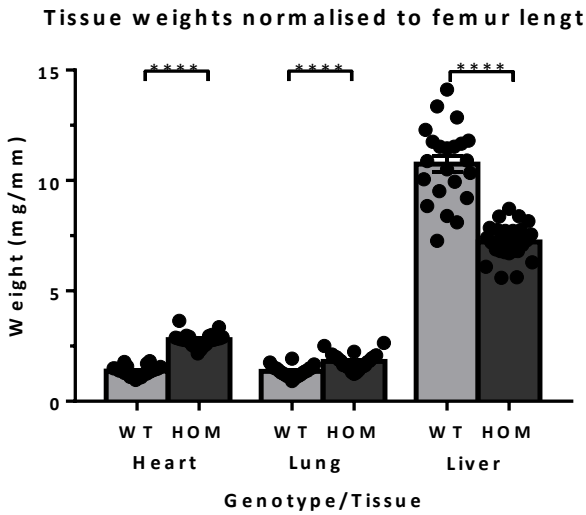

Figure 3.25. Tissue weights normalised to femur length, expressed as mg of tissue weight per mm length of femur. Similarly to the un-normalised tissue weights in figure 3.23 heart and lung weights reveal a significant increase in *Ecsit*$^{N209I/N209I}$ animals compared to wild type controls, whilst liver weights show the reverse trend. (Mean ± SEM, ****p<0.0001).

3.8.7. Histology Time Course

Hearts were taken from 3 wild type and 3 *Ecsit*$^{N209I/N209I}$ animals (2 sections per animal) at various time points to assess the development of the cardiomyopathy. No preferences were made for sex of the animals as this was unreliable at very early time points. *Ecsit*$^{N209I/N209I}$ hearts show signs of cardiomyopathy from as early as 6 weeks of age (Figure 3.26), with the development of mineralisation (yellow arrows Figure 3.27) which progresses over time to become apparent at 12 weeks of age. Vacuolation is apparent in some areas of the heart at 6 weeks of age (black arrows Figure 3.27) and progresses so that the majority of 12 week old heart tissue shows signs of severe vacuolation. Also present, but difficult to quantify, is cardiomyocyte hypertrophy and disorganisation. In wild type hearts (Figure 3.27) cardiomyocytes can be seen in well organised striated patterns. At 6 weeks of age *Ecsit*$^{N209I/N209I}$ hearts show regions where cardiomyocytes appear to be marginally enlarged and no longer form this organised structure. At 12 weeks, *Ecsit*$^{N209I/N209I}$ cardiomyocytes no longer show any signs of structure and appear completely disorganised.

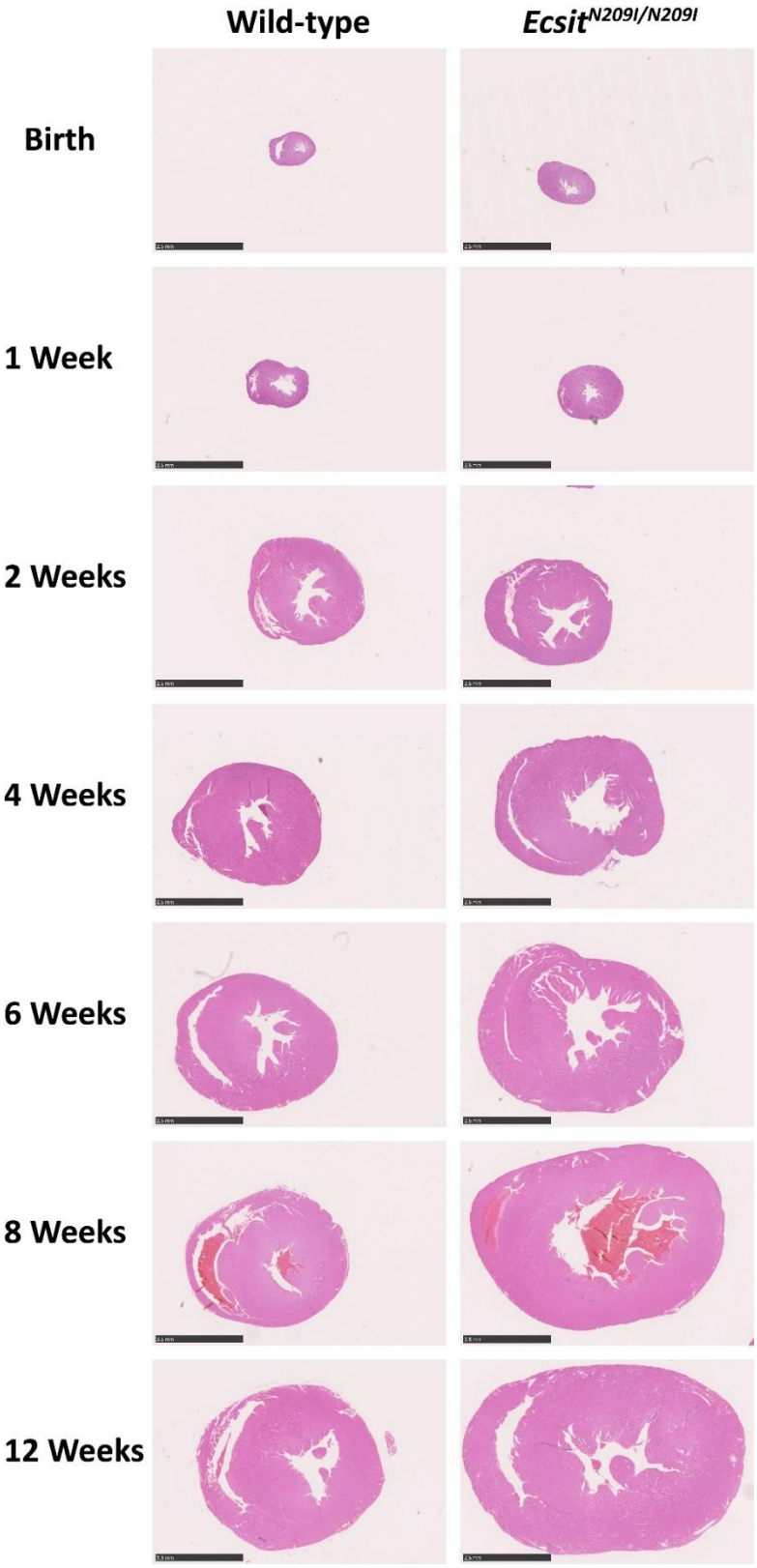

Figure 3.26. Time course of histology (1.25x) on wild type and *Ecsit*$^{N209I/N209I}$ hearts showing development of cardiomyopathy in mutant animals. Enlargement of *Ecsit*$^{N209I/N209I}$ hearts is first apparent around 6 weeks of age and progresses up to 12 weeks of age where a significant enlargement is apparent. Scale bar = 2.5mm.

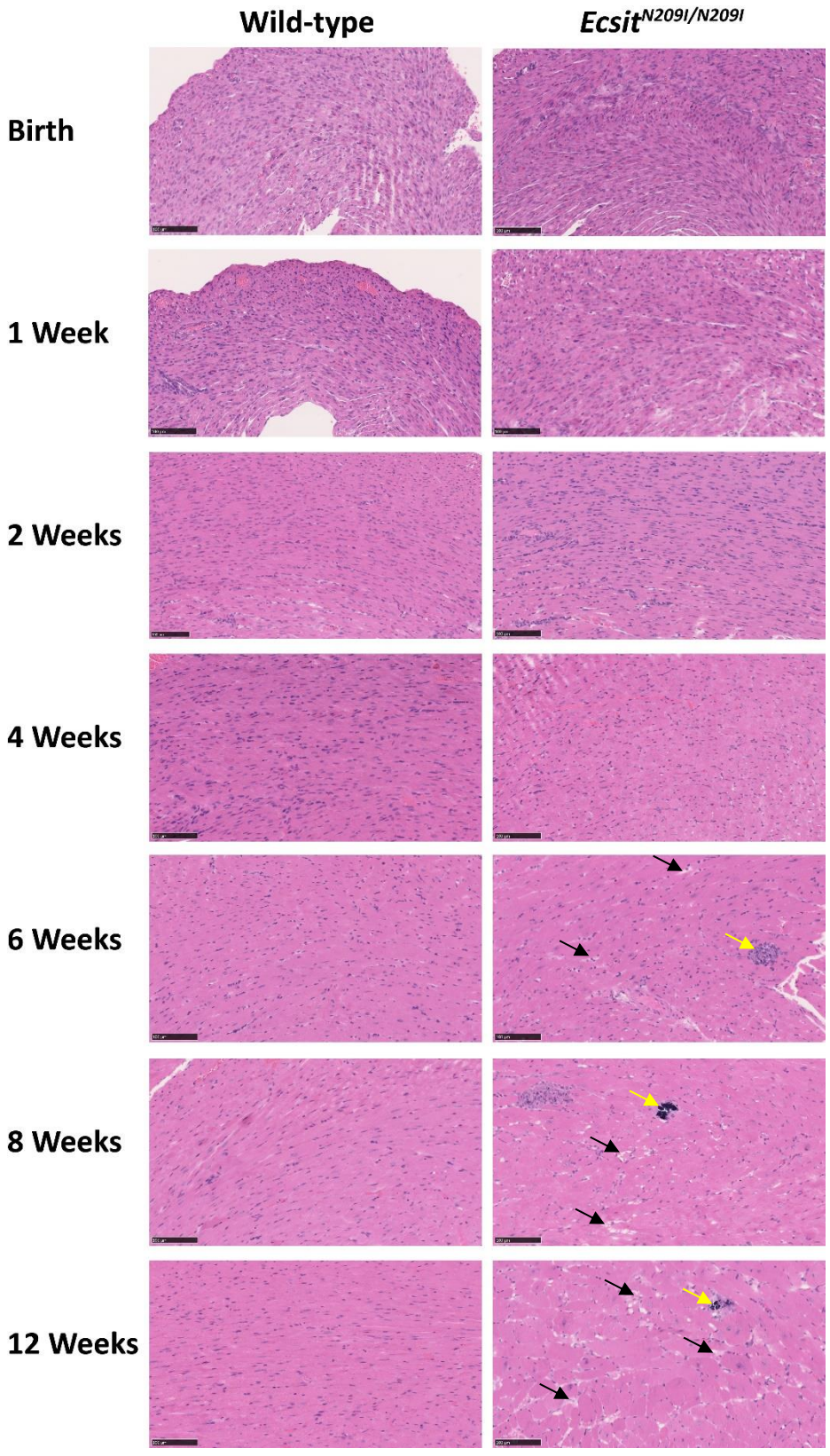

Figure 3.27. Histology time course at 20x magnification demonstrating structure of the cardiac tissue and showing vacuolation (black arrows) and mineralisation of tissue (yellow arrows) in *Ecsit*$^{N209I/N209I}$ hearts from 4-6 weeks of age which is not seen in wild type controls. Also present are signs of cardiomyocyte hypertrophy and disorganisation from 4 weeks of age. Scale bar= 100µm.

3.8.8. Echocardiography

Echocardiography, performed on incipient congenic backcross mice at 10 weeks of age shows significant differences in heart size and contractility (Male WT:7, HOM:9, Female WT:6, HOM:9). During diastole both the anterior and posterior left ventricular walls show a significant increase in thickness in *Ecsit*$^{N209I/N209I}$ animals compared to wild type (Figure 3.28). This is also reflected in the left ventricular interior diameter (Figure 3.29) which shows a significant increase in *Ecsit*$^{N209I/N209I}$ animals during both diastole and systole. During systole the posterior wall no longer shows a significant increase in thickness in *Ecsit*$^{N209I/N209I}$ animals, whilst the anterior wall remains significantly enlarged (Figure 3.28).

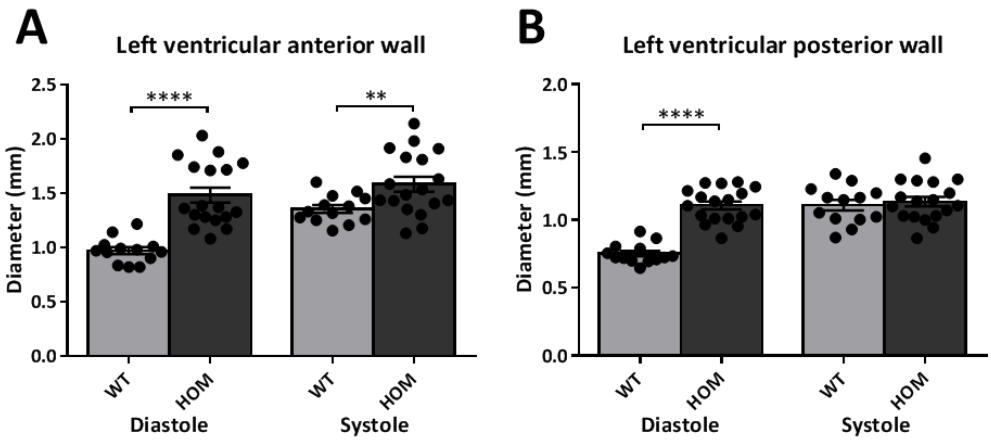

Figure 3.28. Echocardiographic measurements of the left ventricular anterior (A) and posterior (B) walls during diastole and systole showing a significant increase in anterior wall thickness during both systole and diastole and a significant thickening of the posterior wall during diastole which is unchanged during systole. (Mean ± SEM, **p<0.01, ****p<0.0001).

Left ventricular volume and mass show a significant increase in *Ecsit*$^{N209I/N209I}$ animals during both systole and diastole (Figure 3.29) indicating an enlargement of not only the muscle mass but also a dilation of the heart cavity. The ejection fraction in *Ecsit*$^{N209I/N209I}$ animals is significantly reduced, demonstrating a reduction in the contractility of the heart muscle (Figure 3.30). Heart rate taken during the echocardiograph measurements (Figure 3.30) shows a reduction in average beats per minute (BPM) in *Ecsit*$^{N209I/N209I}$ animals, which was not seen earlier in the ECG measurements. Heart rate is coupled with stroke volume (end diastolic volume – end systolic volume) (Figure 3.30) to allow for the calculation of cardiac output (stroke volume x heart rate) (Figure 3.30), giving an

overall impression of the function of the heart in *Ecsit*$^{N209I/N209I}$ animals. Taken together these data indicate a profound cardiomyopathy with characteristics that may be attributed to both dilated and hypertrophic cardiomyopathy.

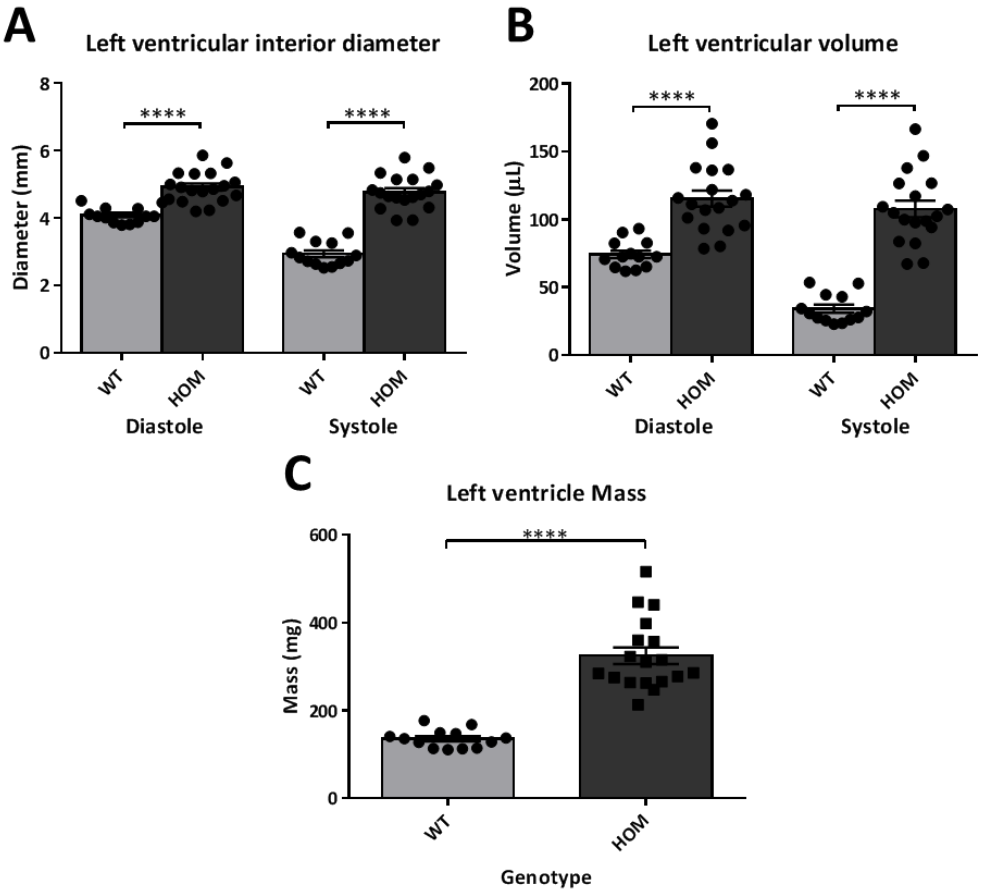

Figure 3.29. Left ventricular interior diameter (A) measured by echocardiograph and volume (B) calculated from changes in diameter, both showing an enlargement of the left ventricle in *Ecsit*$^{N209I/N209I}$ animals during both diastole and systole, suggestive of a dilated cardiomyopathy. Calculated left ventricular mass (C) indicates an overall enlargement of the left ventricle. (Mean ± SEM, ****p<0.0001).

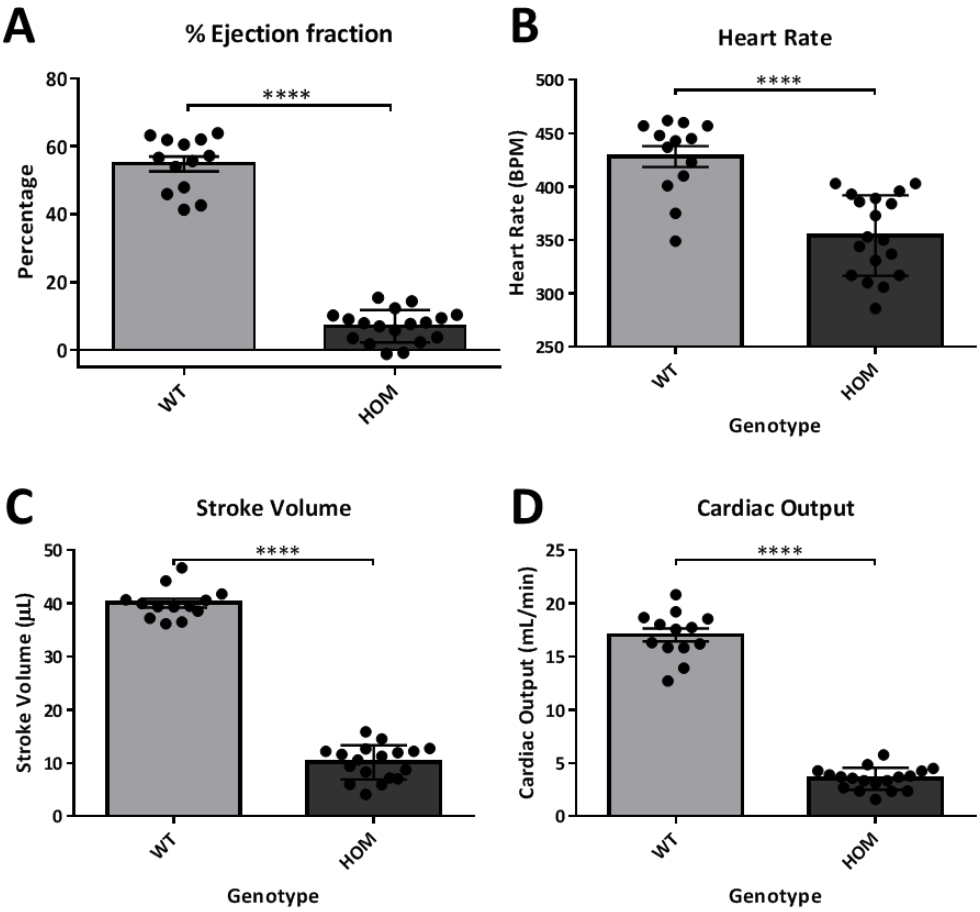

Figure 3.30. Ejection fraction (A) demonstrates a significant reduction in Ecsit$^{N209I/N209II}$ animals compared to wild types. Heart rate (B) measured during echocardiography readings can be coupled with the calculated stroke volume (C) to give an overall cardiac output (D). (Mean ± SEM, ****p<0.0001).

3.8.9. Cardiac Electrophysiology

Electrocardiogram (ECG) was performed on 12 week old wild type (M:6, F:5), *Ecsit*$^{N209I/+}$ (M:9, F:3) and *Ecsit*$^{N209I/N209I}$ (M:5, F: 5) animals from an early cohort prior to backcrossing to C3H.Pde6b+ for 5 generations to obtain the incipient congenic line. Results were obtained by signal averaging across the length of the trace obtained. No significant differences were detected in any of the parameters measured (Figure 3.31) showing that the N209I mutation has no effect on signal transduction through the cardiac tissue. This result is unsurprising as the cardiomyopathy would not necessarily be reflected by changes in the conductive tissue of the heart and hence in ECG abnormalities. Given this result, further phenotyping was not performed on later backcrosses so as to reduce the strain on animals under anaesthesia.

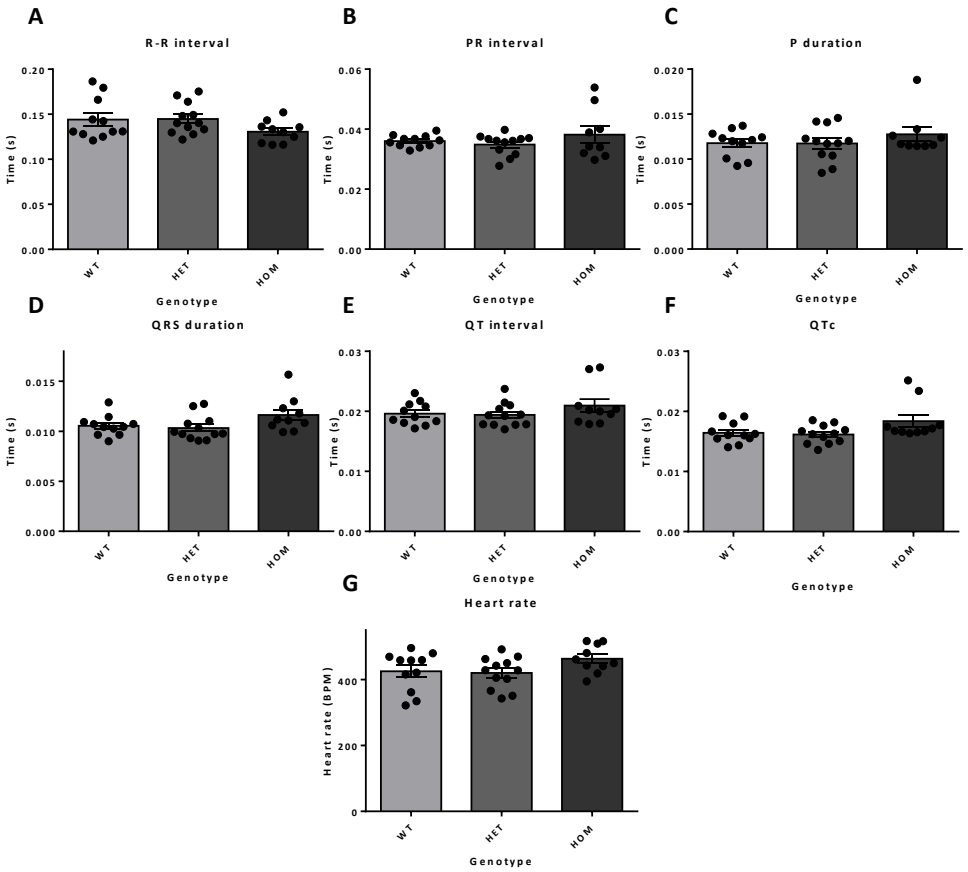

Figure 3.31. ECG parameters measured in 12 week old wild type (n=11), *Ecsit*$^{N209I/+}$ (n=12) and *Ecsit*$^{N209I/N209I}$ (n=10) animals. Results show no significant differences in R-R interval (A), PR interval (B), P duration (C), QRS duration (D), QT interval (E), corrected QT interval (QTc) (F) or heart rate (G). (Mean ± SEM).

3.8.10. Muscle Fibre Typing

Muscle fibre typing was performed on soleus and extensor digitorum longus (EDL) muscles isolated from 3 wild type and 3 *Ecsit*$^{N209I/N209I}$ male animals by Saleh Salman Omairi at the University of Reading. Fibres were classified as either oxidative or non-oxidative according to profiling of succinate dehydrogenase (SDH) and were classified according to myosin heavy chain (MHC) proportions of MHC I, MHCIIA, MHC IIX, and MHC IIB. Results show no differences in the proportion of oxidative to non-oxidative fibres in either the EDL or the soleus (Figure 3.33) indicating that the mutation of ECSIT does not affect the metabolic profile of these muscles.

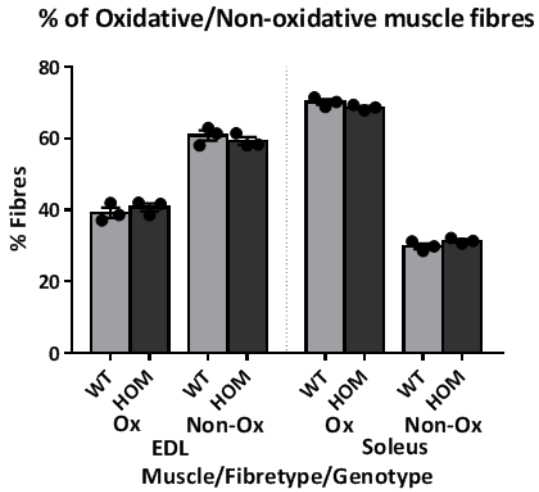

Figure 3.32. Percent oxidative and non-oxidative fibres in (EDL) and soleus muscles from wild type and *Ecsit*$^{N209I/N209I}$ animals. Results show no significant differences between genotypes in either of the muscles investigated. Mean ± SEM.

Following MHC profiling, muscle fibres were counted and cross sectional area measured in both the EDL and the soleus. From these data (Figure 3.33) we can see that there are no significant differences in the MHC ratio in either muscle. Soleus is primarily a slow twitch muscle type with a predominance of MHC I and IIA fibres, this is unchanged in *Ecsit*$^{N209I/N209I}$ animals when compared to wild types (Figure 3.33). EDL is a faster twitch muscle type with high levels of MHC IIB fibres which again is not significantly altered in *Ecsit*$^{N209I.N209I}$ animals compared to wild-types.

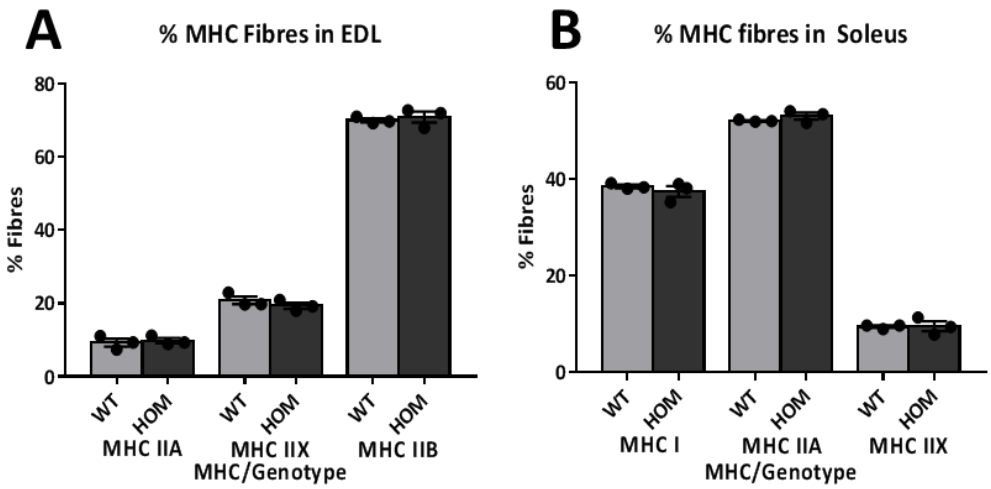

Figure 3.33. Percent of each fibre type in EDL (A) and soleus (B) in wild type and *Ecsit*$^{N209I/N209I}$ animals showing no significant differences between genotypes in either muscle investigated. Mean ± SEM.

Cross sectional area (CSA) was determined from the average of 100 CSAs of each fibre type in each sample. Results here show a significant reduction in all fibre types in both muscles measured in *Ecsit*$^{N209I/N209I}$ animals compared to wild types (Figure 3.34). This reduction in CSA in all fibre types in *Ecsit*$^{N209I/N209I}$ animals is likely to be related to the reduction in overall lean mass seen in section 3.8.3.

Collectively, these data do not demonstrate a significant alteration to the muscular phenotype of *Ecsit*$^{N209I/N209I}$ animals when compared to wild type controls.

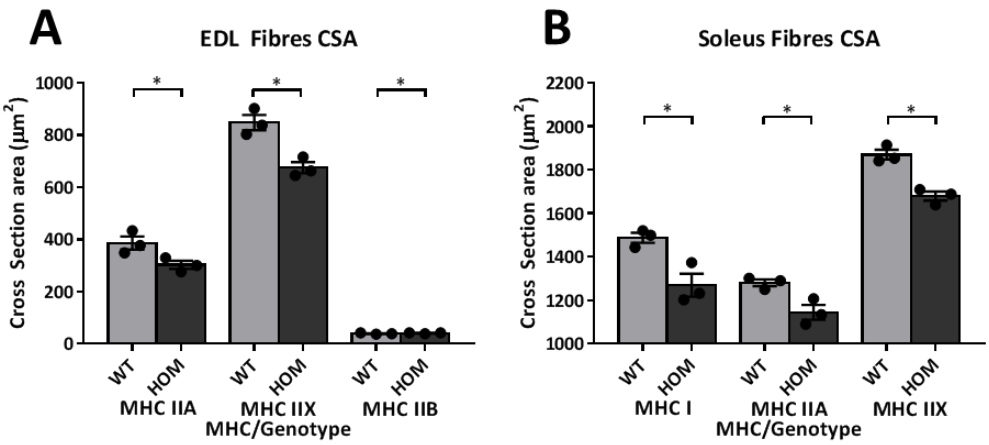

Figure 3.34. Cross sectional areas of fibre types in EDL (A) and soleus (B) showing a significant reduction in all fibre type sizes in *Ecsit*$^{N209I/N209I}$ animals compared to wild type controls. Mean ± SEM, *p<0.05.

3.9. Compound Heterozygote Phenotyping

To confirm that the Ecsit N209I mutation is causative of the hypertrophic cardiomyopathy seen in homozygous animals, compound heterozygotes (*Ecsit*$^{N209I/-}$) were generated from the intercrossing of *Ecsit*$^{N209I/+}$ and *Ecsit*$^{+/-}$ animals. Ecsit$^{+/-}$ animals were obtained from the laboratory of Professor Sankar Ghosh at Columbia University Medical Centre (NY, USA).

The *Ecsit*$^{N209I/-}$ offspring are heterozygous for the N209I mutation and the surrounding region inherited from the original C57BL/6J mutagenized parent, and hence should not exhibit the cardiomyopathy phenotype without a complementary knockout allele of the causative gene, in this case *Ecsit*. Similarly, *Ecsit*$^{+/-}$ animals are not known to exhibit any cardiomyopathy phenotype, indicating that *Ecsit* is haplosuffcient with regards to this phenotype.

All 4 possible genotypes of the intercross were assessed for heart weight (absolute and normalised) at 10 weeks of age. In all cases (Figure 3.35), hearts from *Ecsit*$^{N209I/-}$ animals show a significant increase in mass when compared to all other genotypes. This demonstrates that the N209I mutation is the causative allele inherited from the ENU mutagenized C57BL/6J ancestor and also confirms that *Ecsit* is haplosufficient in relation to the cardiomyopathy phenotype.

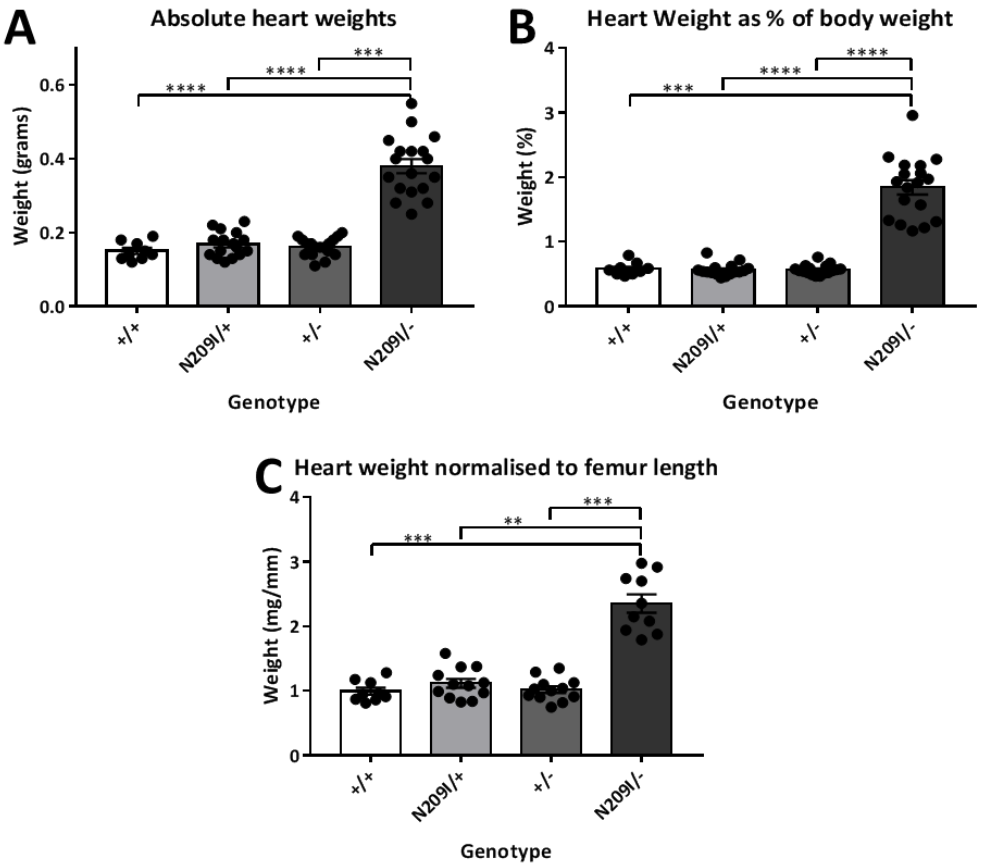

Figure 3.35. Absolute (A), and normalised to; body weight (B); and femur length, (C) heart weights from wild type (n=9 (M:3, F:6)), *Ecsit*$^{N209I/+}$ (A, B: n=16 (M:9, F:7) , C: n=12 (M:6, F:6)), *Ecsit*$^{+/-}$ (A, B, n=17 (M:9, F:8), C: n=12 (M:6, F:6)) and *Ecsit*$^{N209I/-}$ (A, B: n=18 (M:9, F:9), C: n=10 (M:5, F:5)) animals. By all methods of assessment, *Ecsit*$^{N209I/-}$ animals show a significant increase in tissue weight over all control genotypes. Mean ± SEM, **p<0.01, ***p<0.001, ****p<0.0001.

3.10. Discussion

Through SNP mapping and whole genome sequencing a single coding mutation was identified in a good candidate gene, *Ecsit,* which results in an asparagine to isoleucine change at position 209 of the protein. Through successive back crosses and using Sanger and pyro sequencing, together with the complementation assay, the mutation was confirmed as causative of the primary cardiomyopathy phenotype seen in affected animals. Protein prediction softwares indicate that the mutation has a deleterious effect on the structure or function of the protein. Given that the domains of mouse ECSIT are homologous to those of the human protein we can infer that the mutation lies in the pentatricopeptide (PPR) region of the protein, which is potentially involved in mitochondrial processes through binding and stabilising RNA molecules.

The compound heterozygote of $Ecsit^{N209I}$ and *Ecsit* knock-out was produced to confirm the genotype-phenotype interaction in the $Ecsit^{N209I/N209I-}$ animals. A lack of phenotype in heterozygote ($Ecsit^{N209I/+}$) animals indicates that *Ecsit* is haplosufficient and a single copy of the mutant allele is insufficient to cause a phenotype. This is also seen in the heterozygous knockouts ($Ecsit^{+/-}$), where no phenotype is present despite the loss of one allele.

ECSIT is known to bind and stabilise the complex I assembly factor NDUFAF1 and to be involved in complex I assembly as part of the mitochondrial complex I assembly (MCIA) complex, however the domain responsible for this role is unclear. With this role in mind, phenotyping focused on traits typically associated with mitochondrial complex I deficiency, including lactic acidosis, failure to thrive, myopathy, cardiomyopathy, sight loss and encephalopathy.

Through analysis of plasma taken from both the original backcross 1 animals, and from the incipient congenic line it is apparent that there are some key differences in some of the metabolites measured and that this reflects a change in the function of the kidney. Elevated potassium as well as urea and creatinine are indicative of failure of the kidney's filtration barrier, indicating that the N209I mutation in ECSIT is affecting the function of the kidney. It is unclear if this is primary (direct effect of loss of mitochondrial function in kidneys) or secondary (altered cardiac function leading to kidney failure) or whether this may be an effect of one of the other pathways ECSIT is involved in.

In addition, elevated bilirubin, ALP and AST, indicate that there may be a loss of function of the liver including elevated bilirubin, ALP and AST. However, the differences seen between wild type and *Ecsit*$^{N209I/N209I}$ animals in all of these metabolites is very small, and with the exception of a small number of outliers the ranges of the *Ecsit*$^{N209I/N209I}$ animals overlap the wild types considerably, furthermore these values do not exceed the reference ranges established at MRC Harwell for these tests.

Plasma levels of triglycerides, glycerol, ketone bodies, glucose and fructosamine, suggest an increased metabolism of both glucose and triglycerides and may reflect an energy deficiency of the heart and/or other tissues which the body is attempting to compensate for by increasing overall metabolism of substrates. Intra peritoneal glucose tolerance test (IPGTT) results show a significant improvement in glucose tolerance of *Ecsit*$^{N209I/N209I}$ animals at one time point (T=60 minutes). Whilst this is not consistent across all time points it may indicate an improvement in glucose tolerance due to reduced fat mass in *Ecsit*$^{N209I/N209I}$ animals or it may be directly related to the reduced glucose levels seen in the clinical chemistry results. Taken together these data may suggest an alteration in the metabolic phenotype of *Ecsit*$^{N209I/N209I}$ animals, either towards metabolising glucose, as is often seen in the failing heart, or in a general increase in metabolism of all substrates, potentially in an attempt to compensate for a loss of complex I efficiency.

Mutant animals are indistinguishable from wild type littermates up to the age of 6-8 weeks when differences in body weight first become apparent. It is around the same time point that differences in cardiac tissue can first be seen, with very early tell-tale signs of cardiomyopathy beginning to develop, including mineralisation of tissue and some signs of cardiomyocyte disorganisation. At 12 weeks of age, the phenotype has progressed to a distinct and severe cardiomyopathy of the left ventricle with no signs of right ventricular involvement, and is ultimately lethal. The cardiomyopathy is hypertrophic in nature but has some traits typically associated with dilated cardiomyopathy, including an increased left ventricular volume.

ECG measurements show no significant changes from wild type to *Ecsit*$^{N209I/N209I}$ animals, despite the cardiomyopathy changes. Indicating that the cause of the cardiomyopathy

phenotype is unrelated to an electrophysiological defect and that conductive tissues are unaffected by the ECSIT N209I mutation.

Whilst mutant animals appear smaller in terms of overall bodyweight and lean/fat mass, the length of long bones such as the femur is unchanged in comparison to wild types indicating that growth is normal. It is primarily the accumulation of fat that leads to overall body weight differences. This is further reflected in the relatively small differences in lean mass as late as 14 weeks of age.

Despite profound differences in cardiac muscle, differences in skeletal muscle measured by grip strength were less robust, with *Ecsit*$^{N209I/N209I}$ animals actually showing a moderately increased grip strength compared to wild types when normalised to overall body weight. This again is likely a reflection of the reduction in fat mass without a significant loss of lean or muscle mass, which would distort the normalised results. Further to this, muscle fibre typing shows no significant differences in fibre numbers or types of either soleus or EDL. *Ecsit*$^{N209I/N209I}$ animals do show a reduction in cross sectional area of all fibre types measured in both the soleus and EDL which may be reflective of the loss in lean mass seen in animals at later time points. However, given the lack of any grip strength phenotype, this is unlikely to be a pathological loss and unlikely to represent a true myopathy phenotype.

Taking into consideration the phenotypes assessed, and the lack of any obvious encephalopathy or neurological phenotype observed, it appears that *Ecsit*$^{N209I/N209I}$mice are affected by a left ventricular hypertrophic cardiomyopathy with no effects on brain, muscle or liver function. Some significant changes in kidney function are apparent from clinical chemistry analysis however it is unclear without further investigation, what the nature of the kidney defect is and whether it is a primary, or secondary phenotype associated with the severe cardiomyopathy. The overall metabolic profile of the *Ecsit*$^{N209I/N209I}$ animals is likely significantly altered from that of the wild types, with an increase in glucose and triglyceride metabolism, and further work on the function of the mitochondria may reveal more about the causes of this.

Chapter 4: Effect of mutation on the Toll-Like Receptor and Bone Morphogenetic Protein Pathways

4.1. Roles of ECSIT

ECSIT has a diverse set of roles including as a key signal intermediary in the toll-like receptor response and as a co-factor of SMAD4 in the bone-morphogenetic protein (BMP) pathway. Previous studies have shown that knocking out ECSIT can lead to increased susceptibility to intracellular bacteria via a suppression of the TLR response [229] and embryonic lethality due to failure of gastrulation via loss of expression of genes under the control of the BMP pathway [230]. Either of these pathways could be implicated in the development of the cardiomyopathy phenotype and it was investigated whether either of them were affected by the N209I mutation of ECSIT.

4.2. Toll like receptor response

ECSIT's role in the TLR pathway was assessed to confirm that this did not contribute to the phenotype observed, as an enlargement of the cardiac muscle could be attributed to a pro-inflammatory phenotype. Alongside its role in traditional innate immune response, the TLR response has been implicated in the development of myocardial inflammation. The most highly expressed TLR in heart is TLR4 which can cause the expression of pro-inflammatory cytokines via the MYD88 dependant and independent activation pathways, both of which involve the activation of ECSIT's binding partner, TRAF6 [289].

To investigate the TLR response in wild type and *Ecsit*$^{N209I/N209I}$ animals, three different approaches were used. Firstly, circulating leukocytes were assessed to determine if there was a shift to a pro-inflammatory phenotype. Secondly, the role of ECSIT in the TLR pathway was determined by assessing its interaction with the known TLR pathway binding partner TRAF6. Finally, bone marrow derived monocytes were isolated and derived into macrophages which were in turn activated with lipopolysaccharide (LPS) to determine if the TLR pathway was activated as normal in *Ecsit*$^{N209i/N209I}$ animals.

4.2.1. Flow cytometry of immune cells

Fluorescence associated cell sorting (FACS) allows for the determination of proportions of leukocytes of each type and from this it is possible to infer if the ECSIT N209I results in a significant alteration of the immune phenotype of *Ecsit*$^{N209I/N209I}$ animals. FACS was performed on whole blood collected from wild type and *Ecsit*$^{N209I/N209I}$ animals and the

percentage of lymphocytes, monocytes, neutrophils and macrophages expressed as a % of total leukocytes (Figure 4.1).

Results show no differences in the levels of monocytes or neutrophils when comparing wild type and *Ecsit*$^{N209I/N209I}$ animals. However, a statistically significant difference is visible in both lymphocytes and macrophage counts, where both show a significant reduction in *Ecsit*$^{N209I/N209I}$ animals when compared to wild type controls.

This reduction in lymphocytes and macrophages reflects a reduced immune response in both innate and adaptive immunity. Unfortunately, as macrophages exist as both pro- (M1) and anti- (M2) inflammatory populations; and this analysis is unable to distinguish between the two; it is not immediately possible to determine if this result truly reflects a reduction in systemic inflammation or if the ratio of M1:M2 macrophages may be shifted towards a pro-inflammatory phenotype.

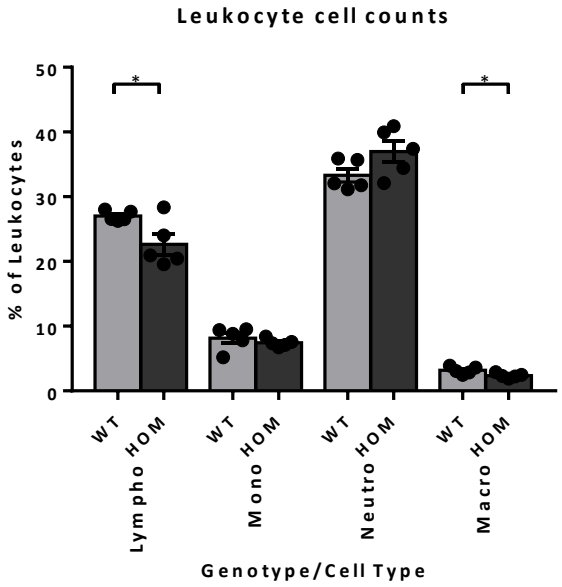

Figure 4.1. Percent of leukocyte types as a % of total leukocytes identified by FACS analysis. Mono(cytes) and neutro(phils) show no significant changes whilst lympho(cytes) and macro(phages) both show a significant reduction in *Ecsit*$^{N209I/N209I}$ animals compared to wild type controls. FACS analysis performed by Dr. Pratik Vikhe – MRC Harwell. Mean ± SEM, *p<0.05.

4.2.2. Co-Immunoprecipitation of ECSIT and TRAF6

Full length wild type and mutant ECSIT created by site directed mutagenesis (AC-HIS) as well as TRAF6 (Entry (C, DDK-Myc)) were cloned into pCMV6 vectors (Origene) and transiently transfected into HEK293T cells (ECACC 12022001). Co-immunoprecipitation of the proteins from cell lysate using antibodies against the relevant tags (Figure 4.2) shows that both proteins are expressed in transfected cells (lane 2 and 3) but not in untransfected cells (lane 1). Co-transfecting wild type ECSIT with TRAF6 and immunoprecipitating with either anti-His (lane4) or anti-Myc (lane 6) primary antibody show that the two proteins interact and can be co-immunoprecipitated. Transfecting N209I ECSIT with wild type TRAF6 demonstrates that the introduction of the mutation by site-directed mutagenesis does not affect the interaction with TRAF6. Control lanes using empty His (lanes 5 and 9) and entry (Myc) vector (lanes 7 and 11), that only express the tag and neither of the proteins of interest, with the respective primary antibody demonstrate that the co-immunoprecipitation is not possible without the respective interacting partner protein expressed. Therefore it is possible to conclude that the N209I mutation of ECSIT has no effect on the interaction with TRAF6.

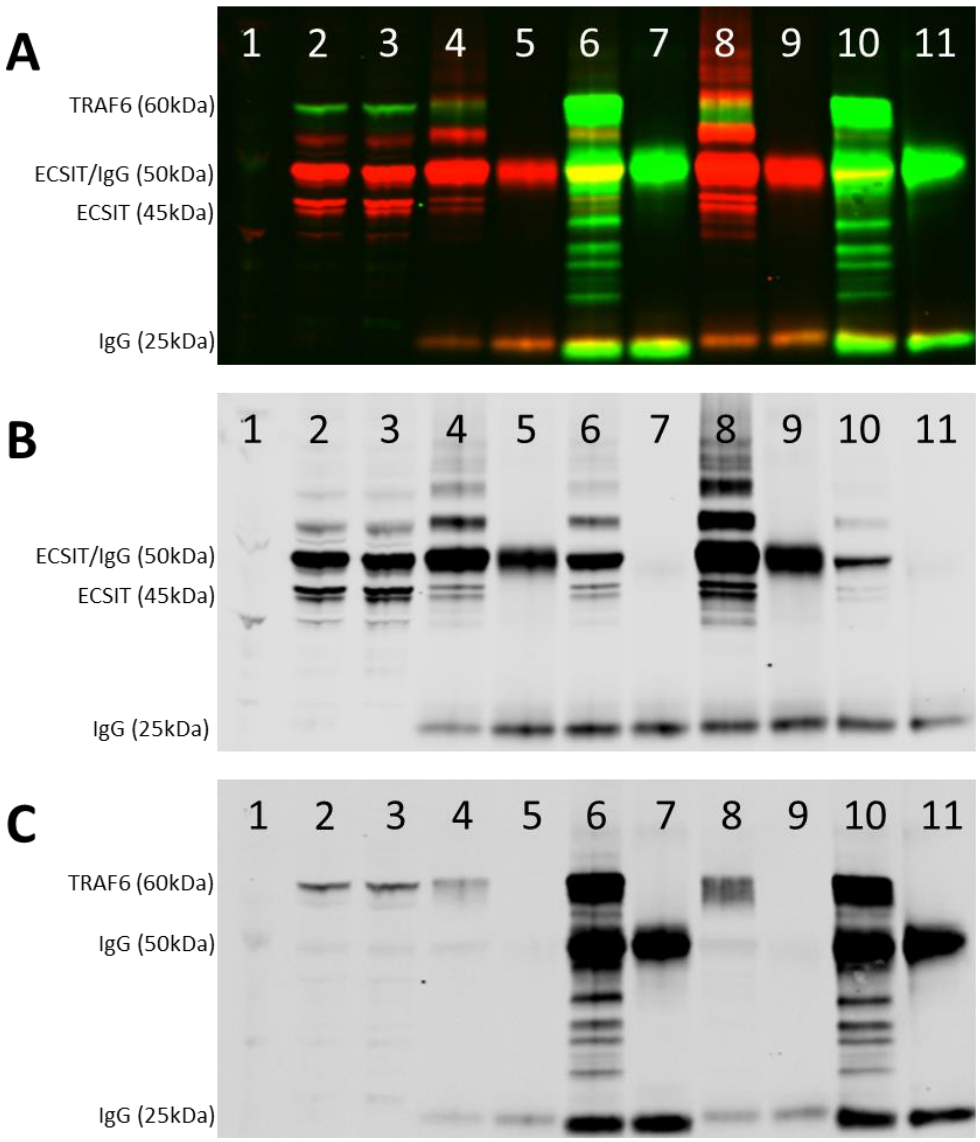

Figure 4.2. Immunoprecipitation of wild type and mutant ECSIT (His tagged) (45 and 50kDa) with full length wild type TRAF6 (Myc tagged) (60kDa). (A) Shows combined channels with secondary antibodies against mouse (green – Myc) and rabbit (red – His). (B) and (C) show the separated channels of demonstrating the anti-rabbit (Anti-His) and anti-mouse (Anti-Myc) secondary antibodies respectively. 1. Untransfected input lysate, 2. Wild type ECSIT(His) + wild type TRAF6(Myc) input lysate 3. ECSIT N209I(His) + wild type TRAF6(Myc) input lysate, 4. Wild type ECSIT(His) + wild type TRAF6(Myc) anti-His immunoprecipitation, 5. Empty AC-His vector + wild type TRAF6(Myc) anti-His immunoprecipitation, 6. Wild type ECSIT(His) + wild type TRAF6(Myc) anti-Myc immunoprecipitation, 7. Wild type ECSIT(His) + empty entry(Myc) vector anti-Myc immunoprecipitation, 8. N209I ECSIT(His) + wild type TRAF6(Myc) anti-His immunoprecipitation, 9. Empty AC-His vector + wild type TRAF6(Myc) anti-His immunoprecipitation, 10. N209I ECSIT(His) + wild type TRAF6(Myc) anti-Myc immunoprecipitation, 11. N209I ECSIT + empty entry(Myc) vector anti-Myc immunoprecipitation.

4.2.3. Macrophage Stimulation with Lipopolysaccharide

To determine if the mutation of ECSIT significantly affects activation of the toll like response, monocytes were isolated from the bone marrow of wild type and *Ecsit*$^{N209I/N209I}$ animals and differentiated into macrophages before treating with lipopolysaccharide. Macrophages are immune cells that form part of the innate immune response and are typically rich in toll like receptors, including TLR4, which recognises LPS and acts upstream of ECSIT in the TLR response [237].

Bone marrow derived macrophages isolated from wild type and *Ecsit*$^{N209I/N209I}$ animals were exposed to 100ng/ml of LPS to induce the TLR response and assess the role of ECSIT in activating JNK, p38 MAPK and NFκB via MAP3K1 and TAK1 which form one of the final steps in the TLR response. The phosphorylation of the 3 proteins was assessed and compared to total protein expression levels to determine activation level.

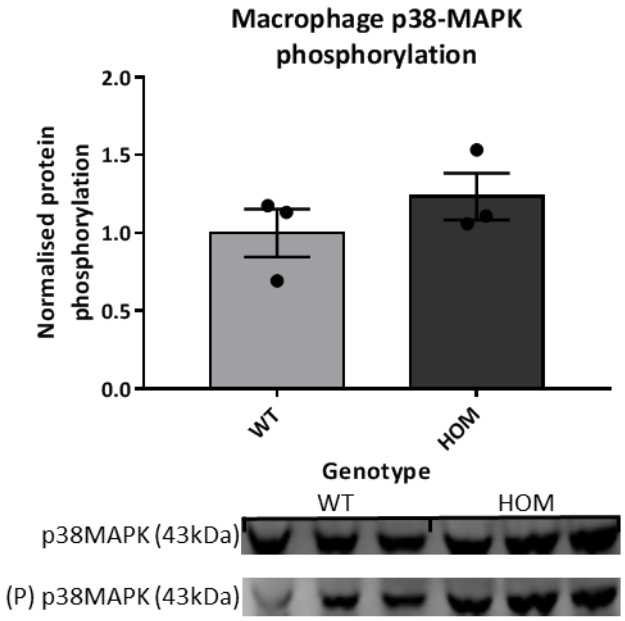

Figure 4.3. Quantification of p38-MAPK phosphorylation in cultured BMDMs activated with LPS. Representative blot shows total and phosphorylated p38-MAPK. Results indicate there are no significant changes between wild type and *Ecsit*$^{N209I/N209I}$ BMDMs. (Mean ± SEM).

The phosphorylation of p38MAPK was assessed on the same immunoblot as the total protein and phosphorylated protein primary antibodies were raised in different species and hence could be overlaid and separated in the green and red channels. Results show no increase in phosphorylation levels of p38MAPK in bone marrow derived

macrophages induced by LPS from *Ecsit*$^{N209I/N209I}$ animals (Figure 4.3) compared to wild type controls.

JNK phosphorylation was assessed across two individual immunoblots as the total and phosphorylated primary antibodies were raised in the same species. Protein levels were normalised to α-tubulin and then the level of phosphorylation determined. Results show no differences in total JNK protein expression (Figure 4.4) whilst levels of phosphorylated JNK (Figure 4.4) show a trend towards a reduction in overall phosphorylation but do not achieve significance. It is possible that further repeats of the experiment would increase the level of significance but as these results tend towards a reduction in inflammatory phenotype and not a pro-inflammatory phenotype, as might cause hypertrophy, this was not performed.

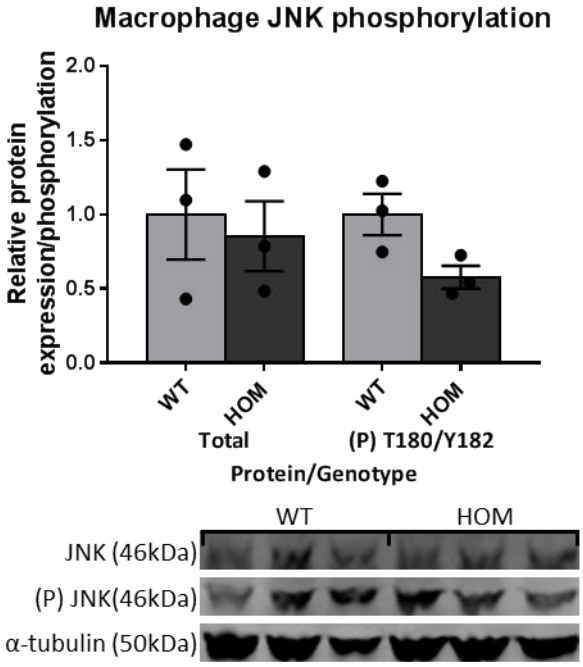

Figure 4.4. Quantification of total and phosphorylated (T183/Y185) JNK and normalised to the loading control α-tubulin. Phosphorylated JNK is normalised to total JNK levels. Representative blots show total and phosphorylated JNK as well as the loading control, α-tubulin. (Mean ± SEM).

Levels of NFκB, both total and phosphorylated, were unable to be assessed due to a lack of signal from both primary antibodies. This may have been due to poor storage of the lysates, although the same lysates were used for both the p38 MAPK and JNK immunoblots so this is unlikely, or it may have been due to an old or unreliable batch of antibody. As this was part of a larger section of work, and all other results showed a

trend in the same direction, it was decided not to persevere with this particular protein as its contribution to the overall results was likely insignificant.

4.3. Assessment of developmental pathways in mutant ECSIT mice

The role of the BMP pathway has primarily been investigated in relation to the developing myocardium, especially the growth and differentiation of myocardium precursors from the primitive streak of the early embryo. However, there is an emerging role for BMP signalling in the differentiation of adult stem cells into cardio myocytes, with BMP2 seemingly playing an important role in the regeneration of cardiac tissue following myocardial infarction [290].

The indispensable role of ECSIT in the bone morphogenetic protein (BMP) pathway occurs at a very early time point and it is difficult to tell from existing literature whether this pathway could contribute significantly to the cardiomyopathy phenotype. Knockout animals display embryonic lethality long before it would be possible to detect any cardiac phenotype [230]. Similarly, knockouts of ECSITs partner in the BMP pathway, SMAD4, also show early stage embryonic lethality. It is noteworthy that whilst this embryonic lethality occurs before complete heart development, it does appear that this process is impaired in these embryos. Cardiac cell lineages appear to begin to differentiate normally but normal heart development is impaired, with only primitive features being visible [291, 292]. Conditional knockout mice with a cardiac specific deletion of SMAD4 also demonstrate embryonic lethality, although this was at the slightly later time point of E13.5-14.5. Histology from knockout embryos revealed a defective alignment of cardiac outflow tracts. Despite this marked effect, heterozygous animals (*Smad4*$^{flox/+}$) developed normally despite a reduction in growth factor signalling [293].

These previous studies would suggest that any significant impairment of this pathway should result in embryonic lethality. However, it is important to determine whether or not this pathway is affected by the N209I mutation and therefore if it could possibly have any role in cardiac phenotype development, potentially due to a reduction in growth factor signalling that is insufficient to result in embryonic lethality.

4.3.1. Co-Immunoprecipitation of ECSIT and SMAD4

The interaction of ECSIT and SMAD4 was previously demonstrated by co-immunoprecipitation of the two proteins in mouse embryonic carcinoma cells (P19 cells) [230]. To determine if the N209I mutation may affect this binding event full length wild

type and mutant *Ecsit* as well as full length Smad4 were cloned into pCMV6 vectors in order to generate a tagged protein (Ecsit – His, Smad4 – Myc). Expression of the plasmids in Hek293T cells was confirmed and co-immunoprecipitation performed to assess the interaction of both the wild type proteins and the mutant ECSIT with wild type SMAD4. Co-immunoprecipitation was performed using antibodies against the relevant tags (mouse anti-myc, rabbit anti-6xHis) and immunoblotting visualised using the same primaries with fluorescent secondaries (anti-mouse alexafluor 568, anti-rabbit alexafluor 488). Lanes 1, 2 and 3 of figure 4.5 show the un-transfected, wild type ECSIT(50/45kDa)/wild type SMAD4 (60kDa) and mutant ECSIT(45/50kDa)/wild type SMAD4 cell lysates prior to immunoprecipitation, confirming successful transfection and the expression of the tagged proteins. Lane 4 (Figure 4.5) shows the wild type ECSIT co-transfected with SMAD4 and immunoprecipitated using anti-His antibody which should draw down the ECSIT protein and the partnered SMAD4 protein. However, whilst it is possible to see the 45kDa ECSIT protein (the 50kDa protein is masked by the 50kDa immunoglobulin) confirming successful immunoprecipitation, the 60kDa SMAD4 is not present in this lane. The same is true when the reverse immunoprecipitation is performed (Lane 6, Figure 4.5), pulling down using the anti-Myc antibody we can see no presence of either of the ECSIT isoforms. Unfortunately, without the ability to confirm the immunoprecipitation results from Xiao *et al.* (2003) [230] in wild type proteins it is impossible to determine whether or not the N209I mutation is affecting the interaction.

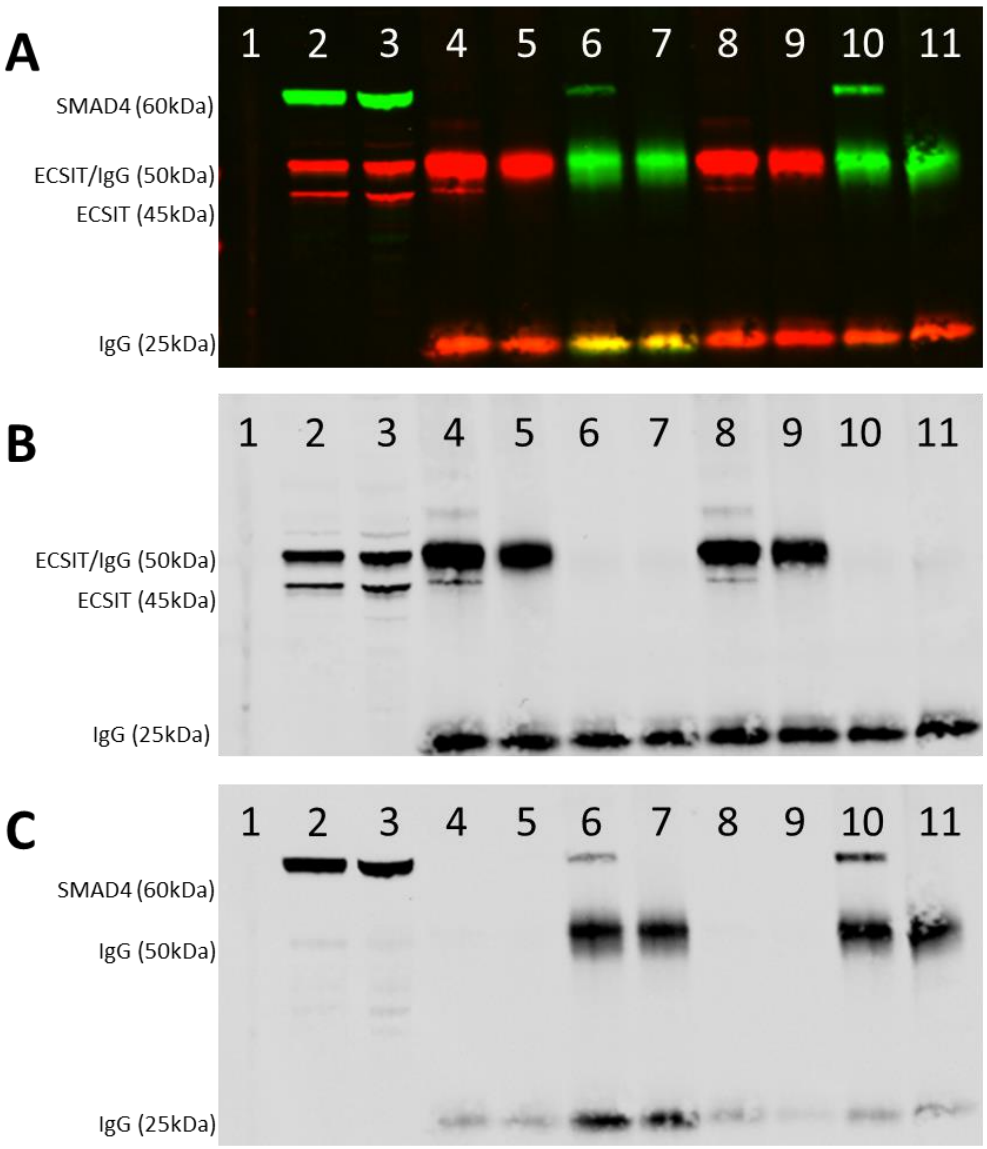

Figure 4.5. Immunoprecipitation of wild type and mutant ECSIT (His tagged) (45 and 50kDa) with full length wild type SMAD4 (Myc tagged) (60kDa). (A) shows combined channels with secondary antibodies against mouse (green – Myc) and rabbit (red – His). (B) and (C) show the separated channels demonstrating the anti-rabbit (Anti-His) and anti-mouse (Anti-Myc) secondary antibodies respectively. 1. Untransfected input lysate, 2. Wild type ECSIT(His) + wild type SMAD4(Myc) input lysate 3. ECSIT N209I(His) + wild type SMAD4(Myc) input lysate, 4. Wild type ECSIT(His) + wild type SMAD4(Myc) anti-His immunoprecipitation, 5. Empty AC-His vector + wild type SMAD4(Myc) anti-His immunoprecipitation, 6. Wild type ECSIT(His) + wild type SMAD4(Myc) anti-Myc immunoprecipitation, 7. Wild type ECSIT(His) + empty entry(Myc) vector anti-Myc immunoprecipitation, 8. N209I ECSIT(His) + wild type SMAD4(Myc) anti-His immunoprecipitation, 9. Empty AC-His vector + wild type SMAD4(Myc) anti-His immunoprecipitation, 10. N209I ECSIT(His) + wild type SMAD4(Myc) anti-Myc immunoprecipitation, 11. N209I ECSIT + empty entry(Myc) vector anti-Myc immunoprecipitation.

4.3.2. Embryonic Expression of *Tlx2*

The interaction of ECSIT with SMAD4 leads to the expression of the gene *Tlx2* and knocking out *Ecsit* results in a loss of Tlx2 expression [230]. To assess if the N209I mutation had any effect on *Tlx2* expression and therefore may be affecting the BMP pathway and embryogenesis, *Tlx2* expression was assessed by qRT-PCR in E7.5 day embryos. Litters of embryos from wild type x wild type or mutant x mutant crosses were pooled in order to increase overall RNA yields.

Results (Figure 4.6) indicate an approximately 50% reduction in *Tlx2* expression in *Ecsit*$^{N209I/N209I}$ embryos compared to wild types indicating that the mutation of ECSIT may have an effect on the BMP pathway and accordingly on the expression of downstream genes. However, statistical analysis was not performed as one WT sample had to be excluded due to inconsistent results.

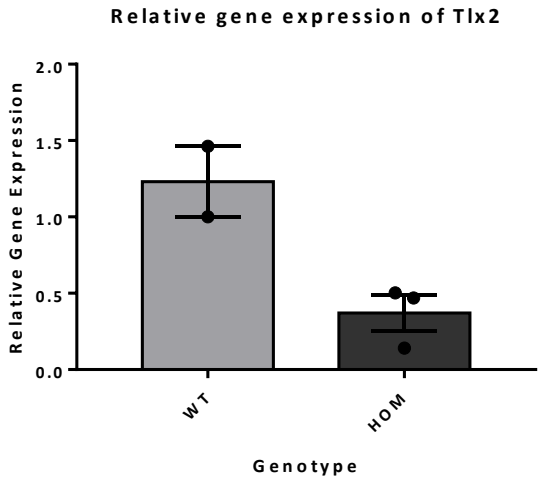

Figure 4.6. Relative gene expression of *Tlx2* in wild type and *Ecsit*$^{N209I/N209I}$ pooled embryos shows a reduction in the expression of *Tlx2* expression in *Ecsit*$^{N209I/N209I}$ embryos at E7.5. Mean ± SEM.

4.4. Discussion

The role of ECSIT in both the TLR and BMP response has the potential to explain the cardiomyopathy phenotype observed. Such functional studies will also help define important functional domains with the ECSIT protein. However, from the results obtained here it isn't possible to draw meaningful conclusions about the role of these pathways in the development of this phenotype, or indeed that this mutation can be considered pathogenic in either of these pathways. Further investigation into these pathways specifically in heart tissue may reveal more about the individual contribution of these pathways to HCM, or how ECSIT may link these pathways to a metabolic impairment, ultimately leading to HCM.

Results from experiments assessing the TLR pathway and its activation appear to show that ECSIT is still able to perform its role normally with respect to binding to TRAF6 and activating downstream proteins through indirect phosphorylation. The interaction of ECSIT with TRAF6 in human is known to occur between amino acids 200 and 257 of the human ECSIT protein [239], which aligns well with the mouse protein. This would place the N209I mutation at the start of this region and make this pathway an obvious candidate to suffer a significant loss of function. However, as can be seen from the co-immunoprecipitation performed with TRAF6, it does not appear that the mutation affects the binding of the two proteins and given its position, it is unlikely to affect the ubiquitination of ECSIT at K372 [238]. Furthermore, the downstream phosphorylation of 2 of the 3 key proteins (p38 MAPK and JNK) that are activated by this interaction show no significant changes in phosphorylation levels and are unlikely to result in a pro-inflammatory phenotype that could cause inflammation or enlargement of the cardiac muscle. Unfortunately, due to the issues with antibodies against NFκB it wasn't possible to determine if the N209I mutation may affect the formation of the TAK1-ECSIT-TRAF6 complex [239] that would lead to activation of IKK proteins and ultimately NFκB phosphorylation.

Despite gaps in the data, results do not implicate the effect of the N209I mutation on the TLR response as the main driving force behind the phenotype development. As this work was undertaken in macrophages, there may still be a great deal to learn from investigating the pathway further in heart tissue, or specifically in cardiomyocytes.

Unfortunately, results relating to the role of ECSIT in the BMP pathway are mixed. There are no signs of reduced viability of *Ecsit*$^{N209I/N209I}$ embryos indicating that the pathway is not significantly impacted. However, there is a reduction in the expression of Tlx2 in *Ecsit*$^{N209I/N209I}$ embryos at E7.5 suggesting that the mutation of ECSIT does affect signalling through the pathway to a measurable degree. It is important to note that these results are taken from pooled embryos and it is difficult to age match embryos at such a small and early time point, and to ensure that the entire embryo is collected correctly.

The co-immunoprecipitation of ECSIT with SMAD4 may have provided much needed clarity on the issue however as this was unsuccessful, further investigation is warranted. Taken together these data seem to indicate that the mutation of ECSIT does not result in a null allele with regards to its function in the BMP pathway, as embryos that are homozygotes are born at the expected mendelian ratio and *Tlx2* expression, whilst reduced, is present.

Overall these data provide an incomplete picture of the role of ECSIT in the BMP and TLR pathways and further investigation is warranted. However, given the minimal changes seen in these pathways, it seems prudent to investigate a mitochondrial role for ECSIT further before focusing on small changes to these pathways.

Chapter 5: Characterisation of Mitochondrial Function

5.1. Introduction

With data implicating the toll like receptor response and the bone morphogenetic pathway as causes of the phenotype seen in *Ecsit*$^{N209I/N209I}$ animals mixed, the focus shifted towards the more obvious candidate pathway; ECSIT's role in complex I assembly. Several papers had shown how ECSIT interacts with a number of other complex I assembly factors (ACAD9, NDUFAF1, TMEM126B and TIMMDC1) to form the mitochondrial complex I assembly (MCIA) complex and assist in the assembly process. As it is established that defects in mitochondrial function can lead to cardiomyopathy, amongst other phenotypes, this process warranted in depth investigation. Assessment of mitochondrial function began with structural analysis and quantification before determining the protein levels and function of the electron transport chain through a variety of methods including seahorse analysis of cultured cells and isolated mitochondria. ECSIT protein levels and its interaction with known binding partners was also assessed by SDS-PAGE and co-immunoprecipitation, revealing a previously undescribed 16kDa fragment detected by the antibody in wild type cardiac tissue but absent from mutants, offering a potential mechanism for the tissue specific phenotype seen.

Once dysfunction was established, it was possible to begin looking at how the mutation of ECSIT affects the construction of complex I and investigate this across tissues. This work demonstrates that ECSIT may work differently in heart and brain, leading to tissue differences in complex I assembly.

Finally, work was undertaken to identify the 16kDa fragment detected in wild type cardiac tissue using immunoprecipitation and mass-spectrometry.

5.2. Structure and Quantification

Structure of mitochondria as well as total mitochondrial mass are assessable via a variety of methods. Mitochondrial structure was assessed by transmission electron microscopy examining the cross sectional area of mitochondria as well as the structure of the cristae. Quantification of mitochondria was attempted using a variety of different methods due to the variability between them. Mitochondrial DNA quantification does not necessarily reflect an increase or decrease in total mitochondrial mass due to a non-linear relationship between mtDNA and actual mass. Inner and outer mitochondrial

membrane proteins may give a better reflection of total mitochondrial mass however variation between the two membranes can occur with variations in mitochondrial structure.

5.2.1. Transmission Electron Microscopy

Transmission electron microscopy (TEM) images of wild type and *Ecsit*$^{N209I/N209I}$ cardiac mitochondria demonstrate some qualitative changes in mitochondrial ultrastructure in mutant animals (Figure 5.1). Both interfibrillar and perinuclear mitochondria in wild type samples show a characteristic shape and evenly stacked cristae structure with no signs of disorganisation or mitochondrial swelling. Sub-sarcolemmal mitochondria were not imaged due to limitations with sample preparation and access to TEM facilities. When compared to wild type controls, interfibrillar mitochondria from *Ecsit*$^{N209I/N209I}$ hearts have some signs of highly condensed cristae, forming uneven stacks through the mitochondria. Also apparent are disorganised cristae which do not form the clean, uniform stacks seen in wild type mitochondria. Perinuclear mitochondria from *Ecsit*$^{N209I/N209I}$ hearts also show signs of cristae disorganisation, although no signs of hyper condensed cristae were seen in this sub-population. It is difficult to quantify what proportion of mitochondria display these characteristics in each population as the cristae are not clearly visible in each mitochondria to the same degree, many mitochondria in *Ecsit*$^{N209I/N209I}$ tissues did not show any of the cristae abnormalities mentioned here.

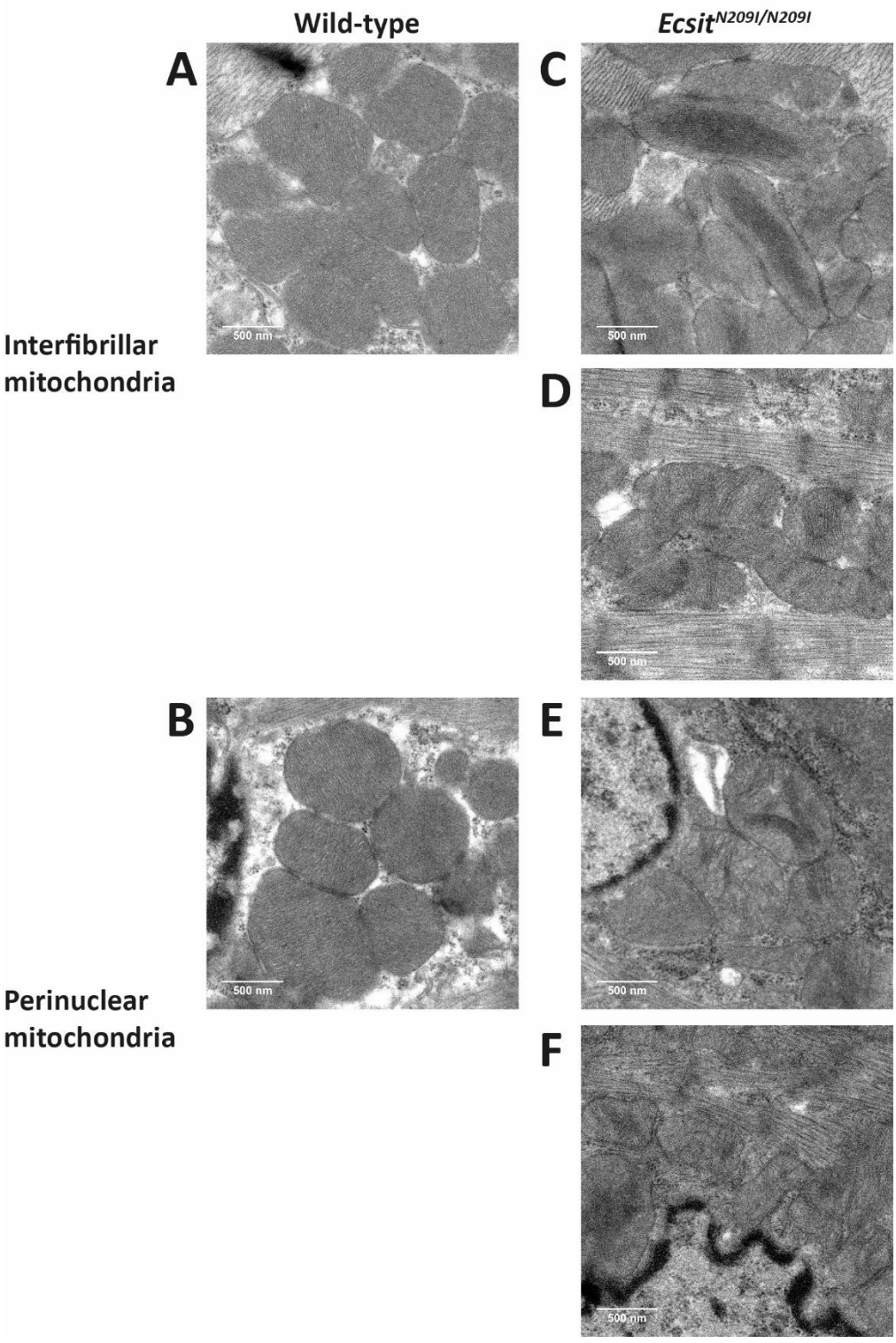

Figure 5.1. Representative TEM images of wild type and *Ecsit*$^{N209I/N209I}$ interfibrillar and perinuclear mitochondria from cardiac tissue demonstrating structural abnormalities observed in *Ecsit*$^{N209I/N209I}$ samples. Wild type interfibrillar (A) and perinuclear (B) mitochondria demonstrate consistent evenly stacked cristae with no signs of disorganisation. Mutant interfibrillar mitochondria demonstrate phenotypes such as hyper condensed (C) and disorganised cristae (D). Perinuclear mitochondria from mutant hearts also demonstrate disorganisation (E and F) although hyper packed cristae were not observed. Scale bars = 500nm.

To determine if there was any mitochondrial swelling present in *Ecsit*$^{N209I/N209I}$ cardiac mitochondria, cross sectional areas of mitochondria from all populations were assessed in FIJI (Image J) by manually drawing around whole visible mitochondria and measuring the area within the double membrane (Figure 5.2). Mitochondria without a complete membrane in view in an image were excluded from this analysis. Contrary to what might be expected, results demonstrate a small reduction in cross sectional area of both interfibrillar and perinuclear mitochondria in *Ecsit*$^{N209I/N209I}$ cardiac tissue, although this result is not statistically significant with the small n number used.

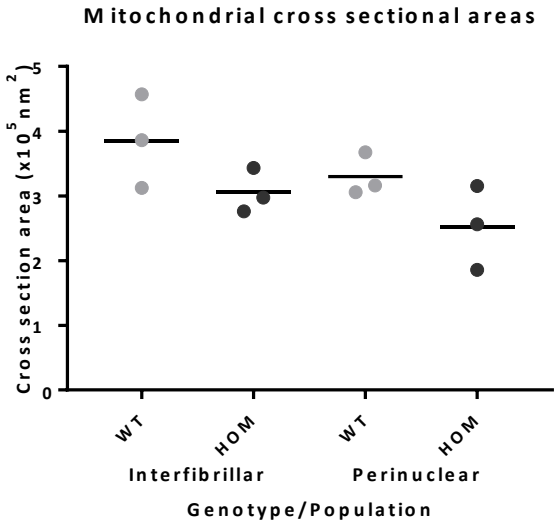

Figure 5.2. Cross sectional areas of mitochondria were assessed in wild type and *Ecsit*$^{N209I/N209I}$ animals in both interfibrillar and perinuclear mitochondria populations. Results demonstrate a small reduction in mitochondrial sizes in *Ecsit*$^{N209I/N209I}$ populations which does not achieve statistical significance.

5.2.2. Nuclear to Mitochondrial DNA ratio

A crude method for quantification of total mitochondria is to assess the ratio of mitochondrial DNA (mtDNA) to nuclear DNA (nDNA) in a tissue or cell sample of interest. DNA was isolated from heart tissue taken from 16 week old wild type and *Ecsit*$^{N209I/N209I}$ animals and assessed using NovaQUANT™ mouse mitochondrial to nuclear ratio kit. This kit uses quantitative PCR to determine the copy number of 2 nuclear (*Becn1* and *Neb*) and 2 mitochondrial genes (*trLEV* and *12S*) and through comparison of copy number it is possible to determine mtDNA copy number compared to nDNA. Three male and 3 female wild type *Ecsit*$^{N209I/N209I}$ animals were compared, however, results from one plate (female samples) showed no amplification from nuclear genome DNA and were excluded from the final analysis. Results (Table 5.1) show no significant differences in the copy number of the mtDNA between wild type and *Ecsit*$^{N209I/N209I}$ animals (Figure 5.3). However, a significant caveat to this observation is the great deal of variance in the *Ecsit*$^{N209I/N209I}$ samples in comparison to the tightly clustered wild type samples, furthermore, small N numbers limit meaningful interpretation of the results. Taking this result as it is, there do not appear to be gross differences in the mtDNA copy number between wild type and *Ecsit*$^{N209I/N209I}$ animals in heart tissue, although further investigation is warranted.

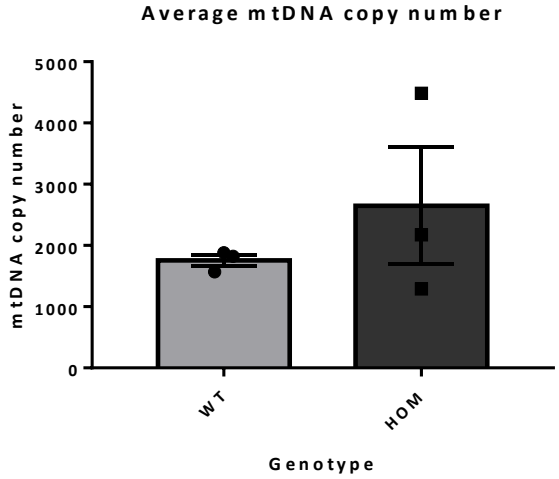

Figure 5.3. Novaquant™ mouse mitochondrial to nuclear ratio kit results showing mitochondrial DNA copy number in cardiac left ventricle tissue as a multiple of nuclear DNA copy number. Results show no significant difference in the mean of the two genotypes. (Mean ± SEM)

Sample	Target	Ct	ΔCt	$2^{\Delta Ct}$	Average copy mtDNA number
***Ecsit*$^{+/+}$ 1**	*trLEV*	19.082	10.810	1795.3	1822
	Becn1	29.892			
	12S	17.662	10.852	1848.3	
	Neb	28.514			
***Ecsit*$^{+/+}$ 2**	*trLEV*	18.187	10.592	1543.5	1567
	Becn1	28.779			
	12S	16.795	10.635	1590.2	
	Neb	27.43			
***Ecsit*$^{+/+}$ 3**	*trLEV*	18.303	10.667	1625.9	1881
	Becn1	28.97			
	12S	16.952	11.061	2136.5	
	Neb	28.013			
***Ecsit*$^{N209I/N209I}$ 1**	*trLEV*	16.081	12.168	4601.9	4484
	Becn1	28.249			
	12S	14.767	12.092	4365.7	
	Neb	26.859			
***Ecsit*$^{N209I/N209I}$ 2**	*trLEV*	15.563	11.242	2422.0	2172
	Becn1	26.805			
	12S	14.269	10.908	1921.5	
	Neb	25.177			
***Ecsit*$^{N209I/N209I}$ 3**	*trLEV*	15.732	10.351	1306.1	1290
	Becn1	26.083			
	12S	14.549	10.315	1273.9	
	Neb	24.864			

Table 5.1. Novaquant™ mouse mitochondrial to nuclear ratio kit results showing mitochondrial DNA copy number in cardiac left ventricle tissue as a multiple of nuclear DNA copy number. Nuclear and mitochondrial genes are divided into 2 pairs (mtNDA/nDNA) for analysis (*trLEV*/*Becn1*, *12S*/*Neb*).

5.2.3. Protein

In contrast to mtDNA copy number, which may vary regardless of mitochondrial mass, mitochondrial membrane proteins may be quantified for a more accurate representation of overall mitochondrial mass when normalised to a cytosolic protein such as α-tubulin. Two proteins were quantified, TOMM20, a mitochondrial outer membrane protein, and COXIV, a mitochondrial inner membrane protein. The quantification of these two proteins may also provide clues about changes in mitochondrial morphology, as a differential change in one over the other may represent a change in the abundance of one membrane over the other. Results (Figure 5.4) show no significant differences between wild type and *Ecsit*$^{N209I/N209I}$ inner or outer mitochondrial membrane proteins in cardiac tissue. This result indicates that the mitochondrial mass per cell in the heart is unchanged, although as could be seen in histology, cell size is increased so it is possible to interpret that the overall mitochondrial mass of the heart is increased accordingly.

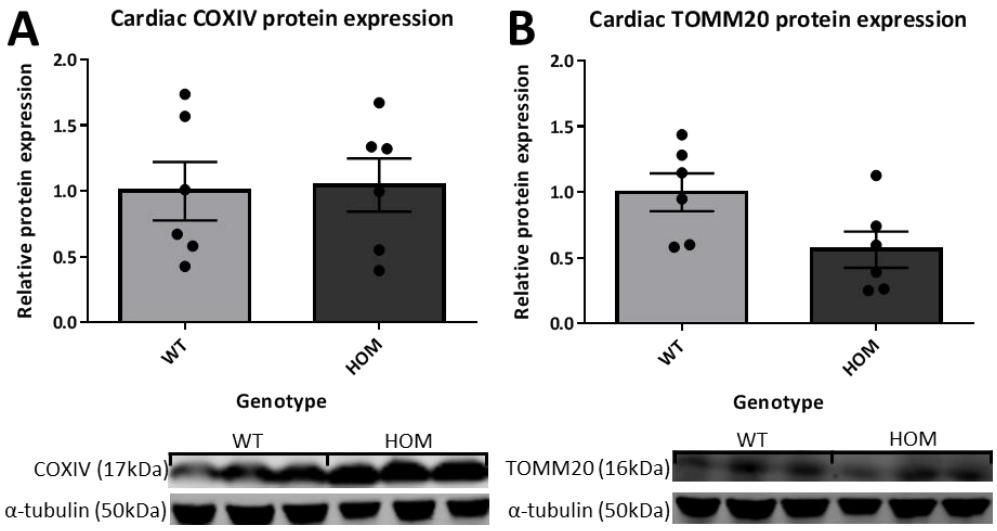

Figure 5.4. Normalised protein expression levels of inner mitochondrial membrane protein COXIV (A) and outer mitochondrial membrane protein TOMM20 (B). Showing no differences in protein levels between wild type and *Ecsit*$^{N209I/N209I}$ animals. (Mean ± SEM).

5.2.4. Biogenesis

In addition to determining the existing mass of mitochondria within cardiac tissue, it is also possible to determine the cellular demand for the production of new mitochondria, or mitochondrial biogenesis in tissues. Protein levels of the master regulator of mitochondrial biogenesis, PGC1α, show a significant upregulation in cardiac tissue of *Ecsit*$^{N209I/N209I}$ animals over wild types indicating increased mitochondrial biogenesis, although this is not reflected in actual mitochondrial mass. Other tissues tested, liver, kidney and brain do not reflect the upregulation of PGC1α indicating that this is a tissue specific change in demand, isolated to the heart tissue.

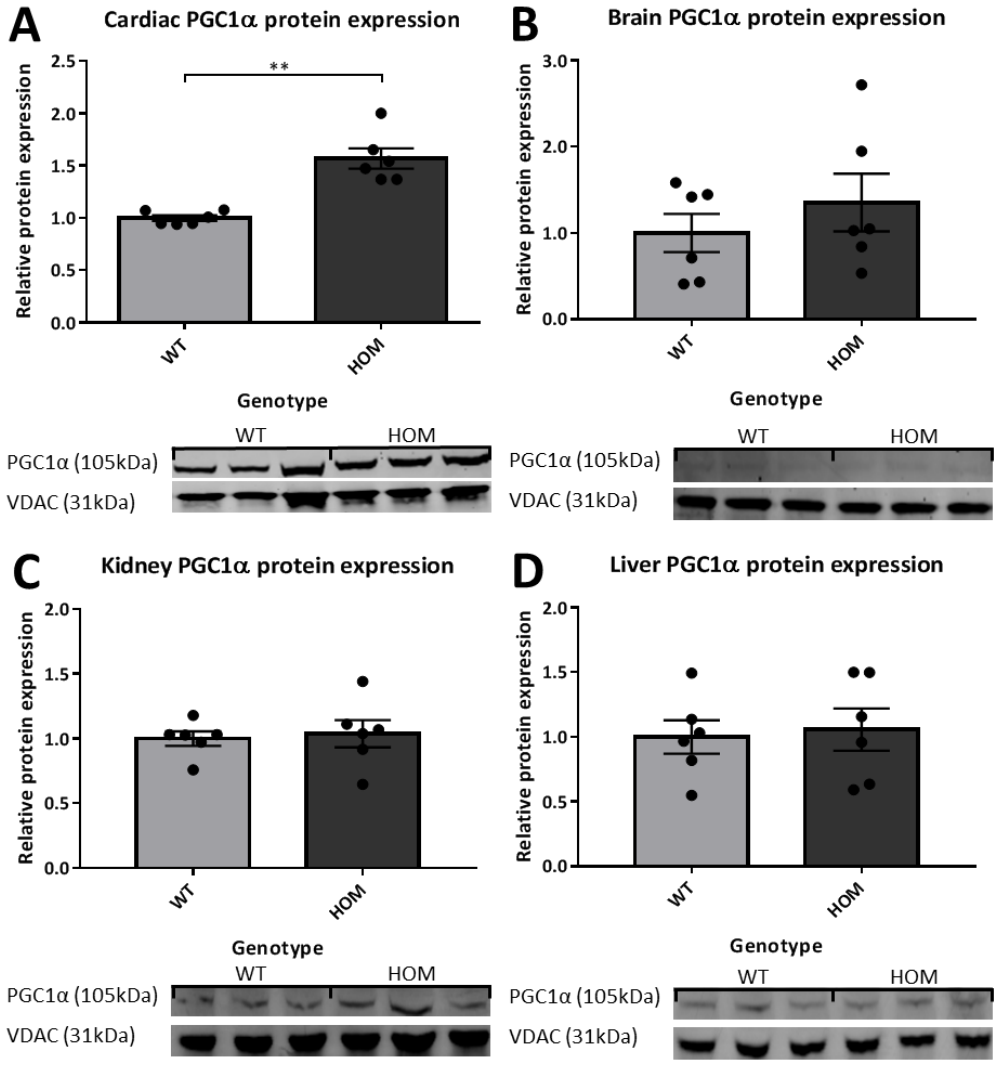

Figure 5.5. Quantified protein levels and representative immune blots of mitochondrial biogenesis regulator PGC1α normalised to VDAC are elevated in cardiac tissue of *Ecsit*$^{N209I/N209I}$ animals compared to wild type controls (A). Levels in other tissues, brain (B), kidney (C) and liver (D) remain significantly indistinguishable from wild types. Mean ± SEM, **p<0.01.

5.3. Electron Transport Chain Function

As results indicated that the N209I mutation in ECSIT was unlikely to result in a pro-inflammatory phenotype through the TLR response and differences in the BMP pathway were inconclusive, further work was focused on the role of ECSIT in the assembly of mitochondrial complex I. To determine if and how this role was affected, complex I levels and activity as well as the assembly process was assessed in a variety of tissues. As the primary phenotype was cardiac, initial characterisation took place in mitochondria and tissue lysates from the heart. Further investigation was also carried out in brain tissue as this is a tissue typically associated with complex I deficiency related phenotypes. Where possible comparisons have also been made to kidney, liver and muscle samples.

5.3.1. Electron transport chain proteins

Quantification of electron transport chain proteins was used as a crude assessment of overall complex levels and activity across all tissues available. Tissues tested were taken from male (n=3) and female (n=3) wild type and *Ecsit*$^{N209I/N209I}$ animals at 16 weeks of age. Results show a consistent reduction in complex I protein (NDUFB8) levels across tissues tested (Figures 5.6-5.10) with the exception of skeletal muscle. The most significantly affected of these tissues is the heart, with a >95% reduction in total complex I protein levels. Other tissues form a continuum from no (muscle) or very mild (brain) affect to a moderate reduction (liver) indicating that the effect of the N209I mutation in ECSIT does not uniformly affect complex I production across all tissue and cell types. None of the tissues tested show a reduction in any of the remaining electron transport chain proteins tested, and interestingly, none show an elevation of the remaining proteins as might be seen with a potential compensatory effect.

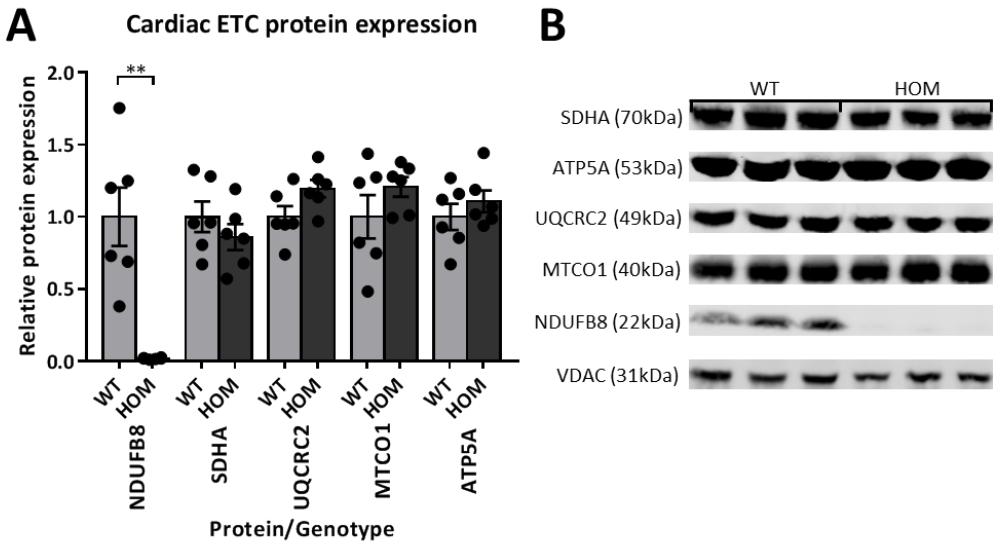

Figure 5.6. Quantification of cardiac electron transport chain proteins (A) NDUFB8 (CI), SDHA (CII), UQCRC2 (CIII), MTCO1 (CIV) and ATP5A (CV) from wild type and *Ecsit*$^{N209I/N209I}$. Results show a significant reduction in the complex I protein NDUFB8 in *Ecsit*$^{N209I/N209I}$ heart tissue, with no changes in any of the remaining complexes. Representative blots (B) reflect this change with a profound loss of NDUFB8 seen in *Ecsit*$^{N209I/N209I}$ (HOM) samples. Mean ± SEM, **p<0.01.

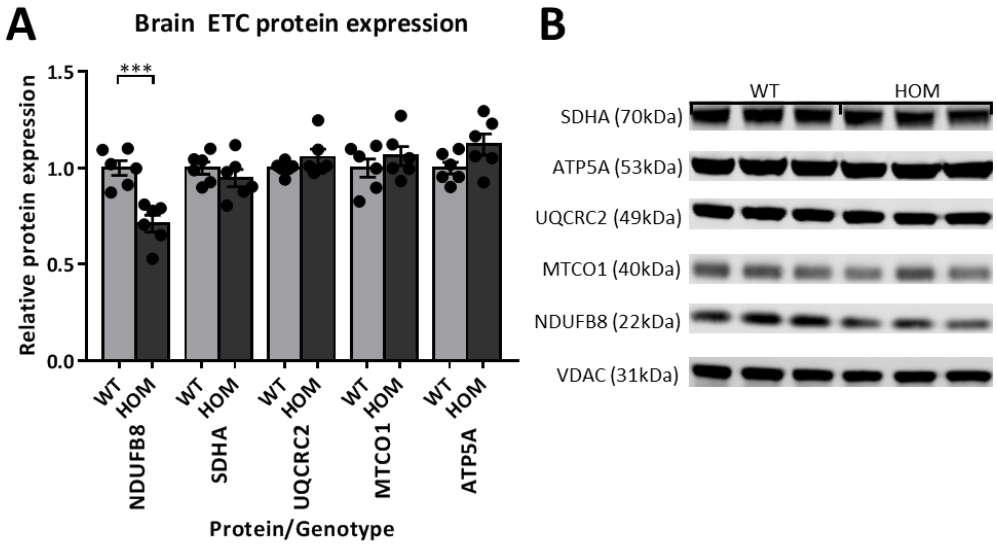

Figure 5.7. Quantification of brain electron transport chain proteins (A) NDUFB8 (CI), SDHA (CII), UQCRC2 (CIII), MTCO1 (CIV) and ATP5A (CV) from wild type and *Ecsit*$^{N209I/N209I}$. Results show a significant reduction in the complex I protein NDUFB8 in *Ecsit*$^{N209I/N209I}$ brain tissue, with no changes in any of the remaining complexes. Representative blots (B) reflect this change with a slight reduction of NDUFB8 seen in *Ecsit*$^{N209I/N209I}$ (HOM) samples. Mean ± SEM, ***p<0.001.

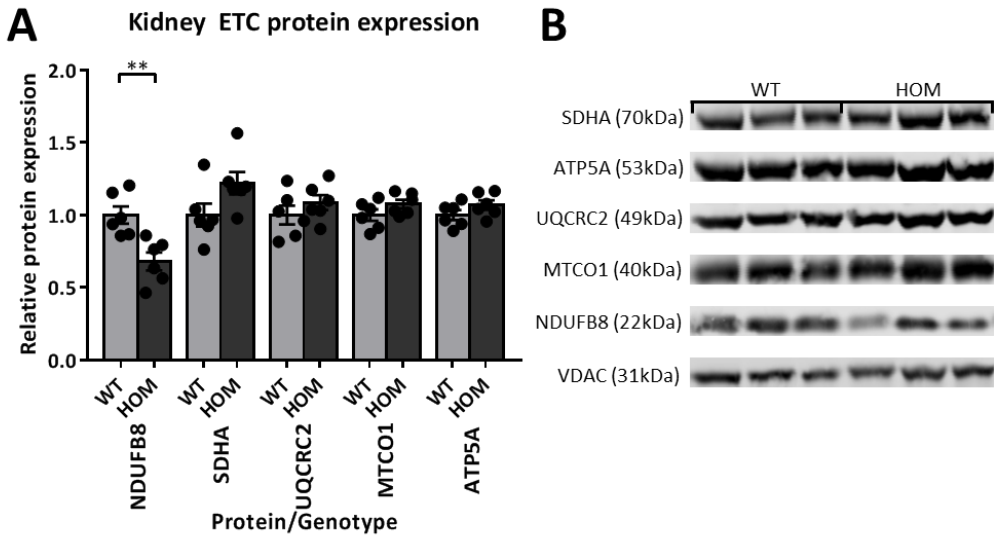

Figure 5.8. Quantification of kidney electron transport chain proteins (A) NDUFB8 (CI), SDHA (CII), UQCRC2 (CIII), MTCO1 (CIV) and ATP5A (CV) from wild type and *Ecsit*$^{N209I/N209I}$. Results show a significant reduction in the complex I protein NDUFB8 in *Ecsit*$^{N209I/N209I}$ kidney tissue, with no changes in any of the remaining complexes. Representative blots (B) reflect this change with a slight reduction of NDUFB8 seen in *Ecsit*$^{N209I/N209I}$ (HOM) samples. Mean ± SEM, **p<0.01.

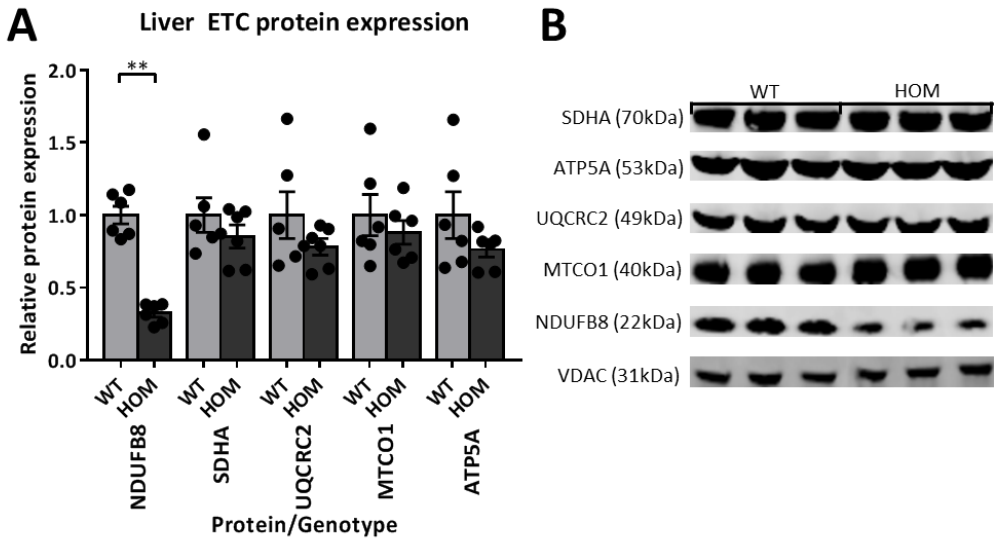

Figure 5.9. Quantification of liver electron transport chain proteins (A) NDUFB8 (CI), SDHA (CII), UQCRC2 (CIII), MTCO1 (CIV) and ATP5A (CV) from wild type and *Ecsit*$^{N209I/N209I}$. Results show a significant reduction in the complex I protein NDUFB8 in *Ecsit*$^{N209I/N209I}$ liver, with no changes in any of the remaining complexes. Representative blots (B) reflect this change with a moderate reduction in NDUFB8 seen in *Ecsit*$^{N209I/N209I}$ (HOM) samples. Mean ± SEM, **p<0.01.

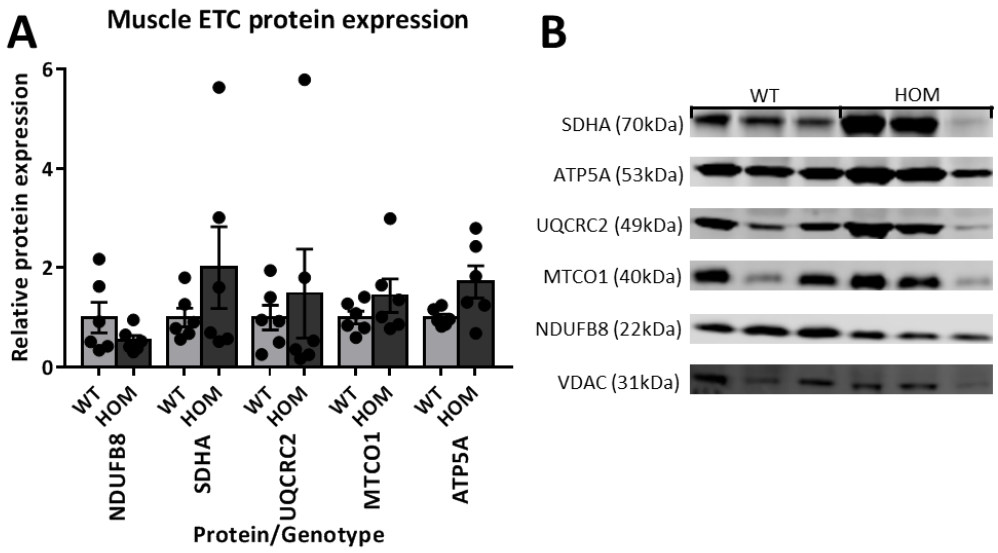

Figure 5.10. Quantification of skeletal muscle electron transport chain proteins (A) NDUFB8 (CI), SDHA (CII), UQCRC2 (CIII), MTCO1 (CIV) and ATP5A (CV) from wild type and *Ecsit*$^{N209I/N209I}$. Results show no significant changes in any of the electron transport chain proteins assessed. Representative blots (B) show no consistent changes between wild type and mutant samples. Mean ± SEM.

5.3.2. Other Complex I proteins

As complex I is a large protein with many sub-complexes and a convoluted assembly process, it is foreseeable that the reduction in NDUFB8 levels seen in the previous section may not hold true for all complex I proteins or subcomplexes. To investigate this, a selection of proteins from each of the complex I sub-complexes was blotted to determine protein levels in both heart (Figure 5.11) and brain (Figure 5.12) tissue. Tissues tested were taken from male (n=3) and female (n=3) wild type and *Ecsit*$^{N209I/N209I}$ animals at 16 weeks of age. The proteins tested show a significant reduction in the levels of all complex I sub-complexes but not in all proteins tested. NDUFV2 is a constituent of the N sub-complex and shows a reduction in both heart and brain tissue, however, as with NDUFB8 this reduction is more severe in cardiac tissue (>95%) than in brain tissue (~25%). Constituent proteins of the Q sub-complex, NDUFS2 and S8, show a less significant reduction in heart tissue (70-90%) than NDUFV2, whilst the protein NDUFS3 does not show a significant reduction at all in heart tissue. In the brain this same pattern is seen, however, the level of reduction of the affected proteins is less severe in brain tissue (30-40%) than in cardiac, with NDUFS3 unchanged. One of the proteins of the proximal portion of the membrane arm, NDUFC2 shows the same pattern of significant reduction in heart (>95%) with only a moderate decrease in brain (~50%). The other,

NDUFA8 shows a steep reduction in heart (>95%) with no difference in brain. Unfortunately, MT-ND1, which shows no difference in cardiac tissue was unable to be detected in brain tissue. The proteins of the distal portion of the membrane arm demonstrate the most consistent results in both tissues NDUFB11 and B3 show a greater reduction in cardiac tissue (70-80%) than in brain tissue (~25%). Finally, the accessory protein, NDUFA10 maintains the trend with a greater than 95% reduction in heart tissue and only a 25% reduction in brain tissue. Taken together, these data suggest that the effect of the N209I mutation in ECSIT is not observed uniformly across all proteins and sub-complexes of complex I with proteins of the membrane arm more consistently affected than those in the N or Q subunits. It is also noteworthy that the mitochondrially encoded protein MT-ND1 was the only protein of the membrane arm tested that showed no significant reduction in cardiac tissue.

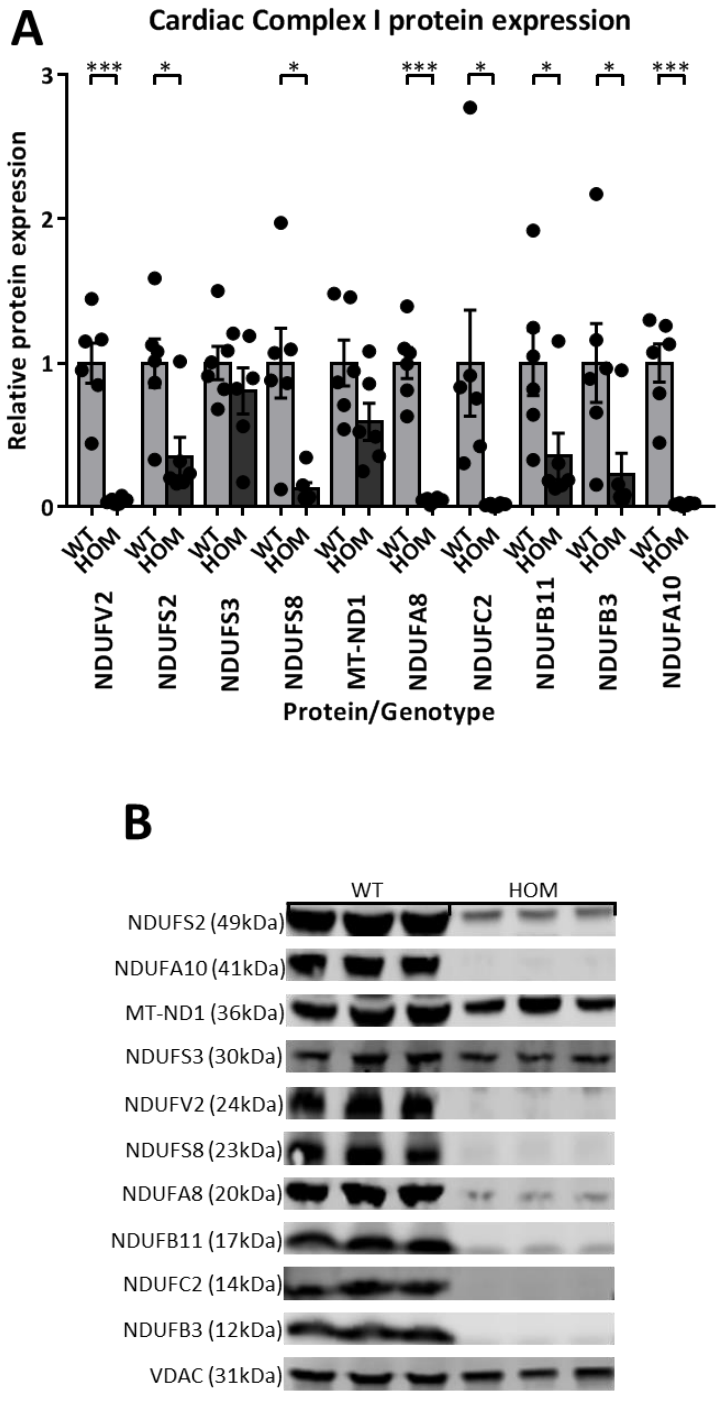

Figure 5.11. Quantification (A) and representative blots (B) of other complex I proteins in heart tissue. The proteins tested represent the various subcomplexes of complex I, N (V2), Q (S2, S3, S8), P_P (ND1, A8, C2), P_D (B11, B3) and the accessory protein NDUFA10. Quantification (Normalised to VDAC, relative to WT average) shows a significant reduction in protein levels of all except 2 proteins, NDUFS3 and MT-ND1. Mean ± SEM, *p<0.05, ***p<0.001.

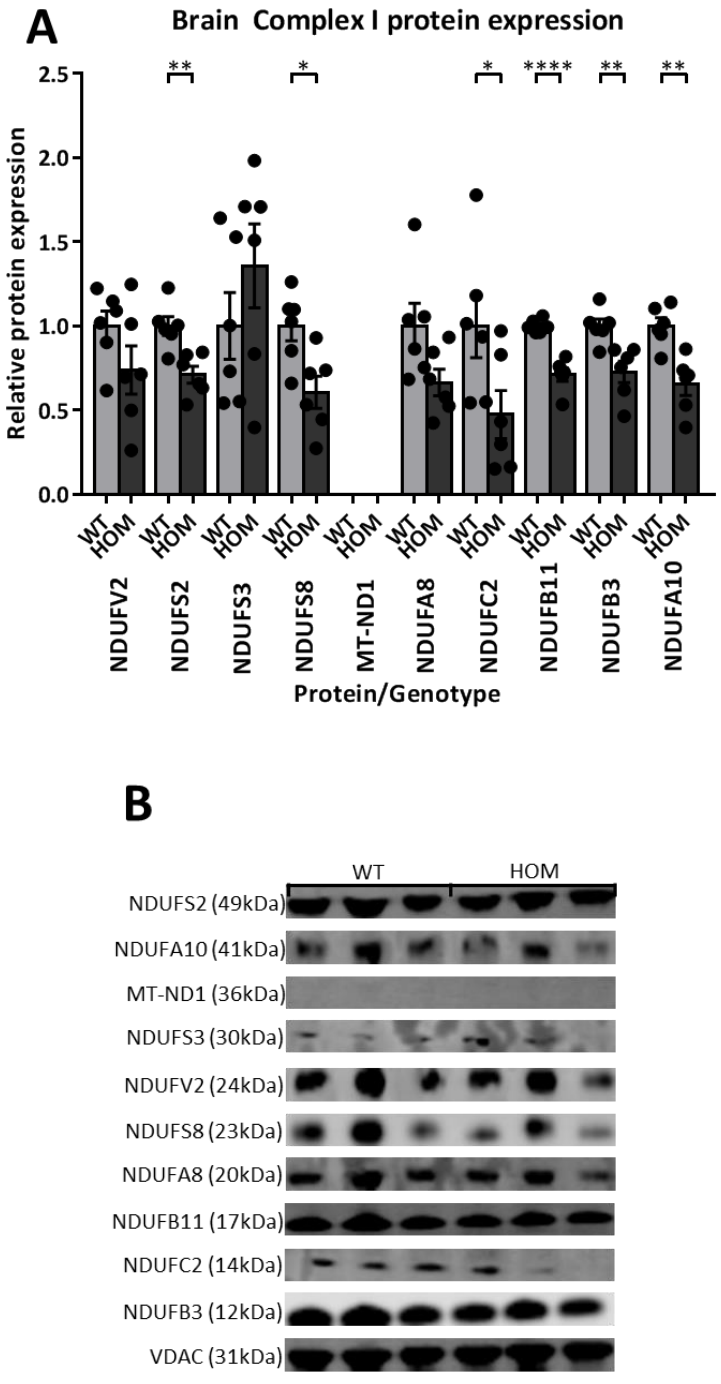

Figure 5.12. Quantification (A) and representative blots (B) of other complex I proteins in brain tissue. As in heart tissue proteins tested represent the various subcomplexes of complex I, N (V2), Q (S2, S3, S8), P_P (ND1, A8, C2), P_D (B11, B3) and the accessory protein NDUFA10. Quantification (Normalised to VDAC, relative to WT average) shows a significant reduction in protein levels of NDUFS2, S8, C2, B11, B3, A10. NDUFV2, S3 and A8 show no significant changes in protein levels in brain tissue and MT-ND1 was undetectable on blots. Mean ± SEM, *p<0.05, **p<0.01, ****p<0.0001.

5.3.3. Electron Transport Chain Proteins in 2 Week Old Hearts

The changes in complex I protein levels are most distinct in cardiac tissue with a >95% reduction in complex I protein levels whilst other tissues show a comparatively modest reduction. As the tissue samples used for previous immunoblotting were obtained from 16 week animals, long after the onset of the cardiac phenotype, it is difficult to determine if the complex I deficiency is causative of the cardiac phenotype, or if the ECSIT N209I mutation affects the tissue in a different manner and the complex I deficiency is secondary to this effect.

To investigate this further, cardiac tissue was collected from 2-week old wild type and *Ecsit*$^{N209I/N209I}$ animals to determine if the mitochondrial dysfunction precedes the cardiac phenotype first seen at around 4 weeks of age. Western blots were performed in the same manner as those shown previously. Results (Figure 5.13) demonstrate a reduction in complex I protein levels (NDUFB8) as was seen in 16-week old cardiac tissue though at this time point it is of a smaller magnitude (~60%). As with the 16 week old hearts, no changes in any other mitochondrial complexes are apparent in the 2 week old hearts.

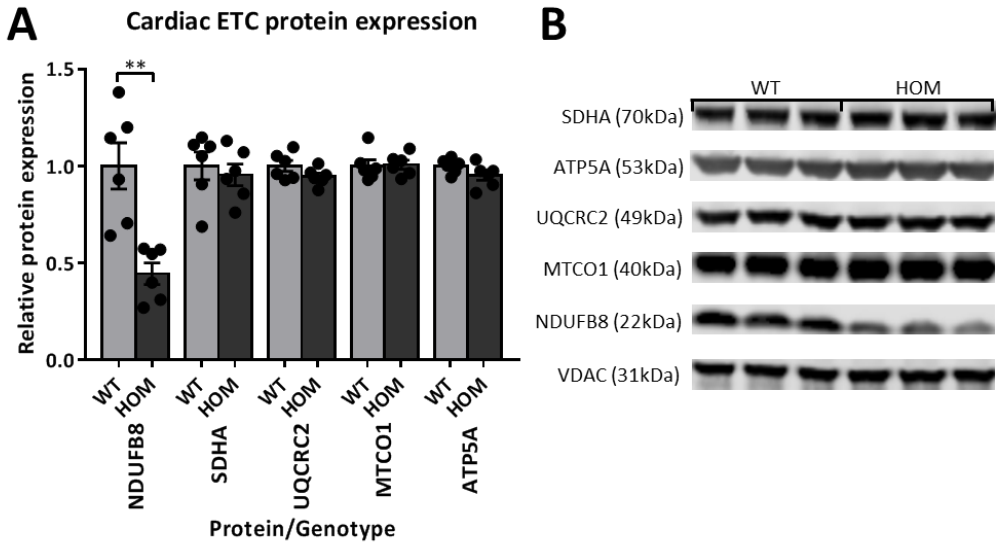

Figure 5.13. Quantification of cardiac electron transport chain proteins (A) NDUFB8 (CI), SDHA (CII), UQCRC2 (CIII), MTCO1 (CIV) and ATP5A (CV) from wild type and *Ecsit*$^{N209I/N209I}$ 2 week old hearts. Results show a consistent reduction in the complex I protein NDUFB8 in *Ecsit*$^{N209I/N209I}$ heart tissue, as well as a consistent elevation of complex IV protein MTCO1. Representative blots (B) reflect the changes seen in the quantification. (Mean ± SEM), **p<0.01.

5.3.4. In Gel Activity

Whilst a reduction in complex I proteins gives an idea of how much complex I is available to function as part of the electron transport chain, it does not reflect the true levels of the fully assembled complex or the activity of those fully assembled units. By isolating intact mitochondria from tissue and running on native first dimensional PAGE it is possible to isolate the intact complex I and assess its activity by supplying substrate in the form of NADH. This assay couples the oxidation of NADH to the reduction of the compound nitro-blue tetrazolium which forms a dark blue stain when reduced. Accordingly, the depth of the staining corresponds directly to the activity of the fully assembled complex I. Mitochondria were isolated from male (n=3) and female (n=3) wild type and *Ecsit*$^{N209I/N209I}$ animals at 16 weeks of age.

Whilst difficult to quantify, the results in figure 5.14 demonstrate a reduction in complex I activity in *Ecsit*$^{N209I/N209I}$ hearts when compared to wild type. Furthermore, whilst a significant reduction in complex I protein levels was seen in brain, the same difference is not apparent in the activity of complex I seen in figure 5.14. It is also worth noting the presence of super-complexes in the wild type lanes of the heart, and in both wild type and mutant lanes in the brain. The formation of these super-complexes is dependent on the presence of complex I and the absence of any super-complexes in the *Ecsit*$^{N209I/N209I}$ lanes of the heart assay is another indication that complex I levels are significantly reduced.

In addition to complex I activity, it is also possible to assess complex IV activity by a similar means. In this case, complex IV is isolated as with complex I above, and supplied with reduced cytochrome C as a substrate. The oxidised cytochrome C then oxidizes DAB to form a brown stain corresponding to the level of complex IV activity. As can be seen in figure 5.15, and as with the protein levels shown previously, this assay demonstrates no changes in complex IV activity between wild type and *Ecsit*$^{N209I/N209I}$ animals in either heart or brain tissue. This supports the hypothesis that ECSIT is only involved in complex I assembly and plays no role in the activity of other electron transport chains.

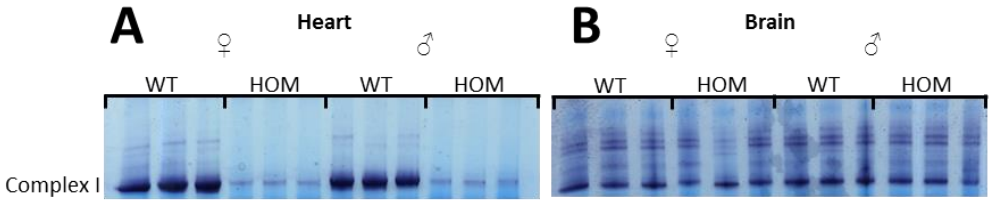

Figure 5.14. In gel activity assay of complex I in mitochondria isolated from heart and brain tissue of wild type and *Ecsit*$^{N209I/N209I}$ animals. Depth of stain corresponds to complex I activity with deeper staining reflecting greater activity. Results show a reduction in complex I activity of *Ecsit*$^{N209I/N209I}$ hearts, whilst brains show no differences between genotypes.

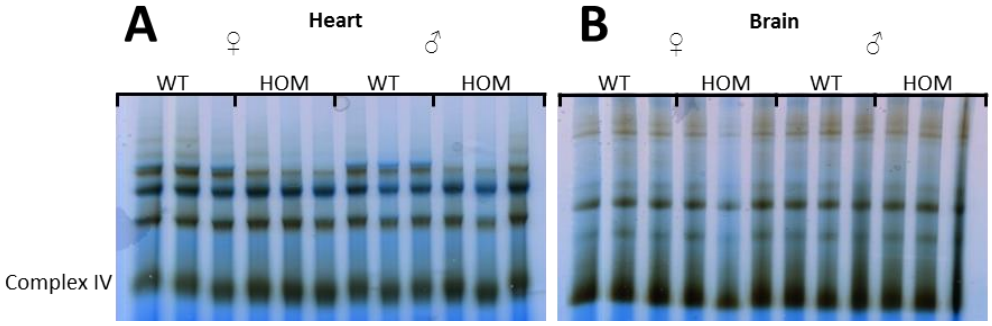

Figure 5.15. In gel activity assay of complex IV in mitochondria isolated from heart and brain tissue of wild type and *Ecsit*$^{N209I/N209I}$ animals. Depth of stain corresponds to complex IV activity with deeper staining reflecting greater activity. Results show no differences between wild type and *Ecsit*$^{N209I/N209I}$ animals in either mitochondria isolated from heart or brain.

5.3.5. Complex I Assay

Due to the difficulty in accurately quantifying the in gel activity of complex I, a further experiment using a plate based assay was performed. This assay captures the intact complex I on the plate using a monoclonal antibody before a substrate is supplied allowing complex I to couple the oxidation of NADH to NAD^+ to the reduction of a die that absorbs light at 450nm. The increase in absorbance at 450nm over time can then be plotted, with the slope of the line corresponding to the level of complex I activity.

For this assay, complex I from both heart (WT n=6, HOM n=6) and brain (WT n=6, HOM n=6) lysates was used to determine the activity of complex I in wild types and *Ecsit*$^{N209I/N209I}$ in both tissues. From figure 5.16 it is apparent that the slope of the lines in both *Ecsit*$^{N209I/N209I}$ heart and brain differs significantly from the wild type. Figure 5.16-A shows the individual plotted averages from heart samples at each time point with error, demonstrating that *Ecsit*$^{N209I/N209I}$ samples give a negative slope with regards to

optical density over time. This would indicate that complex I is either not present or is completely inactive in this tissue as no change in NADH oxidation can be observed. Complex I activity in both wild type and *Ecsit*$^{N209I/N209I}$ brains show a positive slope and whilst the difference in slope is significant (Figure 5.16) the *Ecsit*$^{N209I/N209I}$ samples show a similar slope to wild type samples taken from the heart tissue of the same animals.

Taken together these data indicate that there is a significant impairment of complex I activity in the heart tissue of *Ecsit*$^{N209I/N209I}$ animals and there is a significant although less profound reduction in the complex I activity in brains of these same animals when compared to wild types. It is important to note that this assay is antibody based and if the complex I in heart is unable to bind to the antibody then no activity would be observed. It is also noteworthy that *Ecsit*$^{N209I/N209I}$ brain shows a similar level of complex I activity to wild type heart.

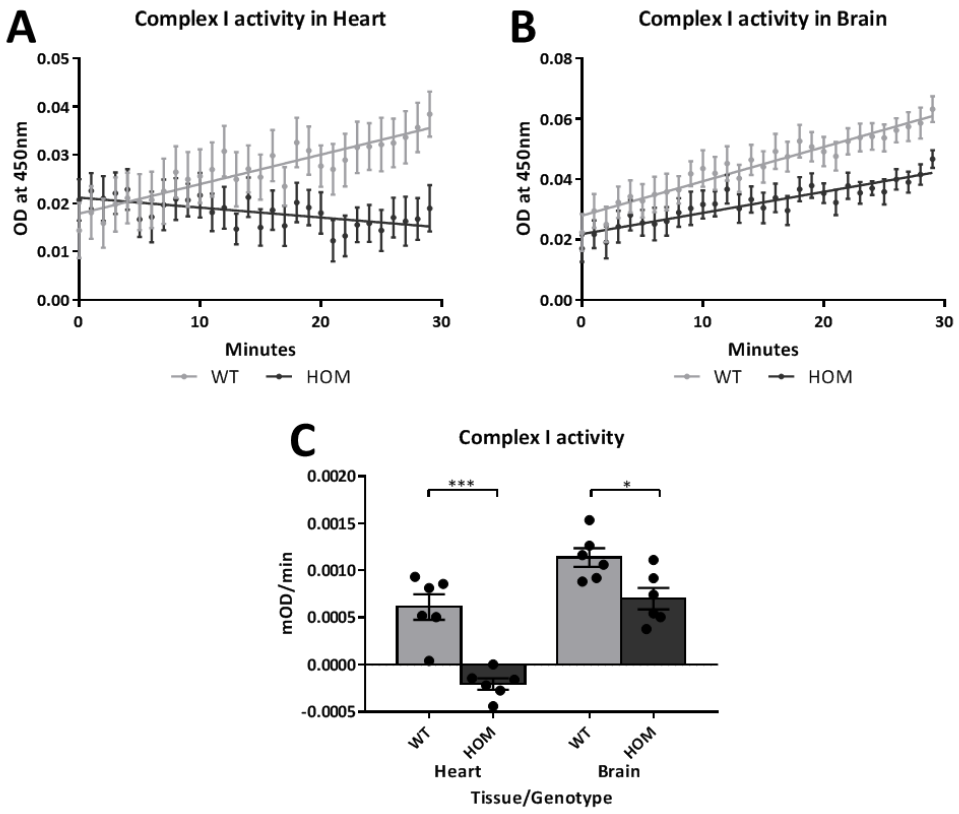

Figure 5.16. Plotted average optical density (OD) at 450nm, against time in heart (A) and brain (B) of wild type (n=6) and *Ecsit*$^{N209I/N209I}$ (n=6) samples. Average slope for each genotype (C) reveals significant differences between wild type and *Ecsit*$^{N209I/N209I}$ animals in both tissues, however, *Ecsit*$^{N209I/N209I}$ in brain shows a similar level of activity to wild type hearts. Mean ± SEM, *p<0.05, ***p<0.001.

5.3.6. Seahorse Analysis of Mouse Embryonic Fibroblasts

To determine if the loss of complex I protein levels and activity translated to an *in vitro* loss of electron transport chain function, mouse embryonic fibroblasts (MEFs) were cultured from wild type and *Ecsit*$^{N209I/N209I}$ embryos and seahorse was performed to measure the response of the cells to a variety of metabolically active compounds.

Basal rates of both oxygen consumption (OCR) and extra cellular acidification (ECAR) were initially measured for 5 cycles to determine the typical respiration rates of the cells without the introduction of any compounds to induce metabolic stress. Under basal conditions no significant differences were observed in either OCR (Figure 5.17-A) or in ECAR (Figure 5.17-B) in cultured MEFs.

Following the basal measurements, oligomycin is added which inhibits the ATP synthase and blocks the electron transport chain. This test indicates whether there is an increased 'leakiness' of the mitochondrial membrane. This is due to the fact that the electron transport chain is unable to continue to function as the H^+ gradient builds up across the inner membrane without the activity of ATP synthase gradually transporting protons in order to power ATP synthesis. Again, no differences can be seen in either OCR or ECAR between wild type and *Ecsit*$^{N209I/N209I}$ MEFs.

To measure maximal oxygen consumption without the inhibitory effect of the H^+ ion gradient across the mitochondrial inner membrane FCCP is added which collapses the gradient. Under these conditions a small but not statistically significant difference can be seen between wild type and *Ecsit*$^{N209I/N209I}$ MEFs indicating that there may be small reduction in the electron transport chain function of these cells, potentially due to the loss of complex I protein.

Finally, rotenone and antimycin A act as complete blocks in the electron transport chain by inhibiting ubiquinone and complex III and preventing the passage of electrons through the chain. Measurements taken at this point represent non-ETC oxygen consumption and can be compared to measurements taken under the influence of oligomycin to determine the oxygen consumption as a result of H^+ ion leakage across the inner mitochondrial membrane. As with the measurements taken in the presence of oligomycin there are no differences in either OCR or ECAR between wild type and *Ecsit*$^{N209I/N209I}$ MEFs.

Taken together these data suggest that the ECSIT N209I mutation has no effect on the ECAR of cultured MEFs, indicating that glycolysis levels are maintained at normal levels despite the loss of complex I protein. Results also demonstrate a small reduction in the maximal OCR of cultured *Ecsit*$^{N209I/N209I}$ MEFs when compared to wild type controls which does not achieve statistical significance. Without any changes in basal or minimal oxygen consumption rates, these data suggest that these mitochondria do not have a significant structural defect and are capable of functioning under normal, 'un-stressed' conditions and may only contribute to a phenotype under stressed conditions. However, without statistical significance, further investigation is required to determine if this small effect is relevant to the phenotype observed in *Ecsit*$^{N209I/N209I}$ animals.

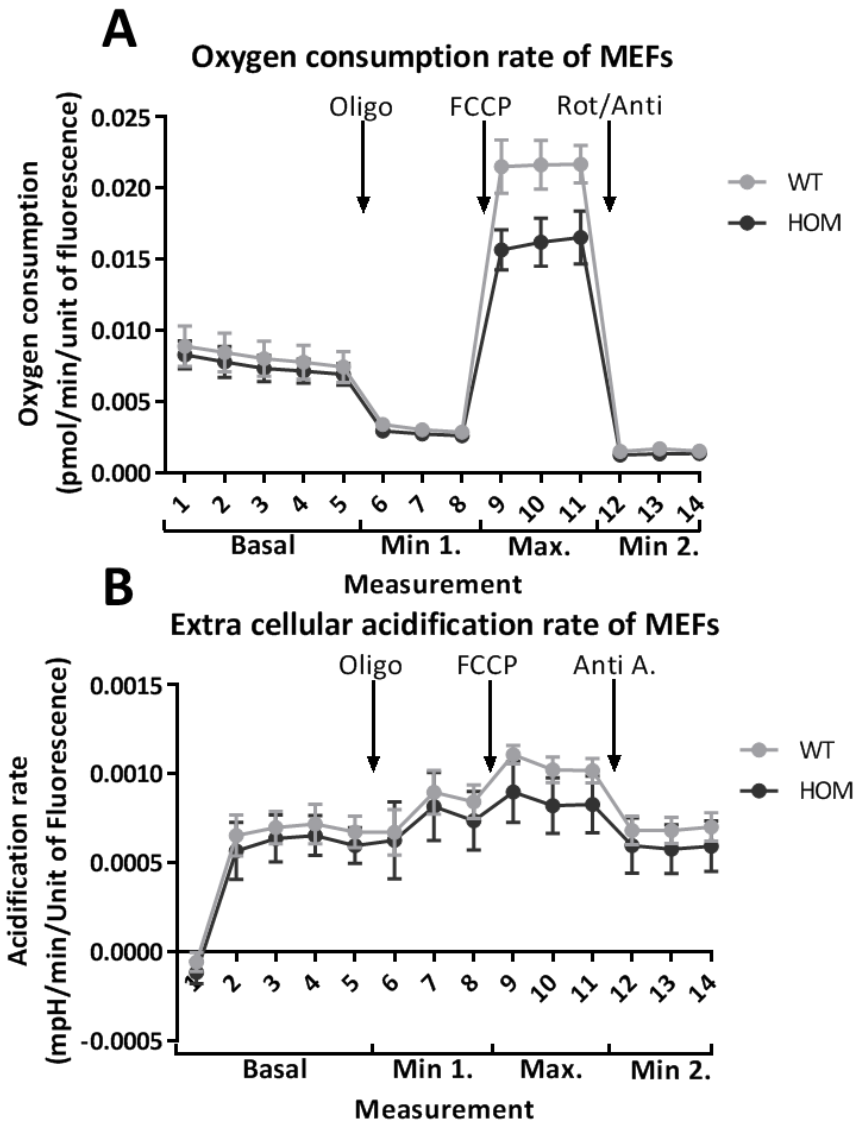

Figure 5.17. Oxygen consumption rate (A) and extra cellular acidification rate (B) of cultured wild type (n=4) and *Ecsit*$^{N209I/N209I}$ (n=4) mouse embryonic fibroblasts. Compounds to induce different respiration states are added to the media between measurements and oxygen consumption at each state is measured. Results show no significant changes in oxygen consumption between wild type and *Ecsit*$^{N209I/N209I}$ MEFs in either oxygen consumption or extra cellular acidification rates. Mean ± SEM.

5.3.7. Seahorse Analysis of Isolated Neonatal Cardiomyocytes

As relatively small, non-significant differences were seen in MEFs from wild type and *Ecsit*$^{N209I/N209I}$ animals and given the tissue specific results seen in protein levels in addition to activity levels it would appear that tests on MEFs would not accurately represent the potential complex I deficiency seen in *Ecsit*$^{N209I/N209I}$ cardiac tissue. To account for this seahorse measurements on cultured neonatal mouse cardiomyocytes were attempted to better investigate the observed in vivo defect. To begin with, neonatal cardiomyocytes were isolated and cultured only from wild type animals to validate the protocol and perform titrations of cell concentration and compounds for optimum seahorse results. Results (Figure 5.18) from these titrations showed a cell concentration of 100,000 cells/well was optimal to give a robust OCR curve without affecting oxygen partial pressure. For FCCP, a concentration of 4µM was selected as it gave a more robust response than any lower levels and higher concentrations gave negligible increase in OCR whilst increasing the likelihood of toxic effects.

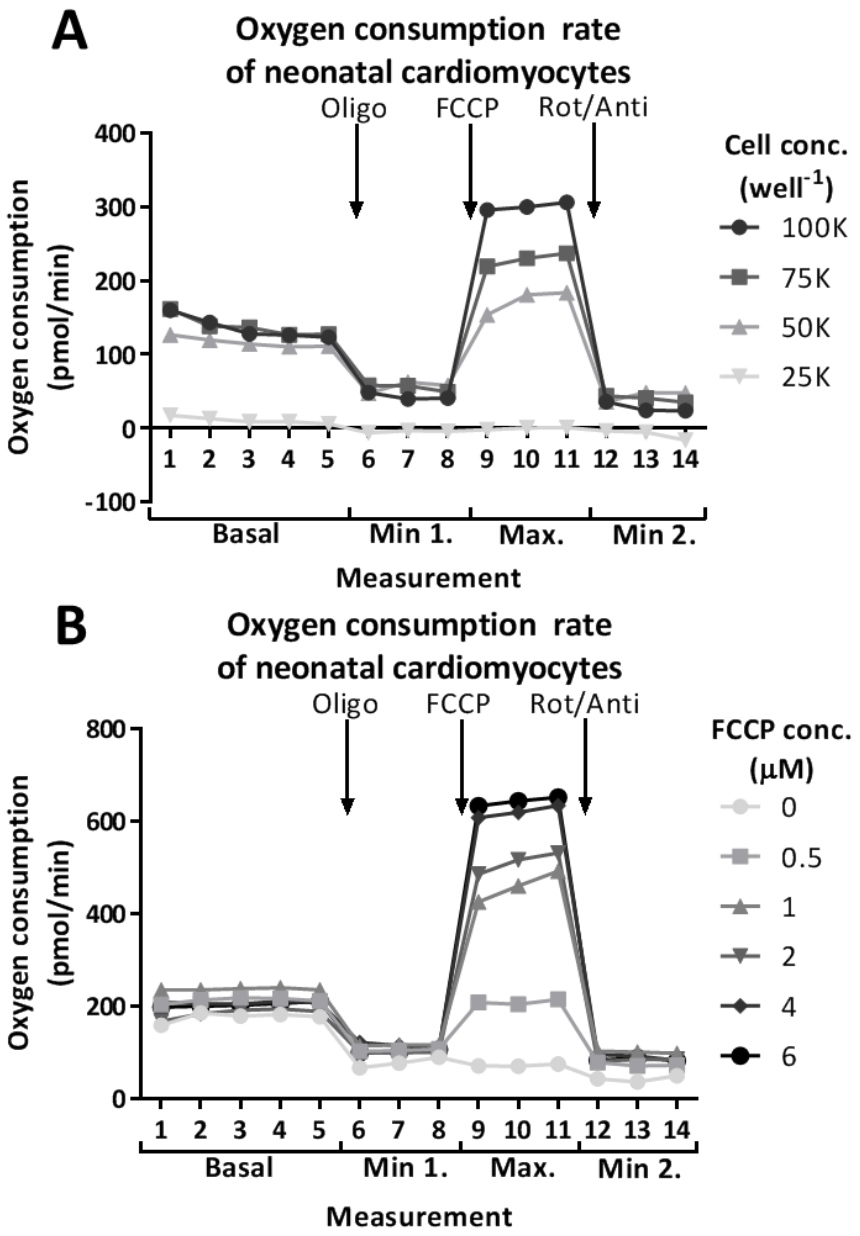

Figure 5.18. Oxygen consumption rates of wild type neonatal cardiomyocytes under cell (A) and FCCP (B) titration conditions. Results indicate that 100K cells/well provides the best oxygen consumption curve and that 4µM FCCP gave a robust response.

Despite these early successes in culturing and measuring oxygen consumption in wild type cardiomyocytes, it was not possible to obtain any results from *Ecsit*$^{N209I/N209I}$ cardiomyocytes. When isolated *Ecsit*$^{N209I/N209I}$ failed to thrive in tissue culture and showed none of the characteristic signs of spontaneous contraction and spreading as was seen in the wild type. Nonetheless, seahorse experiments were attempted and oxygen consumption curves showed no response of mutant cells to any of the compounds (oligomycin, FCCP, rotenone/antimycin A) added to the media during OCR

measurements. As a result, this approach was abandoned in favour of isolated mitochondria.

5.3.8. Seahorse Analysis of Isolated Mitochondria

Because of difficulties using both MEFs and cardiomyocytes, and to further investigate mitochondrial function in the relevant tissues, mitochondria from wild type and *Ecsit*$^{N209I/N209I}$ heart and brain were isolated and seahorse analysis was performed. This assay determines if the defects in complex I assembly in multiple tissues result in an *ex vivo* loss of mitochondrial function or if mitochondria were capable of functioning relatively normally despite a reduction in complex I levels. For this assay, mitochondria were isolated from hearts and brains of wild type and *Ecsit*$^{N209I/N209I}$ animals and plated on a seahorse XF24 plate. The seahorse then measures oxygen consumption of the mitochondria as various compounds are added to induce different mitochondrial respiration states.

Mitochondria begin in state II (pseudo state IV) where substrate is available in the form of glutamate and malate but the absence of ADP forces the mitochondria into a low oxygen consumption state. Readings taken at this time (Figure 5.19) demonstrate no difference between any of the four groups tested. After adding ADP mitochondria increase their oxygen consumption as respiration increases into state III, and is limited only by the speed of the respiratory chain. Here it is apparent that mitochondria from *Ecsit*$^{N209I/N209I}$ hearts have a deficiency in respiratory chain activity (Figure 5.19) as can be seen by the reduction in oxygen consumption compared to wild type heart mitochondria as well as both wild type and *Ecsit*$^{N209I/N209I}$ brain mitochondria. The addition of oligomycin inhibits the ATP synthase and blocks respiration through the electron transport chain, resulting in a dramatic decrease in oxygen consumption. This is an artificial state IV (state IVo), as the rate of respiration is decreased by the presence of oligomycin and not by a lack of ADP in the substrate. At this point there are no differences between any of the mitochondrial groups tested. FCCP then uncouples oxygen consumption by the ETC from ATP production and allows for maximal oxygen consumption during an uncoupled state III (state IIIu). In state IIIu, mitochondria from *Ecsit*$^{N209I/N209I}$ hearts show no significant changes in oxygen consumption from the state III rate measured previously, whilst wild type heart mitochondria show an increase in

oxygen consumption rate. This lack of increased O_2 consumption demonstrates a lack of reserve capacity of the *Ecsit*$^{N209I/N209I}$ heart mitochondria and is reflected in a significant difference between wild type and *Ecsit*$^{N209I/N209I}$ heart mitochondria at this measurement, no significant differences were observed between wild type and *Ecsit*$^{N209I/N209I}$ brain mitochondria. The final measurement takes place in the presence of antimycin a, which binds to and blocks complex III, preventing any oxygen consumption by the electron transport chain. At this point, oxygen consumption rates should be 0, however this is rarely the case due to incomplete binding, leakage and other cellular or mitochondrial processes. As with the state IVo, there are no significant differences between any of the groups measured.

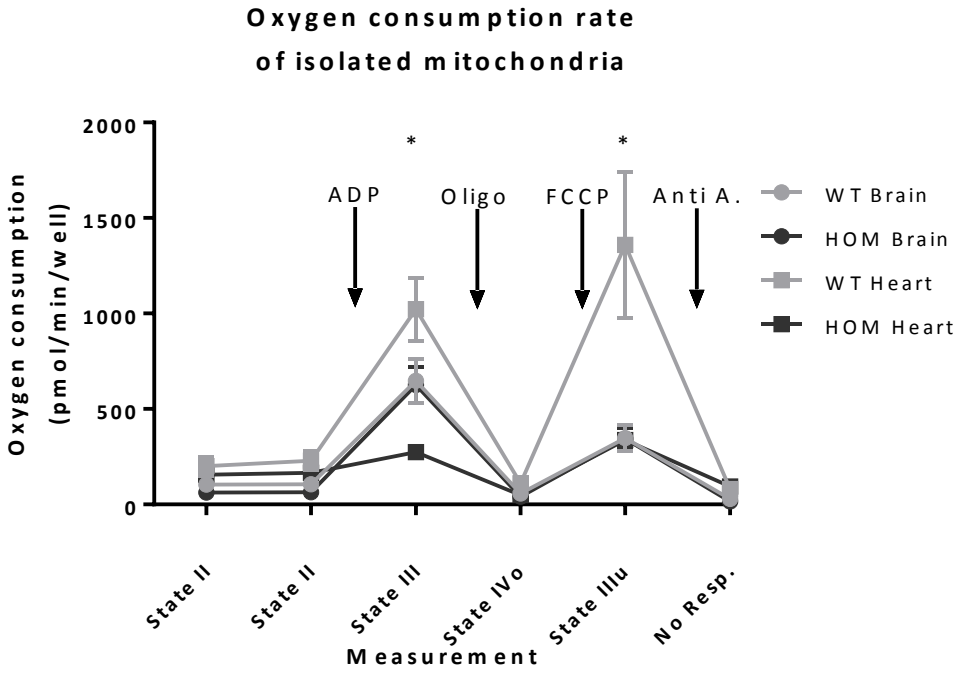

Figure 5.19. Seahorse oxygen consumption rate measurements from wild type and *Ecsit*$^{N209I/N209I}$ heart and brain mitochondria. Compounds to induce different respiration states are added to the media between measurements and oxygen consumption at each state is measured. Significant differences can be seen between wild type and *Ecsit*$^{N209I/N209I}$ heart mitochondria during state III and state IIIu respiration. No differences are seen between wild type and *Ecsit*$^{N209I/N209I}$ brain mitochondria. Mean ± SEM, *p<0.05.

Taken together these data demonstrate a loss of function of the electron transport chain of *Ecsit*$^{N209I/N209I}$ heart mitochondria. However, the mitochondria do retain some residual activity that appears to be sufficient for low steady state respiration, but insufficient to increase respiration during periods of high demand. Furthermore, brain mitochondria

from both genotypes show no significant changes in respiration despite a decrease in complex I protein levels demonstrated previously.

5.4. ECSIT

Whilst it is apparent that complex I protein levels, activity and assembly are affected by the N209I mutation in ECSIT, it was also relevant to look at how the mutation affected the expression of ECSIT protein, as well as its interactions with known binding partners and complex I proteins. This may provide clues to the mechanism of ECSIT in complex I assembly and to how the N209I mutation affects this mechanism.

5.4.1. ECSIT protein blots

ECSIT is known to have two different isoforms in mouse tissue, a 50kDa cytosolic full length isoform, and a 45kDa mitochondrially localised isoform [231]. The 45kDa isoform is formed from the full length 50kDa isoform via the loss of a 5kDa N-terminal mitochondrial localisation signal (amino acids 1-48) that is cleaved upon transport into the mitochondria. As the N209I mutation is approximately 150 amino acids downstream of the N-terminal targeting sequence it is unlikely that it interferes with the importation machinery of ECSIT, but the processing of ECSIT was investigated to determine if there was any effect of the mutation on this process. Tissues tested were taken from male (n=3) and female (n=3) wild type and *Ecsit*$^{N209I/N209I}$ animals at 16 weeks of age.

Interestingly, both 50kDa and 45kDa ECSIT protein show increased levels in cardiac tissue of *Ecsit*$^{N209I/N209I}$ animals compared to wild type controls (Figure 5.20). This could indicate a compensatory upregulation of ECSIT to compensate for its reduced capacity to produce fully assembled complex I. On further investigation however, I observed a third, previously undescribed band detected with the ECSIT antibody of approximately 16kDa. This 16kDa fragment is almost completely absent from the cardiac tissue of *Ecsit*$^{N209I/N209I}$ animals, whilst it is present in the wild type heart tissue (Figure 5.20). This upregulation of 50 and 45kDa ECSIT protein is unique to the heart, with no change in the protein levels of either isoform in brain, kidney, liver or skeletal muscle (Figure 5.21). In contrast to heart tissue, none of these tissues showed any presence of the 16kDa fragment of ECSIT in either wild type or *Ecsit*$^{N209I/N209I}$ samples. Taken together these data suggest that heart tissue processes ECSIT protein in a different manner to other

tissues and this may explain why *Ecsit*$^{N209I/N209I}$ animals are absent other major defects, and only display a significant cardiac phenotype.

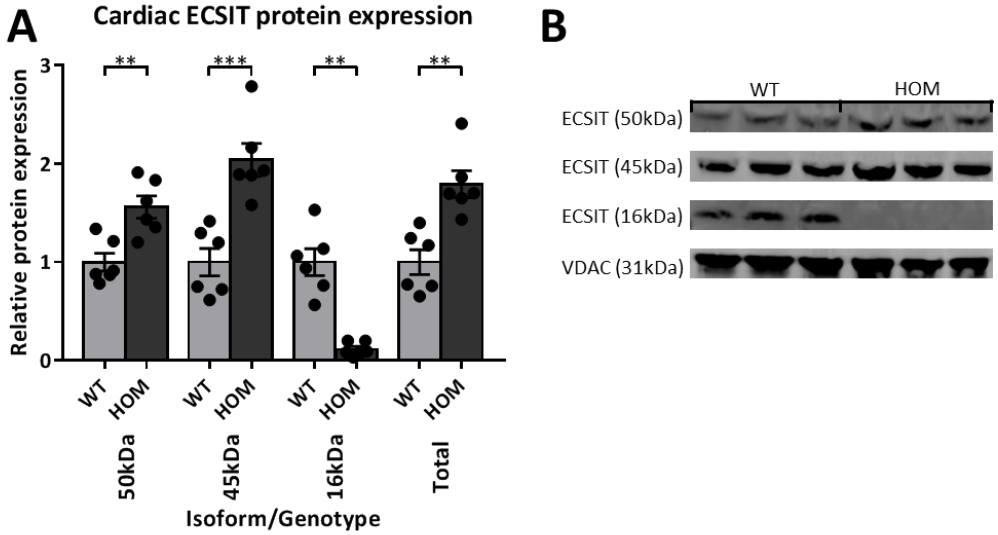

Figure 5.20. Quantification (A) and representative blots (B) or ECSIT protein, normalised to loading control VDAC. Results show an increase in both 50kDa and 45kDa ECSIT protein in *Ecsit*$^{N209I/N209I}$ animals compared to wild type controls. In contrast, 16kDa ECSIT demonstrates a significant reduction in *Ecsit*$^{N209I/N209I}$ animals, to the point where it is essentially undetectable in cardiac tissue from these animals. Mean ± SEM, **p<0.01, ***p<0.001, ****p<0.0001.

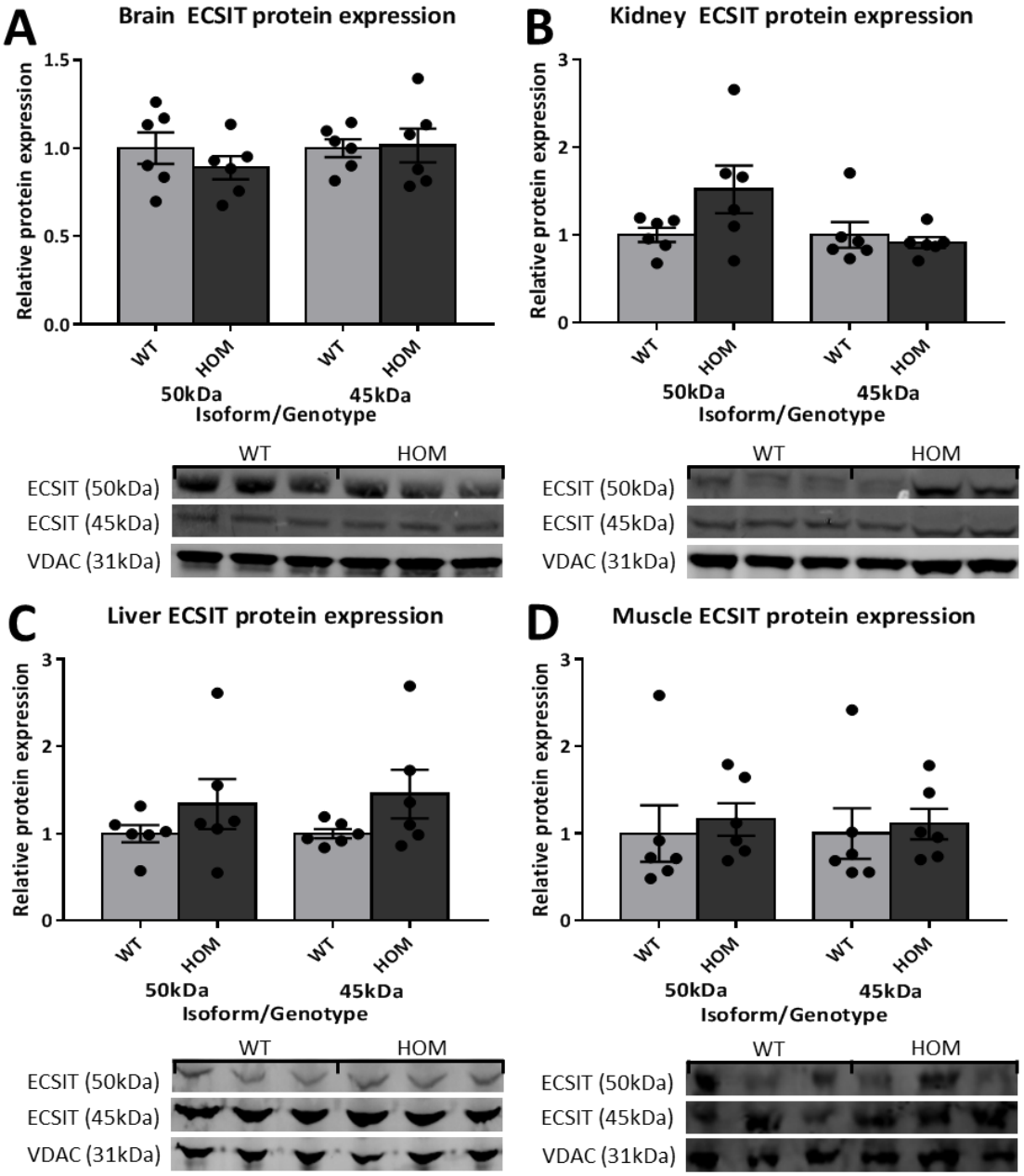

Figure 5.21. Quantification and representative blots from Brain (A), Kidney (B), Liver (C) and skeletal muscle (D) of wild type and *Ecsit*$^{-N209I/N209I}$ animals. In contrast to results from heart tissue, none of the tissues tested show any increase of either 50 or 45kDa ECSIT protein isoforms and the 16kDa fragment seen in heart tissue was undetectable in any of the remaining tissues tested. Mean ± SEM.

5.4.2. ECSIT Protein in 2 Week Old Hearts

I investigated whether or not the elevation or reduction of ECSIT protein preceded the development of the cardiac phenotype by immunoblotting proteins from 2-week-old hearts, where there is no overt sign of cardiomyopathy.

Results (Figure 5.22) show a similar reduction in ECSIT protein in regards to the unconfirmed 16kDa fragment. However, 50 and 45kDa ECSIT protein isoforms do not show the same elevation that was seen in the 16-week hearts. This may be a factor of the age of the hearts, with older hearts accumulating these larger fragments with time as they are unable to undergo the normal degradation process due to the mutation, or build up in an attempt to improve complex I assembly efficiency. These data confirm that the absence of the 16kDa fragment precedes the development of the cardiomyopathy phenotype.

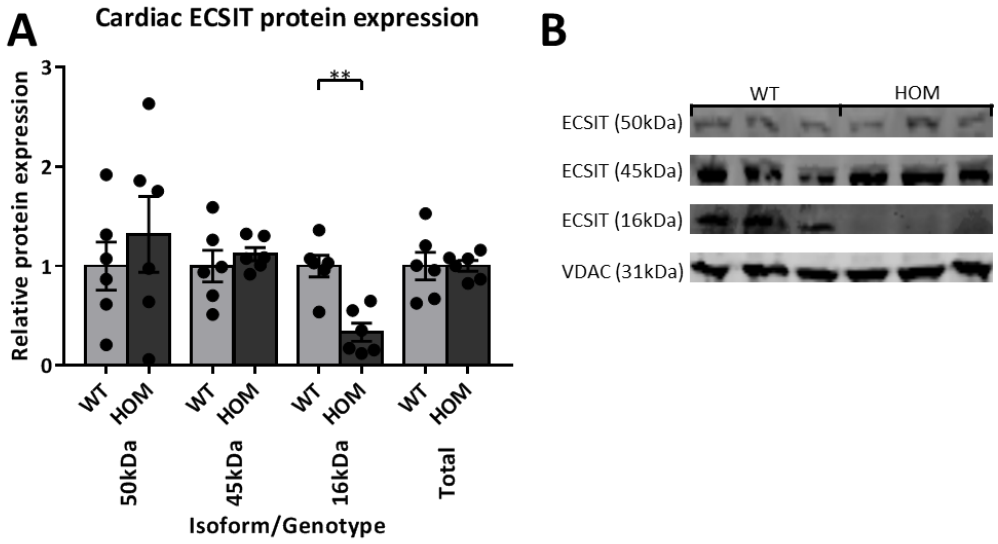

Figure 5.22. Quantification (A) and representative blots (B) or ECSIT protein, normalised to loading control VDAC from wild type and *Ecsit*$^{N209I/N209I}$ 2 week old cardiac tissue. Results show an increase in both 50kDa and 45kDa ECSIT protein in *Ecsit*$^{N209I/N209I}$ animals compared to wild type controls. 16kDa ECSIT demonstrates a reduction in *Ecsit*$^{N209I/N209I}$ animals as was seen in 16 week old cardiac tissue. Mean ± SEM.

5.4.3. NDUFAF1 protein blots

NDUFAF1 is a binding partner of ECSIT, as part of the MCIA complex and the interaction of these two proteins is key to the assembly of complex I. As ECSIT protein levels were elevated in cardiac tissue it was prudent to investigate the protein levels of NDUFAF1 in at least the same tissue. However, commercial antibodies against NDUFAF1 proved to be unsuitable as no protein could be detected in cardiac tissue. To combat this an antibody against human NDUFAF1 was obtained from the lab of Dr Leo Nijtmans (Radboud University Medical Centre). Unfortunately, this antibody resulted in a large number of non-specific binding events and it is impossible to tell which band on the immunoblot membrane belongs to the NDUFAF1 protein. As a result it was not possible to quantify NDUFAF1 protein levels.

5.4.4. ACAD9 protein blots

As with NDUFAF1, ACAD9 is a binding partner of ECSIT and another member of the MCIA complex. Immunoblots were performed to assess the ACAD9 protein levels in various tissues (Figure 5.23). Tissues tested were taken from male (n=3) and female (n=3) wild type and *Ecsit*$^{N209I/N209I}$ animals at 16 weeks of age. Results show no significant changes in the ACAD9 protein levels in any of the tissues tested. These results were expected for the brain, kidney and liver, as no differences were seen in ECSIT protein levels in these tissues. However, as ECSIT protein levels were altered in cardiac tissue it may have been expected that ACAD9 would also show differential levels of protein expression in cardiac tissue. This may indicate that whilst ECSIT protein is not fully functional in complex I assembly its interaction with ACAD9 is unaffected.

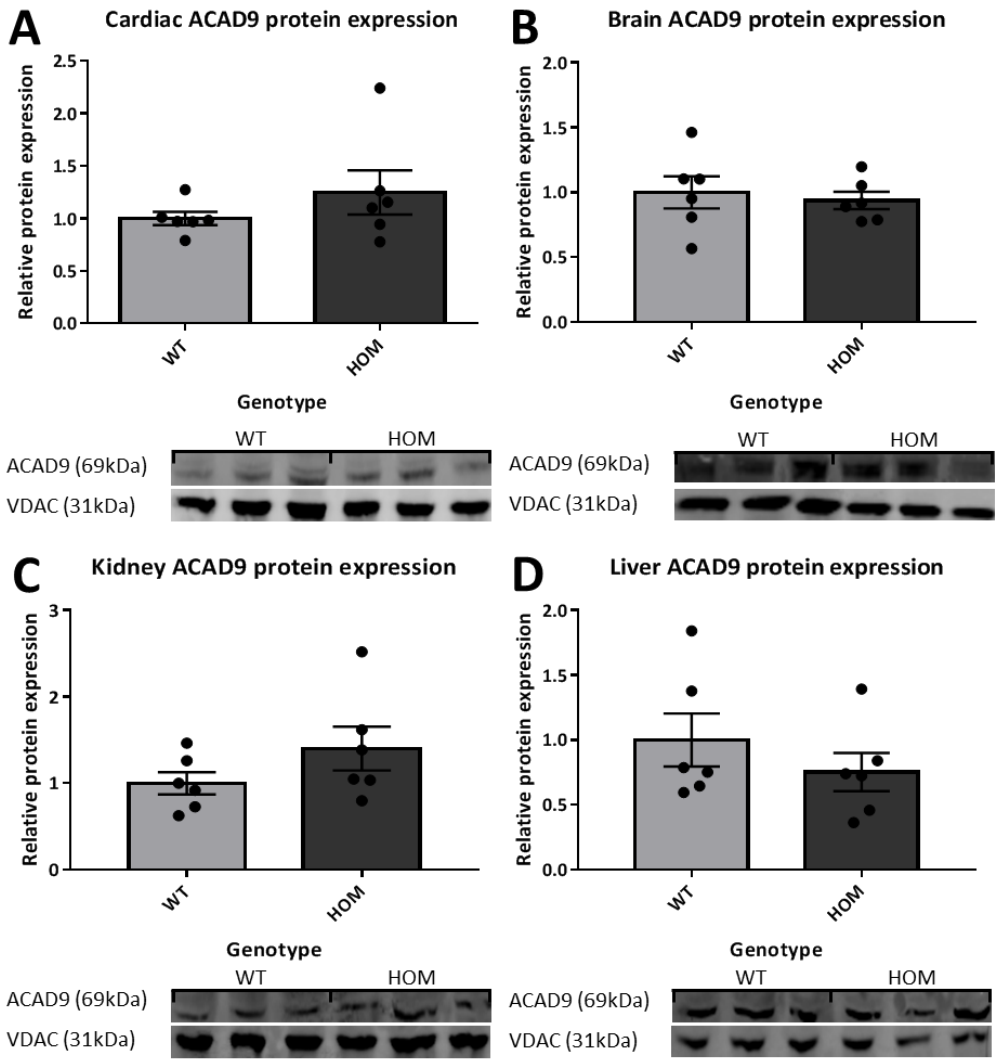

Figure 5.23. Quantification and representative blots of ACAD9 in wild type and *Ecsit*$^{N209I/N209I}$ tissues. Heart (A), brain (B), kidney (C) and liver (D) show no differences in ACAD9 protein levels. Mean ± SEM.

5.4.5. Co-Immunoprecipitation with NDUFAF1

To investigate the interaction of ECSIT protein with the known binding partner NDUFAF1, both full length proteins were cloned into expression vectors (pCMV6) to produce tagged proteins (ECSIT – His, NDUFAF1 – Myc). Site directed mutagenesis was used to introduce the N209I point mutation into the ECSIT ORF to produce the mutant protein. Wild type or N209I ECSIT was then co-transfected into HEK293T cells with the NDUFAF1 clone. Cell lysates were used for immunoprecipitation against one of the protein tags used and the products run on SDS-PAGE to determine if the proteins were interacting. Results (Figure 5.24) show that both wild type (lane 2) and mutant ECSIT (lane 3) as well as NDUFAF1 (lanes 2 and 3) were successfully expressed in HEK293T cells whilst untransfected (lane 1) cells show no expression of either protein. Furthermore, both proteins can be seen expressed as both a cytosolic (ECSIT – 50kDa, NDUFAF1 – 42kDa) and mitochondrially localised (ECSIT – 45kDa, NDUFAF1 – 37kDa) isoforms. Immunoprecipitation against the His tag of wild type ECSIT (lane 4) shows that both isoforms of ECSIT as well as both isoforms of NDUFAF1 are pulled down, indicating that wild type ECSIT is interacting with NDUFAF1 in both the cytosol and the mitochondria. This is confirmed by the reverse reaction, of pulling down NDUFAF1 via its Myc tag, showing the same proteins precipitated (lane 6). Lanes 5 and 7 are empty vector controls confirming that the His tag alone is incapable of pulling down the Myc tagged NDUFAF1 protein, and the Myc tag is incapable of pulling down the His tagged ECSIT. Lanes 8 and 11 demonstrate the same experimental procedure using the mutant N209I form of the ECSIT protein instead of the wild type. This again shows that in both cases the ECSIT and NDUFAF1 proteins are interacting and capable of being co-immunoprecipitated. Ultimately, these data are important in telling us that the N209I mutation has no impact on the interaction of ECSIT with NDUFAF1 and that the two proteins interact not only in the mitochondria, but also in the cytosol as is demonstrated by the presence of both cytosolic isoforms in all of the co-immunoprecipitation lanes.

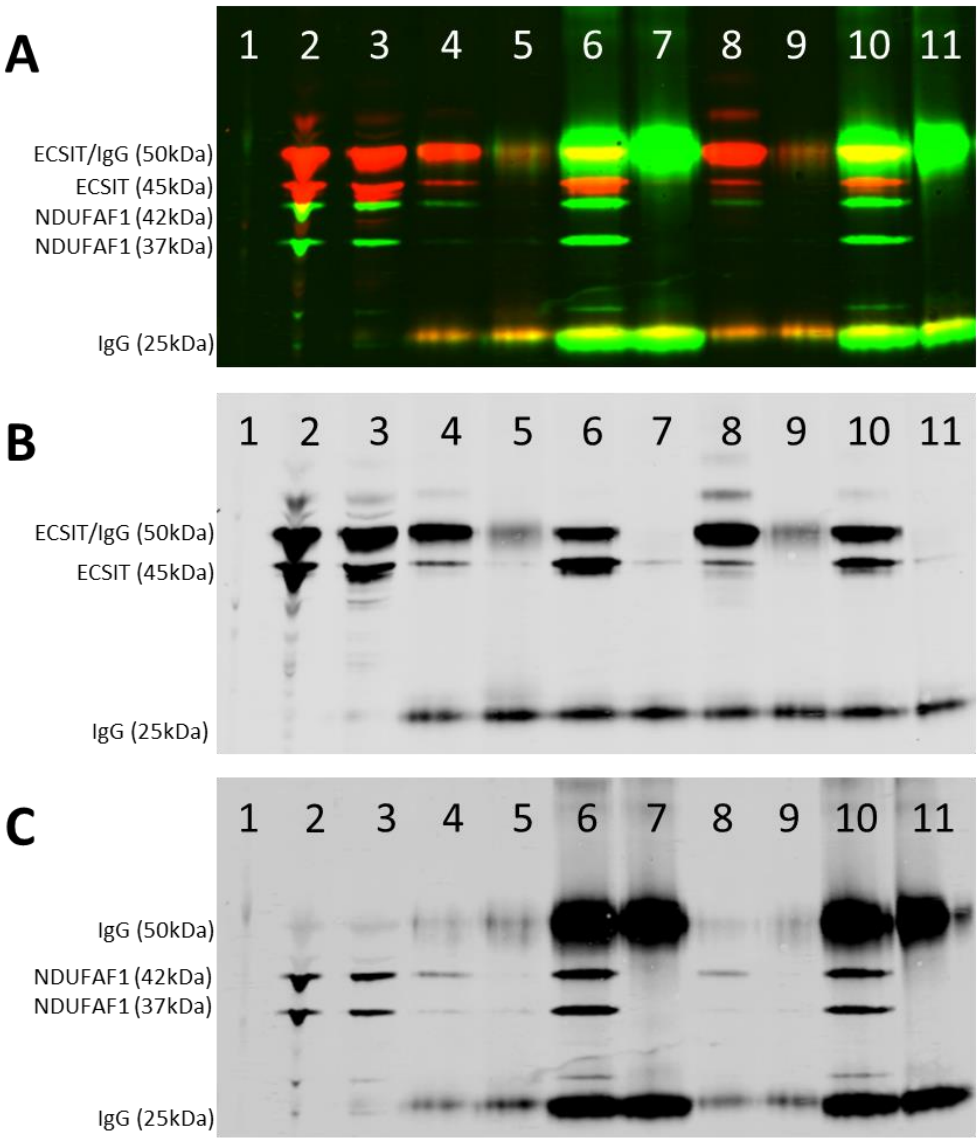

Figure 5.24. Immunoprecipitation of wild type and mutant ECSIT (His tagged) (45 and 50kDa) with full length wild type NDUFAF1 (Myc tagged) (42 and 37kDa). (A) shows combined channels with secondary antibodies against mouse (green – Myc) and rabbit (red – His). (B) and (C) show the separated channels demonstrating the anti-rabbit (Anti-His) and anti-mouse (Anti-Myc) secondary antibodies respectively. 1. Untransfected input lysate, 2. Wild type ECSIT(His) + wild type NDUFAF1(Myc) input lysate 3. ECSIT N209I(His) + wild type NDUFAF1(Myc) input lysate, 4. Wild type ECSIT(His) + wild type NDUFAF1(Myc) anti-His immunoprecipitation, 5. Empty AC-His vector + wild type NDUFAF1(Myc) anti-His immunoprecipitation, 6. Wild type ECSIT(His) + wild type NDUFAF1(Myc) anti-Myc immunoprecipitation, 7. Wild type ECSIT(His) + empty entry(Myc) vector anti-Myc immunoprecipitation, 8. N209I ECSIT(His) + wild type NDUFAF1(Myc) anti-His immunoprecipitation, 9. Empty AC-His vector + wild type NDUFAF1(Myc) anti-His immunoprecipitation, 10. N209I ECSIT(His) + wild type NDUFAF1(Myc) anti-Myc immunoprecipitation, 11. N209I ECSIT + empty entry(Myc) vector anti-Myc immunoprecipitation.

5.4.6. Co-Immunoprecipitation with ACAD9

As with NDUFAF1, ACAD9 is known to interact with ECSIT as part of the MCIA complex and the potential for the interaction to be destabilised or affected by the N209I mutation in the ECSIT protein was assessed to confirm whether or not this was the cause of the complex I deficiency. As previously, full length wild type and mutant ECSIT were cloned in the pCMV6-AC-His vector (Origene) to produce a His tagged ECSIT protein containing either the wild type asparagine or mutant isoleucine residue at position 209. Similarly, ACAD9 was expressed with a Myc tag in the pCMV6-ENTRY vector (Origene). Transfection of both vectors into HEK293T cells was performed and cell lysates assessed for the presence of the proteins by immunoblotting (Figure 5.25). Whereas ECSIT produces tagged proteins of 50 and 45kDa in size, ACAD9 is expressed as two protein isoforms of 69 (cytosolic) and 64 (mitochondrial) kDa. Successful transfection is confirmed in lanes 2 and 3 of figure 5.25, showing the presence of both ECSIT and both ACAD9 isoforms and the absence of either in lane 1 confirms a lack of contamination in the cell line. Lane 3 demonstrates that immunoprecipitation of the wild type ECSIT by anti-His antibody co-immunoprecipitates both isoforms of the Myc tagged ACAD9 protein. The same is demonstrated in lane 6 by immunoprecipitation of the ACAD9 by anti-Myc antibody showing the presence of the 50 and 45kDa ECSIT isoforms, although the 50kDa isoform shows very minimal quantities. The same procedure with the mutant N209I ECSIT shows that the interaction in both ways is unaffected by the presence of the mutation. The absence of any ECSIT or ACAD9 in the empty vector controls lanes 5, 7, 9 and 11 confirm that the interaction is a result of the protein:protein interaction of ECSIT with ACAD9 and not between the His and Myc tags, or cross specificity of the antibody used.

Taken together, these data confirm that ECSIT and ACAD9 interact within the mitochondria, most likely as part of the MCIA complex. It also suggests that there is some interaction between the proteins in the cytosol although this is a very small proportion of the overall interaction visible. Introducing the N209I mutation into ECSIT has no effect on the interaction of the two proteins, suggesting it is not through the binding of ACAD9 that the ECSIT N209I mutation leads to complex I deficiency.

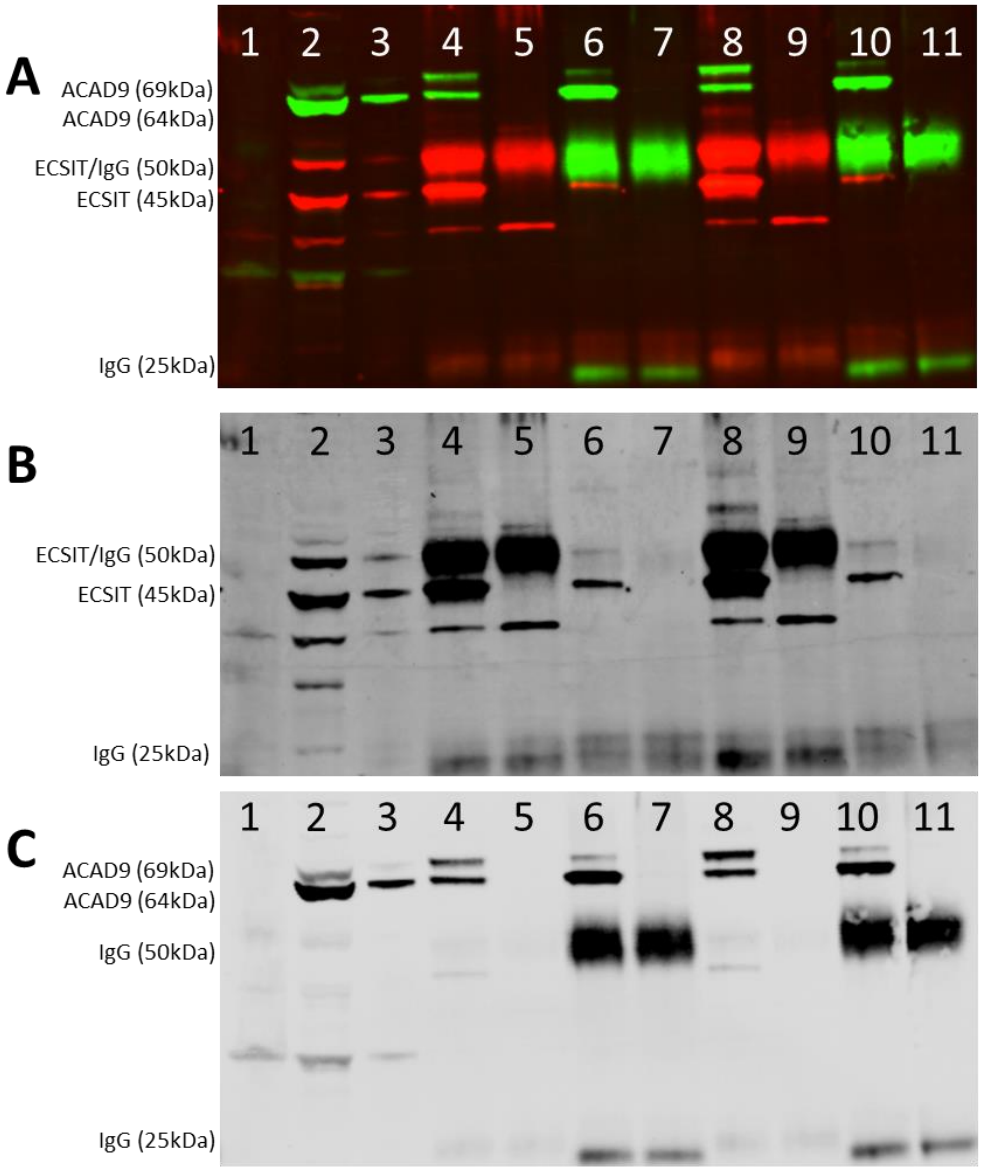

Figure 5.25. Immunoprecipitation of wild type and mutant ECSIT (His tagged) (45 and 50kDa) with full length wild type ACAD9 (Myc tagged) (69 and 64kDa). (A) shows combined channels with secondary antibodies against mouse (green – Myc) and rabbit (red – His). (B) and (C) show the separated channels demonstrating the anti-rabbit (Anti-His) and anti-mouse (Anti-Myc) secondary antibodies respectively. 1. Untransfected input lysate, 2. Wild type ECSIT(His) + wild type ACAD9(Myc) input lysate 3. ECSIT N209I(His) + wild type ACAD9(Myc) input lysate, 4. Wild type ECSIT(His) + wild type ACAD9(Myc) anti-His immunoprecipitation, 5. Empty AC-His vector + wild type ACAD9(Myc) anti-His immunoprecipitation, 6. Wild type ECSIT(His) + wild type ACAD9(Myc) anti-Myc immunoprecipitation, 7. Wild type ECSIT(His) + empty entry(Myc) vector anti-Myc immunoprecipitation, 8. N209I ECSIT(His) + wild type ACAD9(Myc) anti-His immunoprecipitation, 9. Empty AC-His vector + wild type ACAD9(Myc) anti-His immunoprecipitation, 10. N209I ECSIT(His) + wild type ACAD9(Myc) anti-Myc immunoprecipitation, 11. N209I ECSIT + empty entry(Myc) vector anti-Myc immunoprecipitation.

5.5. Complex I Assembly

As ECSIT is a known complex I assembly factor, work was undertaken to determine which step in complex I assembly was primarily affected by the N209I mutation. To do this, mitochondria are isolated from tissue using gentle homogenisation and differential centrifugation. Isolated mitochondria can then be run on Native PAGE to separate the intact complexes and investigate the proteins that comprise these complexes. This is done both in first dimension as a semi-quantitative assessment, and in second dimension where complexes are then denatured, as a more qualitative assessment [294].

5.5.1. 1st Dimensional Blue Native PAGE

First dimensional blue native polyacrylamide gel electrophoresis (BN-PAGE) was performed on mitochondria isolated from hearts of male (n=3) and female (n=3) wild type and *Ecsit*$^{N209I/N209I}$ animals. These were probed using antibodies against complex I subunits, as well as ECSIT itself to determine the level of each protein within the fully assembled complex I.

5.5.1.1. Complex I subunits

Antibodies against each of the main complex I subunits were used to confirm their compatibility with native conditions, and to confirm that the isolation and gel electrophoresis was not destructive of the fully assembled complex I. Figure 5.26 shows the bands corresponding to the proteins incorporated into fully assembled complex I for each of the antibodies tested. NDUFV2 (N), S2 (Q), B11 (P_D-a), B1 (P_D-b), B8 (P_D-c) and A10 (accessory) all confirm the reduction of fully assembled complex I seen in earlier denaturing blots (Section 5.3.2). NDUFC2 (P_P) does not show any banding at the level of fully assembled complex I in either wild type or *Ecsit*$^{N209I/N209I}$ heart mitochondria, possibly indicating an incompatibility with native conditions, or an inability of the antibody to bind to the epitope as it is hidden within the complex structure.

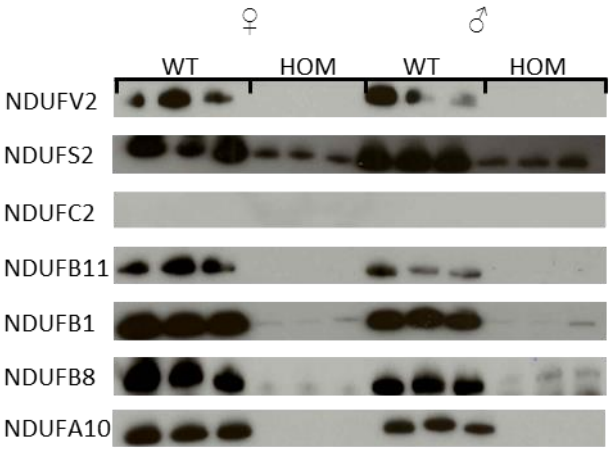

Figure 5.26. First dimensional BN-PAGE blots showing only fully assembled complex I in mitochondria isolated from hearts of wild type and *Ecsit*$^{N209I/N209I}$ animals. Rest of blots is not shown as no other banding was seen.

5.5.1.2. ECSIT

First dimensional BN-PAGE of ECSIT (Figure 5.27) confirms the reduction of fully assembled complex I in *Ecsit*$^{N209I/N209I}$ cardiac mitochondria, in comparison to wild type controls. This result is unexpected as the ECSIT antibody shows a band of fully assembled complex I in the wild type mitochondria, despite previous knowledge suggesting that ECSIT is not a constituent of fully assembled complex I. It also suggests that this may be the 16kDa fragment noted in cardiac western blots as both 45 and 50kDa ECSIT were significantly upregulated in previous experiments.

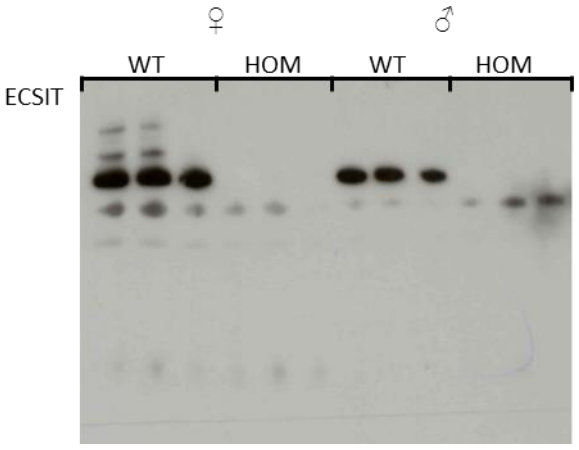

Figure 5.27. First dimensional BN-PAGE blot of ECSIT demonstrating localisation of ECSIT protein with fully assembled complex I.

5.5.2. 2nd Dimensional Blue Native PAGE

Second dimensional blue native PAGE allows for further understanding of the assembly process of complex I, by revealing the proteins involved in each sub-assembly and where the process may be getting 'stuck' as a result of the ECSIT N209I mutation. To investigate this, samples were first run under the native first dimensional conditions, before the gel slice was excised and treated with SDS to denature the proteins in the gel. The slice was run under denaturing conditions to separate the individual proteins from the fully assembled complex. Samples were taken from male wild type (n=3) and *Ecsit*$^{N209I/N209I}$ (n=3) animals. As with the first dimensional BN-PAGE, antibodies against proteins in each of the complex I subassemblies were used to determine which, if any, the ECSIT N209I mutation had a great effect on. Mitochondria from both heart and brain of wild type and *Ecsit*$^{N209I/N209I}$ animals were used to compare the assembly pathway in the affected heart tissue to that of the seemingly unaffected brain tissue.

Results (Figure 5.28) show a reduction in most of the proteins at the level of complex I without the accumulation of any assembly intermediates, making it difficult to determine at which point in the assembly process is affected. NDUFS2, NDUFB8 and NDUFA10 show no differences between wild type and *Ecsit*$^{N209I/N209I}$ mitochondria from heart, with the majority of these proteins being present in a band of a size corresponding to fully assembled complex I. NDUFS2, also shows some evidence of assembly intermediates with a size slightly smaller than fully assembled complex I, but again this is not different between the wild type and *Ecsit*$^{N209I/N209I}$ heart samples. NDUFV2, NDUFC2 and NDUFB1 show a reduction or absence of the protein in complete complex I but do not show an accumulation of assembly intermediates, either because these are broken down rapidly, or do not accumulate as any that is produced is incorporated into complex I, albeit at a much lower total amount. Only NDUFB11 shows a change in the patterning of the blot, with an accumulation of a smaller assembly intermediate, with a modest reduction in the amount incorporated into complete complex I.

Of the proteins investigated in heart tissue, only those with significant differences were investigated further in mitochondria from brain tissue. Of these 4 proteins, NDUFV2, NDUFC2 and NDUFB11 did not show the same reduction in complete complex I or an accumulation of any assembly intermediates as was seen in heart mitochondria.

NDUFB1 was undetectable in brain tissue, likely not due to an absence of the protein, but perhaps a reduction in the amount of complex I or a loss of effectiveness of the antibody.

Overall these data show that the loss of ECSIT function in *Ecsit*$^{N209I/N209I}$ animals is more profound in heart tissue than in the brain, and that not all of the subunits of complex I are affected. From the work of Guerrero-Castillo *et al.* (2016) [72] it is known that ECSIT is bound to proteins of the P_P subassembly and potentially operates in its assembly. These data support that, with a difference seen in NDUFC2. However, the difference in the P_D-a protein of NDUFB11 also suggests that ECSIT may play a role either in the assembly of the P_D subunit or in the marrying of the two subunits together during complex I assembly.

5.5.2.1. Complex I Subunits

Results (Figure 5.28) show a reduction in most of the proteins at the level of complex I, without the accumulation of any assembly intermediates, thus making it difficult to determine which point in the assembly process is affected. NDUFS2, NDUFB8 and NDUFA10 show no differences between wild type and *Ecsit*$^{N209I/N209I}$ mitochondria from heart, with the majority of these proteins being present in a band of a size corresponding to fully assembled complex I. NDUFS2, also shows some evidence of assembly intermediates with a size slightly smaller than fully assembled complex I, but again this is not different between the wild type and mutant heart samples.

NDUFV2, NDUFC2 and NDUFB1 show a reduction or absence of the protein in complete complex I but do not show an accumulation of assembly intermediates. This is likely to be either because these are broken down rapidly, or do not accumulate as any that are produced are incorporated into complex I, albeit at a much lower total level. Only NDUFB11 shows a change in the patterning of the blot, with an accumulation of a smaller assembly intermediate, with a modest reduction in the amount incorporated into complete complex I.

Of the proteins investigated in heart tissue, only those with overt differences were investigated further in mitochondria from brain tissue. Of these 4 proteins, NDUFV2, NDUFC2 and NDUFB11 did not show the same reduction in complete complex I or an accumulation of any assembly intermediates as was seen in heart mitochondria.

NDUFB1 was undetectable in brain tissue, which is unlikely to be due to an absence of the protein, but more likely a reduction in the amount of complex I or a loss of effectiveness of the antibody.

Overall these data shows that the reduction of ECSIT function with regard to complex I assembly in *Ecsit*$^{N209I/N209I}$ animals is more profound in heart tissue than in the brain, and that not all of the subunits of complex I are affected. From the work of Guerrero-Castillo *et al.* [72] it is known that ECSIT is bound to proteins of the P_P subassembly and potentially operates in its assembly. These data support that, with a significant reduction difference seen in NDUFC2. However, the difference in the P_D-a protein of NDUFB11 also suggests that ECSIT may play a role in either the assembly of the P_D subunit or in the marrying of the two subunits together during complex I assembly.

Protein (kDa)	Sub-complex	Genotype	Heart (High Mw→ Low Mw)	Brain (High Mw→ Low Mw)
NDUFV2 (24)	N	WT		
		HOM		
NDUFS2 (49)	Q	WT	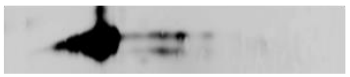	No Difference in Heart
		HOM	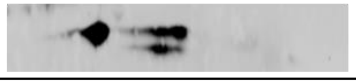	
NDUFC2 (14)	P_P	WT		
		HOM		
NDUFB11 (17)	P_D-a	WT		
		HOM		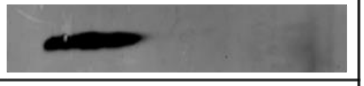
NDUFB1 (12)	P_D-b	WT		Undetectable in brain
		HOM		
NDUFB8 (22)	P_D-c	WT		No Difference in Heart
		HOM		
NDUFA10 (41)	-	WT		No Difference in Heart
		HOM		

Figure 5.28. Representative 2nd dimensional BN-PAGE blots from wild type and *Ecsit*$^{N209I/N209I}$ hearts and brains. Brain mitochondria were only run where a difference was seen in heart mitochondria. In each panel, the high molecular weight complexes are on the left and the low molecular weight on the right.

5.5.2.2. ECSIT

Given the unexpected result in the first dimensional BN-PAGE of ECSIT it was prudent to run the 2nd dimensional blots to determine if the hypothesis about the first dimension was correct i.e. that it was the 16kDa fragment that was co-migrating with complex I. Mitochondria from wild type and *Ecsit*$^{N209I/N209I}$ hearts and brains were run in the first dimension and then in the second dimension to determine which fragments of ECSIT were co-migrating with which complexes of the mitochondria.

2D BN-PAGE blots from wild type and *Ecsit*$^{N209I/N209I}$ hearts (Figure 5.29-A/B) show the presence of the 50kDa band of ECSIT sitting to the left hand side of the blot at a first dimensional size much larger than complex I. Indicating that the 50kDa fragment may be associated with a very large complex or structure, this could be in the form of a mitochondrial import machinery or ribosome.

The 45kDa ECSIT band shows two patches, one small, to the right of the blot, which may be unbound ECSIT, free in the mitochondria, or may be a small protein complex such as MCIA. There are also signs of 45kDa ECSIT at a much larger size in the middle of the blot likely as part of a much larger complex, potentially as part of a complex I assembly intermediate. Importantly for both the 50 and 45 kDa fragments, no differences can be seen between wild type and *Ecsit*$^{N209I/N209I}$ hearts.

Where a difference is visible is the 16kDa fragment, as was seen with the standard SDS-PAGE, the 16kDa fragment is reduced to the point where it is not visible in the *Ecsit*$^{N209I/N209I}$ heart (Section 5.4.1). This blot also confirms that it is the 16kDa fragment that co-migrates with complex I, suggesting that it may form part of the complete complex.

In the brain (Figure 5.29-C/D) 50kDa ECSIT appears as part of a large complex, as it does in heart tissue, however there is no evidence of either the 45 or 16 kDa fragments in either the wild type or *Ecsit*$^{N209I/N209I}$ samples. This is in contrast to the SDS-PAGE of brain tissue where 45kDa ECSIT could be seen albeit at a reduced level, but is in line with the SDS-PAGE with respect to the 16kDa fragment that was not visible in brain tissue.

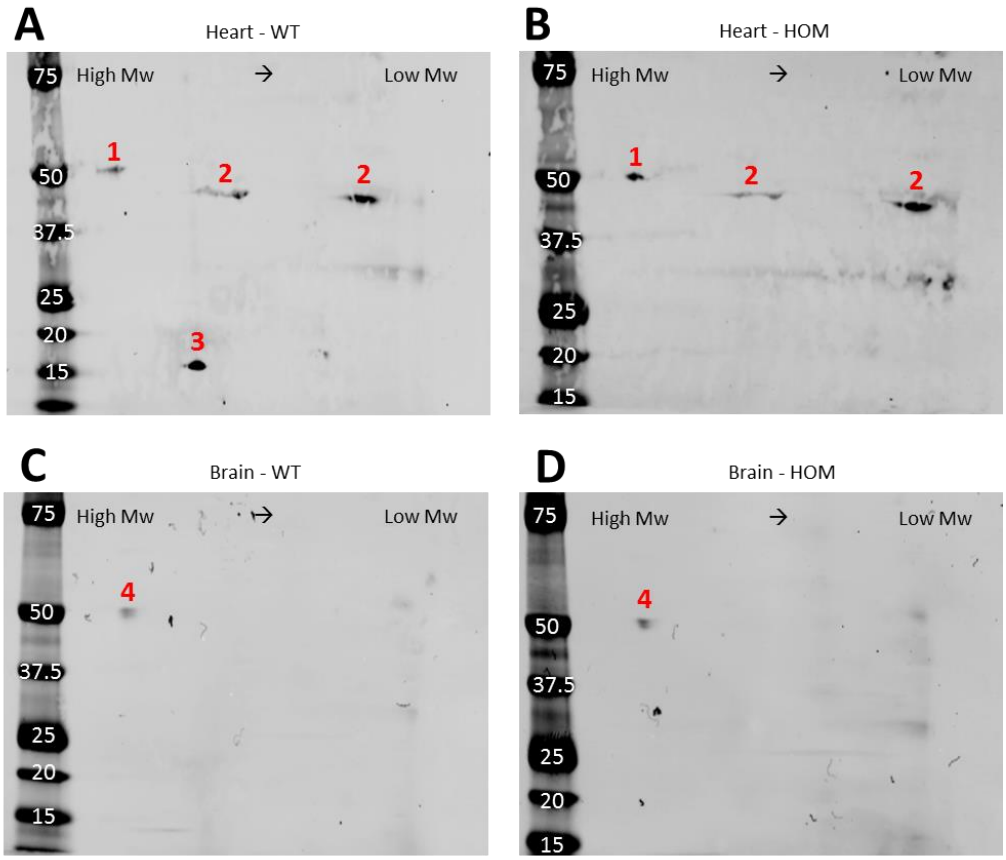

Figure 5.29. Second dimensional BN-PAGE in heart (A and B) and brain (C and D) of wild type and *Ecsit*$^{N209I/N209I}$ animals. Proteins associated with large complexes lie to the left of the blot, and smaller or unbound proteins to the right. Heart shows the presence of 50 (1) and 45 kDa (2) ECSIT in both wild type and *Ecsit*$^{N209I/N209I}$ blots whilst 16kDa (3) is only visible in the wild type. Brain shows only the presence of the 50kDa ECSIT (4).

5.6. Nature of 16kDa fragment

The 16kDa fragment identified initially in SDS-PAGE and later in BN-PAGE appears to be key to complex I assembly in cardiac tissue. However, this may not be the case in all tissues, as even those without the presence of 16kDa in wild type blots show some degree of complex I assembly defect (kidney, liver and brain). To determine the nature of this protein fragment and provide clues as to how the N209I mutation may affect its formation I have attempted to isolate it for mass-spectrometric analysis.

5.6.1. Immunoprecipitation

Immunoprecipitation was performed using a variety of techniques in an attempt to find a method that successfully immunoprecipitated the 16kDa fragment of ECSIT so that it, as well as the 45 and 50 kDa fragments, could be sent for reliable mass-spectrometry.

Initial immunoprecipitation used a method similar to that used for the co-immunoprecipitations of ECSIT with ACAD9, TRAF6 and SMAD4 shown previously. Protein was isolated from wild type heart tissue in RIPA buffer and immunoprecipitated with anti-ECSIT antibody (Abcam) and protein G sepharose beads. Following western blot (Figure 5.30-A) however, no ECSIT protein could be seen indicating that the protein was not immunoprecipitated by the antibody under these conditions, despite all isoforms being visible in the original input protein.

A second attempt was made using a milder incomplete RIPA buffer which should have reduced the chance of loss of binding affinity between the antibody and the protein (Figure 5.30-B). Results show the presence of both the 50 and 45 kDa isoforms in the input lane, however the 16kDa fragment is very faint and none of the isoforms are visible following immunoprecipitation. This may indicate that this lysis buffer is insufficient to liberate the 16kDa fragment from this tissue but given the failure of the immunoprecipitation there appears to be little chance of this protocol being successful.

In a final attempt to immunoprecipitate ECSIT using the original Abcam antibody (Ab21288) immunoprecipitation was performed using a lysis buffer containing triton x-100 instead of SDS and NP-40 as was described by Soler-López et al. (2011) [295] and recommended by the manufacturer as part of trouble shooting procedures. Results (Figure 5.30-C) show robust extraction of all isoforms of ECSIT as seen in the input lane,

however, immunoprecipitation was still unsuccessful with no protein visible in the IP lane. No control is shown.

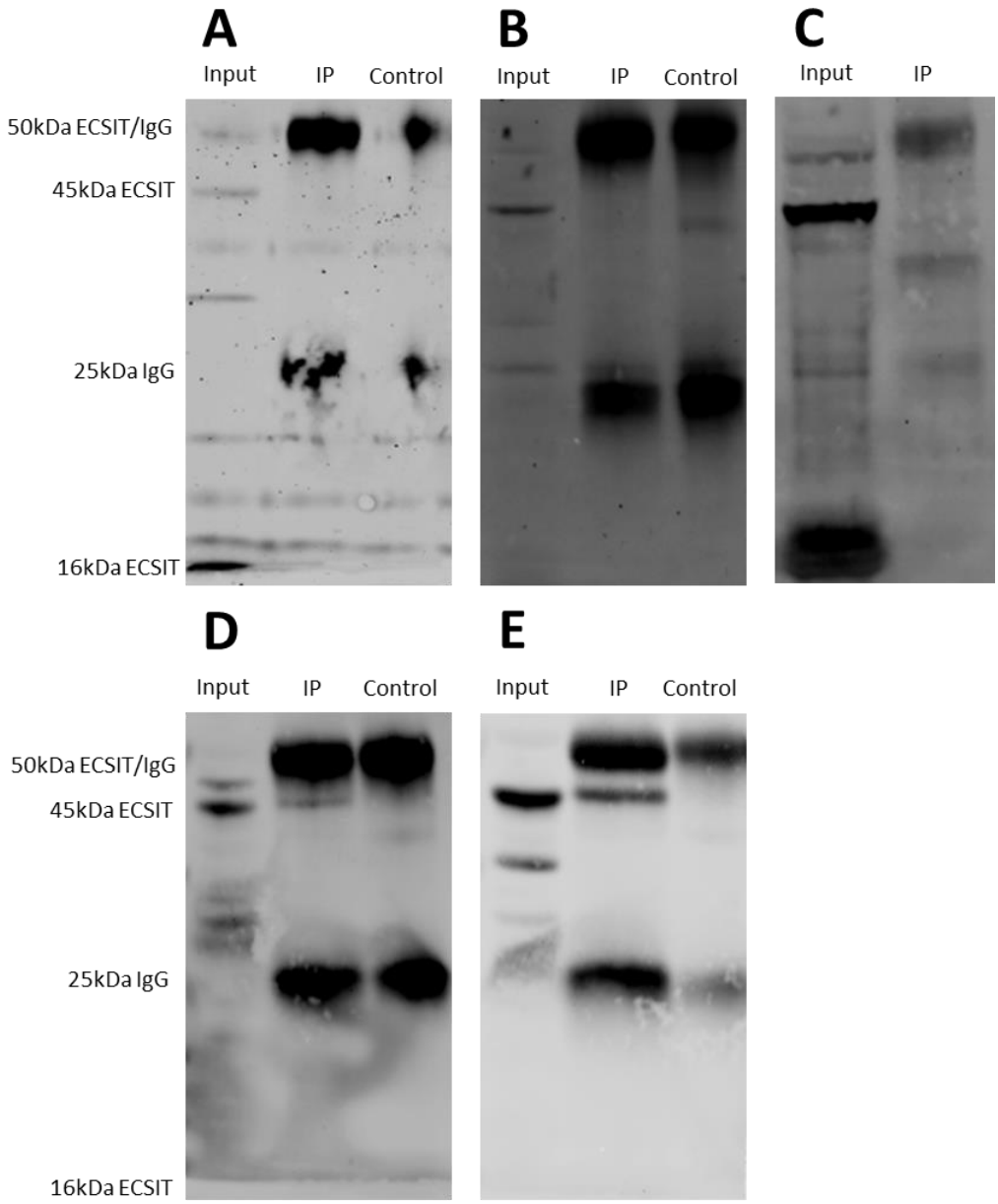

Figure 5.30. Western blots following immunoprecipitation using original Abcam ab21288 anti-ECSIT antibody with proteins extracted using RIPA (A), mild RIPA (B) and triton lysis buffer (C). Westerns of immunoprecipitations using alternative antibodies from Abcam (ab66380) (D) and Atlas (HPA042979) (E) show successful detection and immunoprecipitation of 50 and 45kDa ECSIT but not the 16kDa fragment of interest.

As the ab21288 Abcam antibody appeared unsuitable for immunoprecipitation I decided to try the original RIPA protein extraction protocol with alternative antibodies to determine if mass-spec could be performed in this manner. Anti ECSIT antibodies from

Abcam (ab66380) (Figure 5.30-D) and Atlas (HPA042979) (Figure 5.30-E) both demonstrated an ability to detect and immunoprecipitate the larger fragments of ECSIT, but neither detected or was able to immunoprecipitate the 16kDa fragment.

5.6.2. Mass Spec Results

With the inability of the antibodies used to immunoprecipitate the 16kDa fragment of ECSIT I decided to attempt mass-spectrometry on gel slices taken from 2D BN-PAGE to provide the cleanest possible result and give an overview of the proteins in association with ECSIT at each position in the gel. Four fragments, 50kDa, 45kDa complex bound, 45kDa unbound and 16kDa ECSIT, were excised from a 2D BN-PAGE run using wild type heart mitochondria and showing the presence of all 3 isoforms of ECSIT (Figure 5.31).

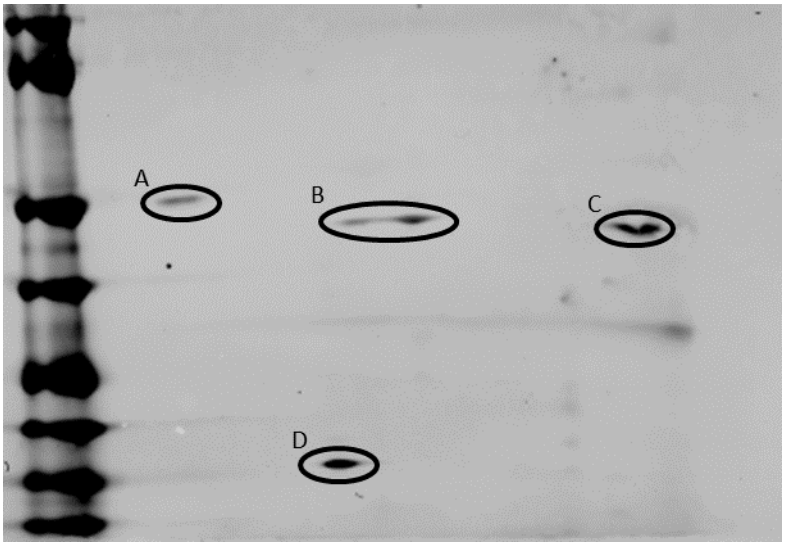

Figure 5.31. Image of wild type 2nd dimensional BN-PAGE showing the 4 fragments excised from the gel and sent for mass-spec. 50kDa ECSIT (A), 45kDa complex bound ECSIT (B), 45kDa unbound ECSIT (C) and 16kDa ECSIT (D).

Mass spectrometric analysis (Appendix 1) failed to identify ECSIT in any of the gel fragments sent for sequencing. Although the presence of a large number of complex I proteins representing all sub-assemblies of complex I was confirmed in gel slice D, confirming the co-migration of this potential ECSIT fragment with complex I.

5.6.3. Validation of ECSIT antibody

As it was not possible to confirm the nature of any of the ECSIT isoforms by mass-spectrometry, confirmation that the antibody was detecting ECSIT protein reliably was tested by transfecting HEK293T cells with the His tagged ECSIT produced for the CO-IP experiments and running lysate on an SDS-PAGE gel. Following western blotting membranes were incubated with both the anti His antibody and the Abcam anti-ECSIT (ab21288) antibody used for the majority of experiments. Co-localisation of the two antibody signals confirmed the specificity of the ab21288 antibody (Figure 5.32). The results are confounded slightly by the presence of the native ECSIT protein in the HEK293T cells that were not transfected, and by the presence of what appears to be extra bands in the transfected cells. However, in reality these extra bands are the combination of both the untagged and tagged protein which will be 1kDa larger than the untagged protein due to the size of the 6x His tag. Unfortunately, as the 16kDa fragment of ECSIT is not produced in HEK293T cells it was not possible to determine if this was a specific antibody interaction or not.

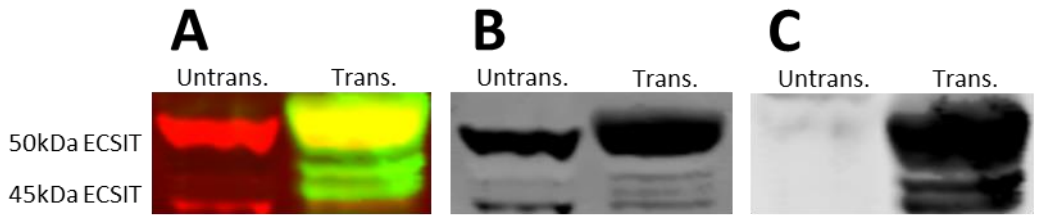

Figure 5.32. Immunoblots of transfected and un-transfected HEK293T cells showing the binding of both the anti-ECSIT (Abcam ab21288) and anti HIS antibodies binding to the tagged ECSIT protein at both 45 and 50 kDa. (A) shows the combined channels (Red – Anti ECSIT, Green – Anti HIS). (B) shows only the red channel and (C) only the green. Native ECSIT protein is visible in the un-transfected cells in the red channel.

5.7. Discussion

Results indicate a mild structural defect in *Ecsit*$^{N209I/N209I}$ cardiac mitochondria with a tendency towards highly compacted and disorganised cristae, as well as a reduction in mitochondrial size. This may reflect a tendency of mitochondria to form more fragmented networks or may simply be an artefact of the way the TEM slides were cut, further investigation using TEM to image mitochondria from other tissues may help to determine if this is a valid result.

Investigating nDNA:mtDNA ratio and mitochondrial inner and outer membrane proteins in cardiac showed mixed results. nDNA:mtDNA hinted at some differences between wild type and *Ecsit*$^{N209I/N209I}$ mitochondria quantities but with limited successful results this method was abandoned for more robust methods. Inner and outer membrane proteins showed that there was no difference in total mitochondrial mass in cardiac tissue and as such this was not further investigated in other tissues where no phenotype was seen. Finally, the levels of the master regulator of mitochondrial proliferation, PGC1α, showed a slight upregulation in cardiac tissue, with no changes in other tissues measured. This result, when coupled with the two previous tests suggests that the cells of the heart are attempting to upregulate total mitochondrial mass through the action of PGC1α but the elevation of mitochondrial mass is impaired, either due to impaired synthesis, or increased degradation.

This section also attempted to determine why a mutation in a ubiquitously expressed complex I assembly protein (ECSIT) appears to have such a devastating effect on cardiac tissue without devastating body wide phenotypes, as is typical with complex I deficiency.

Firstly, these data demonstrate that whilst the phenotype seen in *Ecsit*$^{N209I/N209I}$ animals is primarily cardiac, the loss of complex I protein level is more universal. The reduction in complex I varies significantly from tissue to tissue with an almost complete loss of complex I protein in heart and only mild reductions in kidney and brain. This alone hints at the cause of the tissue specific phenotype. This loss of NDUFB8 in heart tissue is also supported by the loss of a number of other complex I proteins in heart tissue. However not all proteins are reduced, indicating that the N209I mutation in ECSIT may affect different subassemblies of complex I to different degrees. Again, this loss of proteins in cardiac tissue is also seen in brain tissue, to only a mildly reduced level, hinting again at

a tissue specific level of activity of ECSIT in complex I assembly. Work was also undertaken to show that a loss of functional complex I protein precedes the cardiac phenotype observed. Secondly, it suggests two possibilities for the regulation of NDUFB8 protein levels, the first being that NDUFB8 levels are lost over time with the N209I mutation leading to cardiomyopathy, or secondly that NDUFB8 protein levels increase over time with the development of the cardiac tissue and the ECSIT N209I mutation inhibits this.

To investigate the mechanism by which ECSIT is involved in complex I assembly, protein levels of ECSIT in multiple tissues were assessed. Initial results showed a surprising upregulation of both 50 and 45 kDa ECSIT in *Ecsit*$^{N209I/N209I}$ hearts compared to wild types. No similar upregulation of these isoforms was seen in brain, kidney, liver or muscle. Furthermore, during this investigation a previously undescribed 16kDa fragment was identified by the antibody used in wild type cardiac tissue. This fragment was absent from *Ecsit*$^{N209I/N209I}$ cardiac samples and was not identified in any of the other tissues tested, providing the first evidence of a potential tissue specific mechanism of ECSIT in complex I assembly. As with the complex I protein levels, ECSIT protein levels I cardiac tissue were also assessed in 2 week hearts to confirm that the upregulation of 50 and 45 kDa ECSIT and the loss of the putative 16kDa fragment preceded the development of cardiomyopathy. As expected, 50 and 45kDa ECSIT protein is elevated above wild types in *Ecsit*$^{N209I/N209I}$ hearts and there is a loss of 16kDa ECSIT in *Ecsit*$^{N209I/N209I}$ hearts isolated from 2 week old animals. These data suggest that the loss of the 16kDa fragment precedes the onset of hypertrophy in .*Ecsit*$^{N209I/N209I}$ animals.

As ECSIT is known to be part of the MCIA complex, its binding to other members of this complex was assessed. The two key members of the MCIA complex that were assessed were NDUFAF1 and ACAD9. ACAD9 protein levels showed no differences in heart, kidney, liver or brain, but it was not possible to accurately measure NDUFAF1 due to a lack of reliable antibody. Further investigation focused on the use of Co-immunoprecipitation using tagged proteins to determine if the interaction of ECSIT with ACAD9 and NDUFAF1 was affected by the N209I mutation. Results showed that the mutation had no effect on the interaction of these proteins, indicating that mutant ECSIT

is still capable of forming part of the MCIA complex and at least initiating complex I assembly.

Complex I assembly itself was assessed by blue native PAGE which shows the formation of subcomplexes and the isoforms of each protein present in each subassembly. These data showed that *Ecsit*$^{N209I/N209I}$ animals show a defect in complex I assembly in cardiac tissue but not in brain tissue. This defect is most apparent when looking at the P_P and P_D subunits especially the P_D-a which demonstrated a shift towards unincorporated protein. Taken together these data support the work of Guerrero-Castillo *et al*. (2016) [72] which showed ECSIT is involved in the assembly of the membrane arm of complex I. BN-PAGE also demonstrated that the putative 16kDa ECSIT fragment is a constitutive part of fully assembled complex I. This may be as a result of a tissue specific cleavage of the protein during the complex I assembly process, although the reasons for having such a mechanism remain elusive.

Finally, mass-spectrometry was employed to determine the nature of the 16kDa fragment seen in wild type hearts but absent from mutant hearts and other tissues examined. As ECSIT was not detected in any samples despite its presence being known at 45 and 50kDa sizes this leaves an open ended question that justifies further investigation. Determining the nature of this fragment is of utmost importance to the project and could possibly be done through the use of cultured wild type cardiomyocytes transfected with a tagged protein and immunoprecipitated using an antibody against the tagged protein. Unfortunately, cardiomyocytes are not readily transfectable and given the lack of the 16kDa protein in other tissue types, it is unlikely other cell types would produce the required fragment.

In summary, results from this leave us with a working hypothesis that ECSIT exists as 3 potential proteins. A 50kDa cytosolic isoform that localizes to mitochondria when poly-ubiquitinated and is imported following the cleavage of a 5kDa mitochondrial targeting sequence. This process leaves a 45kDa mitochondrially localised isoform that is present in most tissues and required for the production of complex I through the MCIA complex. To this point, there is evidence to support this mechanism across all tissues and cell types and that the mutation of ECSIT only mildly inhibits this assembly process resulting in mild reduction of functional complex I and no obvious phenotypes in tissues outside

the heart. However, the data obtained during this project suggests that this is also the point where heart tissue diverges from other tissues in the way complex I is assembled. It would appear that at this point the 45kDa ECSIT protein is cleaved in heart tissue allowing for the incorporation of the 16kDa fragment into complex I and the process to continue, resulting in fully assembled complex I. The N209I mutation of ECSIT seems to inhibit this cleavage process, resulting in a premature arrest of the complex I assembly process and an accumulation of both 45 and 50Kda ECSIT in cardiac tissue.

This difference in heart tissue may be due to the increased energy demands of the heart and hence in this situation ECSIT acts not only as an assembly factor, but also as a supernumerary subunit to improve complex I efficiency, a role that is not required in other tissues.

Chapter 6: Mitochondrial Response to Complex I Dysfunction

6.1. Changes in Mitochondrial Network Dynamics

Mitochondrial fusion and fission are the methods by which mitochondria form large dynamic networks in order to exchange DNA, ETC elements and maintain membrane potential ($\Delta\psi_m$). Fusion is governed by the GTPases MFN1, MFN2 and OPA1 whilst fission is mainly centred on the protein DRP1, which has various phosphorylation sites that either inhibit (Ser637) or activate (Ser616) the mechanism of the protein. Under typical circumstances mitochondria form dynamic networks with balanced levels of fusion and fission resulting in a variety of mitochondrial network sizes. During periods of mitochondrial stress or dysfunction the balance between fusion and fission may become disturbed, leading to a shift, one way or the other, resulting in highly fragmented or inefficient networks that do not function normally. As a result, the levels of mitochondrial fusion and fission proteins were assessed to determine if this pathway was affected by the mutation in ECSIT. Samples analysed are from male (n=3) and female (n=3) wild type and *Ecsit*$^{N209I/N209I}$ hearts at 16 weeks of age.

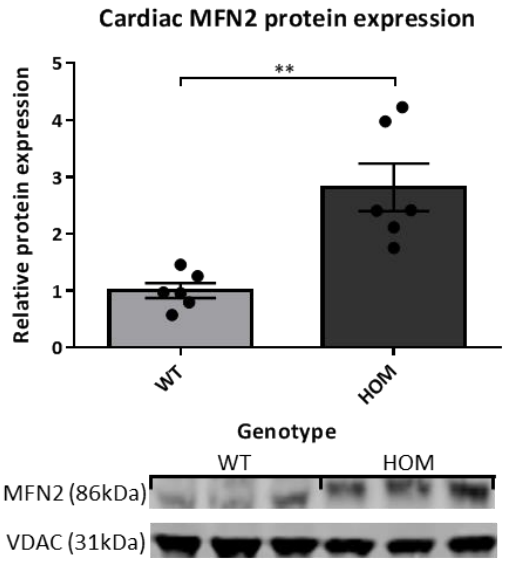

Figure 6.1. Quantification and representative blots of total MFN2 protein in cardiac tissue of wild type and *Ecsit*$^{N209I/N209I}$ animals. Results show a significant elevation of MFN2 in *Ecsit*$^{N209I/N209I}$ animals suggesting an increase in mitochondrial fusion as a result of the ECSIT N209I mutation. Mean ± SEM, **p<0.01.

Results here show an increased amount of MFN2 protein (Figure 6.1) in the hearts of *Ecsit*$^{N209I/N209I}$ animals when normalised to the mitochondrial loading control VDAC. This may indicate a shift towards mitochondrial fusion and an increase in the amount of

mitochondria incorporated into large networks. In addition, the protein levels of OPA1 (Figure 6.2) were assessed in the same samples as this protein works in tandem with MFN2 to cause mitochondrial fusion. It is noteworthy that OPA1 has 6 known isoforms in mouse tissue whilst only 3 were identifiable here, further investigation is required with additional techniques. Unfortunately, time restraints prevented this from being possible. Regardless, these three isoforms were quantified, and whilst there is no difference in levels between wild type and *Ecsit*$^{N209I/N209I}$ animals in the smallest size band, the larger two do show a significant reduction in protein levels in *Ecsit*$^{N209I/N209I}$ animals. This is suggestive of a reduction in fusion of the inner membrane.

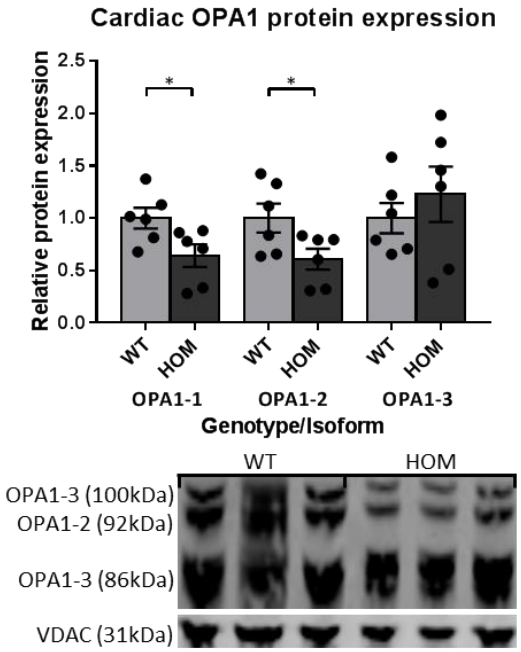

Figure 6.2. Quantification and representative blots of total OPA1 protein in cardiac tissue from wild type and *Ecsit*$^{N209I/N209I}$ animals. Of the 6 known OPA1 isoforms in mouse, only 3 were identifiable and only these 3 were analysed. Of these 3 bands the first 2 show a significant reduction of protein levels in *Ecsit*$^{N209I/N209I}$ hearts whilst the 86kDa band shows no significant changes. The remaining 3 bands showed faint traces on the blot but could not be visualised without overexposing the 3 bands shown here. Mean ± SEM, *p<0.05.

Mitochondrial fission was assessed by measuring the phosphorylation of DRP1 (Figure 6.3) at two known serine residues. Overall DRP1 levels were unchanged between wild type and *Ecsit*$^{N209I/N209I}$ hearts indicating that if changes in the fission rate were apparent it must come from varying phosphorylation of the protein sites. Phosphorylation of the two serine residues have opposing roles, with serine 637 being inhibitory to the

activation of DRP1 whilst serine 616 is the activating site. Both residues show no significant alterations in the amount of phosphorylation that has occurred, indicating that mitochondrial fission shows no change in regulation.

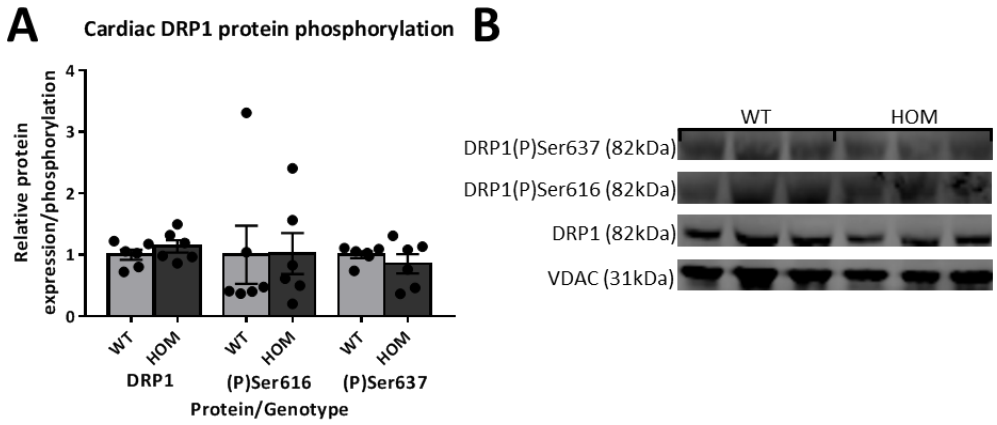

Figure 6.3. Quantification (A) and representative blots (B) of total DRP1, DRP1(P)Ser637 (inhibitory) and DRP1(P)Ser616 (activating). Results show no significant differences in the level of total protein or in the phosphorylation of either of the serine sites within DRP1. Mean ± SEM.

Taken together these data hint at an increase in mitochondrial outer membrane fusion with an increase in MFN2 levels. However, fusion of the inner membrane is likely reduced due to a reduction in levels of long chain OPA1 isoforms. These results also indicate that there is not a cellular response leading to elevated mitochondrial fission as levels of the fission protein DRP1 show no changes in expression levels of phosphorylation of either activating or inhibitory residues.

6.2. Regulation of Mitophagy in response to mitochondrial Dysfunction

Mitophagy is the process by which dysfunctional mitochondria are removed from the cell through the action of PINK1, Parkin and autophagosomes. Typically, PINK1 accumulates on the mitochondria and is broken down by being internalised and degraded. Where mitochondria are defective PINK1 accumulates on the outer membrane and marks mitochondria for degradation. Samples analysed are from male (n=3) and female (n=3) wild type and *Ecsit*$^{N209I/N209I}$ hearts at 16 weeks of age. Results below (Figure 6.4) show a significant elevation of PINK1 protein levels in the hearts of *Ecsit*$^{N209I/N209I}$ animals indicating that there is an increase in defective mitochondria present in this tissue and PINK1 is accumulating as a result.

These data suggest that the mutation of ECSIT leads to a significant level of mitochondrial dysfunction leading to attempts by the cell to remove dysfunctional mitochondria via this mitophagy pathway.

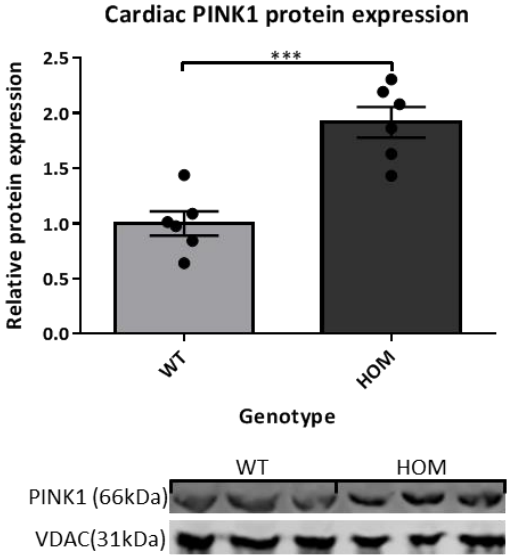

Figure 6.4. Quantification and representative blots of PINK1 in wild type and *Ecsit*$^{N209I/N209I}$ heart tissue. Results demonstrate a significant increase in PINK1 protein in *Ecsit*$^{N209I/N209I}$ hearts indicating an increase in mitophagy. Mean ± SEM, ***p<0.001.

6.3. Regulation of Mitochondrial Unfolded Protein Response

The mitochondrial unfolded protein response is upregulated as a reaction to the accumulation of unfolded proteins in the mitochondria. In the case of *Ecsit*$^{N209I/N209I}$ hearts it might be expected that this response is activated to deal with the accumulation of complex I assembly intermediates that are not incorporated into functional complex I and may inhibit other mitochondrial processes by remaining in the inter membrane space (IMS). Samples analysed are from male (n=3) and female (n=3) wild type and *Ecsit*$^{N209I/N209I}$ tissues at 16 weeks of age.

Protein levels of key UPR^{mt} proteases and chaperones were assessed for any significant alterations to protein levels in the cardiac tissue of *Ecsit*$^{N209I/N209I}$ animals when compared to wild types. Results (Figure 6.5) show an elevation of the proteases CLPP as well as LONP1 indicating that there is an increase in protease activity in response to the accumulation of complex I assembly intermediates. In addition, the chaperone protein HSP60 also shows a significant elevation in *Ecsit*$^{N209I/N209I}$ hearts in comparison to wild

types. Of the proteins assessed, only the chaperone GRP75 does not show any elevation in *Ecsit*$^{N209I/N209I}$ animals.

To contrast this these same proteins were measured in brain tissue (Figure 6.6) to show that the activation of the UPR^{mt} corresponds to the blockage in complex I assembly seen in heart and not just as a result of mutant ECSIT being present in mitochondria. Results from brain show no significant changes in the levels of the 4 proteins measured (CLPP, LONP1, HSP60 and GRP75) thus confirming that it is not mutant ECSIT that activates the UPR^{mt} but the accumulation of misfolded complex I assembly intermediates.

In addition to the protein levels of these key chaperones and proteases, the phosphorylation of the translation initiation factor EIF2α was assessed (Figure 6.7). This protein is phosphorylated by PKR to suppress protein translation in response to the accumulation of misfolded proteins. Results do not show a significant increase in the phosphorylation levels of EIF2α in *Ecsit*$^{N209I/N209I}$ heart tissue.

Whilst the list of proteins assessed here is not exhaustive, and does not include the transcription factors CLPP or CEBPβ that are responsible for initiation, these data suggest that there is activation of some arms of the UPR^{mt}.

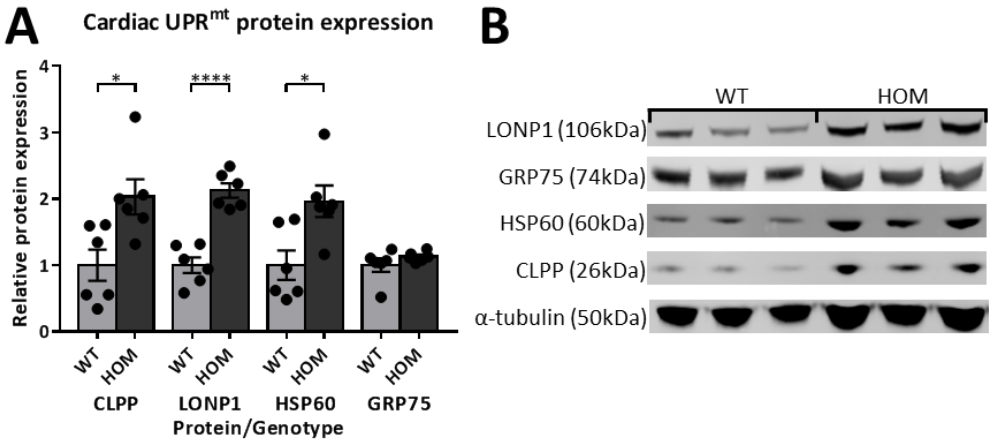

Figure 6.5. Quantification (A) and representative blots (B) in heart of the proteases CLPP and LONP1 and the chaperones HSP60 and GRP75 which are known to be part of the UPR^{mt}. Results show significant elevation of CLPP, LONP1 and HSP60, suggesting a robust activation of the UPR^{mt} in response to the accumulation of assembly intermediates created by the loss of ECSIT function in cardiac tissue. Mean ± SEM, *p<0.05, ****p<0.0001.

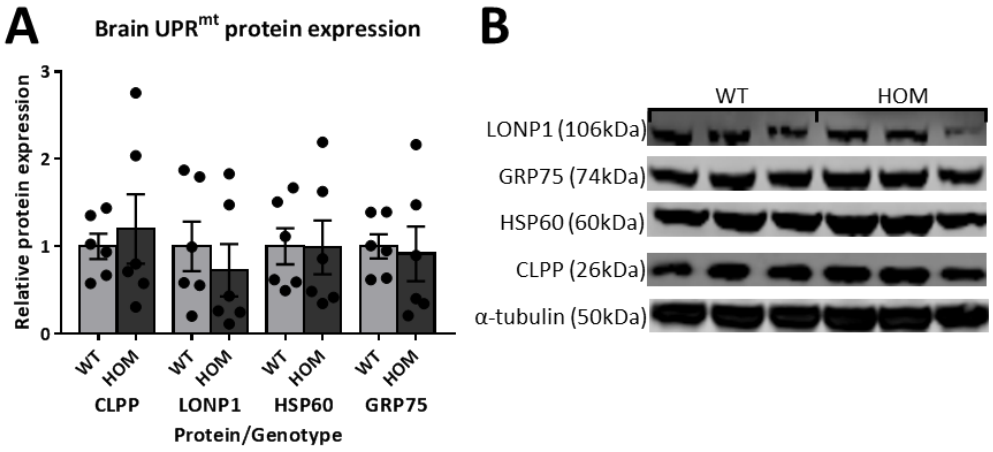

Figure 6.6. Quantification (A) and representative blots (B) in brain of the proteases CLPP and LONP1 and the chaperones HSP60 and GRP75 which are known to be part of the UPR^{mt}. In contrast to heart tissue, results in brain show no significant changes in the expression of any of the UPR^{mt} proteins measured here. Mean ± SEM.

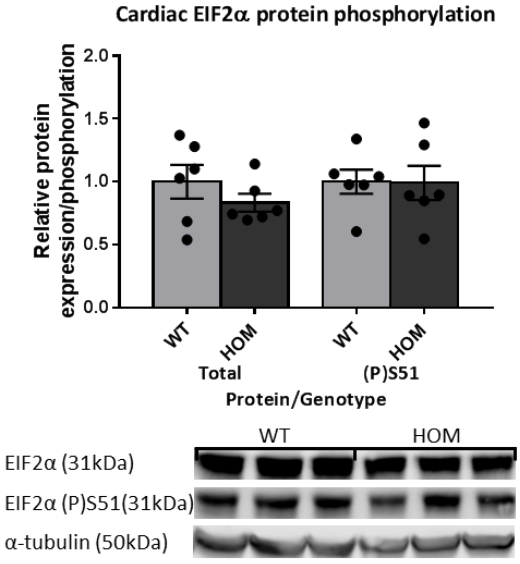

Figure 6.7. Quantification and representative blots of total and phosphorylated EIF2α in wild type and *Ecsit*$^{N209i/N209I}$ hearts. Results show no change in overall EIF2α protein levels or in the level of phosphorylation of the protein. Mean ± SEM.

6.4. Regulation of Reactive Oxygen Species Production Following Complex I Dysfunction

Reactive oxygen species (ROS) are produced as a by-product of oxidative phosphorylation during normal mitochondrial function. However, defects in the electron transport chain can lead to elevated levels of ROS created by the mitochondria which normal anti-oxidant mechanisms are unable to cope with. In situations like this ROS leads to mitochondrial and cellular damage and ultimately to cell death and inflammation. Due to previous difficulties in culturing neonatal cardiomyocytes it was difficult to measure superoxide or H_2O_2 species production *in vitro* and it was decided to measure the concentration of 4-hydroxynonenal (4-HNE) in cardiac tissue of wild type and *Ecsit*$^{N209I/N209I}$ animals instead. 4-HNE is the product of lipid peroxidation by ROS and unlike most ROS it is long lived, meaning measurements in *ex vivo* tissues are possible. Samples analysed are from male (n=3) and female (n=3) wild type and *Ecsit*$^{N209I/N209I}$ hearts at 16 weeks of age.

Results from this assay (Figure 6.8) show a reduction in cardiac levels of 4-HNE and by proxy a corresponding reduction in ROS produced by the mitochondria. This result is perhaps unsurprising given the large reduction in the levels of intact complex I seen in cardiac tissue without a corresponding elevation of complex III. As complex I and III are the main sites of ROS production in the mitochondria an overall reduction in the ROS producing sites would logically result in reduced ROS despite mitochondrial dysfunction.

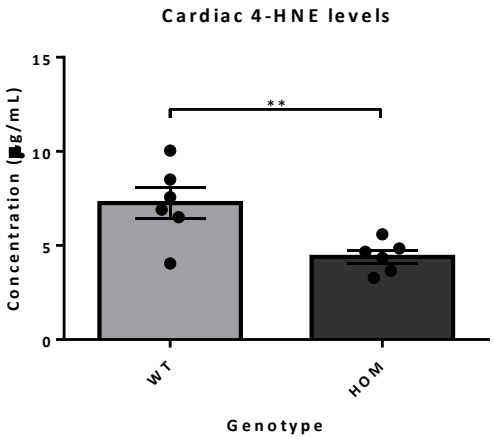

Figure 6.8. Cardiac 4-hydroxynonenal levels in cardiac tissue from wild type and Ecsit$^{N20I/N209I}$ animals. Results indicate a reduction in 4-HNE levels and correspondingly it can be assumed that ROS production is decreased too. Mean ± SEM, **p<0.01.

6.5. Energy Insufficiency of Tissue with Complex I Dysfunction

The idea of the failing heart being an energy starved organ is well established with reduction in ATP and PCr levels being reported in patients as well as animal models [101, 106, 108]. To determine if this was the case in *Ecsit*$^{N209I/N209I}$ animals both ADP:ATP ratio and AMPK activation were assessed. Samples analysed are from male (n=3) and female (n=3) wild type and *Ecsit*$^{N209I/N209I}$ hearts at 16 weeks of age.

6.5.1. ADP:ATP Ratio

The ADP:ATP ratio was assessed in freeze clamped hearts collected from both wild type and *Ecsit*$^{N209I/N209I}$ animals by enzylight™ ADP/ATP ratio assay kit. This kit allows for first the measurement of ATP as it reacts with the D-luciferin substrate and then, following the conversion of ADP to ATP, for the indirect measurement of ADP concentration.

Results (Figure 6.9) show no significant changes in the concentration of ATP or ADP between wild type and *Ecsit*$^{N209I/N209I}$ animals. However, the ratio of ADP to ATP shows a small but significant elevation in *Ecsit*$^{N209I/N209I}$ animals. This increase in [ADP] relative to [ATP] suggests increased turnover of ATP in the myocardium which is temporarily elevating ADP levels whilst they await conversion back to ATP. This result alone does not provide a clear picture of what is going on in the cardiac tissue regarding energy insufficiency as there are no changes in ATP levels and without PCr readings it is impossible to draw a meaningful conclusion.

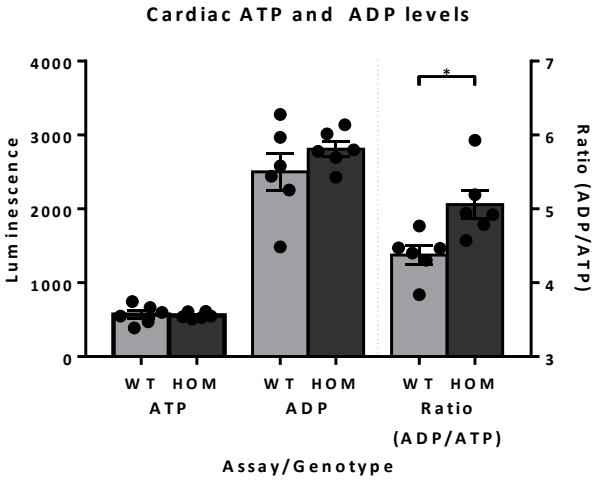

Figure 6.9. Luminescence readings of [ATP] and [ADP] as well as ADP/ATP ratio in wild type and *Ecsit*$^{N209I/N209I}$ animals. Results show no significant differences in [ATP] or [ADP] but do demonstrate a small elevation in ADP/ATP which in itself is difficult to interpret. Mean ± SEM, *p<0.05.

Further limitations with this result come from the fact that ATP may be readily converted to ADP once the sample has been taken or indeed following lysis in solution, therefore artificially increasing [ADP] whilst diminishing the [ATP]. This fact may explain the unexpected ratio of ADP:ATP in these samples. Typically [ATP] would be expected to be maintained at around 10mmolL^{-1} whilst [ADP] would be around 50µmolL^{-1}, 3 orders of magnitude lower than [ATP] and the opposite of what is observed in this assay. With this in mind, the results from this assay will not be taken into consideration when drawing conclusions.

6.5.2. AMPK Phosphorylation

As a less direct but potentially more readily measurable metric of energy insufficiency of the heart, the phosphorylation levels of AMPK can be measured. AMPK is phosphorylated by an upstream kinase (AMPK kinase) in response to high AMP levels which occur when [ADP] is elevated and [ATP] reduced. Activated AMPK is then responsible for remodelling the energy supply systems of the cell to focus them towards ATP production.

AMPK activation levels (Figure 6.10) in *Ecsit*$^{N209I/N209I}$ animals show a surprising decrease in comparison to wild type in heart tissue. This result is opposed to that of the ADP/ATP ratio which, whilst difficult to interpret and inconclusive, suggested that there may be a slight elevation of [ADP] in the hearts of *Ecsit*$^{N209I/N209I}$ animals.

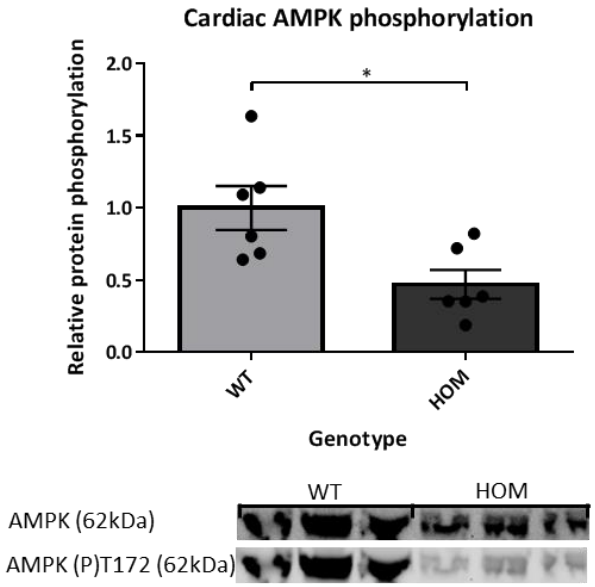

Figure 6.10. Quantification and representative blots of total and phosphorylated AMPK in wild type and *Ecsit*$^{N209I/N209I}$ cardiac tissue collected by clamp freezing. Contrary to expectations results show a marked decrease in AMPK phosphorylation levels in *Ecsit*$^{N209I/N209I}$ samples when compared to wild types, suggesting that [AMP] concentration is high and by association so too is [ATP]. Mean ± SEM, *p<0.05.

6.6. Discussion

The aim of this chapter was to determine which downstream pathways may be activated in response to the mutation of *Ecsit* and may be responsible for the development of the cardiac phenotype as the previous chapter had demonstrated that the OXPHOS deficiency preceded the development of cardiomyopathy.

Results from this chapter are mixed and provide an incomplete picture of the downstream effects of the N209I mutation in ECSIT that warrants further investigation. Firstly, the balance of mitochondrial fusion and fission seems to be shifted slightly in favour of fusion, with an elevation of MFN2 which is responsible for outer membrane fusion. However, this is not consistent as the inner membrane fusion protein shows a reduction in the level of isoforms typically associated with inner membrane fusion. There are also no changes in the activation of fission proteins.

Mitophagy appears to be moderately upregulated which may be a response to dysfunctional mitochondrial subunits or may be the indirect result or unfolded protein response activation which was also seen. UPR^{mt} activation is apparent due to the increased protein levels of the proteases CLPP and LONP1 and the chaperone HSP60 in heart tissue. This same activation pattern was not seen in brain tissue suggesting that it is the result of the complex I assembly defect that was only seen in heart in the previous chapter. However, it is of note that surgical models of ischemia/reperfusion injury in rats also demonstrate an activation of the UPR^{er} which shares some components with the UPR^{mt}. This may suggest that the activation seen here is not a direct result of misfolded mitochondrial protein, but is part of the normal response to cardiomyopathy [296].

The first in a series of unexpected results was the reduction in the production of reactive oxygen species as measured indirectly by 4-HNE levels. Further reflection on this would suggest the initial expectation was misguided, as complex I is a key site of ROS production and with a reduction in functional complex I, logic would dictate that ROS should display a similar reduction.

Finally, energy insufficiency was assessed as it is well associated with heart failure. This result however provided the second surprise as ADP/ATP ratio appeared only slightly elevated and it was difficult to draw meaningful conclusions as [ATP] was unchanged. It

is noteworthy that this result is suspect simply due to limitations of the assay. This assay is primarily designed for assessing viability of cell populations in culture and reliably measuring [ATP] in tissue samples presents a great number of challenges, not least maintaining ATP throughout the sample collection and measurement process as it may be quickly converted to ADP once the lysis of tissue is performed.

In addition AMPK activation levels were significantly reduced, suggesting that [AMP] and by association [ATP] was high in these hearts, indicating no presence of energy insufficiency although as a single measurement further evidence would be beneficial.

Chapter 7: Discussion of Results

7.1. Summary of Results

Throughout the experiments performed to this point, a unifying goal has been to determine how the mutation of *Ecsit* ultimately leads to cardiomyopathy through a complex I dysfunction without the presence of other obvious phenotypes.

Initial phenotyping took place in a mixed background of C57BL/6J and C3H.Pde6b+ with the mutation lying in a C57BL6/J region of the genome. Through whole genome sequencing a mutation in *Ecsit* was identified and confirmed by Sanger and pyro sequencing. The mutation is an asparagine to isoleucine change at residue 209 of the ECSIT protein with protein prediction software indicating that the mutation would have a deleterious or disease causing effect on the protein structure or function. Sequence homology to human ECSIT protein suggested that this mutation would lie in a putative pentatricopeptide (PPR) with a potential role in processing RNA, although no evidence exists for this function in ECSIT. With a putative function in RNA processing, as well as the assembly of complex I, it is possible to envisage a role for ECSIT in the regulation of expression of complex I subunits. This may take the form of negative regulation wherein ECSIT, or a fragment of it, is re-tasked as a signalling protein following successful complex I assembly. This new signalling peptide could then act directly on the expression of complex I proteins or indirectly, perhaps via PGC1α.

Further phenotyping on incipient congenic animals obtained by 5 back-crosses to the C3H.de6b+ strain confirmed a cardiomyopathy in homozygous mutant animals. The phenotype was assessed by histology and echocardiography and was observed from roughly 4 weeks of age in $Ecsit^{N209I/N209I}$ animals. This cardiomyopathy had characteristics of both hypertrophic (increased wall thickness, hypertrophy of cardiomyocytes) and dilated cardiomyopathy (increased left ventricular volume). This cross-over between the two main cardiomyopathy types may represent an attempt to remodel the heart tissue in response to an initial development of one of these conditions. Further histological analysis with more consistent tissue collection techniques may allow for this question to be answered. However, it is my opinion that this is most likely a hypertrophic cardiomyopathy given the prevalence of this condition in association with mitochondrial disease and the overwhelming size and weight of the heart muscle seems unlikely to be a tissue response to dilated cardiomyopathy.

Ecsit$^{N209I/N209I}$ animals also displayed some changes in body fat deposition, with homozygous animals displaying a reduced body weight from as early as 6 weeks of age and a reduced adiposity that was apparent from 14 weeks of age. This result may be directly related to the increase in triglyceride metabolism indicated by the clinical chemistry results. Decreased triglyceride as well as elevated glycerol and ketone bodies, in addition to changes in glucose and fructosamine concentrations, hint at a change in metabolism in *Ecsit*$^{N209I/N209I}$ animals. Both of these results are suggestive of an increase in metabolism of their respective substrates, free fatty acids and glucose, without indicating a shift in the primary substrate being used, as might be expected with a failing heart shifting towards glucose metabolism. Clinical chemistry also revealed an increase in plasma concentrations of urea, creatinine and potassium, highly suggestive of kidney dysfunction. Whilst the presence of a kidney phenotype is not in question, whether it is a primary or secondary phenotype remains to be determined. Kidney disease has a well-established link with hypertension [297] whilst HCM is more typically associated with hypotension [298]. However, some evidence exists to suggest that hypotension is a risk factor for chronic kidney disease [299] but it would seem more likely that the kidney failure is a direct result of the mitochondrial dysfunction and requires further investigation. It is interesting to note that the *Ecsit*$^{N209I/N209I}$ samples seem to segregate into two groups, those with creatinine that is slightly elevated (18-25µmol/l) and those with a higher elevation of creatinine (30-40µmol/l). This stratification of the creatinine concentration in plasma may be a symptom of the mixed genetic background that these animals exhibit, despite being incipient congenic animals on the C3H.Pde6b+ background. We know from prior experience with kidney disease mutants that have arisen from the Harwell Ageing Screen that the C3H.Pde6b+ background exhibits an increased susceptibility to the development of kidney disease whilst the C57BL/6J seems to confer some protection (data unpublished). It is therefore conceivable that this stratification is influenced by a region of the genome that maintains a C57BL/6J nature in a proportion of these animals. It would be possible to further characterise this in the congenic *Ecsit*$^{N209I/N209I}$ animals on both a C57BL/6J and C3H.Pde6b+ background.

Results in chapter 2 focused on the potential roles of both the toll like receptor response and the morphogenetic protein pathway in the development of cardiomyopathy seen in the *Ecsit*$^{N209I/N209I}$ animals. Results pertaining to the activity of ECSIT in the TLR pathway

indicate that it's interaction with the binding partner TRAF6 is unaffected by the N209I mutation and that the inflammatory response may actually demonstrate a mild impairment in *Ecsit*$^{N209I/N209I}$ animals, suggesting that this pathway is unlikely to lead to increased inflammation and subsequent cardiomyopathy. The data to support this decrease in activation is limited as the activation of JNK showed a trend but did not reach significance, it is possible that further repeats would achieve significance.

As for the BMP pathway no signs of impairment were demonstrated at all. The fact that knockouts are embryonic lethal due to a significant impairment of this pathway is suggestive that this pathway is unhindered by the N209I mutation. Furthermore, impairment of this pathway could be expected to cause reduced viability of *Ecsit*$^{N209I/N209I}$ embryos, as is the case for *Ecsit*$^{-/-}$. However, a reduction in the number of *Ecsit*$^{N209I/N209I}$ animals at weaning was not seen, suggesting that the BMP pathway is not significantly impaired. The key metric in this section is the expression of embryonic *Tlx2* which is lost in its entirety when *Ecsit* is knocked out but only shows a 50% reduction in *Ecsit*$^{N209I/N209I}$ animals in comparison to wild types, although this result is not statistically significant. This reduction seems to be insufficient to significantly affect the viability of *Ecsit*$^{N209I/N209I}$ embryos through the BMP pathway.

The focus of this work was the role of ECSIT in complex I assembly, as this appeared as the most likely candidate to be affected by the N209I mutation. Initial work showed that mitochondria from *Ecsit*$^{N209I/N209I}$ hearts showed some level of structural abnormalities, with the presence of hyper condensed, disorganised cristae as well as a small reduction in mitochondrial cross sectional area of both interfibrillar and perinuclear mitochondria. Protein and mtDNA levels did not demonstrate a change in the overall abundance of mitochondria in heart tissue although the level of PGC1α, the master regulator of mitochondrial biogenesis, was slightly elevated in heart tissue. This result may indicate that whilst there is an upregulation of the pathway that drives mitochondrial biogenesis, the mutation of ECSIT either inhibits the actual process or results in the production of defective mitochondria or mitochondrial subunits that are quickly eliminated by either mitophagy or the mitochondrial unfolded protein response.

Analysis of complex I protein levels confirmed that there was a significant reduction in complex I levels in heart as well as in other tissues: brain, kidney, liver. The extent of

reduction varies considerably between tissues with the brain showing only a small reduction of around 25% whilst the heart shows a >95% reduction in NDUFB8 protein levels. This reduction in complex I protein level is not reflected across all proteins of complex I, with a more robust reduction in membrane arm proteins than in matrix arm proteins. Some proteins (NDUFS3 and MT-ND1) showed no significant reduction at all in heart tissue, potentially indicating that the control of expression of these proteins exists outside of that of the majority of complex I proteins. This would make sense for the mitochondrially encoded MT-ND1 as it is controlled and expressed entirely within the mitochondria, however the nuclear encoded NDUFS3 is nuclear encoded would logically follow the same regulatory controls as other nuclear encoded mitochondrial OXPHOS proteins. In the brain a greater number of proteins showed no significant changes in levels (NDUFV2, NDUFS3, NDUFA8) and of those that do, there is an overall smaller reduction in their levels. This may indicate that there is some sort of hierarchy to the regulation of these proteins, with the reduction in levels of lower levelled proteins (NDUFV2, NDUFS3 etc.) only occurring when higher level proteins are reduced below a certain threshold. However, this may also reflect the fact that some of these proteins are essential to the assembly of complex I (MT-ND1), or are required early in the assembly process, and others are at least partially disposable, or required later in the assembly process. This would mean that when stressed cellular processes focus on the essential building blocks first, maintaining them at close to normal levels where possible.

Results also demonstrated that, whilst protein levels are reduced in a number of tissues, the activity of complex I does not necessarily follow suit in these tissues. Comparing heart and brain using in-gel activity and seahorse analysis of isolated mitochondria revealed that complex I activity and mitochondrial respiration were severely impacted by the presence of the N209I mutation in heart tissue. However, this was not true for complex I or mitochondria isolated from brain tissue, which showed comparable levels in wild type and *Ecsit*$^{N209I/N209I}$ mitochondria in both assays. Whilst further investigation of other tissues is desirable, these data alone support the hypothesis that there are tissue specific differences in the complex I assembly process, and in particular the stage(s) controlled by ECSIT.

Protein levels of ECSIT tell a slightly different, and unexpected, story. ECSIT exists as a cytosolic (50kDa) and mitochondrial (45kDa) form in mouse tissues and the levels of these two protein products was upregulated in the cardiac tissue of *Ecsit*$^{N209I/N209I}$ animals compared to wild types. Interestingly this pattern of regulation was not repeated in any other tissue tested, in fact, no differences could be seen at all in other tissues, suggesting why the main outcome of the mutation was cardiomyopathy with little effect observed in other tissues. Of most interest was the identification of a previously undescribed ~16kDa fragment in wild type heart tissue, which was absent from *Ecsit*$^{N209I/N209I}$ hearts as well as all other wild type and *Ecsit*$^{N209I/N209I}$ tissues. It is conceivable that this fragment is a portion of ECSIT produced by the cleavage of the 45kDa ECSIT as part of the normal assembly process for complex I. If this is the case then it may be that the N209I mutation inhibits the cleavage, leading to an accumulation of the larger 45 and 50kDa ECSIT isoforms. Without identifying a specific protease responsible for this hypothetical cleavage it is difficult to determine how the N209I mutation might affect the cleavage of 45kDa ECSIT. However, if cleavage was to occur at this residue it would result in two products roughly 19 and 46 kDa in size. Although neither of these is the exact 16kDa size seen on the western blots it is possible that further cleavage of one of these two products occurs or that the size on the western blot is not does not reflect an accurate size of the protein product.

Investigation of ETC and ECSIT protein levels in two week old hearts confirmed that the changes in the levels of these proteins precede the cardiomyopathy phenotype and are not an artefact of the phenotype. Interestingly, the levels of 45 and 50kDa ECSIT did not show increased levels in these 2 week old hearts whilst there was a reduction in the 16kDa fragment. This probably indicates that these larger ECSIT proteins have not had time to accumulate in the mitochondria or cytosol yet and that this accumulation is a gradual process. The accumulation of these larger fragments may be a contributing factor to the development of cardiomyopathy, further investigation across more time points may reveal if this is the case.

In addition to the alterations in ECSIT protein levels, data in this section also demonstrated that the mutation of ECSIT protein had no impact on the interaction

between ECSIT and other proteins of the MCIA complex such as NDUFAF1 and ACAD9, which also showed no changes in protein levels in any tissues tested.

To assess complex I assembly, first and second dimensional blue-native PAGE was performed on mitochondria extracts from heart and brain of wild type and *Ecsit*$^{N209I/N209I}$ animals. This revealed that *Ecsit*$^{N209I/N209I}$ animals had some defects in some aspects of complex I assembly in heart tissue, but not in brain tissue. These defects are mainly related to the assembly of the membrane arm of complex I although some loss of other subunits was also seen. Interestingly, none of the same defects were seen in mitochondria isolated from brain tissue of the same animals. This further supports the hypothesis that complex I assembly is not a universal process but has tissue specific intricacies that result in an altered process and differential levels of complex I in tissues where an assembly factor mutation is present.

Taken together, these data suggest that the N209I mutation of ECSIT has no impact on the formation of the protein's previously described larger fragments (50 and 45kDa) or on the interaction between ECSIT and the MCIA proteins NDUFAF1 and ACAD9. There are two salient facts to remember when arguing a case for the importance of the 16kDa ECSIT protein. Firstly, that complex I assembly and activity in brain tissue are unaltered and those tissues tested that did show complex I protein level differences are less severely affected than heart tissue. The second is that the formation of the MCIA complex appears to be unaffected by the presence of the N209I mutation in ECSIT, reflected by the normal interaction of ECSIT with both NDUFAF1 and ACAD9, and by the normal protein expression of ACAD9 in the tissues tested. Taken together this suggests that the MCIA complex functions as expected in ECSIT$^{N209I/N209I}$ animals and if we accept this as true then the mechanism for the defect seen in cardiac tissue must lie elsewhere, potentially in the presence of the 16kDa fragment identified in wild type heart tissue.

From this work, I have developed the following working hypothesis based on existing knowledge and experimental results described to this point. In wild type animals ECSIT is expressed as full length 50kDa protein in all tissues and according to demand is poly-ubiquitinated and targeted to mitochondria where it is imported and the mitochondrial targeting sequence cleaved, leaving a 45kDa ECSIT protein. Once localised to the mitochondria ECSIT forms part of the MCIA complex along with NDUFAF1 and ACAD9.

To this point, the N209I mutation of ECSIT has little to no impact on the activity of the protein. The MCIA complex is then involved in the assembly of the membrane arm of complex I through an, as yet unknown, mechanism. Following this, the mutation of ECSIT must impact complex I assembly as there are small differences seen in liver, kidney and brain. However, this role is different to that seen in the heart, as the defect in heart is considerably greater than in these other tissues. It is conceivable that whilst the MCIA complex forms correctly and functions in complex I assembly, that its efficacy is reduced by a small degree due to a reduced binding affinity or structural change that leads to a reduction in complex I activity.

However, in the heart the role for ECSIT in complex I assembly differs, with a role for the 16kDa fragment identified in wild type heart. It is possible that this only exists in heart tissue due to a modification of this process that is not required in less energy demanding tissues. It would seem likely that this product is produced by cleavage of the 45kDa fragment, which may create multiple fragments, although this cannot currently be confirmed. Data suggests that this 16kDa fragment forms a constitutive part of complex I and it may be assumed that in this manner ECSIT-16kDa behaves as an accessory subunit of complex I in a tissue specific manner. Whilst it is unclear why ECSIT-16kDa is only an accessory subunit in heart, or why loss of it would lead to reduced complex I levels in heart when it is not required in other tissues, there is a relationship between complex I activity levels and ECSIT-16kDa presence in heart tissue. Further work should focus on confirming the identity of the ECSIT-16kDa fragment and determining its sequence and role in complex I assembly.

Following on from the identified defect of complex I assembly in heart tissue, work focused on identifying the downstream effects of complex I deficiency in an attempt to understand how the complex I deficiency results in cardiomyopathy. Mitochondrial fusion and fission exist in a delicate balance able to respond to alterations in mitochondrial function and eliminate defective subunits. In *Ecsit*$^{N209I/N209I}$ animals, the fusion/fission mechanism appears to be slightly disturbed, with an elevation of the outer membrane fusion protein MFN2 but a reduction in long isoforms of OPA1 and no change in DRP1 activation. Ultimately, this process warrants further investigation, potentially

through the quantification of mitochondrial network dynamics rather than controlling proteins.

Elevation of PINK1 protein levels suggest that mitophagy is elevated in *Ecsit*$^{N209I/N209I}$ hearts which may be a result of a change in mitochondrial fusion/fission dynamics or a result of the inability of the UPR^{mt} to cope with an accumulation of misfolded mitochondrial proteins. The UPR^{mt} is seemingly robustly activated, indicating that it recognises the accumulation of misfolded complex I proteins and that the mutation of ECSIT does not impair the UPR^{mt} response, which may have been a possibility given that ECSIT activates JNK2, a key activator of the UPR^{mt}. As such it may be possible that the disruption of mitochondrial network dynamics feed directly in to the increase in mitophagy or that the accumulation of misfolded proteins simply accumulate too fast for the UPR^{mt} to cope.

Finally, there was an expectation that reactive oxygen species would be elevated and that there would be a substantial energy insufficiency in the heart of *Ecsit*$^{N209I/N209I}$ animals. However, neither of these mechanisms were observed, with 4-HNE (as a measure of ROS) significantly reduced and AMPK activation also reduced. In hindsight, the reduction of ROS is not an unexpected result due to complex I being a significant site of ROS production. If the mechanism of complex I was impaired via a mutation of a key protein then it might make sense that ROS would accumulate due to defective electron transport. The actual mechanism is a reduction in total complex I abundance, which reduces the sites for ROS production and accordingly, reduces ROS levels. When taken into consideration, this result is in line with what would be expected given what is known about ECSIT's role in complex I assembly. However, the reduction of AMPK is unexpected and more difficult to explain. AMPK is typically activated in response to an elevation of [AMP], which would be expected with the loss of [ATP] that typically accompanies mitochondrial deficiency. The most likely explanation is that the measurements were taken at a point preceding a measureable change in [ATP], as this is maintained at or close to normal levels by the buffering capacity of phosphocreatine until late stage disease. The confounding issue for this explanation is that AMPK activation is not maintained at or close to normal levels but are in fact reduced in *Ecsit*$^{N209I/N209I}$ hearts,

suggesting that [AMP] is lower than in wild type controls, and therefore [ATP] is higher than controls.

In summary, the N209I mutation in ECSIT results in a severe cardiomyopathy with some changes in glucose and fatty acid metabolism as well as mild kidney impairment and a reduction in weight, lean mass and fat mass of *Ecsit*$^{N209I/N209I}$ animals. The TLR and BMP pathways appear mostly unaffected by the mutation, indicating that this region of ECSIT is either not key to the function of these pathways, or the change of this amino acid is tolerated. The mutation of ECSIT results in a defect in complex I assembly in multiple tissues with varying degrees of severity in various tissues. The effect on complex I assembly is most severe in heart tissue and this may be a result of an altered function or processing of ECSIT protein in this tissue. It is possible that, instead of functioning only as an assembly factor, a portion of ECSIT also acts as an accessory subunit of complex I in heart tissue and that the N209I mutation impairs this role, leading to a greater loss of complex I function and a severe cardiomyopathy.

7.2. Implications for the Field of Mitochondrial Dysfunction Research

Diagnosis of mitochondrial disease is typically performed on a muscle or skin biopsy to determine the mitochondrial function and biochemical basis of the disease [300]. The research I have undertaken as part of this thesis suggests that this method may obscure the diagnosis of a proportion of mitochondrial diseases due to tissue specific differences in mitochondrial function and behaviour. Whilst whole genome screening is becoming more prevalent [301] this relies on a complete understanding of the proteins, and therefore genes, involved in mitochondrial function to determine appropriate candidates.

Furthermore, much work on the structure and function of complex I and assembly factors involved takes place in cardiac tissue from various species due to the relative abundance of mitochondria. The work I have completed so far suggests that this research should be diversified to determine how mitochondrial assembly processes are undertaken in other tissues and cell types. The possibility exists that there are many differences in mitochondrial complexes and/or their assembly, even from one cell type to another within the same tissue. Through a better understanding of these differences, it may be possible to develop better tailored therapies which are capable of targeting

specific cell or tissue types in order to restore function to defective mitochondria where it is most needed.

7.3. Future Work

The work completed so far has raised many questions, which I have been unable to answer given the limitations of time and a suitable in vitro experimental system. First amongst these is the question of whether or not the 16kDa fragment is a portion of the ECSIT protein or whether it is an off target binding event of the antibody that only occurs in heart tissue. Given that ECSIT has limited sequence homology to any other known proteins it would be unexpected for this to be an off target binding event, however the possibility cannot be eliminated by this fact alone.

If this were an off target binding of the antibody then there are two possible explanations for the results seen so far. Firstly, this may represent a cardiac specific protein that is reduced in expression in *Ecsit*$^{N209I/N209I}$ hearts due to the development of the cardiomyopathy phenotype. An argument against this is that it is also reduced in 2-week old heart tissue, before the onset of cardiomyopathy, and hence is not lost due to cardiomyopathy but precedes it. Secondly, this may be a mitochondrial protein that is reduced due to a loss of ECSIT function in mitochondria, similar to the way a number of complex I proteins that were tested were reduced. However, if this were the case it would represent an interesting discovery in itself as this protein was not detected in other tissues, suggesting that this may be a tissue specific mitochondrial protein.

Future work could also focus on the tissue specificity of the complex I assembly defect and on identifying the metabolic cause of the alterations to glucose and fatty acid levels seen in plasma.

It would also be desirable to look at the 2D BN-PAGE results in more detail, either through further 2D BN-PAGE experiments in a variety of tissues or by using complexome analysis to analyse multiple tissues or complexes at once and reduce the associated time and labour costs.

It would also be potentially interesting to use an inducible or conditional *Ecsit* knockout mouse to investigate the development of the cardiomyopathy phenotype in more detail.

Ultimately, this work could be validated by screening HCM patient populations for mutations in *ECSIT*, thereby confirming that loss of ECSIT function results in a tissue specific mitochondrial disease.

7.3.1. Identification of 16kDa Fragment

To identify the 16kDa protein fragment seen in wild type and absent from *Ecsit*$^{N209I/N209I}$ cardiac tissue a number of approaches were attempted, these include co-immunoprecipitation using the original antibody as well as two antibodies raised against slightly different epitopes. The original antibody proved to be unsuitable for use in co-immunoprecipitation experiments in any of the conditions tested despite previous publications suggesting it was. Other antibodies used were able to pull down the larger 45 and 50kDa fragments of ECSIT through CO-IP but did not recognise the 16kDa fragment seen with the original Abcam antibody, making identification by co-IP and mass-spec impossible. Another possibility is to use the HIS tagged ECSIT protein cloned for other co-immunoprecipitation experiments and pull down using the anti-his antibody which is already known to be suitable for CO-IP. However, the 16kDa protein was not seen as part of these other CO-IP experiments suggesting that either the HIS tag is cleaved from the protein and is therefore undetectable, the 16kDa fragment is not produced in HEK293T cells that were used in these experiments, or that the 16kDa protein is definitely not a fragment of ECSIT.

To determine which of these explanations is correct, it would be necessary to culture a cardiomyocyte cell line such as HL-1 [302], silence the native ECSIT protein expression by a method such as siRNA and transfect with the tagged HIS-ECSIT construct. This would potentially allow for the expression of all three (50, 45 and 16 kDa) fragments of ECSIT and would by-pass the need for a reliable antibody as the anti-HIS antibody used previously would be suitable. HL-1 cells have transfection efficiencies up to roughly 80% with cationic lipid based transfection systems such as lipofectamine or jetPRIME, although they are notoriously difficult to optimise by this method. Higher efficiencies can be obtained with adenovirus methods.

Using a cardiac specific inducible knockout of *Ecsit* is unlikely to provide any useful information about the 16kDa fragment as loss of ECSIT protein could still lead to a loss of the 16kDa fragment, even if it is not an ECSIT protein fragment, just as is seen in *Ecsit*$^{N209I/N209I}$ animals.

7.3.2. Reliable measurements of ROS and energy insufficiency

Work so far measured ROS production indirectly by assessing the product of lipid peroxidation by ROS, 4-HNE. This method appears to be robust and gives reliable, repeatable measures. However, this is not a direct measurement of ROS production and there may be differences that are not detected as a result. A more direct measurement could be the use of amplex red to measure H_2O_2 production or mitoSOX™ Red to measure mitochondrial superoxide production. The limitation with both of these techniques is they are unsuitable for use with tissue lysates and given the difficulties with the culture of primary neonatal cardiomyocytes from *Ecsit*$^{N209I/N209I}$ mice these techniques were considered inviable and hence the 4-HNE method was used. If cardiomyocyte culture could be optimised to allow for the measurement of ROS levels on *Ecsit*$^{N209I/N209I}$ samples then either of these could be a viable option to support the results seen from the 4-HNE assay.

In addition to ROS production measurements, energy sufficiency measurements were also measured via a proxy (AMPK phosphorylation) as ADP and ATP measurements proved difficult in tissue lysate. A more reliable method for the assessment of energy sufficiency would be the measurement of PCr:ATP ratio in live animals. This is possible using phosphorous-31 magnetic resonance spectroscopy (^{31}P-MRS) on the *in vivo* mouse heart. This technique allows for assessment of both phosphocreatine and ATP levels in the contracting heart in order to determine the myocardial energy status [303]. This technique was not attempted due to a lack of access to the appropriate facilities and expertise, but could be done through an appropriate collaboration.

7.3.3. Further investigation of tissue differences

Significant differences can be seen in the complex I protein levels and activity between various tissues. Work to this point has shown that complex I protein levels are reduced to various levels in heart, kidney, liver, brain and muscle. However, comparison of tissues in more detail has been limited to heart and brain which represented the two extremes of this spectrum. Interestingly the level of complex I protein reduction does not represent the level of mitochondrial deficiency seen in these tissues suggesting that there may be a threshold level of complex I total protein that must be reached before any defect in mitochondrial dysfunction is seen. Investigating the mitochondrial function

of each of the tissues in this spectrum may reveal important information about the possibility of this 'threshold'.

Many of the Seahorse results presented so far have used isolated mitochondria to determine ETC function. The isolation of mitochondria by differential centrifugation is imperfect and only isolates a proportion of the total mitochondrial pool. This results in an incomplete representation of the total mitochondrial pool as the isolation preferentially selects certain mitochondrial populations over others and results in increased fragmentation of those that are isolated successfully [304]. Repeating experiments on permeabilised primary cells from wild type and *Ecsit*$^{N209I/N209I}$ animals would provide a more complete and reliable picture of the mitochondrial function in those tissues in question. The issue with this approach is selecting which cell type to assess, as many of those tissues measured thus far contain multiple cell types, each with their own metabolic demands and intricacies. Furthermore, this approach was attempted with cardiomyocytes with limited success. Successfully culturing cardiomyocytes would also allow for a XF mito fuel flex test to be performed to determine if wild type and *Ecsit*$^{N209I/N209I}$ cardiomyocytes have differing preferences for metabolic fuels. The XF mito fuel flex test is a form of Seahorse assay that provide cultured cells with various metabolic fuels (glucose, glutamine and fatty acid oxidation).

Further Seahorse analysis in the form of sequential impairment of each complex of the electron transport chain could also reveal if the mitochondrial dysfunction is entirely a result of complex I deficiency or if other complexes are also under (or over) performing, despite no changes in protein levels. Furthermore, if this experiment could be performed in primary cells from wild type and *Ecsit*$^{N209I/N209I}$ animals then the mitochondrial function as well as metabolism of a variety of different substrates (glutamine, fatty acids) can be assessed to determine if *Ecsit*$^{N209I/N209I}$ animals preferentially metabolise certain substrates due to the complex I assembly defect in certain tissues.

7.3.4. Changes in Cardiac Metabolism

The clinical chemistry results shown in section 3.8.1 hint at a change in the metabolism of certain substrates, with an increase in metabolism of both glucose and fatty acids. Assessing the levels of a variety of metabolites to give an overall picture of the so-called

'metabolome' could reveal which metabolic pathways are differentially regulated and provide further avenues of investigation regarding the link between cardiomyopathy and mitochondrial dysfunction.

This assessment may be performed using a variety of NMR spectroscopy and mass-spec techniques that can identify a great number of metabolites from tissue extracts and determine the levels of these metabolites. By comparing wild type and *Ecsit*$^{N209I/N209I}$ results we could determine which metabolic pathways are activated and which are suppressed in the hearts (or other tissues) of *Ecsit*$^{N209I/N209I}$ animals.

This work is already underway through a collaboration with Dr. Jules Griffin at the University of Cambridge and will form part of a future publication.

7.3.5. Complexome Analysis

Complexome analysis is the assessment of constituent proteins of complexes by mass spectrometry. For mitochondria, and in particular complex I analysis, this first involves isolating mitochondria and isolating mitochondrial complexes, sub-assemblies and proteins by blue native PAGE. Following blue native PAGE, gels are cut into 60 evenly sized slices and each slice is de-stained, trypsinised and analysed to determine the constituent proteins in each complex or subassembly. This provides results similar to the 2D BN-PAGE performed in chapter 5.5.2 but with a more complete overview that do not rely on the affinity of antibodies. This technique has been employed to determine the assembly pathway of complex I and could be used to determine in greater detail the effect on complex I assembly of the ECSIT N209I mutation.

This method might also be useful to determine if the 16kDa protein fragment identified is ECSIT by looking for ECSIT peptides as a constituent portion of fully assembled complex I. As my data already shows that the only fragment associated with complete complex I is the 16kDa fragment tryptic peptides in complex I must come from this fragment.

7.3.6. Knockout Mice

As constitutive knockouts of *Ecsit* are embryonically lethal it is not possible to study a total loss of ECSIT function in a mouse model. However, using an inducible tissue specific conditional model it may be possible to investigate the development of cardiomyopathy

by looking at the development of complex I dysfunction following knockout of the gene. This method would also allow for the investigation of ECSIT protein half-life and to determine the requirement for ECSIT in adult hearts that are already fully grown. With ECSIT known to be involved in development through the BMP pathway it remains a possibility that the requirement for ECSIT in the heart is a developmental one. It is well documented that foetal cardiac metabolism is focused on glucose metabolism, shifting to fatty acid metabolism sometime after birth and that heart failure is typically associated with a return to this foetal metabolic profile [305, 306]. We can speculate that ECSIT, through its link with both embryonic development and mitochondrial function, has a role in this metabolic switch and that the mutation of ECSIT impairs this role, leading to a continued preference of the heart for glucose metabolism. Whilst this is purely speculation without any supporting evidence, it would be an interesting avenue of investigation given what is known about ECSIT.

7.3.7. Rescue of Phenotype

Ecsit$^{N209I/N209I}$ mice develop a cardiomyopathy phenotype that develops gradually from around 4 weeks of age and is ultimately fatal between 16 and 18 weeks of age. It may be possible to replace the defective gene using a bacterial artificial chromosome (BAC) which expresses the ECSIT gene, replacing the defective protein in *Ecsit*$^{N209I/N209I}$ animals. As transgenic BAC mice would express the functional protein from birth this experiment would determine if rescue was possible before the development of the phenotype. Of more interest would be to return functional ECSIT to the cardiac tissue, or whole body after the cardiomyopathy development has already begun. This could be achieved by administering AAV9 virus expressing the wild type gene allowing for the replacement of the protein at any point during an animals life span [307]. This could be attempted as a time course, with proof of principal potentially taking place in new born animals and further experiments taking place at 4, 8, 12 and 16 weeks to determine if the replacement of ECSIT can rescue not only complex I activity but also the cardiomyopathy phenotype after the cellular and tissue changes have already occurred.

7.4. Concluding Remarks

The use of ENU mutagenesis has led to the identified a novel mouse model of hypertrophic cardiomyopathy resulting from a point mutation (N209I) in the gene *Ecsit*, a complex I assembly factor. The mutation leads to a significant reduction in complex I assembly in cardiac tissue whilst only minimally affecting tissues such as brain, kidney and liver. ECSIT protein is also known to be involved in both the toll-like receptor response and the bone morphogenetic protein pathway, however, data I have generated suggest that these pathways are either unaffected or only minimally affected by this mutation and are not involved in disease pathogenesis.

The working hypothesis I have established based on the data described in this thesis suggests that ECSIT protein is involved in complex I assembly in a tissue specific manner and whilst it is required in all tissues, its role in cardiac tissue differs significantly and it is only this role that is significantly affected by the N209I mutation.

In conclusion, the *Ecsit*^{N209I} mutation represents a novel model of cardiomyopathy as well as a useful tool for investigating the currently poorly understood role of complex I assembly factors in the process of complex I assembly and how this process may differ on a tissue by tissue basis.

References

1. Marín-García, J., *Mitochondria and Their Role in Cardiovasular Disease*. 2013, New York: Springer. 500.
2. Ferrari, R., et al., *Prognostic benefits of heart rate reduction in cardiovascular disease.* European Heart Journal Supplements, 2003. **5**(suppl G): p. G10-G14.
3. Khalifat, N., et al., *Membrane deformation under local pH gradient: mimicking mitochondrial cristae dynamics.* Biophys J, 2008. **95**(10): p. 4924-33.
4. Alberts, B., et al., *Molecular Biology of the Cell 4th Edition*. 2002.
5. Ren, M., C.K. Phoon, and M. Schlame, *Metabolism and function of mitochondrial cardiolipin.* Prog Lipid Res, 2014. **55**: p. 1-16.
6. Schlame, M. and M.L. Greenberg, *Biosynthesis, remodeling and turnover of mitochondrial cardiolipin.* Biochim Biophys Acta, 2017. **1862**(1): p. 3-7.
7. Schlame, M. and M. Ren, *The role of cardiolipin in the structural organization of mitochondrial membranes.* Biochim Biophys Acta, 2009. **1788**(10): p. 2080-3.
8. Fontanesi, F., *Mitochondria: Structure and Role in Respiration.* 2015: p. 1-13.
9. Koves, T.R., et al., *Subsarcolemmal and intermyofibrillar mitochondria play distinct roles in regulating skeletal muscle fatty acid metabolism.* Am J Physiol Cell Physiol, 2005. **288**(5): p. C1074-82.
10. Al-Mehdi, A.B., et al., *Perinuclear mitochondrial clustering creates an oxidant-rich nuclear domain required for hypoxia-induced transcription.* Sci Signal, 2012. **5**(231): p. ra47.
11. Palmer, J.W., B. Tandler, and C.L. Hoppel, *Biochemical properties of subsarcolemmal and interfibrillar mitochondria isolated from rat cardiac muscle.* J Biol Chem, 1977. **252**(23): p. 8731-9.
12. Kuznetsov, A.V., et al., *The cell-type specificity of mitochondrial dynamics.* Int J Biochem Cell Biol, 2009. **41**(10): p. 1928-39.
13. Piquereau, J., et al., *Mitochondrial dynamics in the adult cardiomyocytes: which roles for a highly specialized cell?* Front Physiol, 2013. **4**: p. 102.
14. Jornayvaz, F.R. and G.I. Shulman, *Regulation of mitochondrial biogenesis.* Essays Biochem, 2010. **47**: p. 69-84.
15. Hardie, D.G., *AMP-activated/SNF1 protein kinases: conserved guardians of cellular energy.* Nat Rev Mol Cell Biol, 2007. **8**(10): p. 774-85.
16. Nisoli, E., et al., *Mitochondrial biogenesis in mammals: the role of endogenous nitric oxide.* Science, 2003. **299**(5608): p. 896-9.
17. Lagouge, M., et al., *Resveratrol improves mitochondrial function and protects against metabolic disease by activating SIRT1 and PGC-1alpha.* Cell, 2006. **127**(6): p. 1109-22.
18. Wu, Z., et al., *Transducer of regulated CREB-binding proteins (TORCs) induce PGC-1alpha transcription and mitochondrial biogenesis in muscle cells.* Proc Natl Acad Sci U S A, 2006. **103**(39): p. 14379-84.
19. Scarpulla, R.C., *Transcriptional paradigms in mammalian mitochondrial biogenesis and function.* Physiol Rev, 2008. **88**(2): p. 611-38.
20. Scarpulla, R.C., *Nuclear control of respiratory gene expression in mammalian cells.* J Cell Biochem, 2006. **97**(4): p. 673-83.
21. Schreiber, S.N., et al., *The estrogen-related receptor alpha (ERRalpha) functions in PPARgamma coactivator 1alpha (PGC-1alpha)-induced mitochondrial biogenesis.* Proc Natl Acad Sci U S A, 2004. **101**(17): p. 6472-7.
22. Basu, A., et al., *Regulation of murine cytochrome oxidase Vb gene expression in different tissues and during myogenesis. Role of a YY-1 factor-binding negative enhancer.* J Biol Chem, 1997. **272**(9): p. 5899-908.
23. Giguere, V., *Transcriptional control of energy homeostasis by the estrogen-related receptors.* Endocr Rev, 2008. **29**(6): p. 677-96.
24. Lee, S.S., et al., *Targeted disruption of the alpha isoform of the peroxisome proliferator-activated receptor gene in mice results in abolishment of the pleiotropic effects of peroxisome proliferators.* Mol Cell Biol, 1995. **15**(6): p. 3012-22.

25. Puigserver, P., et al., *A cold-inducible coactivator of nuclear receptors linked to adaptive thermogenesis.* Cell, 1998. **92**(6): p. 829-39.
26. Scarpulla, R.C., *Metabolic control of mitochondrial biogenesis through the PGC-1 family regulatory network.* Biochim Biophys Acta, 2011. **1813**(7): p. 1269-78.
27. Meyers, D.E., H.I. Basha, and M.K. Koenig, *Mitochondrial Cardiomyopathy: Pathophysiology, Diagnosis, and Management.* Texas Heart Institute Journal, 2013. **40**(4): p. 385-394.
28. Scheffler, I.E., *Mitochondrial disease associated with complex I (NADH-CoQ oxidoreductase) deficiency.* J Inherit Metab Dis, 2015. **38**(3): p. 405-15.
29. Diaz, F., et al., *Mitochondrial disorders caused by mutations in respiratory chain assembly factors.* Semin Fetal Neonatal Med, 2011. **16**(4): p. 197-204.
30. Houstek, J., et al., *Mitochondrial diseases and genetic defects of ATP synthase.* Biochim Biophys Acta, 2006. **1757**(9-10): p. 1400-5.
31. Stock, D.L., A.G.W.; Walker, J.E., *Molecular Architecture of the Rotary Motor in ATP Synthase.* Science, 1999. **286**: p. 1700-1705.
32. Sazanov, L.A., *A giant molecular proton pump: structure and mechanism of respiratory complex I.* Nat Rev Mol Cell Biol, 2015. **16**(6): p. 375-88.
33. Hirst, J., *Mitochondrial complex I.* Annu Rev Biochem, 2013. **82**: p. 551-75.
34. Carroll, J., et al., *Analysis of the subunit composition of complex I from bovine heart mitochondria.* Mol Cell Proteomics, 2003. **2**(2): p. 117-26.
35. Stroud, D.A., et al., *Accessory subunits are integral for assembly and function of human mitochondrial complex I.* Nature, 2016. **538**(7623): p. 123-126.
36. Vartak, R.S., M.K. Semwal, and Y. Bai, *An update on complex I assembly: the assembly of players.* J Bioenerg Biomembr, 2014. **46**(4): p. 323-8.
37. Hummer, G. and M. Wikstrom, *Molecular simulation and modeling of complex I.* Biochim Biophys Acta, 2016. **1857**(7): p. 915-21.
38. Wirth, C., et al., *Structure and function of mitochondrial complex I.* Biochim Biophys Acta, 2016. **1857**(7): p. 902-14.
39. Zhu, J., K.R. Vinothkumar, and J. Hirst, *Structure of mammalian respiratory complex I.* Nature, 2016. **536**(7616): p. 354-8.
40. Rutter, J., D.R. Winge, and J.D. Schiffman, *Succinate dehydrogenase - Assembly, regulation and role in human disease.* Mitochondrion, 2010. **10**(4): p. 393-401.
41. Hagerhall, C., *Succinate: Quinone oxidoreductases - Variations on a Conseved Theme.* Biochim Biophys Acta, 1997. **1320**: p. 107-141.
42. Sun, F., et al., *Crystal structure of mitochondrial respiratory membrane protein complex II.* Cell, 2005. **121**(7): p. 1043-57.
43. Quinlan, C.L., et al., *Mitochondrial complex II can generate reactive oxygen species at high rates in both the forward and reverse reactions.* J Biol Chem, 2012. **287**(32): p. 27255-64.
44. Iwata, S.L., J.W.;Okada, K.; Lee, J.K.; Iwata, M.; Rasmussen, B.; Link, T.A.; Ramaswamy, S.; Jap, B.K., *Complete Structure of the 11-Subunit Bovine Mitochondrial cytochrome bc_1 Complex.* Science, 1998. **281**: p. 64-71.
45. Crofts, A.R.H., S.; Ugulava, N.; Barquera, B.; Gennis, R.; Guergova-Kuras, M.; Berry, E.A., *Pathways for proton release during ubihydroquinone oxidation by the bc_1 complex.* Proceedings of the National Academy of Sciences, 1999. **96**: p. 10021-10026.
46. Benit, P., S. Lebon, and P. Rustin, *Respiratory-chain diseases related to complex III deficiency.* Biochim Biophys Acta, 2009. **1793**(1): p. 181-5.
47. Michel, H., *The mechanism of proton pumping by cytochrome c oxidase.* proceedings of the National Academy of Sciences, 1998. **95**: p. 12819-21824.
48. Michel, H., *Cytochrome c Oxidase: Catalytic Cycle and Mechanisms of Proton Pumping - A Discussion.* Biochemistry, 1999. **38**: p. 15129-15140.

49. Tsukihara, T.A., H.; Yamashita, E.; Tomizaki, T.; Yamaguchi, H.; Shinzawa-Itoh, K.; Nakashima, R.; Yaono, R.; Yoshikawa, S., *The Whole Structure of the 13-Subunit Oxidized Cytochrome c Oxidase at 2.8A.* Science, 1996. **272**: p. 1136-1144.
50. Capaldi, R.A., et al., *Coupling between catalytic sites and the proton channel in F1F0-type ATPases.* Trends in Biochemical Sciences, 1994. **19**(7): p. 284-289.
51. Nijtmans, L.G., et al., *Assembly of mitochondrial ATP synthase in cultured human cells: implications for mitochondrial diseases.* Biochim Biophys Acta, 1995. **1272**(3): p. 190-8.
52. von Ballmoos, C., A. Wiedenmann, and P. Dimroth, *Essentials for ATP synthesis by F1F0 ATP synthases.* Annu Rev Biochem, 2009. **78**: p. 649-72.
53. Jonckheere, A.I., J.A. Smeitink, and R.J. Rodenburg, *Mitochondrial ATP synthase: architecture, function and pathology.* J Inherit Metab Dis, 2012. **35**(2): p. 211-25.
54. Collinson, I.R., et al., *F0 Membrane Domain of ATP Synthase from Bovine Heart Mitochondria: Purification, Subunit Composition, and Reconstitution with F1-ATPase.* Biochemistry, 1994. **33**(25): p. 7971-7978.
55. Abrahams, J.P., et al., *Structure at 2.8 A resolution of F1-ATPase from bovine heart mitochondria.* Nature, 1994. **370**(6491): p. 621-8.
56. Watt, I.N., et al., *Bioenergetic cost of making an adenosine triphosphate molecule in animal mitochondria.* Proc Natl Acad Sci U S A, 2010. **107**(39): p. 16823-7.
57. Vartak, R., C.A. Porras, and Y. Bai, *Respiratory supercomplexes: structure, function and assembly.* Protein Cell, 2013. **4**(8): p. 582-90.
58. Lenaz, G., et al., *Complex I function in mitochondrial supercomplexes.* Biochim Biophys Acta, 2016. **1857**(7): p. 991-1000.
59. Chaban, Y., E.J. Boekema, and N.V. Dudkina, *Structures of mitochondrial oxidative phosphorylation supercomplexes and mechanisms for their stabilisation.* Biochim Biophys Acta, 2014. **1837**(4): p. 418-26.
60. Genova, M.L. and G. Lenaz, *Functional role of mitochondrial respiratory supercomplexes.* Biochim Biophys Acta, 2014. **1837**(4): p. 427-43.
61. Acin-Perez, R., et al., *Respiratory complex III is required to maintain complex I in mammalian mitochondria.* Mol Cell, 2004. **13**(6): p. 805-15.
62. Schagger, H., et al., *Significance of respirasomes for the assembly/stability of human respiratory chain complex I.* J Biol Chem, 2004. **279**(35): p. 36349-53.
63. Diaz, F., et al., *Cytochrome c oxidase is required for the assembly/stability of respiratory complex I in mouse fibroblasts.* Mol Cell Biol, 2006. **26**(13): p. 4872-81.
64. Vempati, U.D., X. Han, and C.T. Moraes, *Lack of cytochrome c in mouse fibroblasts disrupts assembly/stability of respiratory complexes I and IV.* J Biol Chem, 2009. **284**(7): p. 4383-91.
65. Chen, Y.C., et al., *Identification of a protein mediating respiratory supercomplex stability.* Cell Metab, 2012. **15**(3): p. 348-60.
66. Jian, C., et al., *Deficiency of PHB complex impairs respiratory supercomplex formation and activates mitochondrial flashes.* J Cell Sci, 2017. **130**(15): p. 2620-2630.
67. Elurbe, D.M. and M.A. Huynen, *The origin of the supernumerary subunits and assembly factors of complex I: A treasure trove of pathway evolution.* Biochim Biophys Acta, 2016. **1857**(7): p. 971-9.
68. Giachin, G., et al., *Dynamics of Human Mitochondrial Complex I Assembly: Implications for Neurodegenerative Diseases.* Front Mol Biosci, 2016. **3**: p. 43.
69. Heide, H., et al., *Complexome profiling identifies TMEM126B as a component of the mitochondrial complex I assembly complex.* Cell Metab, 2012. **16**(4): p. 538-49.
70. Guarani, V., et al., *TIMMDC1/C3orf1 Functions as a Membrane-Embedded Mitochondrial Complex I Assembly Factor through Association with the MCIA Complex.* Molecular and Cell Biology, 2014. **34**.
71. Mimaki, M., et al., *Understanding mitochondrial complex I assembly in health and disease.* Biochim Biophys Acta, 2012. **1817**(6): p. 851-62.

72. Guerrero-Castillo, S., et al., *The Assembly Pathway of Mitochondrial Respiratory Chain Complex I.* Cell Metab, 2016.
73. Mick, D.U., et al., *MITRAC links mitochondrial protein translocation to respiratory-chain assembly and translational regulation.* Cell, 2012. **151**(7): p. 1528-41.
74. Calvo, S.E., et al., *High-throughput, pooled sequencing identifies mutations in NUBPL and FOXRED1 in human complex I deficiency.* Nat Genet, 2010. **42**(10): p. 851-8.
75. Saada, A., et al., *C6ORF66 is an assembly factor of mitochondrial complex I.* Am J Hum Genet, 2008. **82**(1): p. 32-8.
76. Saada, A., et al., *Mutations in NDUFAF3 (C3ORF60), encoding an NDUFAF4 (C6ORF66)-interacting complex I assembly protein, cause fatal neonatal mitochondrial disease.* Am J Hum Genet, 2009. **84**(6): p. 718-27.
77. Hoefs, S.J., et al., *Baculovirus complementation restores a novel NDUFAF2 mutation causing complex I deficiency.* Hum Mutat, 2009. **30**(7): p. E728-36.
78. Ogilvie, I., N.G. Kennaway, and E.A. Shoubridge, *A molecular chaperone for mitochondrial complex I assembly is mutated in a progressive encephalopathy.* J Clin Invest, 2005. **115**(10): p. 2784-92.
79. Sheftel, A.D., et al., *Human ind1, an iron-sulfur cluster assembly factor for respiratory complex I.* Mol Cell Biol, 2009. **29**(22): p. 6059-73.
80. Bych, K., et al., *The iron-sulphur protein Ind1 is required for effective complex I assembly.* EMBO J, 2008. **27**(12): p. 1736-46.
81. Kmita, K. and V. Zickermann, *Accessory subunits of mitochondrial complex I.* Biochem Soc Trans, 2013. **41**(5): p. 1272-9.
82. Sanchez-Caballero, L., S. Guerrero-Castillo, and L. Nijtmans, *Unraveling the complexity of mitochondrial complex I assembly: A dynamic process.* Biochim Biophys Acta, 2016. **1857**(7): p. 980-90.
83. Ong, S.B., A.R. Hall, and D.J. Hausenloy, *Mitochondrial dynamics in cardiovascular health and disease.* Antioxid Redox Signal, 2013. **19**(4): p. 400-14.
84. Dorn, G.W., 2nd, *Mitochondrial dynamics in heart disease.* Biochim Biophys Acta, 2013. **1833**(1): p. 233-41.
85. Song, Z., et al., *Mitofusins and OPA1 mediate sequential steps in mitochondrial membrane fusion.* Mol Biol Cell, 2009. **20**(15): p. 3525-32.
86. Del Dotto, V., et al., *OPA1 Isoforms in the Hierarchical Organization of Mitochondrial Functions.* Cell Rep, 2017. **19**(12): p. 2557-2571.
87. Akepati, V.R., et al., *Characterization of OPA1 isoforms isolated from mouse tissues.* J Neurochem, 2008. **106**(1): p. 372-83.
88. Smirnova, E., et al., *Dynamin-related protein Drp1 is required for mitochondrial division in mammalian cells.* Mol Biol Cell, 2001. **12**(8): p. 2245-56.
89. Zhang, Z., et al., *Drp1, Mff, Fis1, and MiD51 are coordinated to mediate mitochondrial fission during UV irradiation-induced apoptosis.* FASEB J, 2016. **30**(1): p. 466-76.
90. Ni, H.M., J.A. Williams, and W.X. Ding, *Mitochondrial dynamics and mitochondrial quality control.* Redox Biol, 2015. **4**: p. 6-13.
91. Kirkinezos, I.G. and C.T. Moraes, *Reactive oxygen species and mitochondrial diseases.* Semin Cell Dev Biol, 2001. **12**(6): p. 449-57.
92. Murphy, M.P., *How mitochondria produce reactive oxygen species.* Biochem J, 2009. **417**(1): p. 1-13.
93. Kussmaul, L. and J. Hirst, *The mechanism of superoxide production by NADH:ubiquinone oxidoreductase (complex I) from bovine heart mitochondria.* Proc Natl Acad Sci U S A, 2006. **103**(20): p. 7607-12.
94. Kushnareva, Y., A.N. Murphy, and A. Andreyev, *Complex I-mediated reactive oxygen species generation: modulation by cytochrome c and NAD(P)+ oxidation-reduction state.* Biochem J, 2002. **368**(Pt 2): p. 545-53.
95. Liu, Y., G. Fiskum, and D. Schubert, *Generation of reactive oxygen species by the mitochondrial electron transport chain.* J Neurochem, 2002. **80**(5): p. 780-7.

96. Hirst, J. and M.M. Roessler, *Energy conversion, redox catalysis and generation of reactive oxygen species by respiratory complex I.* Biochim Biophys Acta, 2016. **1857**(7): p. 872-83.
97. Scialo, F., et al., *Mitochondrial ROS Produced via Reverse Electron Transport Extend Animal Lifespan.* Cell Metab, 2016. **23**(4): p. 725-34.
98. Chen, L., et al., *OPA1 mutation and late-onset cardiomyopathy: mitochondrial dysfunction and mtDNA instability.* J Am Heart Assoc, 2012. **1**(5): p. e003012.
99. Jung, C., et al., *Dystrophic cardiomyopathy: amplification of cellular damage by Ca2+ signalling and reactive oxygen species-generating pathways.* Cardiovasc Res, 2008. **77**(4): p. 766-73.
100. Chouchani, E.T., et al., *Complex I deficiency due to selective loss of Ndufs4 in the mouse heart results in severe hypertrophic cardiomyopathy.* PLoS One, 2014. **9**(4): p. e94157.
101. Ingwall, J.S. and R.G. Weiss, *Is the failing heart energy starved? On using chemical energy to support cardiac function.* Circ Res, 2004. **95**(2): p. 135-45.
102. Balaban, R.S., *Domestication of the cardiac mitochondrion for energy conversion.* J Mol Cell Cardiol, 2009. **46**(6): p. 832-41.
103. Randle, P.J., et al., *The glucose fatty-acid cycle. Its role in insulin sensitivity and the metabolic disturbances of diabetes mellitus.* Lancet, 1963. **1**(7285): p. 785-9.
104. Nickel, A., J. Loffler, and C. Maack, *Myocardial energetics in heart failure.* Basic Res Cardiol, 2013. **108**(4): p. 358.
105. Maack, C. and B. O'Rourke, *Excitation-contraction coupling and mitochondrial energetics.* Basic Res Cardiol, 2007. **102**(5): p. 369-92.
106. Neubauer, S., et al., *Myocardial phosphocreatine-to-ATP ratio is a predictor of mortality in patients with dilated cardiomyopathy.* Circulation, 1997. **96**(7): p. 2190-6.
107. Schlattner, U., M. Tokarska-Schlattner, and T. Wallimann, *Mitochondrial creatine kinase in human health and disease.* Biochim Biophys Acta, 2006. **1762**(2): p. 164-80.
108. Neubauer, S., *The failing heart--an engine out of fuel.* N Engl J Med, 2007. **356**(11): p. 1140-51.
109. Maslov, M.Y., et al., *Altered high-energy phosphate metabolism predicts contractile dysfunction and subsequent ventricular remodeling in pressure-overload hypertrophy mice.* Am J Physiol Heart Circ Physiol, 2007. **292**(1): p. H387-91.
110. Kwong, J.Q., et al., *Genetic deletion of the mitochondrial phosphate carrier desensitizes the mitochondrial permeability transition pore and causes cardiomyopathy.* Cell Death Differ, 2014. **21**(8): p. 1209-17.
111. Lygate, C.A., et al., *Living without creatine: unchanged exercise capacity and response to chronic myocardial infarction in creatine-deficient mice.* Circ Res, 2013. **112**(6): p. 945-55.
112. Hardie, D.G. and D. Carling, *The AMP-activated protein kinase--fuel gauge of the mammalian cell?* Eur J Biochem, 1997. **246**(2): p. 259-73.
113. Zong, H., et al., *AMP kinase is required for mitochondrial biogenesis in skeletal muscle in response to chronic energy deprivation.* Proceedings of the National Academy of Sciences of the United States of America, 2002. **99**(25): p. 15983-15987.
114. Tian, R., et al., *Increased adenosine monophosphate-activated protein kinase activity in rat hearts with pressure-overload hypertrophy.* Circulation, 2001. **104**(14): p. 1664-9.
115. Jovaisaite, V., L. Mouchiroud, and J. Auwerx, *The mitochondrial unfolded protein response, a conserved stress response pathway with implications in health and disease.* J Exp Biol, 2014. **217**(Pt 1): p. 137-43.
116. Lin, Y.F. and C.M. Haynes, *Metabolism and the UPR(mt).* Mol Cell, 2016. **61**(5): p. 677-82.
117. Zhao, Q., et al., *A mitochondrial specific stress response in mammalian cells.* EMBO J, 2002. **21**(17): p. 4411-9.

118. Aldridge, J.E., T. Horibe, and N.J. Hoogenraad, *Discovery of genes activated by the mitochondrial unfolded protein response (mtUPR) and cognate promoter elements.* PLoS One, 2007. **2**(9): p. e874.
119. Jaeschke, A., et al., *JNK2 is a positive regulator of the cJun transcription factor.* Mol Cell, 2006. **23**(6): p. 899-911.
120. Weiss, C., et al., *JNK phosphorylation relieves HDAC3-dependent suppression of the transcriptional activity of c-Jun.* EMBO J, 2003. **22**(14): p. 3686-95.
121. Rath, E., et al., *Induction of dsRNA-activated protein kinase links mitochondrial unfolded protein response to the pathogenesis of intestinal inflammation.* Gut, 2012. **61**(9): p. 1269-78.
122. Fiorese, C.J., et al., *The Transcription Factor ATF5 Mediates a Mammalian Mitochondrial UPR.* Curr Biol, 2016. **26**(15): p. 2037-2043.
123. Papa, L. and D. Germain, *Estrogen receptor mediates a distinct mitochondrial unfolded protein response.* J Cell Sci, 2011. **124**(Pt 9): p. 1396-402.
124. Radke, S., et al., *Mitochondrial protein quality control by the proteasome involves ubiquitination and the protease Omi.* J Biol Chem, 2008. **283**(19): p. 12681-5.
125. Jin, S.M. and R.J. Youle, *The accumulation of misfolded proteins in the mitochondrial matrix is sensed by PINK1 to induce PARK2/Parkin-mediated mitophagy of polarized mitochondria.* Autophagy, 2013. **9**(11): p. 1750-7.
126. Lin, W. and U.J. Kang, *Characterization of PINK1 processing, stability, and subcellular localization.* J Neurochem, 2008. **106**(1): p. 464-74.
127. Deas, E., et al., *PINK1 cleavage at position A103 by the mitochondrial protease PARL.* Hum Mol Genet, 2011. **20**(5): p. 867-79.
128. Jin, S.M., et al., *Mitochondrial membrane potential regulates PINK1 import and proteolytic destabilization by PARL.* J Cell Biol, 2010. **191**(5): p. 933-42.
129. Okatsu, K., et al., *PINK1 autophosphorylation upon membrane potential dissipation is essential for Parkin recruitment to damaged mitochondria.* Nat Commun, 2012. **3**: p. 1016.
130. Chen, Y. and G.W. Dorn, 2nd, *PINK1-phosphorylated mitofusin 2 is a Parkin receptor for culling damaged mitochondria.* Science, 2013. **340**(6131): p. 471-5.
131. Kane, L.A., et al., *PINK1 phosphorylates ubiquitin to activate Parkin E3 ubiquitin ligase activity.* J Cell Biol, 2014. **205**(2): p. 143-53.
132. Gao, F., et al., *The mitochondrial protein BNIP3L is the substrate of PARK2 and mediates mitophagy in PINK1/PARK2 pathway.* Hum Mol Genet, 2015. **24**(9): p. 2528-38.
133. Matsuda, N., et al., *PINK1 stabilized by mitochondrial depolarization recruits Parkin to damaged mitochondria and activates latent Parkin for mitophagy.* J Cell Biol, 2010. **189**(2): p. 211-21.
134. Narendra, D.P. and R.J. Youle, *Targeting mitochondrial dysfunction: role for PINK1 and Parkin in mitochondrial quality control.* Antioxid Redox Signal, 2011. **14**(10): p. 1929-38.
135. Oka, T., et al., *Mitochondrial DNA that escapes from autophagy causes inflammation and heart failure.* Nature, 2012. **485**(7397): p. 251-5.
136. Tong, M. and J. Sadoshima, *Mitochondrial autophagy in cardiomyopathy.* Curr Opin Genet Dev, 2016. **38**: p. 8-15.
137. Zhu, X., et al., *Pathogenic mutations of nuclear genes associated with mitochondrial disorders.* Acta Biochimica et Biophysica Sinica, 2009. **41**(3): p. 179-187.
138. Gorman, G.S., et al., *Prevalence of nuclear and mitochondrial DNA mutations related to adult mitochondrial disease.* Ann Neurol, 2015. **77**(5): p. 753-9.
139. Fassone, E. and S. Rahman, *Complex I deficiency: clinical features, biochemistry and molecular genetics.* J Med Genet, 2012. **49**(9): p. 578-90.
140. Pagniez-Mammeri, H., et al., *Mitochondrial complex I deficiency of nuclear origin I. Structural genes.* Mol Genet Metab, 2012. **105**(2): p. 163-72.
141. Schuelke, M., et al., *Mutant NDUFV1 subunit of mitochondrial complex I causes leukodystrophy and myoclonic epilepsy.* Nat Genet, 1999. **21**(3): p. 260-1.

142. Benit, P., et al., *Mutant NDUFV2 subunit of mitochondrial complex I causes early onset hypertrophic cardiomyopathy and encephalopathy.* Hum Mutat, 2003. **21**(6): p. 582-6.
143. Benit, P., et al., *Large-scale deletion and point mutations of the nuclear NDUFV1 and NDUFS1 genes in mitochondrial complex I deficiency.* Am J Hum Genet, 2001. **68**(6): p. 1344-52.
144. Loeffen, J., et al., *Mutations in the complex I NDUFS2 gene of patients with cardiomyopathy and encephalomyopathy.* Ann Neurol, 2001. **49**(2): p. 195-201.
145. Berardo, A., O. Musumeci, and A. Toscano, *Cardiological manifestations of mitochondrial respiratory chain disorders.* Acta Myologica, 2011. **30**(1): p. 9-15.
146. Benit, P., *Mutant NDUFS3 subunit of mitochondrial complex I causes Leigh syndrome.* Journal of Medical Genetics, 2004. **41**(1): p. 14-17.
147. Triepels, R.H., et al., *Leigh syndrome associated with a mutation in the NDUFS7 (PSST) nuclear encoded subunit of complex I.* Ann Neurol, 1999. **45**(6): p. 787-90.
148. Loeffen, J., et al., *The first nuclear-encoded complex I mutation in a patient with Leigh syndrome.* Am J Hum Genet, 1998. **63**(6): p. 1598-608.
149. Bourgeron, T., et al., *Mutation of a nuclear succinate dehydrogenase gene results in mitochondrial respiratory chain deficiency.* Nat Genet, 1995. **11**(2): p. 144-9.
150. Horvath, R., et al., *Leigh syndrome caused by mutations in the flavoprotein (Fp) subunit of succinate dehydrogenase (SDHA).* J Neurol Neurosurg Psychiatry, 2006. **77**(1): p. 74-6.
151. King, A., M.A. Selak, and E. Gottlieb, *Succinate dehydrogenase and fumarate hydratase: linking mitochondrial dysfunction and cancer.* Oncogene, 2006. **25**(34): p. 4675-82.
152. Fernandez-Vizarra, E. and M. Zeviani, *Nuclear gene mutations as the cause of mitochondrial complex III deficiency.* Front Genet, 2015. **6**: p. 134.
153. Haut, S., et al., *A deletion in the human QP-C gene causes a complex III deficiency resulting in hypoglycaemia and lactic acidosis.* Hum Genet, 2003. **113**(2): p. 118-22.
154. Barel, O., et al., *Mitochondrial complex III deficiency associated with a homozygous mutation in UQCRQ.* Am J Hum Genet, 2008. **82**(5): p. 1211-6.
155. Miyake, N., et al., *Mitochondrial complex III deficiency caused by a homozygous UQCRC2 mutation presenting with neonatal-onset recurrent metabolic decompensation.* Hum Mutat, 2013. **34**(3): p. 446-52.
156. Gaignard, P., et al., *Mutations in CYC1, encoding cytochrome c1 subunit of respiratory chain complex III, cause insulin-responsive hyperglycemia.* Am J Hum Genet, 2013. **93**(2): p. 384-9.
157. Fernandez-Vizarra, E., V. Tiranti, and M. Zeviani, *Assembly of the oxidative phosphorylation system in humans: what we have learned by studying its defects.* Biochim Biophys Acta, 2009. **1793**(1): p. 200-11.
158. Abdulhag, U.N., et al., *Mitochondrial complex IV deficiency, caused by mutated COX6B1, is associated with encephalomyopathy, hydrocephalus and cardiomyopathy.* Eur J Hum Genet, 2015. **23**(2): p. 159-64.
159. Hejzlarova, K., et al., *Nuclear genetic defects of mitochondrial ATP synthase.* Physiol Res, 2014. **63 Suppl 1**: p. S57-71.
160. Jonckheere, A.I., et al., *A complex V ATP5A1 defect causes fatal neonatal mitochondrial encephalopathy.* Brain, 2013. **136**(Pt 5): p. 1544-54.
161. el Azzouzi, H., et al., *The hypoxia-inducible microRNA cluster miR-199a approximately 214 targets myocardial PPARdelta and impairs mitochondrial fatty acid oxidation.* Cell Metab, 2013. **18**(3): p. 341-54.
162. Bugiani, M., et al., *Clinical and molecular findings in children with complex I deficiency.* Biochim Biophys Acta, 2004. **1659**(2-3): p. 136-47.
163. Breningstall, G.N., J. Shoffner, and R.J. Patterson, *Siblings with leukoencephalopathy.* Semin Pediatr Neurol, 2008. **15**(4): p. 212-5.

164. Zafeiriou, D.I., et al., *MR spectroscopy and serial magnetic resonance imaging in a patient with mitochondrial cystic leukoencephalopathy due to complex I deficiency and NDUFV1 mutations and mild clinical course.* Neuropediatrics, 2008. **39**(3): p. 172-5.
165. Pagniez-Mammeri, H., et al., *Rapid screening for nuclear genes mutations in isolated respiratory chain complex I defects.* Mol Genet Metab, 2009. **96**(4): p. 196-200.
166. Martin, M.A., et al., *Leigh syndrome associated with mitochondrial complex I deficiency due to a novel mutation in the NDUFS1 gene.* Arch Neurol, 2005. **62**(4): p. 659-61.
167. Hoefs, S.J., et al., *Novel mutations in the NDUFS1 gene cause low residual activities in human complex I deficiencies.* Mol Genet Metab, 2010. **100**(3): p. 251-6.
168. Tuppen, H.A., et al., *The p.M292T NDUFS2 mutation causes complex I-deficient Leigh syndrome in multiple families.* Brain, 2010. **133**(10): p. 2952-63.
169. Pagniez-Mammeri, H., et al., *Leukoencephalopathy with vanishing white matter caused by compound heterozygous mutations in mitochondrial complex I NDUFS1 subunit.* Mol Genet Metab, 2010. **101**(2-3): p. 297-8.
170. Ferreira, M., et al., *Progressive cavitating leukoencephalopathy associated with respiratory chain complex I deficiency and a novel mutation in NDUFS1.* Neurogenetics, 2011. **12**(1): p. 9-17.
171. Lebon, S., et al., *A novel mutation in the human complex I NDUFS7 subunit associated with Leigh syndrome.* Mol Genet Metab, 2007. **90**(4): p. 379-82.
172. Lebon, S., et al., *A novel mutation of the NDUFS7 gene leads to activation of a cryptic exon and impaired assembly of mitochondrial complex I in a patient with Leigh syndrome.* Mol Genet Metab, 2007. **92**(1-2): p. 104-8.
173. Procaccio, V. and D.C. Wallace, *Late-onset Leigh syndrome in a patient with mitochondrial complex I NDUFS8 mutations.* Neurology, 2004. **62**(10): p. 1899-901.
174. van den Heuvel, L., et al., *Demonstration of a new pathogenic mutation in human complex I deficiency: a 5-bp duplication in the nuclear gene encoding the 18-kD (AQDQ) subunit.* Am J Hum Genet, 1998. **62**(2): p. 262-8.
175. Budde, S.M., et al., *Combined enzymatic complex I and III deficiency associated with mutations in the nuclear encoded NDUFS4 gene.* Biochem Biophys Res Commun, 2000. **275**(1): p. 63-8.
176. Budde, S.M., et al., *Clinical heterogeneity in patients with mutations in the NDUFS4 gene of mitochondrial complex I.* J Inherit Metab Dis, 2003. **26**(8): p. 813-5.
177. Petruzzella, V., et al., *A nonsense mutation in the NDUFS4 gene encoding the 18 kDa (AQDQ) subunit of complex I abolishes assembly and activity of the complex in a patient with Leigh-like syndrome.* Hum Mol Genet, 2001. **10**(5): p. 529-35.
178. Benit, P., et al., *Genotyping microsatellite DNA markers at putative disease loci in inbred/multiplex families with respiratory chain complex I deficiency allows rapid identification of a novel nonsense mutation (IVS1nt -1) in the NDUFS4 gene in Leigh syndrome.* Hum Genet, 2003. **112**(5-6): p. 563-6.
179. Anderson, S.L., et al., *A novel mutation in NDUFS4 causes Leigh syndrome in an Ashkenazi Jewish family.* J Inherit Metab Dis, 2008. **31 Suppl 2**: p. S461-7.
180. Leshinsky-Silver, E., et al., *NDUFS4 mutations cause Leigh syndrome with predominant brainstem involvement.* Mol Genet Metab, 2009. **97**(3): p. 185-9.
181. Kirby, D.M., et al., *NDUFS6 mutations are a novel cause of lethal neonatal mitochondrial complex I deficiency.* Journal of Clinical Investigation, 2004. **114**(6): p. 837-845.
182. Spiegel, R., et al., *Mutated NDUFS6 is the cause of fatal neonatal lactic acidemia in Caucasus Jews.* Eur J Hum Genet, 2009. **17**(9): p. 1200-3.
183. Ostergaard, E., et al., *Respiratory chain complex I deficiency due to NDUFA12 mutations as a new cause of Leigh syndrome.* J Med Genet, 2011. **48**(11): p. 737-40.
184. Angebault, C., et al., *Mutation in NDUFA13/GRIM19 leads to early onset hypotonia, dyskinesia and sensorial deficiencies, and mitochondrial complex I instability.* Hum Mol Genet, 2015. **24**(14): p. 3948-55.

185. Berger, I., et al., *Mitochondrial complex I deficiency caused by a deleterious NDUFA11 mutation.* Ann Neurol, 2008. **63**(3): p. 405-8.
186. Hoefs, S.J., et al., *NDUFA2 complex I mutation leads to Leigh disease.* Am J Hum Genet, 2008. **82**(6): p. 1306-15.
187. Hoefs, S.J., et al., *NDUFA10 mutations cause complex I deficiency in a patient with Leigh disease.* Eur J Hum Genet, 2011. **19**(3): p. 270-4.
188. Baertling, F., et al., *NDUFA9 point mutations cause a variable mitochondrial complex I assembly defect.* Clin Genet, 2017.
189. Fernandez-Moreira, D., et al., *X-linked NDUFA1 gene mutations associated with mitochondrial encephalomyopathy.* Ann Neurol, 2007. **61**(1): p. 73-83.
190. Potluri, P., et al., *A novel NDUFA1 mutation leads to a progressive mitochondrial complex I-specific neurodegenerative disease.* Mol Genet Metab, 2009. **96**(4): p. 189-95.
191. Pitceathly, R.D., et al., *NDUFA4 mutations underlie dysfunction of a cytochrome c oxidase subunit linked to human neurological disease.* Cell Rep, 2013. **3**(6): p. 1795-805.
192. van Rahden, V.A., et al., *Mutations in NDUFB11, encoding a complex I component of the mitochondrial respiratory chain, cause microphthalmia with linear skin defects syndrome.* Am J Hum Genet, 2015. **96**(4): p. 640-50.
193. Friederich, M.W., et al., *Mutations in the accessory subunit NDUFB10 result in isolated complex I deficiency and illustrate the critical role of intermembrane space import for complex I holoenzyme assembly.* Hum Mol Genet, 2017. **26**(4): p. 702-716.
194. Schon, E.A., S. DiMauro, and M. Hirano, *Human mitochondrial DNA: roles of inherited and somatic mutations.* Nat Rev Genet, 2012. **13**(12): p. 878-90.
195. Silvestri, G., et al., *Maternally inherited cardiomyopathy: a new phenotype associated with the A to G AT nt.3243 of mitochondrial DNA (MELAS mutation).* Muscle Nerve, 1997. **20**(2): p. 221-5.
196. Marin-Garcia, J., M.J. Goldenthal, and G.W. Moe, *Mitochondrial pathology in cardiac failure.* Cardiovasc Res, 2001. **49**(1): p. 17-26.
197. Di Donato, S., *Multisystem manifestations of mitochondrial disorders.* J Neurol, 2009. **256**(5): p. 693-710.
198. Govindaraj, P., et al., *Mitochondrial DNA variations associated with hypertrophic cardiomyopathy.* Mitochondrion, 2014. **16**: p. 65-72.
199. Zurita Rendon, O., et al., *The arginine methyltransferase NDUFAF7 is essential for complex I assembly and early vertebrate embryogenesis.* Hum Mol Genet, 2014. **23**(19): p. 5159-70.
200. Pagniez-Mammeri, H., et al., *Mitochondrial complex I deficiency of nuclear origin II. Non-structural genes.* Mol Genet Metab, 2012. **105**(2): p. 173-9.
201. Alston, C.L., et al., *Biallelic Mutations in TMEM126B Cause Severe Complex I Deficiency with a Variable Clinical Phenotype.* Am J Hum Genet, 2016. **99**(1): p. 217-27.
202. Catteruccia, M., et al., *Persistent pulmonary arterial hypertension in the newborn (PPHN): a frequent manifestation of TMEM70 defective patients.* Mol Genet Metab, 2014. **111**(3): p. 353-359.
203. Vogel, R.O., et al., *Human mitochondrial complex I assembly is mediated by NDUFAF1.* FEBS J, 2005. **272**(20): p. 5317-26.
204. Dunning, C.J.R., et al., *Human CIA30 is involved in the early assembly of mitochondrial complex I and mutations in its gene cause disease.* The EMBO Journal, 2007. **26**(13): p. 3227-3237.
205. Fassone, E., et al., *Mutations in the mitochondrial complex I assembly factor NDUFAF1 cause fatal infantile hypertrophic cardiomyopathy.* J Med Genet, 2011. **48**(10): p. 691-7.
206. Barghuti, F., et al., *The unique neuroradiology of complex I deficiency due to NDUFA12L defect.* Mol Genet Metab, 2008. **94**(1): p. 78-82.
207. Janssen, R.J., et al., *Contiguous gene deletion of ELOVL7, ERCC8 and NDUFAF2 in a patient with a fatal multisystem disorder.* Hum Mol Genet, 2009. **18**(18): p. 3365-74.

208. Herzer, M., et al., *Leigh disease with brainstem involvement in complex I deficiency due to assembly factor NDUFAF2 defect.* Neuropediatrics, 2010. **41**(1): p. 30-4.
209. Pospisilik, J.A., et al., *Targeted deletion of AIF decreases mitochondrial oxidative phosphorylation and protects from obesity and diabetes.* Cell, 2007. **131**(3): p. 476-91.
210. Ellaway, C., et al., *Complex I deficiency in association with structural abnormalities of the diaphragm and brain.* J Inherit Metab Dis, 1998. **21**(1): p. 72-3.
211. Gerards, M., et al., *Defective complex I assembly due to C20orf7 mutations as a new cause of Leigh syndrome.* J Med Genet, 2010. **47**(8): p. 507-12.
212. Saada, A., et al., *Combined OXPHOS complex I and IV defect, due to mutated complex I assembly factor C20ORF7.* J Inherit Metab Dis, 2012. **35**(1): p. 125-31.
213. Pagliarini, D.J., et al., *A mitochondrial protein compendium elucidates complex I disease biology.* Cell, 2008. **134**(1): p. 112-23.
214. Nouws, J., et al., *Acyl-CoA dehydrogenase 9 is required for the biogenesis of oxidative phosphorylation complex I.* Cell Metab, 2010. **12**(3): p. 283-94.
215. Dewulf, J.P., et al., *Evidence of a wide spectrum of cardiac involvement due to ACAD9 mutations: Report on nine patients.* Mol Genet Metab, 2016. **118**(3): p. 185-9.
216. Ghezzi, D., et al., *SDHAF1, encoding a LYR complex-II specific assembly factor, is mutated in SDH-defective infantile leukoencephalopathy.* Nat Genet, 2009. **41**(6): p. 654-6.
217. Bayley, J.-P., et al., *SDHAF2 mutations in familial and sporadic paraganglioma and phaeochromocytoma.* The Lancet Oncology, 2010. **11**(4): p. 366-372.
218. Fernandez-Vizarra, E., et al., *Impaired complex III assembly associated with BCS1L gene mutations in isolated mitochondrial encephalopathy.* Hum Mol Genet, 2007. **16**(10): p. 1241-52.
219. Hinson, J.T., et al., *Missense mutations in the BCS1L gene as a cause of the Bjornstad syndrome.* N Engl J Med, 2007. **356**(8): p. 809-19.
220. Visapaa, I., et al., *GRACILE syndrome, a lethal metabolic disorder with iron overload, is caused by a point mutation in BCS1L.* Am J Hum Genet, 2002. **71**(4): p. 863-76.
221. Blazquez, A., et al., *Infantile mitochondrial encephalomyopathy with unusual phenotype caused by a novel BCS1L mutation in an isolated complex III-deficient patient.* Neuromuscul Disord, 2009. **19**(2): p. 143-6.
222. Tuppen, H.A., et al., *Long-term survival of neonatal mitochondrial complex III deficiency associated with a novel BCS1L gene mutation.* Mol Genet Metab, 2010. **100**(4): p. 345-8.
223. Gil-Borlado, M.C., et al., *Pathogenic mutations in the 5' untranslated region of BCS1L mRNA in mitochondrial complex III deficiency.* Mitochondrion, 2009. **9**(5): p. 299-305.
224. Ghezzi, D., et al., *Mutations in TTC19 cause mitochondrial complex III deficiency and neurological impairment in humans and flies.* Nat Genet, 2011. **43**(3): p. 259-63.
225. Atwal, P.S., *Mutations in the Complex III Assembly Factor Tetratricopeptide 19 Gene TTC19 Are a Rare Cause of Leigh Syndrome.* JIMD Rep, 2014. **14**: p. 43-5.
226. Barrientos, A., et al., *Suppression mechanisms of COX assembly defects in yeast and human: insights into the COX assembly process.* Biochim Biophys Acta, 2009. **1793**(1): p. 97-107.
227. Wang, Z.G., P.S. White, and S.H. Ackerman, *Atp11p and Atp12p are assembly factors for the F(1)-ATPase in human mitochondria.* J Biol Chem, 2001. **276**(33): p. 30773-8.
228. De Meirleir, L., *Respiratory chain complex V deficiency due to a mutation in the assembly gene ATP12.* Journal of Medical Genetics, 2004. **41**(2): p. 120-124.
229. Kopp, E., et al., *ECSIT is an evolutionarily conserved intermediate in the Toll/IL-1 signal transduction pathway.* Genes & Development, 1999. **13**(16): p. 2059-2071.
230. Xiao, C., et al., *Ecsit is required for Bmp signaling and mesoderm formation during mouse embryogenesis.* Genes Dev, 2003. **17**(23): p. 2933-49.
231. Vogel, R.O., et al., *Cytosolic signaling protein Ecsit also localizes to mitochondria where it interacts with chaperone NDUFAF1 and functions in complex I assembly.* Genes Dev, 2007. **21**(5): p. 615-24.

232. Kelley, L.A., et al., *The Phyre2 web portal for protein modeling, prediction and analysis.* Nat Protoc, 2015. **10**(6): p. 845-58.
233. Rackham, O. and A. Filipovska, *The role of mammalian PPR domain proteins in the regulation of mitochondrial gene expression.* Biochim Biophys Acta, 2012. **1819**(9-10): p. 1008-16.
234. Xu, F., et al., *Disruption of a mitochondrial RNA-binding protein gene results in decreased cytochrome b expression and a marked reduction in ubiquinol-cytochrome c reductase activity in mouse heart mitochondria.* Biochem J, 2008. **416**(1): p. 15-26.
235. Lightowlers, R.N. and Z.M. Chrzanowska-Lightowlers, *PPR (pentatricopeptide repeat) proteins in mammals: important aids to mitochondrial gene expression.* Biochem J, 2008. **416**(1): p. e5-6.
236. Baud, V., et al., *Signaling by proinflammatory cytokines: oligomerization of TRAF2 and TRAF6 is sufficient for JNK and IKK activation and target gene induction via an amino-terminal effector domain.* Genes Dev, 1999. **13**(10): p. 1297-308.
237. West, A.P., et al., *TLR signalling augments macrophage bactericidal activity through mitochondrial ROS.* Nature, 2011. **472**(7344): p. 476-80.
238. Mi Wi, S., et al., *Ubiquitination of ECSIT is crucial for the activation of p65/p50 NF-kappaBs in Toll-like receptor 4 signaling.* Mol Biol Cell, 2015. **26**(1): p. 151-60.
239. Wi, S.M., et al., *TAK1-ECSIT-TRAF6 complex plays a key role in the TLR4 signal to activate NF-kappaB.* J Biol Chem, 2014. **289**(51): p. 35205-14.
240. Moustakas, A., S. Souchelnytskyi, and C.H. Heldin, *Smad regulation in TGF-beta signal transduction.* J Cell Sci, 2001. **114**(Pt 24): p. 4359-69.
241. Guo, X. and X.-F. Wang, *Signaling cross-talk between TGF-β/BMP and other pathways.* Cell Research, 2008. **19**(1): p. 71-88.
242. Harvey, P.A. and L.A. Leinwand, *The cell biology of disease: cellular mechanisms of cardiomyopathy.* J Cell Biol, 2011. **194**(3): p. 355-65.
243. Teare, D., *Asymmetrical hypertrophy of the heart in young adults.* Br Heart J, 1958. **20**(1): p. 1-8.
244. Wald, D.S., M. Law, and J.K. Morris, *Mortality from hypertrophic cardiomyopathy in England and Wales: clinical and screening implications.* Int J Cardiol, 2004. **97**(3): p. 479-84.
245. Maron, B.J., et al., *Hypertrophic cardiomyopathy: present and future, with translation into contemporary cardiovascular medicine.* J Am Coll Cardiol, 2014. **64**(1): p. 83-99.
246. Efthimiadis, G.K., et al., *Hypertrophic cardiomyopathy in 2013: Current speculations and future perspectives.* World J Cardiol, 2014. **6**(2): p. 26-37.
247. Walsh, R., et al., *Defining the genetic architecture of hypertrophic cardiomyopathy: re-evaluating the role of non-sarcomeric genes.* Eur Heart J, 2017. **38**(46): p. 3461-3468.
248. Blair, E., et al., *Mutations in the gamma(2) subunit of AMP-activated protein kinase cause familial hypertrophic cardiomyopathy: evidence for the central role of energy compromise in disease pathogenesis.* Hum Mol Genet, 2001. **10**(11): p. 1215-20.
249. Hershberger, R.E., D.J. Hedges, and A. Morales, *Dilated cardiomyopathy: the complexity of a diverse genetic architecture.* Nat Rev Cardiol, 2013. **10**(9): p. 531-47.
250. Herman, D.S., et al., *Truncations of titin causing dilated cardiomyopathy.* N Engl J Med, 2012. **366**(7): p. 619-28.
251. Wabbels, B., et al., *Chronisch-progressive externe Ophthalmoplegie und Kearns-Sayre-Syndrom.* Der Ophthalmologe, 2008. **105**(6): p. 550-556.
252. Young, T.J., et al., *Kearns-Sayre syndrome: a case report and review of cardiovascular complications.* Pacing Clin Electrophysiol, 2005. **28**(5): p. 454-7.
253. Pavlakis, S.G., et al., *Mitochondrial myopathy, encephalopathy, lactic acidosis, and strokelike episodes: a distinctive clinical syndrome.* Ann Neurol, 1984. **16**(4): p. 481-8.
254. Hirano, M., et al., *Melas: an original case and clinical criteria for diagnosis.* Neuromuscul Disord, 1992. **2**(2): p. 125-35.

255. Nesbitt, V., et al., *The UK MRC Mitochondrial Disease Patient Cohort Study: clinical phenotypes associated with the m.3243A>G mutation--implications for diagnosis and management.* J Neurol Neurosurg Psychiatry, 2013. **84**(8): p. 936-8.
256. Kirby, D.M., et al., *Mutations of the mitochondrial ND1 gene as a cause of MELAS.* J Med Genet, 2004. **41**(10): p. 784-9.
257. Liolitsa, D., et al., *Is the mitochondrial complex I ND5 gene a hot-spot for MELAS causing mutations?* Ann Neurol, 2003. **53**(1): p. 128-32.
258. Ravn, K., et al., *An mtDNA mutation, 14453G-->A, in the NADH dehydrogenase subunit 6 associated with severe MELAS syndrome.* Eur J Hum Genet, 2001. **9**(10): p. 805-9.
259. Leigh, D., *Subacute necrotizing encephalomyelopathy in an infant.* J Neurol Neurosurg Psychiatry, 1951. **14**(3): p. 216-21.
260. Lake, N.J., et al., *Leigh syndrome: One disorder, more than 75 monogenic causes.* Ann Neurol, 2016. **79**(2): p. 190-203.
261. Rahman, S., et al., *Leigh syndrome: clinical features and biochemical and DNA abnormalities.* Ann Neurol, 1996. **39**(3): p. 343-51.
262. Carrozzo, R., et al., *The T9176G mtDNA mutation severely affects ATP production and results in Leigh syndrome.* Neurology, 2001. **56**(5): p. 687-690.
263. Irwin, M.H., K. Parameshwaran, and C.A. Pinkert, *Mouse models of mitochondrial complex I dysfunction.* Int J Biochem Cell Biol, 2013. **45**(1): p. 34-40.
264. Kruse, S.E., et al., *Mice with mitochondrial complex I deficiency develop a fatal encephalomyopathy.* Cell Metab, 2008. **7**(4): p. 312-20.
265. Ke, B.X., et al., *Tissue-specific splicing of an Ndufs6 gene-trap insertion generates a mitochondrial complex I deficiency-specific cardiomyopathy.* Proc Natl Acad Sci U S A, 2012. **109**(16): p. 6165-70.
266. Russell, W.L., et al., *Specific-locus test shows ethylnitrosourea to be the most potent mutagen in the mouse.* Proc Natl Acad Sci U S A, 1979. **76**(11): p. 5818-9.
267. Justice, M.J., et al., *Mouse ENU mutagenesis.* Hum Mol Genet, 1999. **8**(10): p. 1955-63.
268. Acevedo-Arozena, A., et al., *ENU mutagenesis, a way forward to understand gene function.* Annu Rev Genomics Hum Genet, 2008. **9**: p. 49-69.
269. Stottmann, R. and D. Beier, *ENU Mutagenesis in the Mouse.* Curr Protoc Hum Genet, 2014. **82**: p. 15 4 1-10.
270. Potter, P.K., et al., *Novel gene function revealed by mouse mutagenesis screens for models of age-related disease.* Nat Commun, 2016. **7**: p. 12444.
271. Brown, S.D. and R.E. Hardisty, *Mutagenesis strategies for identifying novel loci associated with disease phenotypes.* Semin Cell Dev Biol, 2003. **14**(1): p. 19-24.
272. Yu, Q., et al., *ENU induced mutations causing congenital cardiovascular anomalies.* Development, 2004. **131**(24): p. 6211-23.
273. Shen, Y., et al., *Cardiovascular phenotyping of fetal mice by noninvasive high-frequency ultrasound facilitates recovery of ENU-induced mutations causing congenital cardiac and extracardiac defects.* Physiol Genomics, 2005. **24**(1): p. 23-36.
274. Goldsworthy, M.E. and P.K. Potter, *Modelling age-related metabolic disorders in the mouse.* Mamm Genome, 2014. **25**(9-10): p. 487-96.
275. Boukens, B.J., et al., *Misinterpretation of the mouse ECG: 'musing the waves of Mus musculus'.* J Physiol, 2014. **592**(21): p. 4613-26.
276. Omairi, S., et al., *Link between MHC Fiber Type and Restoration of Dystrophin Expression and Key Components of the DAPC by Tricyclo-DNA-Mediated Exon Skipping.* Mol Ther Nucleic Acids, 2017. **9**: p. 409-418.
277. Ehler, E., T. Moore-Morris, and S. Lange, *Isolation and culture of neonatal mouse cardiomyocytes.* J Vis Exp, 2013(79).
278. Uutela, M., et al., *PDGF-D induces macrophage recruitment, increased interstitial pressure, and blood vessel maturation during angiogenesis.* Blood, 2004. **104**(10): p. 3198-204.

279. Winn, M.P., et al., *A mutation in the TRPC6 cation channel causes familial focal segmental glomerulosclerosis.* Science, 2005. **308**(5729): p. 1801-4.
280. Farrugia, A., *Albumin usage in clinical medicine: tradition or therapeutic?* Transfus Med Rev, 2010. **24**(1): p. 53-63.
281. Stocker, R., et al., *Bilirubin is an antioxidant of possible physiological importance.* Science, 1987. **235**(4792): p. 1043-6.
282. Martin, P., *148 - Approach to the Patient with Liver Disease A2 - Goldman, Lee*, in *Goldman's Cecil Medicine (Twenty-Fourth Edition)*, A.I. Schafer, Editor. 2012, W.B. Saunders: Philadelphia. p. 952-956.
283. Streja, D.A., E.B. Marliss, and G. Steiner, *The effects of prolonged fasting on plasma triglyceride kinetics in man.* Metabolism, 1977. **26**(5): p. 505-16.
284. Kemp, M., et al., *Biochemical markers of myocardial injury.* Br J Anaesth, 2004. **93**(1): p. 63-73.
285. Lygate, C.A., et al., *The creatine kinase energy transport system in the failing mouse heart.* J Mol Cell Cardiol, 2007. **42**(6): p. 1129-36.
286. Lee, T.H. and L. Goldman, *Serum enzyme assays in the diagnosis of acute myocardial infarction. Recommendations based on a quantitative analysis.* Ann Intern Med, 1986. **105**(2): p. 221-33.
287. Mythili, S. and N. Malathi, *Diagnostic markers of acute myocardial infarction.* Biomed Rep, 2015. **3**(6): p. 743-748.
288. Sivitz, W.I. and M.A. Yorek, *Mitochondrial dysfunction in diabetes: from molecular mechanisms to functional significance and therapeutic opportunities.* Antioxid Redox Signal, 2010. **12**(4): p. 537-77.
289. Yang, Y., et al., *The emerging role of Toll-like receptor 4 in myocardial inflammation.* Cell Death Dis, 2016. **7**: p. e2234.
290. Yuasa, S. and K. Fukuda, *Multiple roles for BMP signaling in cardiac development.* Drug Discovery Today: Therapeutic Strategies, 2008. **5**(4): p. 209-214.
291. Yang, X., et al., *Generation of Smad4/Dpc4 conditional knockout mice.* Genesis, 2002. **32**(2): p. 80-1.
292. Chu, G.C., et al., *Differential requirements for Smad4 in TGFbeta-dependent patterning of the early mouse embryo.* Development, 2004. **131**(15): p. 3501-12.
293. Azhar, M., et al., *Myocardial deletion of Smad4 using a novel alpha skeletal muscle actin Cre recombinase transgenic mouse causes misalignment of the cardiac outflow tract.* Int J Biol Sci, 2010. **6**(6): p. 546-55.
294. Nijtmans, L.G., N.S. Henderson, and I.J. Holt, *Blue Native electrophoresis to study mitochondrial and other protein complexes.* Methods, 2002. **26**(4): p. 327-34.
295. Soler-Lopez, M., et al., *Interactome mapping suggests new mechanistic details underlying Alzheimer's disease.* Genome Res, 2011. **21**(3): p. 364-76.
296. Zhang, C., et al., *Unfolded protein response plays a critical role in heart damage after myocardial ischemia/reperfusion in rats.* PLoS One, 2017. **12**(6): p. e0179042.
297. Monhart, V., *Hypertension and chronic kidney diseases.* Cor et Vasa, 2013. **55**(4): p. e397-e402.
298. Williams, L. and M. Frenneaux, *Syncope in hypertrophic cardiomyopathy: mechanisms and consequences for treatment.* Europace, 2007. **9**(9): p. 817-22.
299. Franceschini, N., et al., *Orthostatic hypotension and incident chronic kidney disease: the atherosclerosis risk in communities study.* Hypertension, 2010. **56**(6): p. 1054-9.
300. Rodenburg, R.J., *Biochemical diagnosis of mitochondrial disorders.* J Inherit Metab Dis, 2011. **34**(2): p. 283-92.
301. McCormick, E., E. Place, and M.J. Falk, *Molecular genetic testing for mitochondrial disease: from one generation to the next.* Neurotherapeutics, 2013. **10**(2): p. 251-61.
302. Claycomb, W.C., et al., *HL-1 cells: a cardiac muscle cell line that contracts and retains phenotypic characteristics of the adult cardiomyocyte.* Proc Natl Acad Sci U S A, 1998. **95**(6): p. 2979-84.

303. Bakermans, A.J., et al., *In vivo mouse myocardial (31)P MRS using three-dimensional image-selected in vivo spectroscopy (3D ISIS): technical considerations and biochemical validations.* NMR Biomed, 2015. **28**(10): p. 1218-27.
304. Picard, M., et al., *Mitochondrial structure and function are disrupted by standard isolation methods.* PLoS One, 2011. **6**(3): p. e18317.
305. Kolwicz, S.C., Jr. and R. Tian, *Glucose metabolism and cardiac hypertrophy.* Cardiovasc Res, 2011. **90**(2): p. 194-201.
306. Dong, Z., et al., *Astragaloside IV alleviates heart failure via activating PPARalpha to switch glycolysis to fatty acid beta-oxidation.* Sci Rep, 2017. **7**(1): p. 2691.
307. Di Meo, I., et al., *AAV9-based gene therapy partially ameliorates the clinical phenotype of a mouse model of Leigh syndrome.* Gene Ther, 2017. **24**(10): p. 661-667.

Appendix

9.1. Appendix 1

Mass spec results from the 4 gel slices isolated in 2D BN-PAGE showing the proteins identified in each gel slice.

Slice A	Slice B	Slice C	Slice D
ALDH6A1	ABAT	ACAA2	ABCB8
ATP5A1	ABCB8	ACAD10	ACADVL
ATP5B	ACAA2	ACADL	ACOT13
DBT	ACAD10	ACADM	ACTB
DLST	ACAD11	ACADS	AIFM1
DSP	ACAD9	ACADVL	APOO
HELZ2	ACADL	ACAT1	ATP2A2
HSPA9	ACADM	ACO2	ATP5A1
IMMT	ACADVL	ACOT2	ATP5B
KRT1	ACAT1	ACOT9	ATP5C1
KRT10	ACO2	ACOX3	ATP5D
KRT13	ACOT9	ACSL1	ATP5E
KRT2	ACOX1	ACSS1	ATP5F1
KRT42	ACSL1	ACTB	ATP5H
KRT5	ACTB	ACTC1	ATP5J
KRT6B	ACTR3	ADHFE1	ATP5J2
KRT73	ADSSL1	AFG1L	ATP5L
KRT76	AFG3L2	AFG3L2	ATP5O
KRT77	AGK	AGK	BDH1
KRT79	AHSG	AIFM1	CASQ2
KRT82	AIFM1	ANXA2	CCSMST1
SAMM50	ALB	APMAP	CHCHD3
	ALDH2	ATP2A2	CHCHD4
	ALDH5A1	ATP5A1	CKMT2
	ALDH6A1	ATP5B	COL10A1
	ANXA2	BCAT2	COX4I1
	APOH	BCKDHA	COX5A
	ART3	BCL2L13	COX5B
	ATP1A1	BDH1	COX7A1
	ATP1B1	BSG	COX7A2L
	ATP2A2	BZW2	CPT1B
	ATP5A1	CASQ2	CPT2
	ATP5B	CKM	CRAT
	ATP5C1	CKMT2	CS
	ATP5H	COQ6	CSPG4
	ATP5O	COQ8A	CYB5B
	BCKDHA	CPT2	CYC1
	BCL2L13	CRAT	DIAPH3
	BDH1	CS	DSP

	CASQ2	D2HGDH	EPB42
	CKMT2	DECR1	FABP5
	COQ8A	DLD	FAM162A
	COX4I1	DNAJA2	FECH
	COX7A1	DNAJA4	GNB4
	CPT1B	DSP	GOT2
	CPT2	ECI1	GPX4
	CRAT	EEF1A1	HADH
	CS	EHD1	HADHA
	CYC1	EHD2	HADHB
	DECR1	EHD4	HBA
	DES	ENO1	HBB-B1
	DLST	ENO3	HSPA5
	DSG1B	ETFA	HSPA9
	DSP	ETFB	HSPD1
	ECHS1	ETFDH	IDH2
	EEF1A1	FABP5	IMMT
	EEF1A2	FARS2	KIF24
	EHD2	FH	KRT1
	ENO3	FLAD1	KRT10
	EPHX1	FLOT2	KRT14
	FH	GC	KRT2
	GK	GCDH	KRT42
	GLUD1	GNAS	KRT5
	GOT2	GOT2	KRT6A
	HADHA	GRSF1	KRT73
	HADHB	HADH	KRT76
	HBB-B1	HADHA	KRT79
	HK1	HADHB	MB
	HK2	HBB-B1	MDH2
	HSD17B4	HIBADH	MGST3
	HSPA14	HK1	MPC2
	HSPA5	HK2	MPV17
	HSPA8	HNRNPM	MRPL12
	HSPA9	HSD17B4	MRPL17
	HSPD1	HSPA5	MRPL20
	IDH2	HSPA9	MRPL23
	IDH3A	HSPD1	MRPL43
	IDH3G	HTRA1	MRPL49
	IMMT	IARS2	MRPS10
	JUP	IDH1	MRPS23
	KIF27	IDH2	MRPS28
	KRT1	IDH3G	MTCO2
	KRT10	IFT20	MTND3
	KRT14	JUP	NDUFA1
	KRT16	KRT1	NDUFA10

	KRT17	KRT10	NDUFA11
	KRT2	KRT14	NDUFA12
	KRT31	KRT2	NDUFA13
	KRT34	KRT42	NDUFA2
	KRT35	KRT5	NDUFA3
	KRT42	KRT6A	NDUFA4
	KRT5	KRT71	NDUFA5
	KRT6A	KRT79	NDUFA6
	KRT75	KYAT3	NDUFA7
	KRT76	L2HGDH	NDUFA8
	KRT77	LEG1	NDUFAF3
	KRT79	LRIG3	NDUFB11
	KRT81	LRP6	NDUFB3
	KRT85	MDH2	NDUFB4
	LONP1	MGST3	NDUFB5
	LRPPRC	MRM3	NDUFB6
	MCCC2	MRPL37	NDUFB7
	MDH2	MRPS30	NDUFB8
	MFGE8	MTOR	NDUFC2
	MGST3	NADK2	NDUFS1
	MLYCD	NAGA	NDUFS2
	MRC1	NCEH1	NDUFS4
	MRPS30	NDRG2	NDUFS5
	MTCH2	NDUFS2	NDUFS6
	MTCO1	NFS1	NDUFS7
	MTCO2	NNT	NDUFS8
	MT-CO3	OAT	NDUFV1
	NCEH1	OXCT1	NDUFV2
	NDUFS2	OXSM	NES
	NDUFV1	PA2G4	NME2
	NNT	PAFAH1B1	NME3
	OGDH	PDHA1	NPPA
	OPA1	PDHB	OPA1
	PDHX	PDIA6	PCCA
	PLEC	PDK1	PDHA1
	PMPCB	PDK2	PDHB
	PRDX1	PDK4	PHB
	PRX	PGK1	PHB2
	RPS27A	PMPCB	PRDX2
	SAMM50	PRDX2	PRDX5
	SDHA	RPS27A	RICTOR
	SERPINH1	SAMM50	RPS27A
	SFN	SCCPDH	RTN2
	SLC25A12	SDHA	SAMM50
	SLC25A3	SDHB	SCCPDH
	SLC25A4	SEMA4D	SDHA

	SLC25A5	SEPSECS	SDHC
	SLC30A9	SERINC3	SLC25A11
	SLC4A1	SERPINH1	SLC25A12
	SPRR2B	SLC25A12	SLC25A3
	STEAP3	SLC25A13	SLC25A4
	SUCLA2	SLC25A3	SLC25A5
	TGM3	SLC25A4	SLC4A1
	TKTL1	SLC25A46	SUCLA2
	TRIM72	SLC25A5	TMEM11
	TUFM	SLC2A4	TMEM160
	UQCRC1	SQOR	TMEM186
	UQCRC2	SUCLA2	TMEM242
	UQCRFS1	SUCLG2	TOMM22
	VAT1	TIMM44	TUFM
	VDAC2	TM9SF2	UQCR10
	VDAC3	TM9SF3	UQCRB
		TMEM143	UQCRC1
		TMX4	UQCRC2
		TNPO2	UQCRFS1
		TOMM70	UQCRQ
		TPP1	USMG5
		TRMU	VDAC2
		TUBA1B	
		TUFM	
		TXNDC5	
		UQCRC1	
		UQCRC2	
		VDAC2	
		YARS2	